Crystal engineering with coordination, hydrogen- and halogen-bonds, and the construction of porous solids

by

Chamara Abeywickramasinghe Gunawardana

B.S., University of Colombo, 2009

AN ABSTRACT OF A DISSERTATION

submitted in partial fulfillment of the requirements for the degree

DOCTOR OF PHILOSOPHY

Department of Chemistry
College of Arts and Sciences

KANSAS STATE UNIVERSITY
Manhattan, Kansas

2018

Abstract

A set of multifunctional molecules [isomeric forms of 1-(pyridylmethyl)-2,2'-biimidazole] was synthesized and subjected to systematic co-crystallizations with selected hydrogen- and halogen-bond donors in order to explore the impact of interaction type, geometry and electrostatics on the resulting supramolecular architectures. The structural outcome with hydrogen-bond donors (carboxylic acids) is somewhat unpredictable because of the presence of the acid···biimidazole heterosynthon that can compete with biimidazole···biimidazole homosynthon. In contrast, the solid-state supramolecular behavior of those probe molecules is largely unchanged in halogen-bonded co-crystals. Only two types of primary interactions, the two-point hydrogen bonds responsible for pairing biimidazole moieties, and the single-point halogen bonds responsible for the co-crystal formation and structure extension, are present in these systems. The results highlight that, by incorporating geometric biases along with orthogonal interactions, one can effectively prevent synthon crossover which is of paramount importance in complex crystal engineering endeavors.

Heterobifunctional ligands pave the way for elaborate metallo-supramolecular systems, and are also useful for combining metal-ligand bonding with other types of non-covalent interactions. Nine new acetylacetonate ligands featuring either pyridyl- or thiophenyl-heterocycles were successfully prepared, and their metal binding abilities were studied with selected di- and tri-valent transition metal ions. As expected, the acetylacetonate ligation to metal dications remains consistent. In each case, the metal is four-coordinate and resides in a square planar environment. Differences in the overall architectures arise from the role played by the terminal heterocycles and the solvent. In seven (out of nine) structures, the heterocyclic end is involved in a structure-directing interaction and it is more prevalent in ligands bearing 4-pyridinyl unit.

Divergent molecules containing bulky substituents tend to produce porous materials *via* frustrated packing. Two rigid tetrahedral cores, tetraphenylmethane and 1,3,5,7-tetraphenyladamantane, grafted peripherally with four (trimethylsilyl)ethynyl moieties were found to have only isolated voids in their crystal structures. Hence, they were modified into tecton-like entities, tetrakis(4-(iodoethynyl)phenyl)methane [**I_4TEPM**] and 1,3,5,7-tetrakis(4-(iodoethynyl)phenyl)adamantane [**I_4TEPA**], and the effect of motif-forming characteristics of iodoethynyl units on molecular arrangement and crystal porosity was analyzed. **I_4TEPM** not only holds increased free volume compared to its precursor, but also forms one-dimensional channels. Furthermore, it readily co-crystallizes with Lewis basic solvents to afford two-component porous materials even though they suffer from stability issues.

As the binding sites in **I_4TEPM** and **I_4TEPA** are tetrahedrally-predisposed, they can be further utilized for the modular assembly of highly symmetric, three-dimensional extended architectures. With that in mind, these two building blocks were subsequently allowed to react with various halide salts, and it was found that the reactions between **I_4TEPM** and tetraphenylphosphonium halides readily yield four-fold interpenetrated diamondoid networks sustained by C–I···X^- (X^- = chloride, bromide, iodide) halogen-bonding interactions. The halide anions exhibit mutual-induced fitting of their coordination and act as four-connecting tetrahedral nodes, while the tetraphenylphosphonium cations render essential templating information and structural support.

Crystal engineering with coordination, hydrogen- and halogen-bonds, and the construction of porous solids

by

Chamara Abeywickramasinghe Gunawardana

B.S., University of Colombo, 2009

A DISSERTATION

submitted in partial fulfillment of the requirements for the degree

DOCTOR OF PHILOSOPHY

Department of Chemistry
College of Arts and Sciences

KANSAS STATE UNIVERSITY
Manhattan, Kansas

2018

Approved by:

Major Professor
Christer B. Aakeröy

Copyright

Abstract

A set of multifunctional molecules [isomeric forms of 1-(pyridylmethyl)-2,2'-biimidazole] was synthesized and subjected to systematic co-crystallizations with selected hydrogen- and halogen-bond donors in order to explore the impact of interaction type, geometry and electrostatics on the resulting supramolecular architectures. The structural outcome with hydrogen-bond donors (carboxylic acids) is somewhat unpredictable because of the presence of the acid···biimidazole heterosynthon that can compete with biimidazole···biimidazole homosynthon. In contrast, the solid-state supramolecular behavior of those probe molecules is largely unchanged in halogen-bonded co-crystals. Only two types of primary interactions, the two-point hydrogen bonds responsible for pairing biimidazole moieties, and the single-point halogen bonds responsible for the co-crystal formation and structure extension, are present in these systems. The results highlight that, by incorporating geometric biases along with orthogonal interactions, one can effectively prevent synthon crossover which is of paramount importance in complex crystal engineering endeavors.

Heterobifunctional ligands pave the way for elaborate metallo-supramolecular systems, and are also useful for combining metal-ligand bonding with other types of non-covalent interactions. Nine new acetylacetonate ligands featuring either pyridyl- or thiophenyl-heterocycles were successfully prepared, and their metal binding abilities were studied with selected di- and tri-valent transition metal ions. As expected, the acetylacetonate ligation to metal dications remains consistent. In each case, the metal is four-coordinate and resides in a square planar environment. Differences in the overall architectures arise from the role played by the terminal heterocycles and the solvent. In seven (out of nine) structures, the heterocyclic end is involved in a structure-directing interaction and it is more prevalent in ligands bearing 4-pyridinyl unit.

Divergent molecules containing bulky substituents tend to produce porous materials *via* frustrated packing. Two rigid tetrahedral cores, tetraphenylmethane and 1,3,5,7-tetraphenyladamantane, grafted peripherally with four (trimethylsilyl)ethynyl moieties were found to have only isolated voids in their crystal structures. Hence, they were modified into tecton-like entities, tetrakis(4-(iodoethynyl)phenyl)methane [**I_4TEPM**] and 1,3,5,7-tetrakis(4-(iodoethynyl)phenyl)adamantane [**I_4TEPA**], and the effect of motif-forming characteristics of iodoethynyl units on molecular arrangement and crystal porosity was analyzed. **I_4TEPM** not only holds increased free volume compared to its precursor, but also forms one-dimensional channels. Furthermore, it readily co-crystallizes with Lewis basic solvents to afford two-component porous materials even though they suffer from stability issues.

As the binding sites in **I_4TEPM** and **I_4TEPA** are tetrahedrally-predisposed, they can be further utilized for the modular assembly of highly symmetric, three-dimensional extended architectures. With that in mind, these two building blocks were subsequently allowed to react with various halide salts, and it was found that the reactions between **I_4TEPM** and tetraphenylphosphonium halides readily yield four-fold interpenetrated diamondoid networks sustained by C–I···X^- (X^- = chloride, bromide, iodide) halogen-bonding interactions. The halide anions exhibit mutual-induced fitting of their coordination and act as four-connecting tetrahedral nodes, while the tetraphenylphosphonium cations render essential templating information and structural support.

Table of Contents

List of Figures

List of Tables

Acknowledgements

First, I would like to express my devout dignity and heartiest gratitude to my soon-to-be Alma Mater, Kansas State University, for giving me this wonderful opportunity to pursue my doctoral studies under your wing.

There are many people to whom I owe thanks as they were, in one way or another, a crucial part during my stay at KSU.

- Foremost is my supervisor, Prof. Christer Aakeröy. I am greatly indebted to him for his professional guidance, constant encouragement and patience in supervision throughout my graduate school career. Above all, he and his wife, Dr. Yasmin Patell, were such gracious hosts over the years, always providing interesting and engaging conversations.
- I am also grateful to my supervisory committee, Prof. Paul Smith, Prof. Emily McLaurin and Prof. James Edgar (Chemical Engineering) for their valuable time and input. Prof. Scott Smith (Animal Sciences and Industry) is gratefully acknowledged for serving as chairperson of the examining committee for my PhD defense.
- Much of my research has been relied upon single-crystal X-ray crystallography, so the contribution from Dr. John Desper, Dr. Abhijeet Sinha, Dr. Marijana Đaković (University of Zagreb, Croatia), Dr. Victor Day (University of Kansas) and Dr. Eric Reinheimer (Rigaku Americas Corporation) can never be forgotten.
- Thanks are also due to my lab colleagues, especially to Manomi, Janaka, Stefan, Bhupi and Nandini. It has been a pure pleasure to work amongst such talented and amazing friends. Special thanks go to former members, Dr. Tharanga Wijethunga and Dr. Dhanushi Welideniya,

for their helping hands during my initial days in the Aakeröy lab. Noahlana Monzon, a summer REU student, deserves much praise for being a terrific research assistant.

- I have been blessed with wonderful teachers, Prof. Eric Maatta, Prof. Emily McLaurin, Prof. Christopher Levy, Prof. Stefan Bossmann and Prof. Duy Hua. Thank you all so much for helping me to broaden my horizons.
- I would like to thank Dr. Sheelu Panikkattu and Ms. Christa Obermeyer for providing invaluable safety lessons, and Mr. Michael Hinton for guiding me to become a better mentor.
- Thanks to Dr. Leila Maurmann, Dr. Tingting Liu, Mr. Jim Hodgson, Mr. Ron Jackson, Mr. Tobe Eggers, Ms. Mary Dooley and Ms. Kimberly Ross not just for technical support but also for their friendship over the years.
- Last, but not least, my warm thanks go to all my family, particularly to my mother and my darling, Sajini, for their unconditional love and constant support, encouragement and patience. Our bundle of cuteness, Dewmi, merits special mention here because she did an excellent job by serving as a stress buster. Whenever I felt overwhelmed, seeing her smile made it all go away in an instant.

Dedication

To my little princess, *Dewmi*, even though she is way too young to understand the content.

Preface

The research for this dissertation was conducted in the Aakeröy Laboratory at Kansas State University, between December 2013 and June 2018. To the best of my knowledge, this work is original, except where acknowledgements and references have been made to previous work.

A version of Chapter 2 has been published in *Faraday Discussions* (Gunawardana, C. A.; Desper, J.; Sinha, A. S.; Đaković, M.; Aakeröy, C. B., Competition and selectivity in supramolecular synthesis: structural landscape around 1-(pyridylmethyl)-2,2'-biimidazoles. *Faraday Discuss.* **2017,** *203*, 371–388).

A version of Chapter 5 has been published in *Chemical Communications* (Gunawardana, C. A.; Đaković, M.; Aakeröy, C. B., Diamondoid architectures from halogen-bonded halides. *Chem. Commun.* **2018,** *54* (6), 607–610).

The remaining sections will be published in due course.

Chapter 1 - Introduction

This section is devoted to introducing the key goals of my PhD research. For the sake of comprehensiveness, a brief discussion on supramolecular chemistry and crystal engineering is also given as the research described herein is mainly founded upon the concepts of these two fields.

1.1 Supramolecular chemistry

The chemistry of the covalent bond, or simply molecular chemistry, is a powerful discipline for synthesizing molecules by making and breaking covalent bonds as well as for establishing a connection between molecular structure and reactivity. It has long been the practice of chemists and at the heart of many significant advances. In this context, the seminal work of Wöhler (the synthesis of urea in 1828) can serve as a reference point.[1] Since then, the synthetic chemist has gained considerable control over the covalent bond over more than 190 years of research. As exemplified by the original synthesis of vitamin B_{12},[2] it is now possible to make compounds of previously unimagined complexity thanks to the endless number of tools (different reactions, specific catalysts and reagents, protection/deprotection protocols, purification techniques, characterization techniques, *etc.*) that can be explored for developing multi-step synthetic routes.

"Just as there is a field of molecular chemistry based on the covalent bond, there is a field of supramolecular chemistry, the chemistry of molecular assemblies and of the intermolecular bond".[3] Supramolecular chemistry was defined by Lehn as "chemistry beyond molecule" which introduce so-called "supermolecules".[4] Originally termed "übermoleküle" to describe carboxylic acid dimers,[5] supermolecules (or supramolecules) are molecular aggregates held together by diverse types of non-covalent linkages such as hydrogen-bonds (HBs), halogen-bonds (XBs), electrostatic/Coulombic forces, π-π stacking interactions, *etc*. Molecular recognition is a key aspect of supramolecular chemistry with a focus on size, shape, and complementarity match

between the two components (host and guest) of a molecular association event. Even though covalent modifications of molecules can be performed using step-by-step reactions in which intermediate products are generally isolated and purified at each step, supramolecular synthesis has to be carried out in one-pot manner (Figure 1.1).

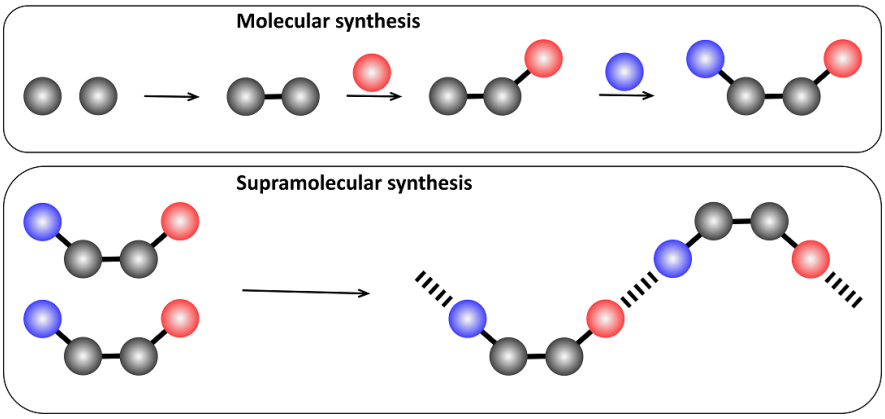

Figure 1.1 Covalent synthesis *versus* supramolecular synthesis.

1.2 Crystal engineering

The idea of making crystalline solids by design or with a purpose was proposed by Pepinsky some 60 years ago, where he used the term "crystal engineering" for the first time.[6] Roughly two decades later, Schmidt brought it back to his work concerning the photo-dimerization in the solid state.[7] However, as a focused and readily identifiable research area, crystal engineering began to flourish only in 1990s.[8]

Desiraju defined crystal engineering as the "understanding of intermolecular interactions in the context of crystal packing and the utilization of such understanding in the design of new solids with desired physical and chemical properties"[9] whereas Dunitz recognized a crystal as the "supermolecule *par excellence*".[10] These notions emphasize that crystal engineering has close

links to concepts and principles developed in supramolecular chemistry. In fact, they often share a common scientific language and a unifying perception, so crystal engineering is better to be treated as a subdivision of supramolecular chemistry. The success we see today in crystal engineering can be credited to tremendous improvements in our understanding of molecular self-assembly in the solid state, and of how supramolecular interactions, such as hydrogen and halogen bonds, steer such processes.[11] Moreover, the sophisticated and reliable analytical tools, fast screening methods as well as computational and knowledge-based predictive methods have accelerated its evolution.

1.2.1 Competition among supramolecular synthons

Any crystal engineering attempt can be divided into three phases; design, construction (*via* a bottom-up approach) and utilization of crystalline materials.[12] As mentioned before, such syntheses need to be carried out in one-pot manner and are mediated by inherently dynamic supramolecular forces. Hence, the success (the target having the desired connectivity, composition and properties) heavily depends on the quality of the designing step. To make life easier for crystal engineers, Desiraju formulated the concept of supramolecular synthons, with which designing becomes less difficult. Supramolecular synthons are "structural units within supermolecules which can be formed and/or assembled by known or conceivable synthetic operations involving intermolecular interactions".[13]

When two confronting multifunctional supramolecular reactants do not have enough complementary binding sites (a mismatch in acceptor/donor ratio) or multiple synthons strive for dominance over one another, they start competing with each other. It can lead to the downfall of the synthetic attempt and take us away from our intended target assembly. Due to variable connectivities and stoichiometries, the outcome becomes less predictable. To render structural

insulation and guarantee the exclusive appearance of a certain synthon (or a set of synthons) from a common pool, while masking all undesired ones, one should rely on empirical knowledge (robustness, reproducibility, transferability and relative strengths) of involving synthons. Co-crystals (*i.e.* multi-component molecular crystals, Figure 1.2)[14] are ideal for studying synthon competition and for gathering necessary empirical knowledge because, by spreading functional groups over multiple molecules, steric influences can be minimized.[15]

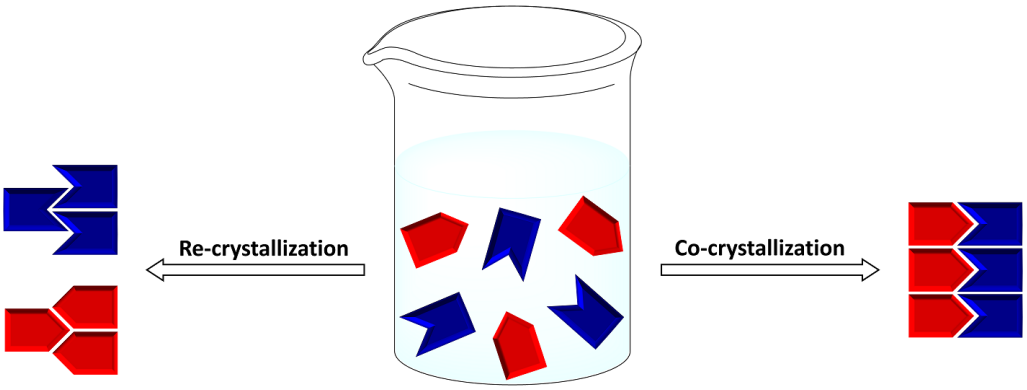

Figure 1.2 Schematic showing the formation of co-crystals.

Let's consider an imaginary co-crystallization experiment involving a heteroditopic acceptor, **X**, and a homoditopic donor, **Y**. Three different ways (among other possibilities) they can associate are shown in Figure 1.3. If the desired product is an **X_2Y-I** trimer comprised of A1···D interactions, any other synthon crossover events (in this case, the formation of A2···D interactions) need to be circumvented. This can be achieved by establishing a hierarchy, that is, designing **X** in such a way that A1 is significantly stronger than A2. If not, the occurrence of undesired synthons may not be completely suppressed, and the desired product will be contaminated with by-products such as **X_2Y-II** and **XY**. Such events not only reduce the supramolecular yield of the expected product but also pose difficulties in obtaining phase-pure

material. In a worst-case scenario, when the competitiveness is really high, the synthesis may become completely ineffective or even counterproductive.

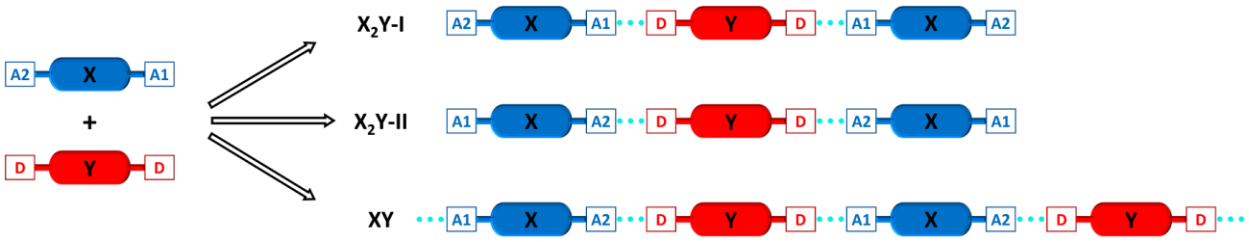

Figure 1.3 Synthon competition can lead to multiple products.

1.2.2 Coordination-driven supramolecular assemblies

Supramolecular interactions in crystal engineering need not necessarily be non-covalent in nature. Technically, any kind of linkage which is sufficiently reversible (*e.g.* dynamic covalent bonds, coordinate-covalent bonds) can be employed to engineer molecules in solid state (Figure 1.4).[16] Indeed, coordination-driven supramolecular assemblies constitute by far the largest class of engineered crystal structures and are arguably one of the fastest growing areas in chemistry. These hybrid materials, made up of organic ligands and metal ions/clusters, are often endowed with remarkable optical, magnetic, catalytic, adsorption and electrochemical properties that can be exploited in various real-world applications.

There are two broad structural classes of metal-organic architectures; finite and infinite.[17] Finite ones are discrete and can be thought of as zero-dimensional molecular species (such as mononuclear complexes, acyclic dimers, rhomboids, triangles, squares, capsules, helices, cages, and other oligomeric structures). Infinite architectures, on the other hand, are coordination compounds of metal ions (or clusters) and organic ligands/linkers that extend infinitely into one, two or three dimensions through repeating coordination entities with more or less covalent, metal-

ligand bonding. They are commonly known as coordination polymers (or coordination networks when extending in two or three dimensions).[18]

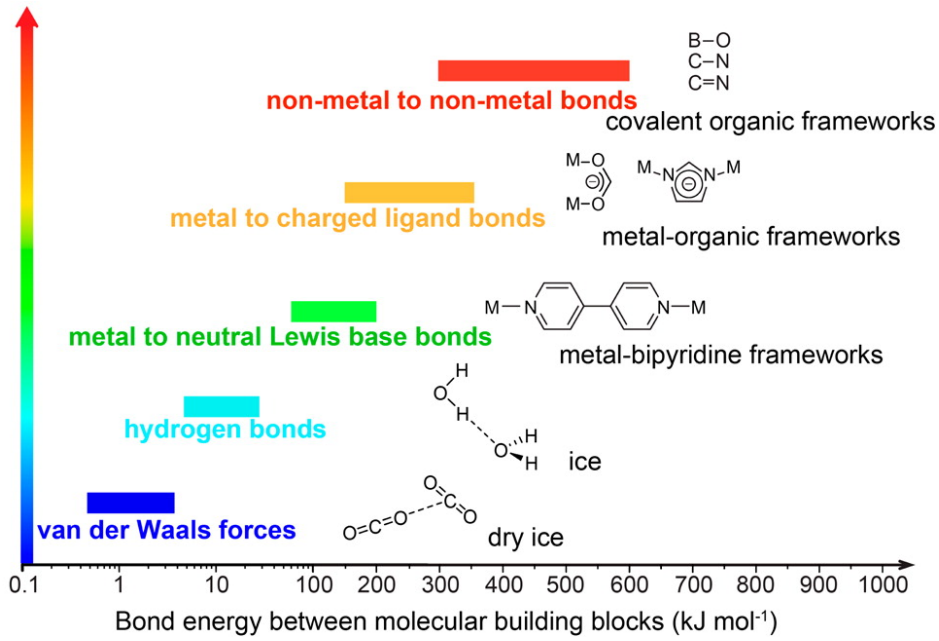

Figure 1.4 Bond types used in crystal engineering and their energies (adapted from ref. 16).

The rapid transition from molecular to periodical coordination chemistry (*i.e.* from coordination complexes to coordination polymers) started in the 1990s through the pioneering work of Hoskins and Robson.[19,20,21] They proposed that "a new and potentially extensive class of scaffolding-like materials may be afforded by linking together centers with either a tetrahedral or an octahedral array of valences by rod-like connecting units"[21] and, by extrapolating Wells's work on inorganic network structures,[22] outlined a net-based approach for the rational construction of coordination polymers. Their "node and linker/spacer" principle has been remarkably successful at producing such extended metal-organic architectures with high degree of precision.[19]

Metal-organic frameworks (MOFs) represent a special family of coordination networks which are crystalline, highly porous, low-density solids with large surface area, yet are inherently

robust and rigid (Figure 1.5).[23] With high levels of architectural stability and permanent porosity (large void space or free volume in the lattice),[24] arising from the high strengths of metal-ligand coordinative bonds and the rigidity and directionality of inorganic joints/nodes and organic struts, MOFs have a range of potential applications in sensing, separation, catalysis, trapping, storage, delivery, *etc.*[25]

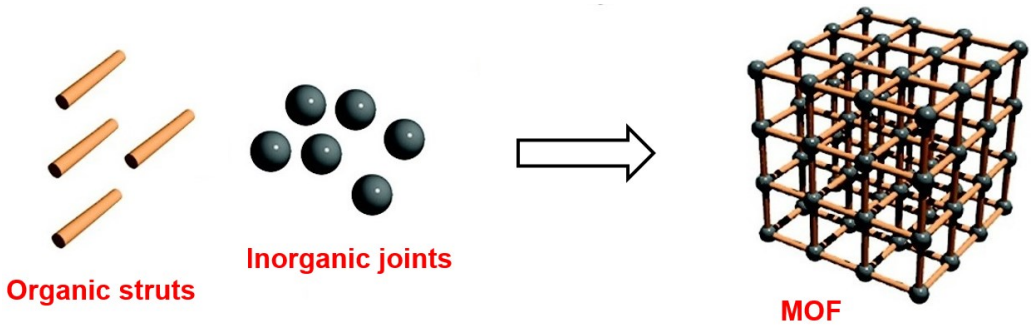

Figure 1.5 Schematic representation of MOF construction.

1.2.3 Porous molecular materials

Most natural (*e.g.* zeolites) and synthetic (*e.g.* metal-organic frameworks, covalent-organic frameworks) materials that show permanent porosity consist of network structures. Inspired by the impressive properties of such framework materials, the preparation of non-network or molecular porous materials (MPMs) has become an emerging area of interest.

According to the principle of close packing, put forward by Kitaigorodskii in mid-1940s,[26] molecules in crystals tend to dovetail and pack as tightly as possible. In other words, void space in crystals is always unfavorable.[27] Thus, the construction of porous materials from discrete organic molecules demands some special tactics.[28,29,30] For example, when the molecules have awkward shapes and/or are grafted with bulky groups, they may no longer have the ability to be drawn closer to each other, leading to so-called extrinsic porous materials.[28] Alternatively, molecules can be

designed in such a way that they contain internal cavities. They can retain their inherent molecular porosity even after close-packing and afford so-called intrinsic porous materials.[30] These two strategies are illustrated in Figure 1.6.

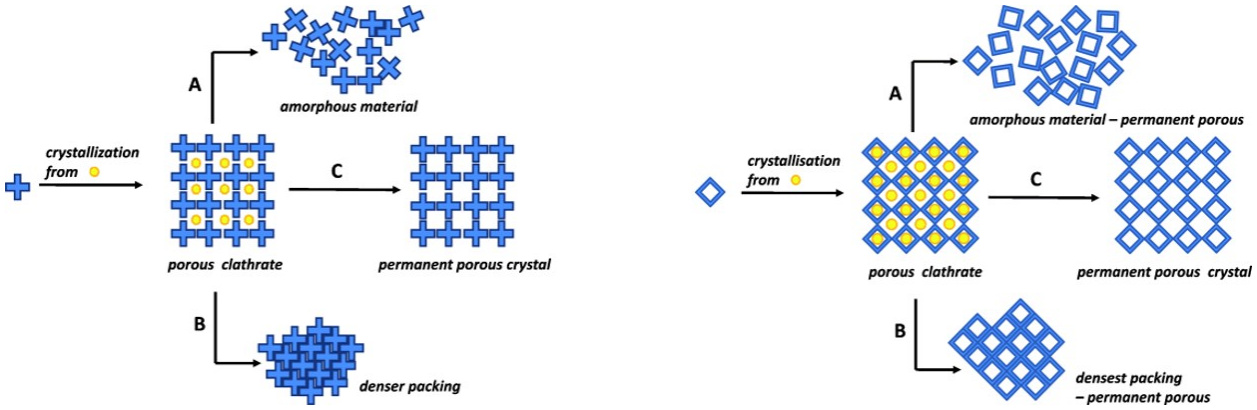

Figure 1.6 Possible pathways to MPMs; (left) extrinsic and (right) intrinsic porosities (adapted from ref. 28).

Since MPMs are held together by weak interactions, they are not as rigid and robust as MOFs and COFs. In most cases, attempts of activation (removal of entrapped guest molecules) result in structural disintegration. Hence, the real challenge lies in attaining permanently porous molecular materials that can behave analogously to framework-type solids (Figure 1.7).

1.2.4 Beauty of the iodoethynyl group

When iodine is directly bonded to an *sp*-hybridized carbon, it is strongly polarized, resulting in an intense σ-hole at the tip along the C–I bond axis.[31] The iodoethynyl functionality is, therefore, a perfect candidate for σ-hole interactions/halogen bonding. In fact, complexation ability between iodoalkynes and various Lewis basic species date back to early 20th century even though the interactions governing the formation of those complexes were not explicitly identified as halogen bonds.[32] The first structural analyses of such charge-transfer (CT) or electron donor-

acceptor (EDA) adducts formed by diiodoacetylene, one of the simplest members in this family, with 1,4-dioxane, 1,4-dithiane, 1,4-diselenane and 1,4-cyclohexanedione were conducted in 1960s.[33] In the same era, the structure of the 1-iodo-2-phenylacetylene/morpholine complex was also reported.[34]

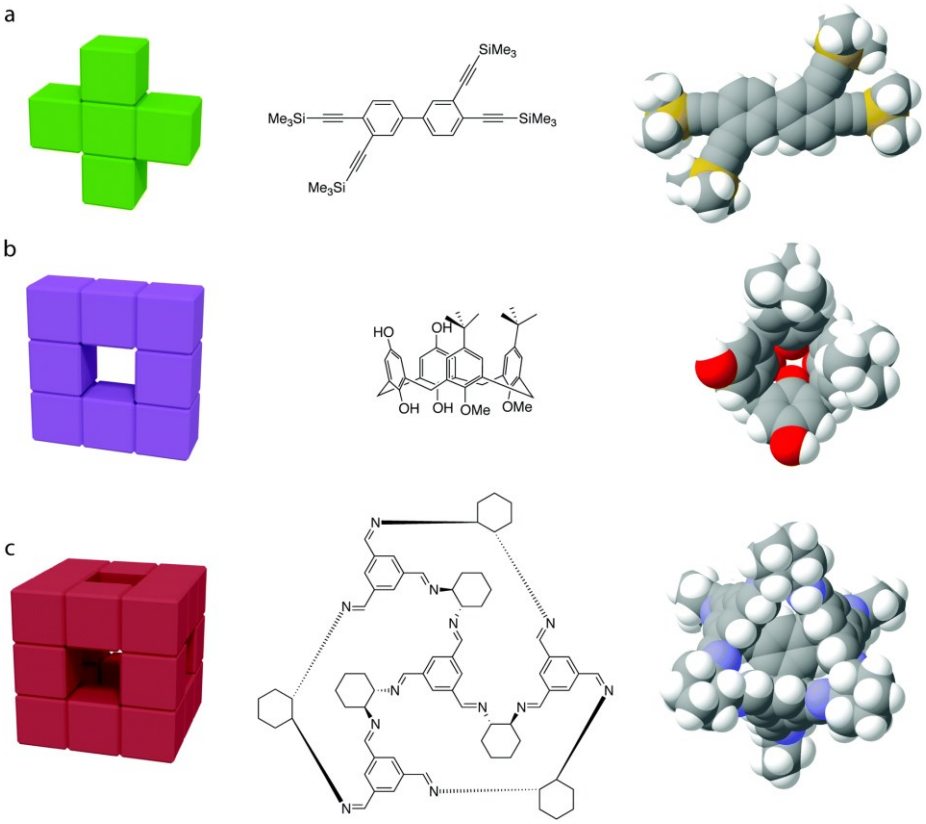

Figure 1.7 Molecules that exhibit permanent porosity (adapted from ref. 30).

Counting on the excellent halogen-bonding capability of iodoalkynes, there have been numerous breakthroughs in the field of crystal engineering. Goroff and co-workers, for example, came up with a clever idea for preparing poly(diiododiacetylene) or PIDA.[35] The polymerization of diiododiacetylene requires selective 1,4-addition that can only be achieved in the solid state *via* adequate amount of topochemical control. In other words, the relative orientation and spacing of

the diacetylene monomers need to be engineered within the crystalline solid so as to impose that essential regioselectivity. By co-crystallizing diiododiacetylene with carefully selected host/template molecules (*e.g.* bis(pyridylmethyl)ureas, bis(pyridylmethyl)oxalamides, bis(cyanoalkyl)oxalamides), they successfully synthesized PIDA, even in a topotactic manner without any phase change (Figure 1.8).

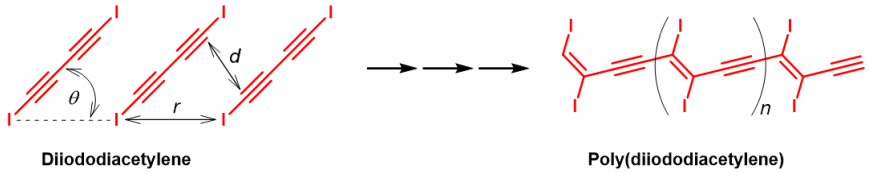

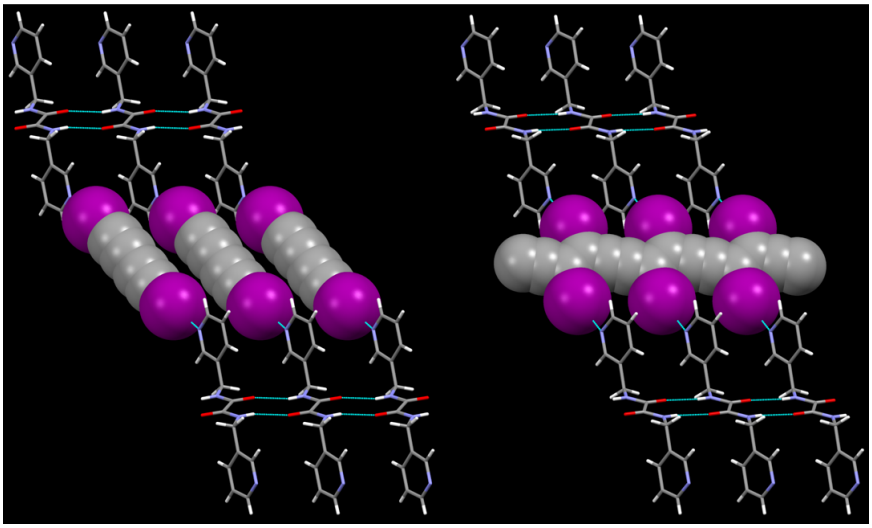

Figure 1.8 Topochemical polymerization of diiododiacetylene templated by *N,N′*-bis(3-pyridylmethyl)oxalamide.

Because of the structural rigidity, space-efficiency, negligible steric hindrance, and core expanding ability, the iodoethynyl unit is well-suited for devising molecular building blocks which are capable of the modular construction of various discrete and polymeric supramolecular assemblies. For example, it has recently been shown that 1,8-diiodoethynylanthracene, containing

two parallelly-arranged iodoethynyl moieties, gives rise to rectangular-shaped assemblies when co-crystallized with linear ditopic XB acceptors (Figure 1.9).[36]

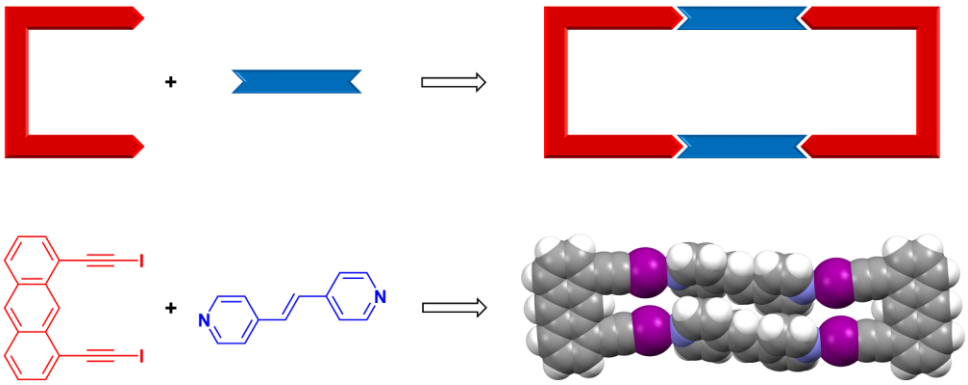

Figure 1.9 Formation of XB-driven molecular rectangles.

1.3 Concise summary of goals

Synthon competition is an inescapable part when dealing with multifunctional supramolecular reagents, For the purpose of studying competition and selectivity of diverse supramolecular synthons, as well as of devising strategies to minimize synthon crossover possibilities, we carried out hydrogen- and halogen-bond driven co-crystallizations with custom-designed multifunctional probe molecules.[37] We also wanted to demonstrate that electrostatic potentials calculated on molecular surfaces can reliably be used as a simple tool to rank different synthons and predict primary supramolecular interactions in the solid state. ► **Chapter 2**

Because of the dominance of carboxylate and *N*-donor heterocyclic ligands in the realm of coordination polymer, other classes of ligands remain largely undeveloped, and acetylacetonate is one of them. The synthetic feasibility of a series of heterobifunctional ligands featuring the

acetylacetonate moiety and either a pyridyl or thiophenyl moiety was studied. Their suitability for preparing MOFs and other metallo-supramolecular assemblies was also explored ► **Chapter 3**

Molecular tectons capable of forming strong hydrogen bond interactions have successfully been employed in making molecular porous materials. However, molecular tectonics based on halogen bonding is still in its infancy. We grafted rigid tetrahedral core units with iodoethynyl arms to investigate the power of those recognition sites in the context of solid-state packing and extrinsic porosity. With the intention of obtaining multi-component porous solids, their ability to co-crystallize with appropriate co-formers was also examined. ► **Chapter 4**

Another effort was aimed at constructing metal-free MOF-like architectures *via* XB-directed modular assembly.[38] By reacting the same XB-donating tetrahedral tectons discussed in Chapter 4 with various halide salts, our primary objective was to construct diamondoid networks with charge-inverted coordination chemistry. Additionally, the mutual-induced fitting ability of halide anions and the structure-directing ability of counter-cations were established. ► **Chapter 5**

1.4 References

1. F. Wöhler, *Ann. Phys.*, 1828, **88**, 253-256.
2. A. Eschenmoser and C. E. Wintner, *Science*, 1977, **196**, 1410-1426.
3. J. M. Lehn, *Pure Appl. Chem.*, 1978, **50**, 871-892.
4. J. M. Lehn, *Science*, 1993, **260**, 1762-1763; J. M. Lehn, *Angewandte Chemie-International Edition in English*, 1990, **29**, 1304-1319; J. M. Lehn, *Angew Chem Int Edit*, 1988, **27**, 89-112; J. M. Lehn, *Science*, 1985, **227**, 849-856; J. M. Lehn, *Proceedings of the National Academy of Sciences of the United States of America*, 2002, **99**, 4763-4768.
5. K. L. Wolf, H. Frahm and H. Harms, *Z. Phys. Chem. (B)*, 1937, **36**, 237-287; K. L. Wolf and R. Wolff, *Angew. Chem.*, 1949, **61**, 191-201.
6. R. Pepinsky, *Phys. Rev.*, 1955, **100**, 971.
7. G. M. J. Schmidt, *Pure Appl. Chem.*, 1971, **27**, 647-678.

8. D. Braga, *Chem. Commun.*, 2003, 2751-2754; C. V. K. Sharma, *Crystal Growth & Design*, 2002, **2**, 465-474; B. Moulton and M. J. Zaworotko, *Chem. Rev.*, 2001, **101**, 1629-1658.
9. G. R. Desiraju, *Crystal Engineering: The Design of Organic Solids*, Elsevier, Amsterdam, 1989.
10. J. D. Dunitz, *Pure Appl. Chem.*, 1991, **63**, 177-185.
11. G. R. Desiraju, *Angew Chem Int Edit*, 2007, **46**, 8342-8356; G. R. Desiraju, *J. Am. Chem. Soc.*, 2013, **135**, 9952-9967.
12. D. K. Bucar, *Crystal Growth & Design*, 2017, **17**, 2913-2918.
13. G. R. Desiraju, *Angewandte Chemie-International Edition in English*, 1995, **34**, 2311-2327.
14. A. D. Bond, *CrystEngComm*, 2007, **9**, 833-834.
15. J. A. Bis, P. Vishweshwar, D. Weyna and M. J. Zaworotko, *Mol Pharm*, 2007, **4**, 401-416.
16. J. C. Jiang, Y. B. Zhao and O. M. Yaghi, *J. Am. Chem. Soc.*, 2016, **138**, 3255-3265.
17. T. R. Cook, Y. R. Zheng and P. J. Stang, *Chem. Rev.*, 2013, **113**, 734-777.
18. L. Ohrstrom, *Crystals*, 2015, **5**, 154-162; S. R. Batten, N. R. Champness, X. M. Chen, J. Garcia-Martinez, S. Kitagawa, L. Ohrstrom, M. O'Keeffe, M. P. Suh and J. Reedijk, *Pure Appl. Chem.*, 2013, **85**, 1715-1724.
19. R. Robson, B. F. Abrahams, S. R. Batten, R. W. Gable, B. F. Hoskins and J. Liu, in *Supramolecular Architecture*, American Chemical Society, 1992, vol. 499, ch. 19, pp. 256-273.
20. B. F. Abrahams, B. F. Hoskins and R. Robson, *J. Am. Chem. Soc.*, 1991, **113**, 3606-3607; S. R. Batten, B. F. Hoskins and R. Robson, *J. Chem. Soc., Chem. Commun.*, 1991, 445-447; B. F. Abrahams, B. F. Hoskins, J. Liu and R. Robson, *J. Am. Chem. Soc.*, 1991, **113**, 3045-3051; R. W. Gable, B. F. Hoskins and R. Robson, *J. Chem. Soc., Chem. Commun.*, 1990, 762-763; B. F. Abrahams, B. F. Hoskins and R. Robson, *J. Chem. Soc., Chem. Commun.*, 1990, 60-61.
21. B. F. Hoskins and R. Robson, *J. Am. Chem. Soc.*, 1990, **112**, 1546-1554.
22. A. F. Wells, *Three-dimensional nets and polyhedra*, Wiley, New York, 1977; A. F. Wells, *Structural Inorganic Chemistry*, Oxford University Press, Oxford, 5th edn., 1984.
23. H. Furukawa, K. E. Cordova, M. O'Keeffe and O. M. Yaghi, *Science*, 2013, **341**, 974-+.
24. A. J. Howarth, Y. Y. Liu, P. Li, Z. Y. Li, T. C. Wang, J. Hupp and O. K. Farha, *Nat Rev Mater*, 2016, **1**.
25. K. K. Gangu, S. Maddila, S. B. Mukkamala and S. B. Jonnalagadda, *Inorg. Chim. Acta*, 2016, **446**, 61-74.
26. A. I. Kitaigorodskii, *Molecular Crystals and Molecules*, Academic Press, New York, 1973; A. I. Kitaigorodskii, *Organic Chemical Crystallography*, Consultants Bureau, New York, 1961; A. I. Kitaigorodskii, *Chem. Soc. Rev.*, 1978, **7**, 133-163; A. I. Kitaigorodskii, *Acta Crystallographica*, 1965, **18**, 585-590; A. I. Kitaigorodskii, *J. Phys. (USSR)*, 1945, **9**, 351-352.
27. J. D. Dunitz, G. Filippini and A. Gavezzotti, *Tetrahedron*, 2000, **56**, 6595-6601; C. P. Brock and J. D. Dunitz, *Chem. Mater.*, 1994, **6**, 1118-1127.
28. M. Mastalerz, *Chem-Eur J*, 2012, **18**, 10082-10091.
29. J. R. Holst, A. Trewin and A. I. Cooper, *Nat. Chem.*, 2010, **2**, 915-920; M. I. Hashim, C. W. Hsu, H. T. M. Le and O. S. Miljanic, *Synlett*, 2016, **27**, 1907-1918; J. Tian, P. K. Thallapally and B. P. McGrail, *CrystEngComm*, 2012, **14**, 1909-1919.

30. J. D. Evans, K. E. Jelfs, G. M. Day and C. J. Doonan, *Chem. Soc. Rev.*, 2017, **46**, 3286-3301.
31. C. B. Aakeröy, M. Baldrighi, J. Desper, P. Metrangolo and G. Resnati, *Chem. Eur. J.*, 2013, **19**, 16240-16247.
32. W. M. Dehn, *J. Am. Chem. Soc.*, 1911, **33**, 1598-1601.
33. O. Holmesland and C. Rømming, *Acta Chem. Scand.*, 1966, **20**, 2601-2610; P. Groth and O. Hassel, *Acta Chem. Scand.*, 1965, **19**, 1733-1740; P. Gagnaux and B. P. Susz, *Helv. Chim. Acta*, 1960, **43**, 948-956.
34. R. H. Baughman, *The Journal of Organic Chemistry*, 1964, **29**, 964-965.
35. H. J. Jin, A. M. Plonka, J. B. Parise and N. S. Goroff, *CrystEngComm*, 2013, **15**, 3106-3110; L. Luo, C. Wilhelm, A. W. Sun, C. P. Grey, J. W. Lauher and N. S. Goroff, *J. Am. Chem. Soc.*, 2008, **130**, 7702-7709; C. Wilhelm, S. A. Boyd, S. Chawda, F. W. Fowler, N. S. Goroff, G. P. Halada, C. P. Grey, J. W. Lauher, L. Luo, C. D. Martin, J. B. Parise, C. Tarabrella and J. A. Webb, *J. Am. Chem. Soc.*, 2008, **130**, 4415-4420; A. W. Sun, J. W. Lauher and N. S. Goroff, *Science*, 2006, **312**, 1030-1034; N. S. Goroff, S. M. Curtis, J. A. Webb, F. W. Fowler and J. W. Lauher, *Org. Lett.*, 2005, **7**, 1891-1893.
36. T. K. Wijethunga, M. Dakovic, J. Desper and C. B. Aakeroy, *Acta Crystallogr B*, 2017, **73**, 163-167.
37. C. A. Gunawardana, J. Desper, A. S. Sinha, M. Dakovic and C. B. Aakeroy, *Faraday Discuss.*, 2017, **203**, 371-388.
38. C. A. Gunawardana, M. Dakovic and C. B. Aakeroy, *Chem. Commun.*, 2018, **54**, 607-610.

Chapter 2 - Competition and selectivity in supramolecular synthesis

2.1 Introduction

Owing to the inherently dynamic nature of non-covalent bonds,[1] the construction of supermolecules with specific architectures and metrics is a very demanding task.[2] When the individual molecular entities (*i.e.* the reactants in any supramolecular synthesis) are relatively simple, the details of their assembly can often be estimated by relying on the concept of supramolecular synthons.[3] However, in the presence of a range of chemical functionalities, it is far more difficult to realize a desired supramolecular product as a result of synthon crossover[4] and synthon polymorphism[5] arising from the structural interference and competition among binding sites. In other words, a non-covalent reaction with more intricate molecular building blocks often leads to variable connectivities and unexpected structural outcomes.[6]

The lack of control over the resulting supramolecular associations can be avoided (or at least minimized) by careful choice of 'reactants' in such a way that only non-interfering molecular recognition events are present/likely to occur within the system (structural insulation).[7] This type of rational design and synthesis, in turn, necessitates a thorough understanding of different synthons and their robustness, reproducibility, transferability and relative strengths. It has been shown[8,9,10] that ranking of synthons based on hydrogen-bonds (HBs) and halogen-bonds (XBs) can readily be achieved by calculating electrostatic potential values of available donor and acceptor moieties, as these non-covalent attractive forces comprise a substantial electrostatic/Coulombic component.[11] Then, by following the best donor–best acceptor rule and a few other empirical guidelines,[12] one can carry out a supramolecular synthesis in a more logical manner. The existence of these straightforward and reliable guidelines, coupled with their strength and directionality,

makes HBs and XBs common synthetic tools utilized within the realms of supramolecular chemistry and crystal engineering.[13]

Molecular tectons aimed at hydrogen- and halogen-bonding interactions typically contain aromatic *N*-heterocycles such as pyridine, pyrimidine, imidazole, pyrazole, triazole, *etc*. Another intriguing member of this family is 2,2'-biimidazole (H_2biim) which has attracted much interest, both in the metallo-supramolecular arena[14] and in organic salts and co-crystals.[15] In contrast, *N,N'*-disubstituted H_2biim derivatives have also been explored with respect to their metal-binding ability,[16] but have not yet found widespread use in the development of pure organic assemblies. We recently studied a set of isomeric *N,N'*-bis(pyridylmethyl)-2,2'-biimidazoles with the intention of mapping out their solid-state binding preferences.[9] Even though they hold two different HB/XB acceptor sites, imidazole-N and pyridine-N, the primary interactions always take place *via* the latter, the best acceptor as ranked by calculated molecular electrostatic potentials. These dipicolyl biimidazoles were previously found to be effective in stabilizing volatile liquid iodoperfluoroalkanes by means of XB-directed co-crystallization/solvate formation.[17]

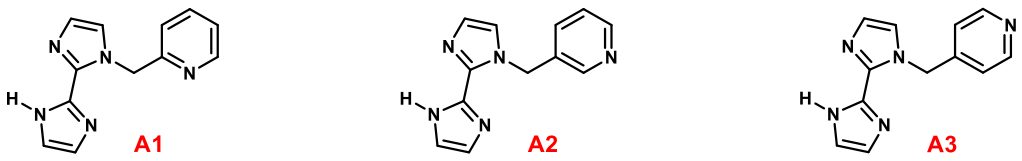

Figure 2.1 *N*-(pyridinylmethyl)-2,2'-biimidazole compounds used in this study.

As a continuation of our effort to identify and develop more reliable supramolecular strategies based upon robust and transferable synthon hierarchies, we herein report the synthesis and systematic structural investigation of mono-picolyl biimidazoles; 1-(pyridin-2-ylmethyl)-2,2'-biimidazole, **A1**, 1-(pyridin-3-ylmethyl)-2,2'-biimidazole, **A2**, and 1-(pyridin-4-ylmethyl)-2,2'-

biimidazole, **A3** (Figure 2.1). Only four *N*-monosubstituted H_2biim compounds, namely 1-methyl-2,2'-biimidazole, 1-butyl-2,2'-biimidazole, 1-(hydroxyethyl)-2,2'-biimidazole and 1-(carboxymethyl)-2,2'-biimidazole, have been crystallographically characterized to date.[18] The paucity of structural data is likely due to considerable synthetic difficulties encountered during their preparation since H_2biim usually prefers symmetric di-substitution even under carefully controlled reaction conditions.

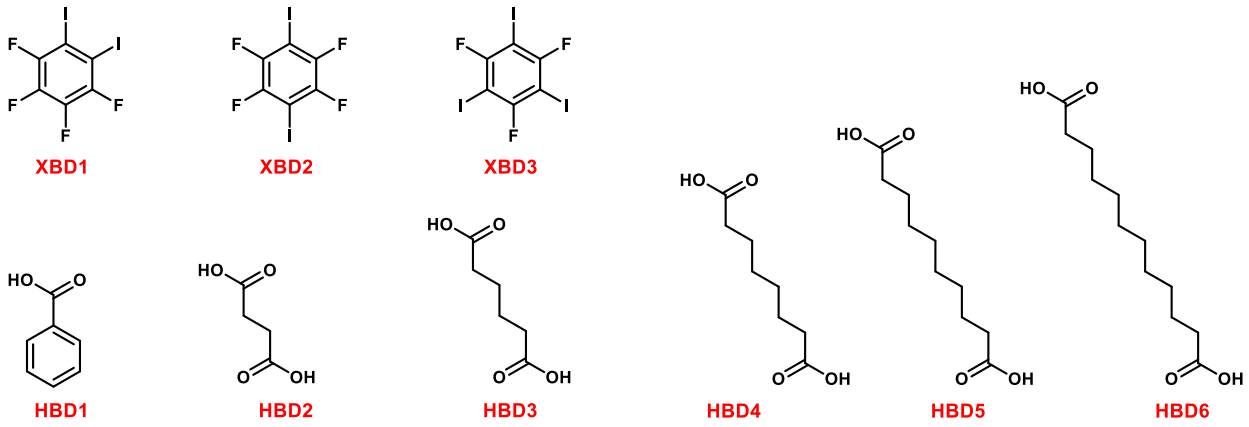

Figure 2.2 Halogen- and hydrogen-bond donors used in this study.

In order to map out the structural landscape around **A1**–**A3**, as well as to establish their intermolecular binding preferences, we employed co-crystallization experiments with a collection of halogen- and hydrogen-bond donors (three perfluoroiodobenzenes and six carboxylic acids, Figure 2.2). In addition, we wanted to establish if any potential selectivity, with respect to the competing HB and XB acceptor sites on **A1**–**A3**, could be rationalized in the context of calculated molecular electrostatic potential surfaces, MEPS.

We specifically selected these single-armed H_2biim species as probe molecules because, being asymmetric, they provide three different sites (one pyridine-N and two inequivalent

imidazole-Ns) for accepting HBs and/or XBs (Figure 2.3a). Moreover, as opposed to *N,N′*-disubstituted analogs, the mono-substitution offers an added level of complexity since each acceptor molecule carries an HB donating N–H functionality on the unsubstituted imidazole ring. This means that **A1**–**A3** are capable of forming self-complementary N–H···N/N···H–N hydrogen-bonding motifs that would mimic the hydrogen-bonding $R^2_2(10)$ network in the parent H_2biim itself.[19] As illustrated in Figure 2.3b, if this two-point homomeric interaction is dominant, it leaves only two sites available for additional interactions with any given co-former. Carboxylic acids, however, may disrupt this homomolecular recognition event; there is an electrostatic and geometric fit between the –COOH group and the H_2biim binding pocket so they can, in principle, partake in the formation of $R^2_2(9)$ heterosynthons composed of N–H···O═C and N···H–O hydrogen bonds, Figure 2.3c.[15]

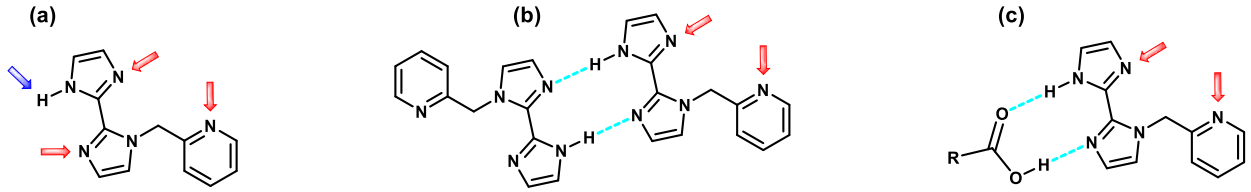

Figure 2.3 *a)* Potential binding sites in **A1** and its isomers; *b)* hydrogen-bonded homosynthon; *c)* hydrogen-bonded heterosynthon.

2.2 Experimental

2.2.1 Materials and methods

All reagents, solvents, precursors (ammonium chloride, glyoxal 40% w/w aqueous solution, picolyl chloride hydrochlorides), hydrogen-bond donors (**HBD1**–**HBD6**) and halogen-bond donors (**XBD1**–**XBD3**) were purchased from commercial sources, and were used as received without further purification. Nuclear magnetic resonance spectra were recorded on a Varian Unity

Plus (400 MHz) NMR spectrometer using residual solvent signal as a reference. A Nicolet 380 FT-IR instrument was used for the infrared spectroscopic analysis. The general synthetic protocol used for the preparation of three acceptor molecules is displayed in Figure 2.4.

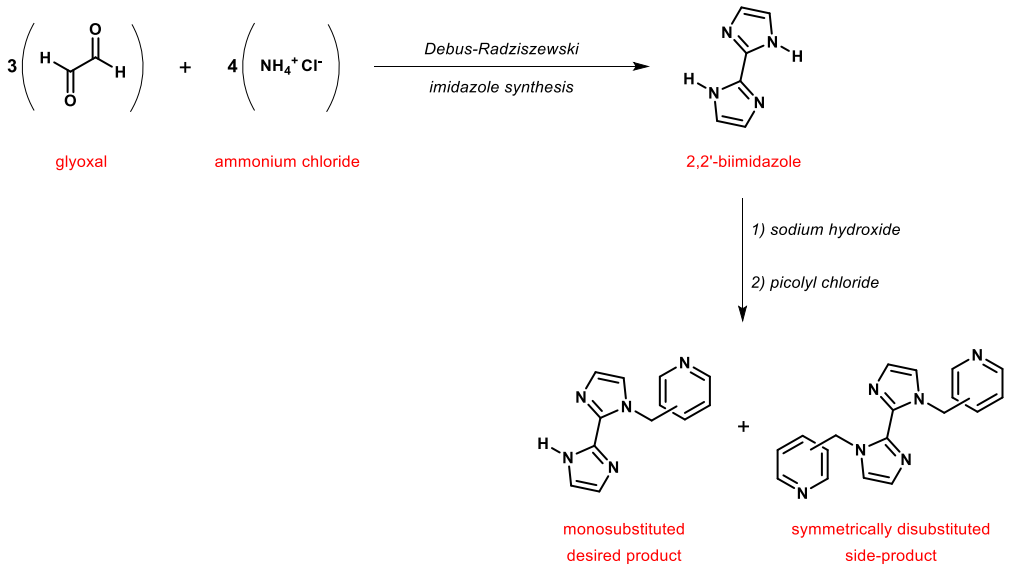

Figure 2.4 Common synthetic route to **A1**–**A3**

2.2.2 Synthesis of 2,2'-biimidazole (H_2biim)

A modified version of Debus-Radziszewski imidazole synthesis was employed.[20] To a slurry of ammonium chloride (35 g, 0.65 mol, 2.5 equiv.) in 35 mL of distilled water maintained at 40–50 °C, glyoxal 40% solution (30 mL, 0.26 mol, 1 equiv.) was slowly added over a 30-minute period while vigorously stirring the mixture. The resulting yellow solution was stirred for an additional 12 hours at room temperature, and then neutralized with a saturated potassium carbonate solution to precipitate a brown solid. It was collected by filtration and re-dissolved in a minimum amount of 1 M hydrochloric acid. The resulting dark red solution was heated to boiling, treated with decolorizing charcoal, and filtered. The filtrate was neutralized again with a saturated

potassium carbonate solution, which afforded a tan colored solid. This solid was re-crystallized from ethylene glycol, washed with acetone and dried at 60 °C for 5 hours to obtain 2,2'-biimidazole as an off-white, needle-shape crystalline material. Yield: 3.37 g (29%). Mp: > 300 °C. ^{1}H NMR (400 MHz, DMSO-d6) δ (ppm): 12.65 (s, br, 2H), 7.13 (s, 2H), 6.99 (s, 2H). ^{13}C NMR (100 MHz, DMSO-d6) δ (ppm): 139.32, 128.26, 117.38.

2.2.3 Synthesis of (chloromethyl)pyridines – general procedure

Picolyl chloride hydrochlorides [*i.e.* (chloromethyl)pyridine hydrochlorides] were neutralized, immediately before their use, by potassium carbonate in an aqueous medium. To a solution of picolyl chloride hydrochloride (1.3532 g, 8.25 mmol) in 15 mL of distilled water was added potassium carbonate (1.1402 g, 8.25 mmol) and was stirred until the gas evolution/effervescence ceased. Then, it was extracted into dichloromethane (3 × 15 mL). The combined organic layers were washed with 15 mL of saturated sodium chloride, dried over anhydrous magnesium sulfate, and concentrated by rotary evaporation. In this way, all three compounds were obtained in quantitative yields as pale yellow, oily liquids.

2-(Chloromethyl)pyridine. ^{1}H NMR (400 MHz, $CDCl_3$) δ (ppm): 8.56 (d, 1H), 7.70 (td, 1H), 7.44 (d, 1H), 7.22 (dd, 1H), 4.66 (s, 2H).

3-(Chloromethyl)pyridine. ^{1}H NMR (400 MHz, $CDCl_3$) δ (ppm): 8.53 (d, 1H), 8.47 (dd, 1H), 7.63 (dt, 1H), 7.20 (dd, 1H), 4.49 (s, 2H).

4-(Chloromethyl)pyridine. ^{1}H NMR (400 MHz, $CDCl_3$) δ (ppm): 8.60 (d, 2H), 7.30 (d, 2H), 4.53 (s, 2H).

2.2.4 Synthesis of 1-(pyridin-2-ylmethyl)-2,2'-biimidazole, A1

To a suspension of 2,2'-biimidazole (1.0060 g, 7.5 mmol, 1 equiv.) in 25 mL of absolute ethanol was added ground sodium hydroxide (0.3000 g, 7.5 mmol, 1 equiv.), and was stirred at

room temperature for 1 hour. With vigorous stirring, 2-(chloromethyl)pyridine (0.9568 g, 7.5 mmol, 1 equiv.) in 10 mL of absolute ethanol was added dropwise into the above red/pink solution and the temperature was increased to 65 °C. After 5 hours, the reaction was quenched by adding 50 mL of saturated ammonium chloride solution. The resultant heterogeneous mixture was subsequently filtered, and the filtrate was extracted with dichloromethane (3 × 20 mL). The residue was also washed with dichloromethane (2 × 20 mL) *via* multiple dispersion/filtration cycles [approximately 0.4 g (40%) of unreacted biimidazole could be recovered collectively from the residue and the aqueous phase]. The organic fractions, *i.e.* both extracts and washings, were combined, washed with distilled water (2 × 20 mL) followed by saturated sodium chloride (20 mL), and dried over anhydrous magnesium sulfate. The removal of solvent *in vacuo* resulted in a brownish orange crude product. It was further purified by column chromatography on silica gel [unreacted picolyl chloride, monosubstituted desired product and symmetrically disubstituted by-product were eluted with hexane/ethyl acetate (1:1), ethyl acetate and ethyl acetate/methanol (9:1) solvent systems, respectively] to yield 1-(pyridin-2-ylmethyl)-2,2'-biimidazole as a yellow solid. Crystals suitable for single-crystal X-ray diffraction were grown from ethyl acetate. Yield: 270 mg (16%). Mp: 156–158 °C. ^{1}H NMR (400 MHz, $CDCl_3$) δ (ppm): 13.53 (s, br, 1H), 8.58 (d, 1H), 7.61 (td, 1H), 7.30 (d, 1H), 7.20 (dd, 1H), 7.12 (s, 2H), 7.10 (s, 2H), 6.10 (s, 2H). ^{13}C NMR (100 MHz, $CDCl_3$) δ (ppm): 157.02, 149.65, 139.43, 139.19, 137.24, 129.44, 128.02, 123.00, 122.68, 122.14, 117.52, 52.70.

2.2.5 Synthesis of 1-(pyridin-3-ylmethyl)-2,2'-biimidazole, A2

A2 was obtained as an off-white solid by following the same procedure stated above for **A1**, but using 3-(chloromethyl)pyridine. Crystals suitable for single-crystal X-ray diffraction were grown from ethyl acetate. Yield: 186 mg (11%). Mp: 117–119 °C. ^{1}H NMR (400 MHz, $CDCl_3$) δ

(ppm): 13.14 (s, br, 1H), 8.63 (d, 1H), 8.54 (dd, 1H), 7.65 (dt, 1H), 7.24 (dd, 1H), 7.16 (s, 1H), 7.11 (d, 1H), 7.09 (s, 1H), 6.95 (d, 1H), 6.01 (s, 2H). ^{13}C NMR (100 MHz, $CDCl_3$) δ (ppm): 149.67, 149.52, 139.32, 139.22, 135.84, 133.02, 129.54, 128.49, 123.92, 121.45, 117.53, 48.59.

2.2.6 Synthesis of 1-(pyridin-4-ylmethyl)-2,2'-biimidazole, A3

A3 was obtained as a yellowish orange solid by following the same procedure stated above for **A1**, but using 4-(chloromethyl)pyridine. Crystals suitable for single-crystal X-ray diffraction were grown from ethyl acetate. Yield: 253 mg (15%). Mp: 155–157 °C ^{1}H NMR (400 MHz, $CDCl_3$) δ (ppm): 13.29 (s, br, 1H), 8.55 (d, 2H), 7.15 (s, 1H), 7.13 (s, 1H), 7.12 (d, 2H), 7.11 (s, 1H), 6.96 (s, 1H), 6.03 (s, 2H). ^{13}C NMR (100 MHz, $CDCl_3$) δ (ppm): 150.42, 146.32, 139.41, 139.01, 129.63, 128.39, 122.32, 121.79, 117.65, 50.02.

2.2.7 Synthesis of co-crystals

Unless otherwise noted, all crystal growth experiments were carried out *via* slow evaporation of methanolic solutions, thereby effectively circumventing any solvent-solute bias across the series. In a typical co-crystallization attempt, a 10 mg (0.044 mmol) portion of acceptor and an equimolar amount of donor were transferred into a 2-dram glass vial, and were fully dissolved in a minimal amount (usually ~ 2 mL) of methanol. The partially-tightened/covered vial was then left undisturbed at ambient conditions to allow the solvent to evaporate slowly. Fourteen donor–acceptor combinations (out of 27) produced crystals suitable for single-crystal X-ray diffraction.

2.2.8 X-ray crystallography

After performing preliminary IR analysis, crystals were subjected to single-crystal X-ray diffraction. Relevant experimental details can be found in Appendix A. All structural images were generated using Mercury.[21]

2.2.9 Electrostatic potential calculations

In order to compute molecular electrostatic potentials of 1-(pyridinylmethyl)-2,2'-biimidazoles (**A1**–**A3**), their geometries were optimized at the hybrid functional B3LYP/6-31G(d) level of theory using Spartan.[22] The visualization of MEP was subsequently attained through mapping its values, determined with a positive point charge in the vacuum as a probe, on the molecular surface defined by an outer contour of 0.002 au electronic density. The numbers, now termed surface potentials, indicate the Coulombic interaction energies (expressed in kJ/mol) between the probe and this isodensity surface at different points.

2.3 Results and discussion

As previously stated, electrostatic potentials computed on molecular surfaces allow the identification and ranking of hydrogen- and halogen-bonding sites; locally most positive surface potentials correspond to electron deficient zones and represent possible hydrogen-bond donating sites whereas strongly negative values reflect regions of higher electron densities indicate hydrogen-bond accepting sites.[10] When there are multiple sites, their magnitudes simply rank them. The calculated molecular electrostatic potential surfaces (MEPS) of **A1**–**A3** are shown in Figure 2.5. Their local minima and maxima (*i.e.* V_{min} and V_{max}) are given in Table 2.1.

The position of the nitrogen atom on the pyridine ring exerts a significant effect upon its own potential as well as on those of the acceptor sites of biimidazole. The relative strengths of the acceptor sites vary in the order of pyridine-N (N_{py}) > substituted imidazole-N (N_{im1}) > unsubstituted imidazole-N (N_{im2}) except for **A1**, in which the best acceptor and second-best acceptor are reversed. As expected, the imidazolyl-NH group of unsubstituted ring (*i.e.* HN_{im2}) holds the highest surface potential in all three compounds.

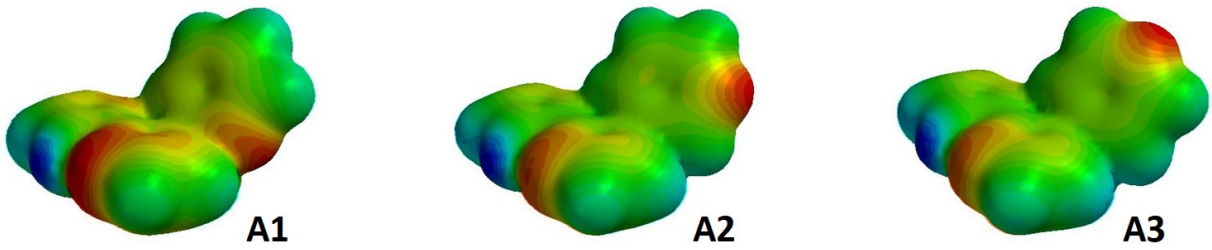

Figure 2.5 Molecular electrostatic maps of the three acceptor molecules.

Altogether, 17 new structures were analyzed in this study. Detailed crystallographic data have been included in Appendix A, and deposited with the Cambridge Crystallographic Data Centre (CCDC 1533284–1533300). The geometries of HBs and XBs of all the structures are summarized in Table C1 and Table C2, respectively.

Table 2.1 Local minima and maxima (given in kJ/mol) in calculated MEPS of **A1**–**A3**.

Molecule	V_{min} (N_{py})	V_{min} (N_{im1})	V_{min} (N_{im2})	V_{max} (HN_{im2})
A1	−154	−163	−138	+198
A2	−187	−151	−134	+210
A3	−193	−149	−135	+211

The crystal structures of the acceptor molecules themselves offer some indications about the preferred mode of intermolecular interactions that may subsequently affect how they act in co-crystals. Both **A1** and **A2** form dimers through homosynthons composed of pairs of $N_{im1}\cdots H–N_{im2}$ hydrogen bonds (Figure 2.6). In **A1**, adjacent dimers are interconnected into a polymeric architecture with the aid of $N_{py}\cdots H–C_{im1}$ secondary interactions. Somewhat surprisingly, the pyridinyl-N of **A2**, however, does not play any significant role in the structure-directing process. In contrast, **A3** exhibits an entirely distinct arrangement. Instead of a homosynthon, it displays $N_{py}\cdots H–N_{im2}$ single-point interactions, generating a chain-like assembly (Figure 2.6, bottom).

Thus, **A1** and **A3** are in agreement with a MEP-based interaction hierarchy and Etter's best donor–best acceptor rule while **A2** is not. This shows the structural bias of **A2** towards the self-complementary N–H···N/N···H–N synthon formation irrespective of the fact that there is a better/stronger acceptor site elsewhere in the molecule.

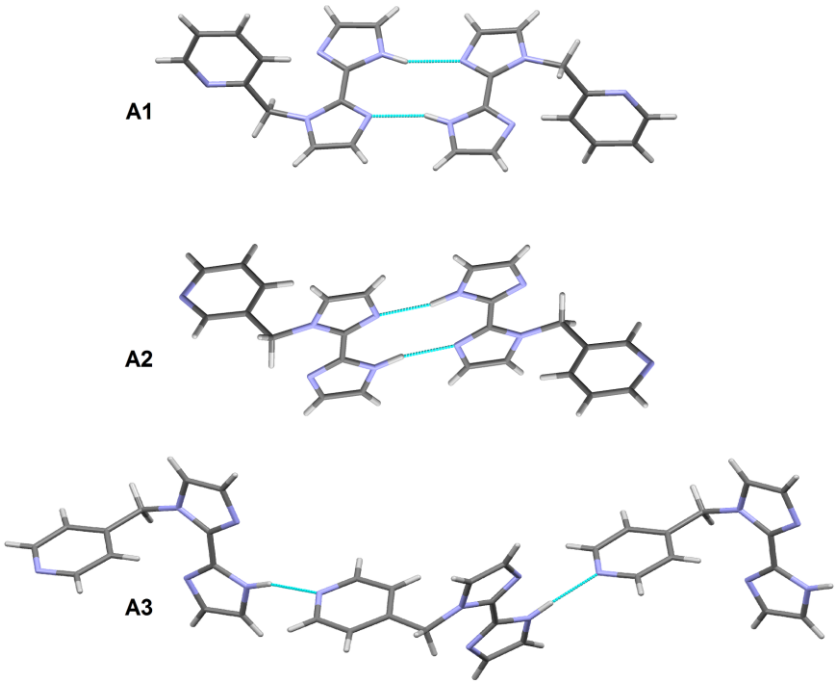

Figure 2.6 Structures of **A1**, **A2** and **A3**.

In order to get more insight into the supramolecular attributes of pure ligands, **A1**–**A3**, and to rationalize their observed primary interaction patterns in solid-state, it is helpful to consider synergistic effects of both thermodynamic and kinetic factors. It can be readily argued that once the first $N_{im1}\cdots H–N_{im2}$ hydrogen-bond is made, the second bond which is required to complete the $R_2^2(10)$ homosynthon, will form rapidly due to the close proximity and favorable orientation of the adjacent molecules. The presence of an $N_{py}\cdots H–N_{im2}$ hydrogen bond will not impart any supramolecular 'pre-organization' that can facilitate the formation of a second such interaction and

consequently, the two-point homosynthon will always be kinetically favored. On the other hand, the thermodynamic bond strength can be approximated by evaluating the combined electrostatic potentials (which is directly correlated with the Coulombic contribution) of the participating donor and acceptor sites (Table 2.2).

Table 2.2 Evaluation of thermodynamic contribution for hydrogen-bonding in **A1**–**A3**.

Molecule	V_{max}(donor) − V_{min}(acceptor) in kJ/mol		Observed outcome
	for $N_{im1}\cdots H–N_{im2}$	for $N_{py}\cdots H–N_{im2}$	
A1	361	352	Homosynthon
A2	361	397	Homosynthon
A3	360	404	Heterosynthon

The eventual outcome of the supramolecular assembly will therefore be the result of a balance between kinetic and thermodynamic contributions. In **A1**, both kinetic and thermodynamic factors support the homosynthon formation which is exactly what is observed experimentally. In both **A2** and **A3**, kinetic considerations favor the homosynthon, whereas approximated hydrogen-bond strengths are in favor of the heterosynthon. The additional thermodynamic stability displayed by the $N_{py}\cdots H–N_{im2}$ bond in **A3** (compared with that in **A2**) is seemingly enough to overcome the kinetic influence and the result is a single-point heterosynthon in **A3** and a two-point homosynthon in **A2**.

A2 and **XBD3** co-crystallize in a 1:1 stoichiometric ratio. The cyclic arrays of $N_{im1}\cdots H–N_{im2}$ hydrogen bonds, *i.e.* $R^2_2(10)$ ring motifs, and $I\cdots N_{py}$ halogen bonds result in tetrameric aggregates (Figure 2.7, top). The structure of **A3**:**XBD1** shows a 2:1 stoichiometry, but the primary intermolecular linkages are identical to those found in **A2**:**XBD3** (Figure 2.7, bottom).

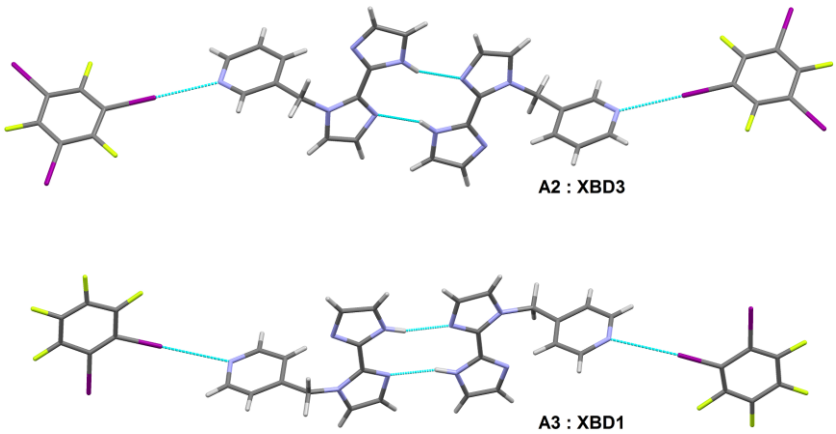

Figure 2.7 Tetramers of **A2**:**XBD3** and **A3**:**XBD1**.

With **XBD2**, a linear ditopic XB donor, all three acceptor molecules give rise to infinite one-dimensional architectures (Figure 2.8). They all are 2:1 co-crystals driven by self-complementary N–H···N/N···H–N hydrogen-bonded homosynthons among biimidazole units, and I···N halogen bonds between **XBD2** molecules and pyridine units. Note that **A3**:**XBD2** is actually a co-crystal solvate; the crystal lattice contains methanol molecules that disrupt half of the intended I···N_{py} interactions by inserting themselves between **XBD2** donor molecules and adjacent 4-pyridyl moieties (Figure 2.8, bottom).

The crystal structure determinations of **A2**:**HBD1** and **A3**:**HBD1** reveal a 1:1 stoichiometry in both cases, and the primary supramolecular motif in each structure is a tetramer built around a central N–H···N/N···H–N hydrogen-bonded homosynthon combined with two symmetry-related O–H···N_{py} interactions that attach two benzoic acid molecules to this core on either side (Figure 2.9).

In each of the crystal structures of **A2**:**HBD3**, **A2**:**HBD5** and **A1**:**HBD6**, the acceptor and the co-former (*i.e.* aliphatic dicarboxylic acid) have combined in a 2:1 stoichiometric ratio to afford supramolecular polymeric chains, similar to what was observed in the **XBD2**-based co-crystals

(Figure 2.10). Again, the two-point $N_{im1}\cdots H–N_{im2}$ and single-point $N_{py}\cdots H–O$(acid) hydrogen bond interactions serve to create these infinite 1-D architectures of alternating building blocks. As can be seen, diacids assume their fully-extended (all-*trans*) conformation irrespective of the length of the carbon backbone.

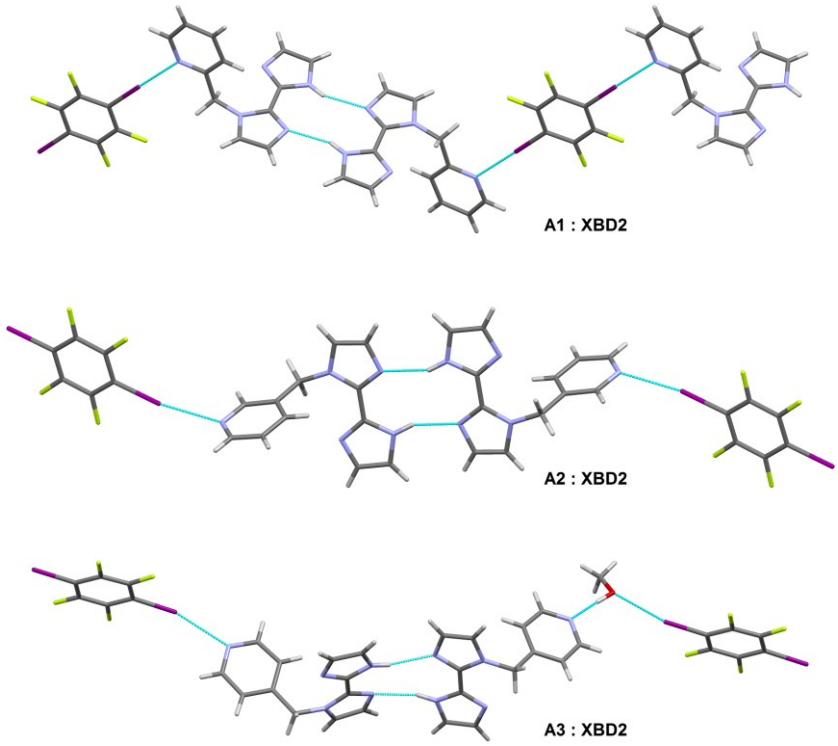

Figure 2.8 Chains of **A1**:**XBD2**, **A2**:**XBD2** and **A3**:**XBD2**.

A3 tends to yield 1:1 binary solids with aliphatic diacids, contrary to **A1** and **A2**. The single-point $O–H\cdots N_{py}$ interactions and $R^2_2(9)$ heterosynthon composed of $C{=}O\cdots H–N_{im2}$ and $O–H\cdots N_{im1}$ interactions are responsible for their assembly into infinite chains (Figure 2.11). Diacid molecules in both structures, succinic acid and adipic acid, exhibit somewhat distorted/folded conformations and place their two terminal carboxyl functions in mutual *syn* orientation, so the resulting chains are zig-zag in shape.

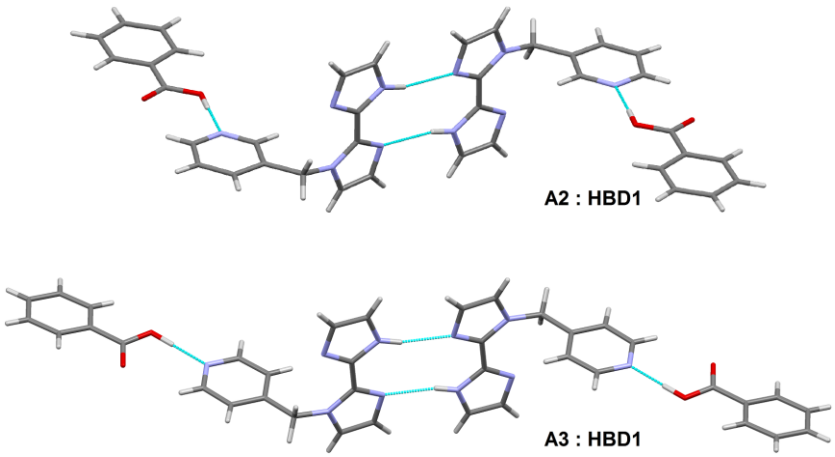

Figure 2.9 Tetramers of **A2**:**HBD1** and **A3**:**HBD1**.

It is not completely clear as to why **A3** deviates from the supramolecular behavior observed in the previous five acid-based co-crystals and forms the two-point heterosynthon. However, it does indicate that the relative influence of the kinetic component (which favors a homosynthon) and the thermodynamic effect of $N_{im1}\cdots H–N_{im2}$ and $C{=}O\cdots H–N_{im2}/O–H\cdots N_{im1}$ hydrogen bonding interactions (which favors homosynthons and heterosynthons, respectively) is very finely balanced. From a thermodynamic point of view, **A3**'s preference for the heteromeric interaction can be ascribed to the additional stabilization gained by replacing two relatively weaker $N_{im1}\cdots H–N_{im2}$ bonds with $C{=}O\cdots H–N_{im2}$ and $O–H\cdots N_{im1}$ bonds of intermediate strength.[23]

The scenario is quite different with **A1**:**HBD4** and **A1**:**HBD2** where proton transfer has occurred from the acid to the biimidazole unit. **A1**:**HBD4** is a 1:1 salt composed of mono-protonated **A1** (*i.e.* 1-(pyridin-2-ylmethyl)-2,2'-biimidazolium monocation) and mono-deprotonated **HBD4** (*i.e.* hydrogen suberate monoanion). The monoanionic **HBD4** adopts the *gauche* conformation and creates a supramolecular polymeric chain with an array of *syn–anti* $C{=}O\cdots H–O$ hydrogen-bonds (Figure 2.12). The cationic **A1** species attach to this anionic chain *via* classical (charge-neutral) $C{=}O\cdots H–N_{im2}$ and charge-assisted $C–O^{-}\cdots H–{}^{+}N_{im1}$ interactions.

Not surprisingly, the ionic hydrogen bond is markedly shorter than the former [O···N separation: 2.5930(18) Å *versus* 2.6980(18) Å]. The carbonyl oxygen at the deprotonated end of the acid engages in bifurcated hydrogen bonds.

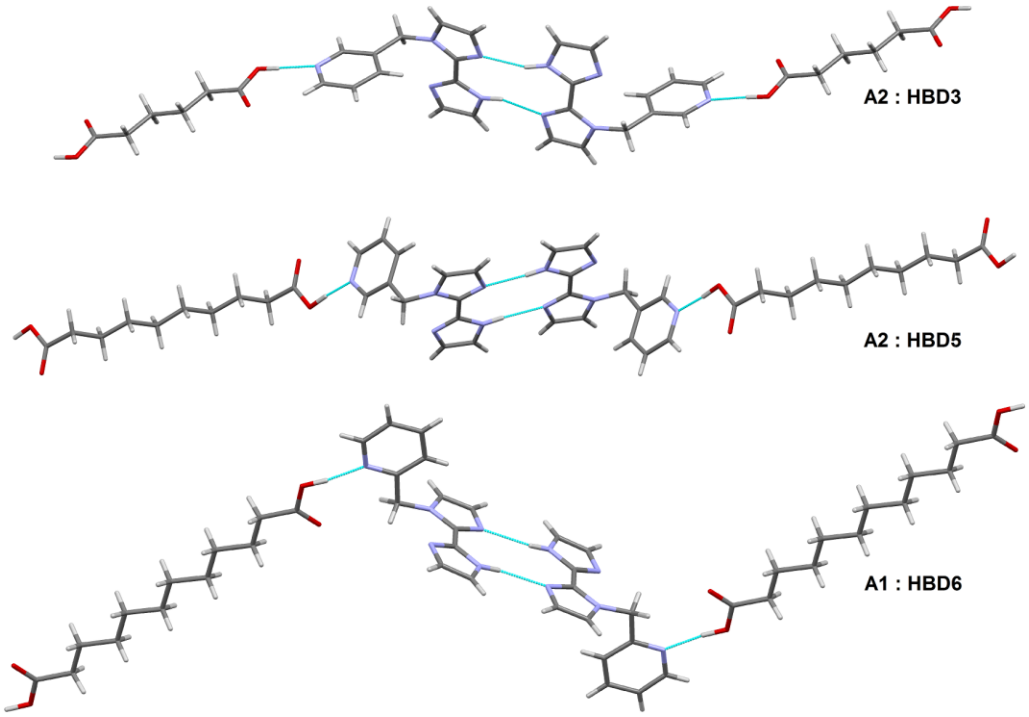

Figure 2.10 Chains of **A2**:**HBD3**, **A2**:**HBD5** and **A1**:**XBD6**.

A1:**HBD2** is also a salt made up of 1-(pyridin-2-ylmethyl)-2,2'-biimidazolium monocations and succinate dianions, but the structure is complicated by the fact that an additional molecule of the neutral acid has been incorporated in the crystal lattice (Figure 2.13). This type of behavior (*i.e.* the co-existence of fully-ionized and neutral forms of the acid) in the solid state is by no means unusual because the latter can deliver additional donor sites needed for satisfying the highly-demanding carboxylate dianions.[24] In both **A1**:**HBD4** and **A1**:**HBD2**, there are not any non-covalent links stemmed from the pyridyl-N.

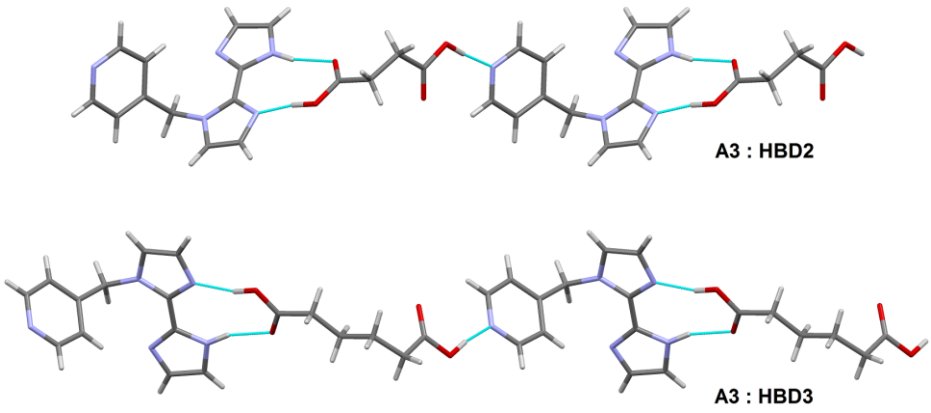

Figure 2.11 Chains of **A3**:**HBD2** and **A3**:**HBD3**.

Although the formation of salts among biimidazole derivatives and carboxylic acids is rather common, in our study, it was observed exclusively in **A1**-containing systems. This can be explained on the basis of calculated MEPS,[25] as proton transfer depends directly on the acidity and basicity of the functional groups involved in hydrogen-bonding. The protonating site of **A1** (*i.e.* the nitrogen on substituted imidazole, N_{im1}) possesses the lowest electrostatic potential compared to that of **A2** or **A3** (Table 2.1), implying its higher basicity and increased propensity for proton abstraction. Hence, **A1**-acid combinations appear to produce salts rather than co-crystals.

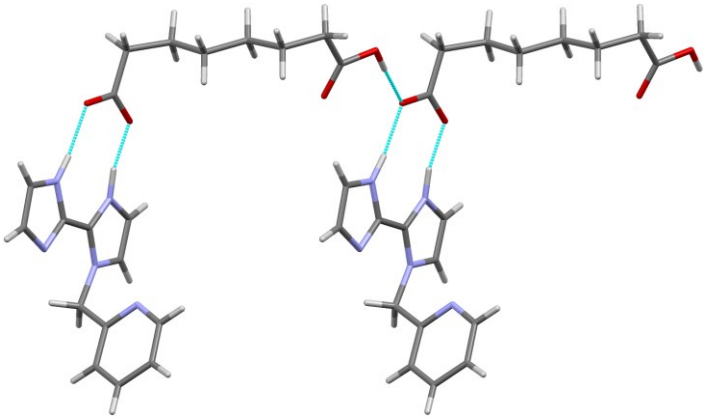

Figure 2.12 Structure of **A1**:**HBD4**.

An examination of the crystal structures of the multicomponent solids in this study clearly demonstrates that the self-complementary N-H···N/N···H-N homosynthon is the preferred mode of interaction in **A1**–**A3**; it occurs in ten out of fourteen cases. Another important element to highlight is that this homodimerization event then offers two picolyl 'arms', arranged in an antiparallel fashion, as suitable attachment points for either hydrogen-bond or halogen-bond based co-formers.

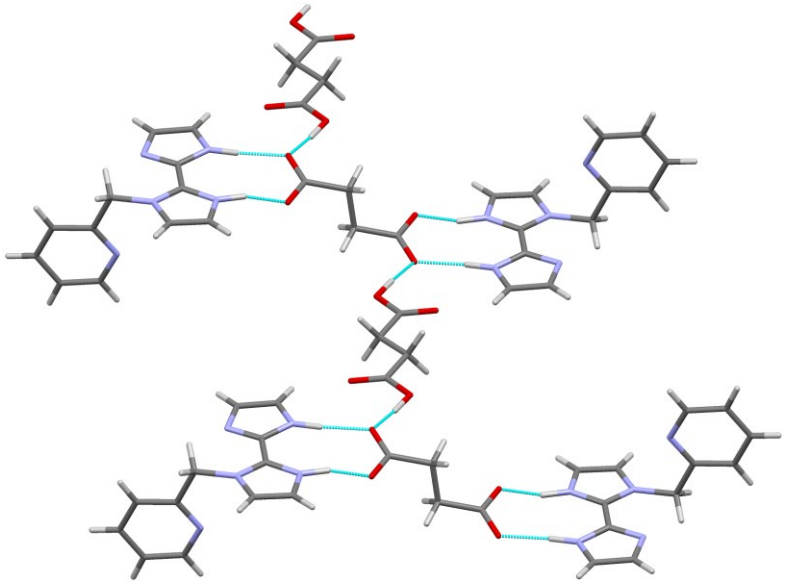

Figure 2.13 Structure of **A1**:**HBD2**.

Even though the main focus of this discussion has been on the primary XB and HB interactions, several weaker secondary interactions such as C–H···N, C–H···O and C–H···π are present and contribute to the detailed arrangement/overall packing of molecules within these structures. For instance, the unsubstituted imidazole-N (*i.e.* N_{im2}), the weakest acceptor as suggested by MEPS that does not participate in any notable intermolecular non-covalent bonding, does consistently form an intramolecular HB interaction with one of the methylene protons. In

fact, such $N_{im2}\cdots$H–C(methylene) contacts (2.29–2.50 Å, 108–128°) exist in all 17 structures, and may explain why the relative orientation of the picolyl substituent with respect to the biimidazole moiety is fairly constant (the torsional variance is only about 10–15° despite the fact that the picolyl group can, in principle, rotate freely). Moreover, in six of seven cases, an $N_{py}\cdots$H–O(acid) hydrogen bond (which essentially drives the co-crystal formation) is accompanied by a C═O···H–C_{py} motif which leads to a co-planar arrangement of the carboxylic functionality and the heterocycle. The two salts, **A1**:**HBD4** and **A1**:**HBD2**, also possess C═O···H–C_{im2} secondary contacts.

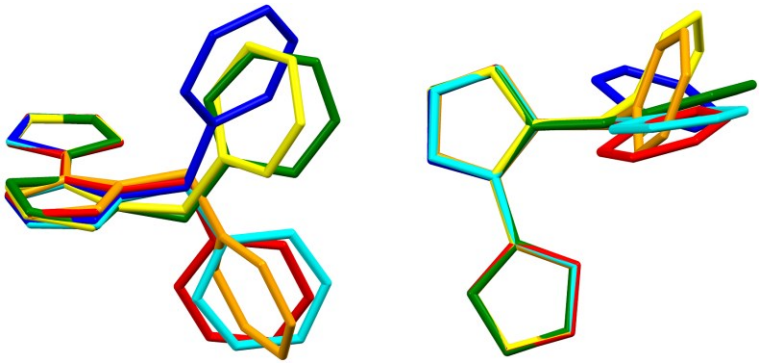

Figure 2.14 Six overlaid **A3** molecules, emphasizing its flexibility (hydrogen atoms have been omitted for clarity).

Finally, it is worth mentioning that the methylene (–CH_2–) spacer group between imidazole and pyridine imparts considerable flexibility to the molecular structures of **A1**–**A3**. This, in turn, allows them to adapt or fine-tune their conformation according to the geometric demands of the co-formers. Moreover, the binding sites of the central biimidazole moiety are sterically less hindered than their disubstituted counterparts. Both these properties, semi-rigidity and high-accessibility, are demonstrated in Figure 2.14 featuring six superimposed **A3** molecules from different crystal structures. Note also that two imidazole rings are essentially coplanar in all cases

even though the integration of only one picolyl pendant unit introduces relatively small barrier to their rotation around C–C bond.

2.4 Conclusions

The structural landscape around three positional isomers of 1-(pyridylmethyl)-2,2'-biimidazole (**A1**–**A3**) has been mapped out through systematic co-crystallizations with selected hydrogen- and halogen-bonding coformers in order to explore the impact of electrostatics and geometry on the resulting architectures. The combination of electrostatic potentials computed on molecular surfaces and structural information from single-crystal X-ray diffraction offers considerable support of the hypothesis that electrostatics has a decisive effect on supramolecular selectivity. However, it is also important to consider electrostatically and geometrically favorable two-point interactions when assessing structural preferences of these biimidazole derivatives. In addition, the two-point synthons do offer a kinetic advantage over the single-point interactions when it comes to influencing the final supramolecular architecture.

With halogen-bond donors, the solid-state supramolecular behavior of **A1**–**A3** is far more consistent. The same structural features are observed in each of the four XB-based co-crystals that display the intended chemical composition (the methanol solvate does, unsurprisingly, contain a slightly altered assembly pattern). All structures are built around the self-complementary N–H···N/N···H–N hydrogen-bonding motifs that create biimidazole···biimidazole adducts and the I···N(pyridine) halogen bonds that connect the XB-donating coformer to this core unit, thereby extending the structure.

Conversely, the products of the reactions between **A1**–**A3** and hydrogen-bond donors are highly unpredictable owing to the emergence of a potentially competing, bidentate

acid···biimidazole heterosynthon. The factors that ultimately determine the choice between homosynthons and heterosynthons are closely matched, and there are small thermodynamic differences between the possible structural outcomes. The occasional proton transfer that accompany co-crystallizations involving carboxylic acids and the torsional freedom of aliphatic diacids add further complexity. Of the nine structures obtained, five contain the biimidazole···biimidazole homosynthon, two contain the acid···biimidazole heterosynthon and the remaining two structures are salts.

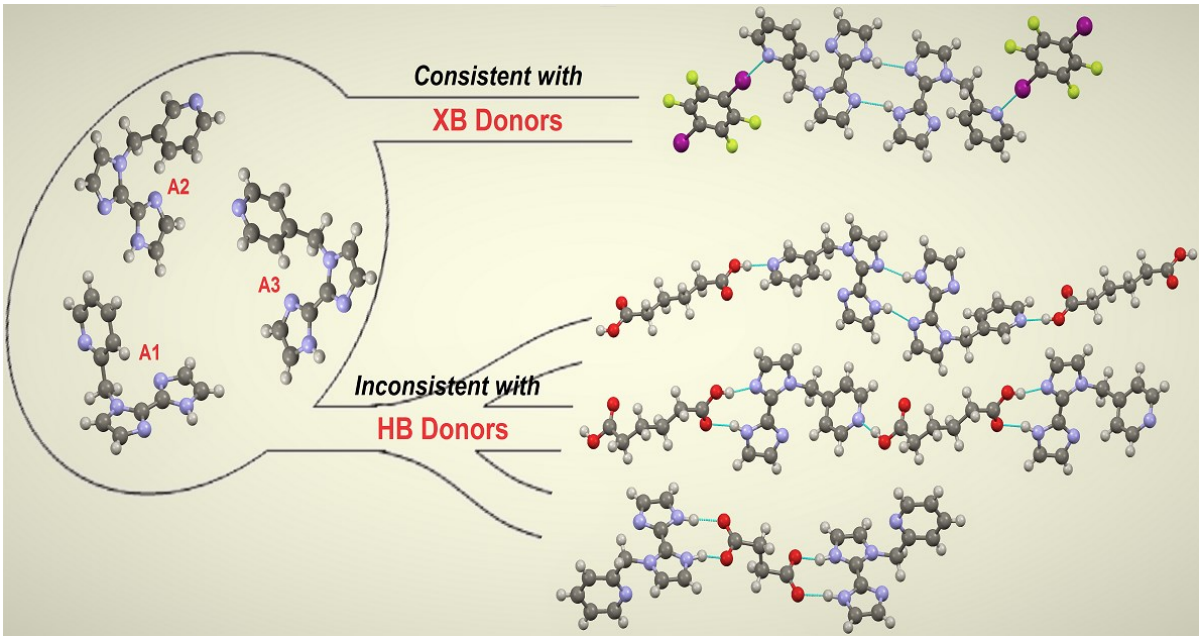

Figure 2.15 Achieving reliability with simultaneous use of HBs and XBs.

In short, this study emphasizes the feasibility of concurrent utilization of HBs and XBs for refining strategies for practical supramolecular synthesis (Figure 2.15). Any interaction bias incorporated within the system (in this case, two-point *versus* single-point) effectively precludes synthon crossover possibilities, allowing us to obtain the final supramolecular product with a significant degree of predictability.

2.5 References

1. J. M. Lehn, *Proceedings of the National Academy of Sciences of the United States of America*, 2002, **99**, 4763-4768; J. M. Lehn, *Pure Appl. Chem.*, 1978, **50**, 871-892.
2. M. J. Zaworotko, *Crystal Growth & Design*, 2007, **7**, 4-9.
3. G. R. Desiraju, *Angewandte Chemie-International Edition in English*, 1995, **34**, 2311-2327; A. Mukherjee, *Crystal Growth & Design*, 2015, **15**, 3076-3085.
4. C. B. Aakeroy, P. D. Chopade, C. Ganser and J. Desper, *Chem. Commun.*, 2011, **47**, 4688-4690; C. B. Aakeroy, P. D. Chopade and J. Desper, *Crystal Growth & Design*, 2011, **11**, 5333-5336.
5. B. R. Sreekanth, P. Vishweshwar and K. Vyas, *Chem. Commun.*, 2007, 2375-2377; A. Mukherjee and G. R. Desiraju, *Chem. Commun.*, 2011, **47**, 4090-4092; M. Gryl, A. Krawczuk and K. Stadnicka, *Acta Crystallographica Section B-Structural Science*, 2008, **64**, 623-632.
6. M. K. Corpinot, S. A. Stratford, M. Arhangelskis, J. Anka-Lufford, I. Halasz, N. Judas, W. Jones and D. K. Bucar, *CrystEngComm*, 2016, **18**, 5434-5439; D. K. Bucar, R. F. Henry, G. G. Z. Zhang and L. R. MacGillivray, *Crystal Growth & Design*, 2014, **14**, 5318-5328.
7. N. A. Mir, R. Dubey and G. R. Desiraju, *Iucrj*, 2016, **3**, 96-101.
8. C. B. Aakeroy, T. K. Wijethunga, J. Desper and M. Dakovic, *Crystal Growth & Design*, 2016, **16**, 2662-2670; M. D. Perera, J. Desper, A. S. Sinha and C. B. Aakeroy, *CrystEngComm*, 2016, **18**, 8631-8636; C. B. Aakeroy, J. Desper and M. M. Smith, *Chem. Commun.*, 2007, 3936-3938; C. A. Hunter, *Angew Chem Int Edit*, 2004, **43**, 5310-5324.
9. C. B. Aakeroy, T. K. Wijethunga, J. Desper and C. Moore, *J. Chem. Crystallogr.*, 2015, **45**, 267-276; C. B. Aakeroy, T. K. Wijethunga and J. Desper, *J. Mol. Struct.*, 2014, **1072**, 20-27; C. B. Aakeroy, T. K. Wijethunga and J. Desper, *New J. Chem.*, 2015, **39**, 822-828.
10. P. Politzer and J. S. Murray, *Crystal Growth & Design*, 2015, **15**, 3767-3774.
11. S. Scheiner, *Hydrogen bonding : a theoretical perspective*, Oxford University Press, New York ; Oxford, 1997; P. Politzer, J. S. Murray and T. Clark, *PCCP*, 2010, **12**, 7748-7757; A. C. Legon, *Angew Chem Int Edit*, 1999, **38**, 2687-2714; D. Hadži, *Theoretical treatments of hydrogen bonding*, Wiley, Chichester, 1997.
12. M. C. Etter, *Acc. Chem. Res.*, 1990, **23**, 120-126; M. C. Etter, *J. Phys. Chem.*, 1991, **95**, 4601-4610; M. C. Etter, *J. Am. Chem. Soc.*, 1982, **104**, 1095-1096; J. Donohue, *J. Phys. Chem.*, 1952, **56**, 502-510.
13. T. Steiner, *Angew Chem Int Edit*, 2002, **41**, 48-76; E. D. Glowacki, M. Irimia-Vladu, S. Bauer and N. S. Sariciftci, *Journal of Materials Chemistry B*, 2013, **1**, 3742-3753; F. Meyer and P. Dubois, *CrystEngComm*, 2013, **15**, 3058-3071; P. Metrangolo, H. Neukirch, T. Pilati and G. Resnati, *Acc. Chem. Res.*, 2005, **38**, 386-395; G. Berger, J. Soubhye and F. Meyer, *Polymer Chemistry*, 2015, **6**, 3559-3580; L. C. Gilday, S. W. Robinson, T. A. Barendt, M. J. Langton, B. R. Mullaney and P. D. Beer, *Chem. Rev.*, 2015, **115**, 7118-7195; G. Cavallo, P. Metrangolo, R. Milani, T. Pilati, A. Priimagi, G. Resnati and G. Terraneo, *Chem. Rev.*, 2016, **116**, 2478-2601.
14. A. H. Pedersen, M. Julve, E. K. Brechin and J. Martinez-Lillo, *CrystEngComm*, 2017, **19**, 503-510; M. Tadokoro, Y. Ohhata, Y. Shimazaki, S. Ishimaru, T. Yamada, Y. Nagao, T. Sugaya, K. Isoda, Y. Suzuki, H. Kitagawa and H. Matsui, *Chem-Eur J*, 2014, **20**, 13698-13709; L. F. Yang, M. L. Cao, Y. Cui, J. J. Wu and B. H. Ye, *Crystal Growth & Design*, 2010, **10**, 1263-1268; C. Borel, K. Larsson, M. Hakansson, B. E. Olsson, A. D. Bond and

L. Ohrstrom, *Crystal Growth & Design*, 2009, **9**, 2821-2827; L. F. Yang, M. L. Cao, H. J. Mo, H. G. Hao, J. J. Wu, J. P. Zhang and B. H. Ye, *CrystEngComm*, 2009, **11**, 1114-1121; Q. H. Jin, L. L. Zhou, L. J. Xu, Y. Y. Zhang, C. L. Zhang and X. M. Lu, *Polyhedron*, 2010, **29**, 317-327; L. M. Gruia, F. D. Rochon and A. L. Beauchamp, *Inorg. Chim. Acta*, 2007, **360**, 1825-1840.

15. K. L. Zhang, H. Huang and S. W. Ng, *Acta Crystallographica Section E-Structure Reports Online*, 2010, **66**, O2919-U1091; X. Liu and W. Q. Zhu, *Acta Crystallographica Section E-Structure Reports Online*, 2010, **66**, O1245-U1249; Y. P. Li and P. Yang, *Acta Crystallographica Section E-Structure Reports Online*, 2006, **62**, O3223-O3224; X.-L. Gao, L.-F. Bian and S.-W. Guo, *Acta Crystallographica Section E*, 2014, **70**, o1221-o1222; X. L. Gao and M. L. Zhu, *Acta Crystallographica Section E-Structure Reports Online*, 2010, **66**, O3124-U3211; X. L. Gao, L. P. Lu and M. L. Zhu, *Acta Crystallogr C*, 2009, **65**, O123-O127.
16. Y. H. Xu, Y. Q. Lan, Y. H. Zhao, D. Y. Du, G. J. Xu, K. Z. Shao, Z. M. Su and Y. Liao, *Inorg. Chem. Commun.*, 2009, **12**, 169-172; R. L. Sang and L. Xu, *Inorg. Chem.*, 2005, **44**, 3731-3737; E. Laurila, L. Oresmaa, E. Kalenius, P. Hirva and M. Haukka, *Polyhedron*, 2013, **52**, 1231-1238; J. L. Gulbransen and C. M. Fitchett, *CrystEngComm*, 2012, **14**, 5394-5397; Y. M. Fu, Y. H. Zhao, Y. Q. Lan, K. Z. Shao, Y. Q. Qiu, X. R. Hao and Z. M. Su, *J. Solid State Chem.*, 2008, **181**, 2378-2385; J. L. Ferguson and C. M. Fitchett, *Crystal Growth & Design*, 2015, **15**, 1280-1288.
17. C. B. Aakeroy, T. K. Wijethunga, J. Benton and J. Desper, *Chem. Commun.*, 2015, **51**, 2425-2428.
18. L. N. Yang, Y. X. Zhi, J. H. Hei, J. Li, F. X. Zhang and S. Y. Gao, *J. Coord. Chem.*, 2011, **64**, 2912-2922; A. X. Tian, X. Hou, N. Sun, R. Xiao, J. Ying, Y. Yang, Y. L. Ning, T. J. Li and X. L. Wang, *Chinese Journal of Inorganic Chemistry*, 2015, **31**, 839-847; G. Lin, H. Collier and R. G. Baughman, *Acta Crystallogr C*, 1999, **55**, 476-478; J. Q. Tao, J. Wang and X. J. Xu, *Acta Crystallogr C*, 2011, **67**, M364-M366.
19. D. T. Cromer, R. R. Ryan and C. B. Storm, *Acta Crystallogr C*, 1987, **43**, 1435-1437.
20. J. R. Cho, S. G. Cho, E. M. Goh and J. K. Kim, *Journal*, 2004.
21. C. F. Macrae, I. J. Bruno, J. A. Chisholm, P. R. Edgington, P. McCabe, E. Pidcock, L. Rodriguez-Monge, R. Taylor, J. van de Streek and P. A. Wood, *J. Appl. Crystallogr.*, 2008, **41**, 466-470.
22. Wavefunction, Inc. Irvine, CA 92612, USA, https://www.wavefun.com/products/spartan.html, (accessed February 15, 2017).
23. A. Gavezzotti, V. Colombo and L. Lo Presti, *Crystal Growth & Design*, 2016, **16**, 6095-6104.
24. S. K. Callear, M. B. Hursthouse and T. L. Threlfall, *CrystEngComm*, 2010, **12**, 898-908; C. B. Aakeroy, M. E. Fasulo and J. Desper, *Mol Pharm*, 2007, **4**, 317-322.
25. A. G. Zhong, H. J. Jiang and H. D. Liang, *Chem. Phys. Lett.*, 2011, **512**, 278-282; P. Nagy, K. Novak and G. Szasz, *Theochem-Journal of Molecular Structure*, 1989, **60**, 257-270; Y. G. Ma, K. C. Gross, C. A. Hollingsworth, P. G. Seybold and J. S. Murray, *J. Mol. Model.*, 2004, **10**, 235-239; S. B. Liu, C. K. Schauer and L. G. Pedersen, *J. Chem. Phys.*, 2009, **131**; S. B. Liu and L. G. Pedersen, *J. Phys. Chem. A*, 2009, **113**, 3648-3655; Y. Huang, L. H. Liu and S. B. Liu, *Chem. Phys. Lett.*, 2012, **527**, 73-78; T. Brinck, *J. Phys. Chem. A*, 1997, **101**, 3408-3415.

Chapter 3 - Heterobifunctional acetylacetonate ligands

3.1 Introduction

Inorganic-organic hybrid materials are structurally diverse and functionally versatile. The design and construction of such materials therefore represent an area of enormous relevance to fundamental crystal engineering and applied materials science alike.[1] Even though their synthesis is usually a multiparameter process, the nature of the organic linker or the ligand is one of the key factors that control both the structure and the subsequent properties of the resulting solids. So far, ligands containing carboxylate moieties[2] and nitrogen heterocycles[3] (pyridine, imidazole, pyrazole, triazole, *etc*.) dominate the arena because of the intermediate strength of the coordinative bonds that simultaneously impart strength and reversibility to the assembly process. This dynamic nature is of paramount importance as it allows for the reversal of undesirable molecular recognition events, thereby facilitating the formation of highly ordered as well as of thermodynamically stable structures. Carboxylate ligands possess several additional features that are responsible for their success. Being negatively-charged, they can lead to electroneutral assemblies where no potentially disruptive counter-anions are present. Their cluster chemistry and node types with many metal ions, which serve as secondary building units (SBUs) in the formation of network structures, are well-studied, so building robust networks having predetermined topologies would be relatively easier.[2]

Another family of compounds used for metal coordination is 1,3-diketones or β-diketones. As the name implies, they have their two keto functionalities separated by a single carbon atom. Even though β-diketones undergo keto-enol tautomerism, and exist as a mixture of diketone and keto-enol forms, they are, by convention, named and reported as diketones. In fact, these tautomers interconvert so rapidly in such a way that the pair can be treated as a single compound in most

applications. Conjugation and intramolecular hydrogen bonding shift this dynamic equilibrium in favor of enol form under most conditions. Further, enol form is favored in nonpolar/less polar solvents whereas keto form predominates in polar solvents.

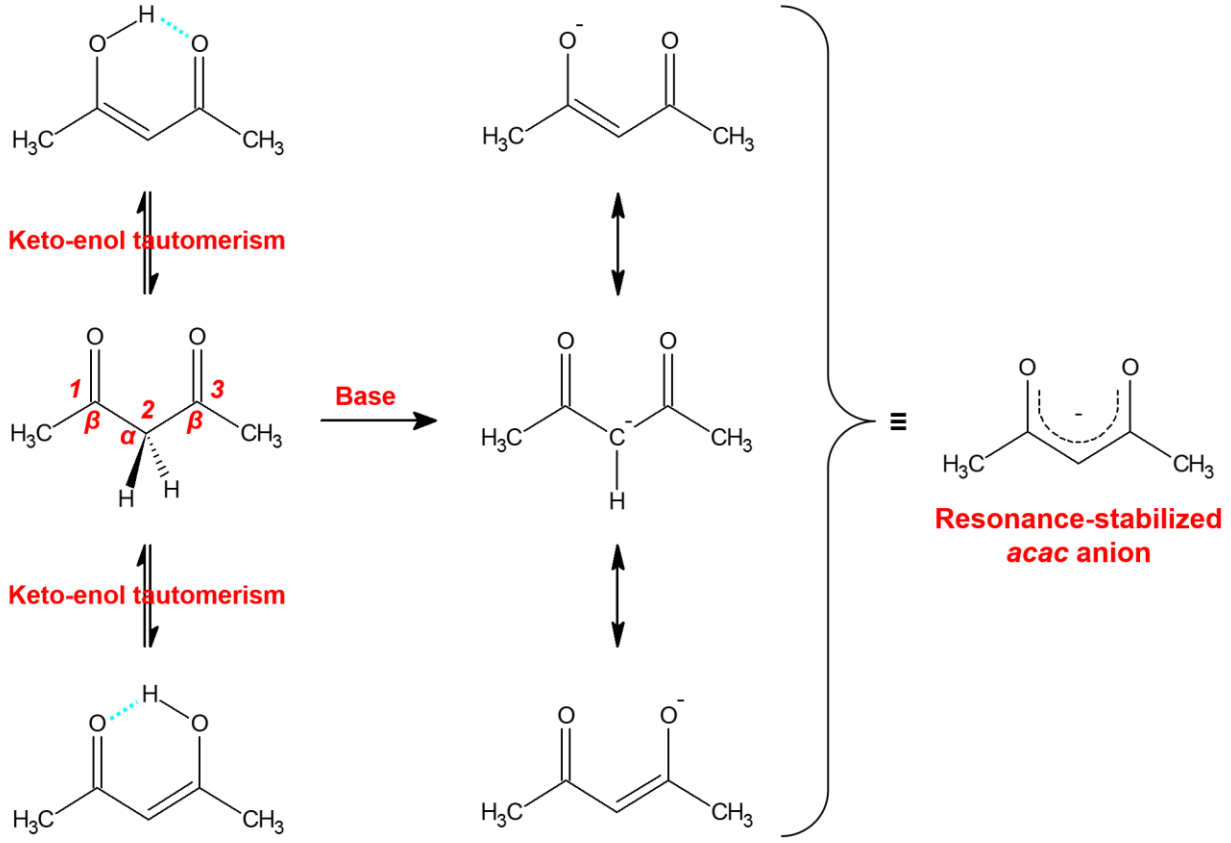

Figure 3.1 Resonance-stabilization of deprotonated acetylacetone.

Deprotonated forms of β-diketones are referred to as β-diketonates. The presence of two neighboring carbonyl groups increases the easiness of α-hydrogen removal, thereby increasing the acidity of β-diketones. This enhanced acidity is due to the fact that the resultant enolate ions are stabilized by delocalization of the negative charge over both carbonyl groups. Figure 3.1 shows the resonance-stabilization of the acetylacetonate or 2,4-pentadionate anion.

When binding to metal ions, β-diketonates act as bidentate ligands and form stable chelates having six-membered heterocyclic rings.[4] The synergistic effect of resonance-stabilization and chelation drives the equilibrium towards complex formation. Acetylacetonate (often abbreviated as ***acac***$^{-}$) is the simplest and one of the most versatile members of this type of ligands. Its homoleptic complexes, in most cases, are neutral and possess the formula M(*acac*)$_2$ or M(*acac*)$_3$, where M^{n+} is usually a di- or tri-valent transition-metal ion (Figure 3.2). Heteroleptic (mixed-ligand) complexes in which *acac* only partially saturates the metal center, are also common.

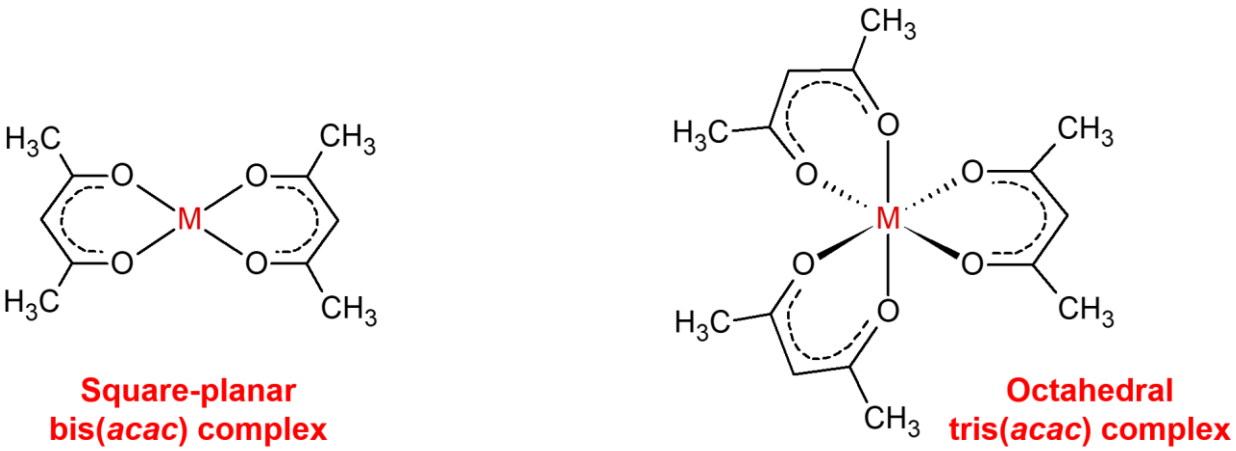

Figure 3.2 Bis- and tris-chelated metal-acac complexation.

Numerous acetylacetone derivatives have been synthesized and studied in the context of coordination chemistry. Among those, centrally-substituted (*i.e.* 3-substituted) acetylacetonates are much more common and have very similar binding vectors to the analogous carboxylates.[5] For example, centrally-substituted bis-acetylacetonates have been successfully employed in the assembly of numerous discrete, oligomeric structures (acyclic dimers, rhomboids, triangles, squares, *etc.*). The simplest is derived from tetraacetylethane, in which the two acac fragments are directly connected to each other at the C3 positions (*i.e.* no spacer).[6] In other cases, the relative

orientation of acac moieties, and hence the coordination vectors, have been manipulated by carefully choosing the spacer and the substitution positions.[7] Acetylacetonate ligands are, however, seldom used in the synthesis of coordination polymers because they are generally stronger than carboxylate ligands and often produce non-crystalline solids. The structural characterization, which is an essential part for any systematic study, would unfortunately be impossible with such amorphous materials. Moreover, compared to carboxylic acids, acetylacetones are synthetically demanding and susceptible to hydrolysis *via* reverse Claisen condensation (retro-Claisen cleavage).[8]

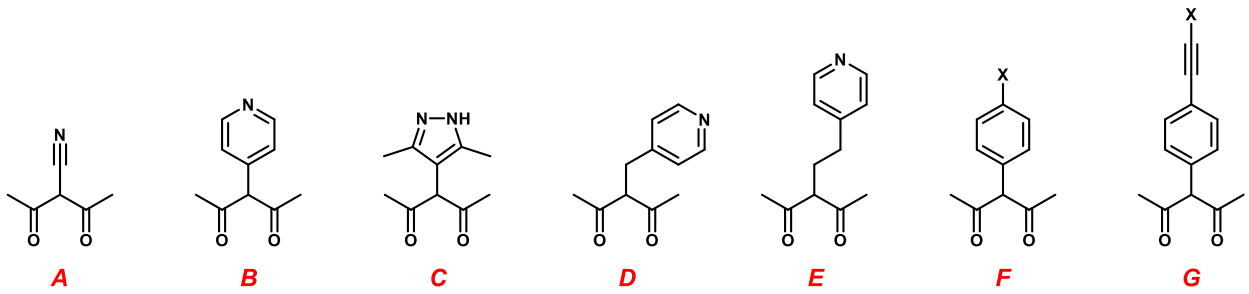

Figure 3.3 Mono-acac ligands bearing secondary interaction sites (X = Cl, Br, I).

One possible way to ameliorate β-diketonate ligands for the construction of crystalline extended solids is to couple them with relatively weaker metal-binding sites such as N-donor substituents.[9] Within this context, 3-cyanopentane-2,4-dione and 3-(pyridin-4-yl)pentane-2,4-dione have gained the most attention during the past two decades (Figure 3.3, **A** and **B**). Pioneering work by Maverick,[10] Domasevitch,[11,12] Nishikiori,[13] Englert,[14] and others[15] show that both ligands are effective for the construction of coordination polymers, especially heterobimetallic infinite assemblies. Though to a lesser extent, 3-(pyridin-4-ylmethyl)pentane-2,4-dione,[16] 3-(2-(pyridin-4-yl)ethyl)pentane-2,4-dione[12] and 3-(3,5-dimethyl-1H-pyrazol-4-yl)pentane-2,4-dione[17] have

also been used (Figure 3.3, **C**, **D** and **E**). In an attempt to introduce halogen-bonding secondary interactions into the metal-directed assemblies, Englert *et al* reacted Fe(III) and Al(III) tris-acac complexes of 3-(pyridin-4-yl)pentane-2,4-dione with tetrafluorodiiodobenzene,[18] and with a similar goal in mind, we studied a series of halophenyl- and haloethynylphenyl-substituted acac derivatives with divalent copper (Figure 3.3, **F** and **G**).[19]

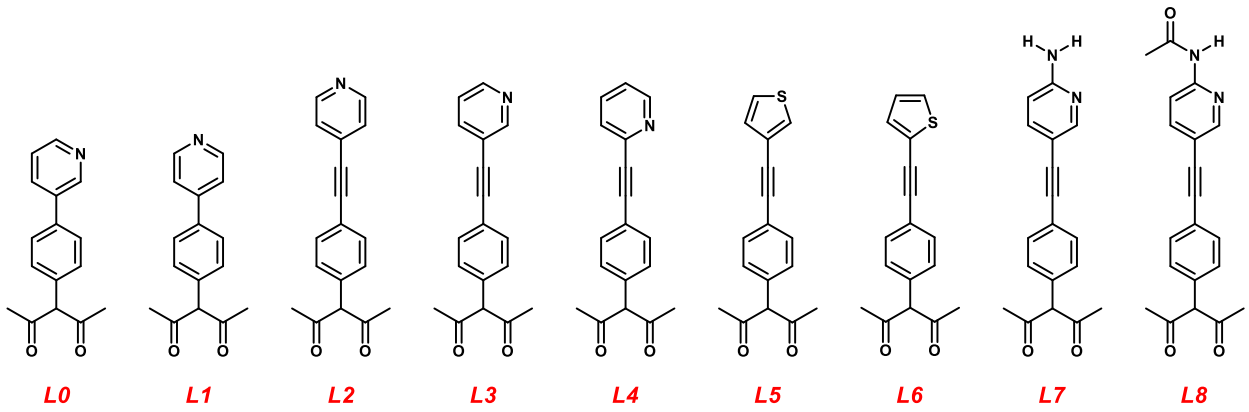

Figure 3.4 New ligands synthesized and explored in this study.

In the study presented herein, we have prepared a series of linear, ditopic, heterobifunctional ligands in which an acac functionality and a heterocyclic moiety are connected through either *p*-phenylene or *p*-phenylene-ethynylene spacer, and examined their metal binding ability with a selected set of transition metal ions.

We postulate that the acac ligation can give rise to several different node types based on the coordination environment around the metal center which, in turn, depends on the nature of the metal ion. Divalent metal ions, for instance, will form linear, rigid struts *via* tetra-coordination of two acac moieties whereas octahedral tris-acac complexes derived from metal trications can serve as trigonal-planar nodes. Large, high-valent metal ions (such as Zr^{4+}, lanthanoid ions, *etc.*) have the ability to accommodate even more acac units and form higher connecting nodes. As the metal

acetylacetonates made up of **L0**–**L8** hold peripheral binding sites, they can undergo further metal binding. Square-planar bis-acac species derived from **L1** and **L2**, for instance, can assume other tetragonal geometries (square-based pyramidal and octahedral) when pyridyl moieties of neighboring bis-acac units bind to the vacant axial sites, thereby creating T-shaped and square-planar nodes, respectively (Figure 3.5).

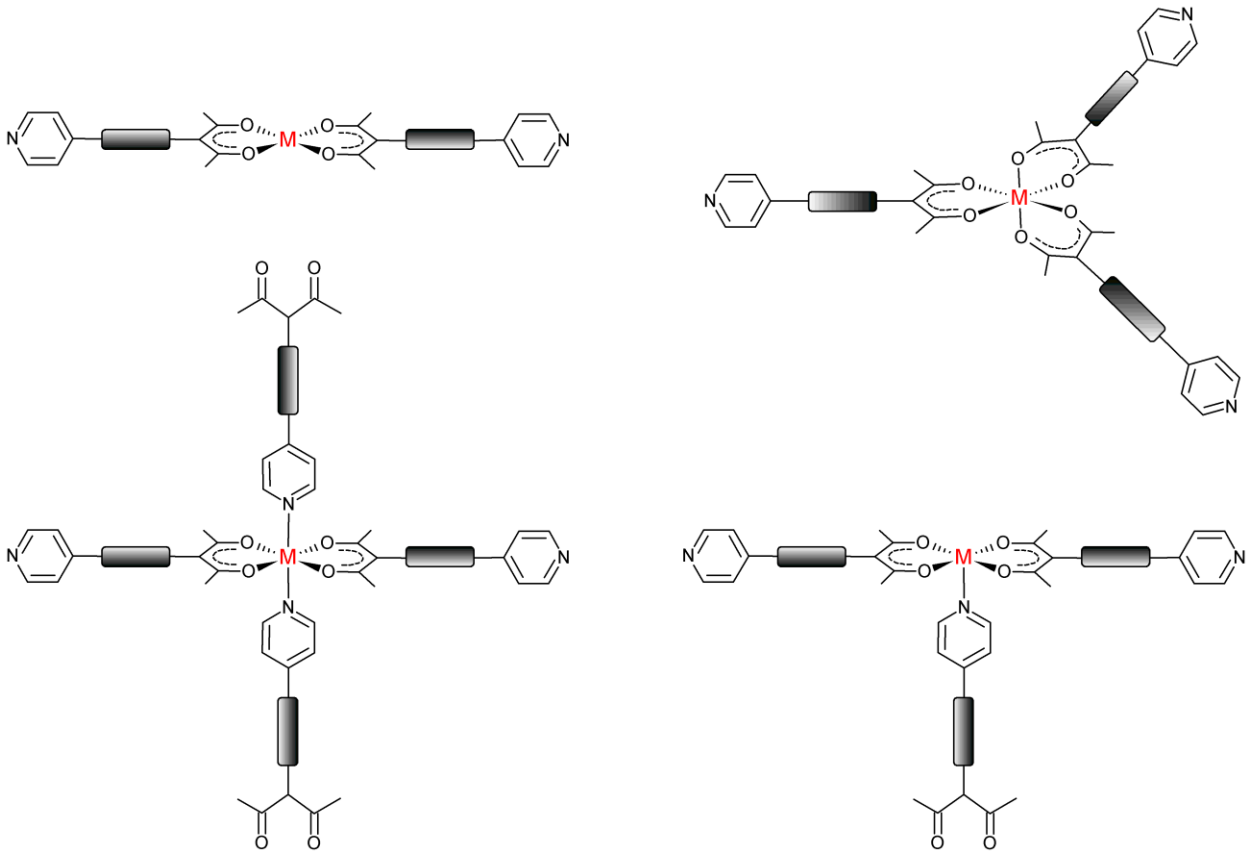

Figure 3.5 Node types anticipated for metal acetylacetonates of **L1** and **L2**.

The heterocycles (pyridine and thiophene) can also be involved in weak secondary interactions such as hydrogen- and halogen-bonds. Particularly, 2-aminopyridine in **L7** can form self-complementary hydrogen-bonds, and 2-acetylaminopyridine in **L8** not only retains its self-complementary hydrogen-bond forming ability but also has the potential to chelate to metal ions

by the ring nitrogen and amide oxygen (Figure 3.6). Ultimately, our ligands can result in a rich variety of architectures.

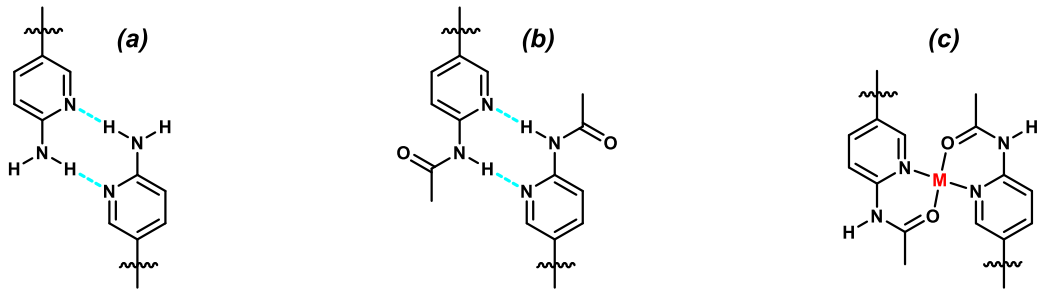

Figure 3.6 Interactions expected from 2-aminopyridine and 2-acetamidopyridine moieties.

3.2 Experimental

3.2.1 Materials and methods

Unless otherwise noted, all chemicals were purchased from commercial sources, and were used as received without further purification. Nuclear magnetic resonance spectra were recorded on a Varian Unity Plus (400 MHz) NMR spectrometer. A Nicolet 380 FT-IR system was used for infrared spectroscopy. Thermogravimetric analysis (TGA) was performed on a TA Instruments TA Q50 analyzer.

3.2.2 Synthesis of 4-(pyridin-4-yl)benzaldehyde (1)

To a 100-mL round-bottom flask containing 4-bromobenzaldehyde (500 mg, 2.70 mmol, 1 equiv.) was added 1,4-dioxane (20 mL) and water (10 mL), and the resulting mixture was degassed by bubbling nitrogen gas for 20 minutes. Potassium carbonate (1.87 g, 13.51 mmol, 5 equiv.), pyridine-4-boronic acid (500 mg, 4.05 mmol, 1.5 equiv.) and tetrakis(triphenylphosphine)palladium(0) catalyst (156 mg, 0.135 mmol, 5 mol%), were introduced and nitrogen gas was bubbled through the flask content again for an additional 10

minutes. It was then stirred at 85 °C under dinitrogen atmosphere for 24 hours, after which the solvents were removed *in vacuo*. The residue was re-dissolved in 75 mL of methylene chloride and filtered through a pad of Celite, using an extra 25 mL portion of solvent to wash the filter pad. The combined filtrate was washed with distilled water (2 × 20 mL) and brine (20 mL), dried over anhydrous magnesium sulfate, and evaporated to dryness under vacuum. The resulting solid was further purified by column chromatography on silica gel using hexanes/ethyl acetate (4:1 to 3:2) mixture, affording 4-(pyridin-4-yl)benzaldehyde as a yellow-colored solid. Yield: 386 mg (2.11 mmol, 78%). ^{1}H NMR (400 MHz, $CDCl_3$) δ (ppm): 10.10 (s, 1H), 8.73 (dd, 2H), 8.01 (d, 2H), 7.81 (d, 2H), 7.55 (dd, 2H).

3.2.3 Synthesis of 2,2,2-trimethoxy-4,5-dimethyl-1,3,2λ^5-dioxaphosphole (2)

A 50-mL round bottom flask was evacuated and re-filled with nitrogen gas. After repeating this process twice to ensure an inert atmosphere, butane-2,3-dione (1.00 mL, 11.38 mmol, 1 equiv.) was transferred into the flask. It was then cooled in an ice bath to 0 °C, and trimethyl phosphite (1.48 mL, 12.52 mmol, 1.1 equiv.) was added slowly while stirring. The resulting yellow-colored mixture was stirred at room temperature for 12 hours under dinitrogen to obtain the biacetyl/trimethyl phosphite adduct as a colorless liquid. This as-prepared dioxaphospholene derivative was kept under nitrogen in a freezer at −10 °C and used for subsequent reactions without further purification. ^{1}H NMR (400 MHz, $CDCl_3$) δ (ppm): 3.40 (d, 3H), 1.64 (s, 2H).

3.2.4 Synthesis of 1-(2,2,2-trimethoxy-4-methyl-5-(4-(pyridin-4-yl)phenyl)-1,3,2λ^5-dioxaphospholan-4-yl)ethan-1-one (3)

A 100-mL round bottom flask containing 4-(pyridin-4-yl)benzaldehyde (350 mg, 1.91 mmol, 1 equiv.) was brought to an inert atmosphere by three cycles of evacuation and nitrogen backfilling. It was placed in an ice bath and, using a cannula, anhydrous methylene chloride (2

mL) followed by freshly-prepared biacetyl/trimethyl phosphite adduct (602 mg, 2.87 mmol, 1.5 equiv.) were vacuum-transferred with continuous stirring. The reaction mixture was then stirred at room temperature for 12 hours under dinitrogen to yield the dioxaphospholane intermediate, **3**, as a clear yellow, viscous liquid. ^{1}H NMR (400 MHz, $CDCl_3$) δ (ppm): 8.66 (dd, 2H), 7.62 (d, 2H), 7.49 (dd, 2H), 7.41 (d, 2H), 4.75 (d, 1H), 3.74 (d, 9H), 1.86 (s, 3H), 1.64 (s, 3H).

3.2.5 Synthesis of 4-hydroxy-3-(4-(pyridin-4-yl)phenyl)pent-3-en-2-one (L1)

The dioxaphospholane derivative, **3**, was immediately used in the methanolysis step. Methanol (50 mL) was added and the resultant clear solution was heated under reflux for 5 hours under nitrogen atmosphere. The clear solution was then concentrated *via* rotary evaporation and cooled to −78 °C. ^{1}H NMR (400 MHz, $CDCl_3$) δ (ppm): 16.73 (s, 1H), 8.68 (dd, 2H), 7.67 (d, 2H), 7.54 (dd, 2H), 7.30 (d, 2H), 1.93 (s, 6H).

3.2.6 Synthesis of 1-(5-(4-iodophenyl)-2,2,2-trimethoxy-4-methyl-1,3,2λ^5-dioxaphospholan-4-yl)ethan-1-one (4)

A 250-mL round bottom flask containing 4-iodobenzaldehyde (1.20 g, 5.17 mmol, 1 equiv.) was made oxygen-free by three cycles of alternating evacuation and replacement with nitrogen. Then, it was placed in an ice bath and freshly-prepared biacetyl/trimethyl phosphite adduct (1.63 g, 7.76 mmol, 1.5 equiv.) was introduced *via* vacuum-transferring. The resulting neat slurry was stirred at room temperature for 12 hours under nitrogen atmosphere to afford the dioxaphospholane intermediate, **4**, as a colorless, viscous liquid. ^{1}H NMR (400 MHz, $CDCl_3$) δ (ppm): 7.65 (d, 2H), 7.03 (d, 2H), 4.62 (d, 1H), 3.70 (d, 9H), 1.82 (s, 3H), 1.58 (s, 3H).

3.2.7 Synthesis of 4-hydroxy-3-(4-iodophenyl)pent-3-en-2-one (5)

The dioxaphospholane derivative, **4**, was directly subjected to methanolysis by adding methanol (100 mL) and refluxing under nitrogen for 12 hours. The clear solution was then

concentrated *via* rotary evaporation and cooled to −78 °C. The white crystalline solid formed upon cooling was collected by filtration, washed with cold methanol and air-dried. Yield: 1.14 g (3.78 mmol, 73% with respect to 4-iodobenzaldehyde). ^{1}H NMR (400 MHz, $CDCl_3$) δ (ppm): 16.66 (s, 1H), 7.73 (d, 2H), 6.93 (d, 2H), 1.88 (s, 6H).

3.2.8 Synthesis of 4-((trimethylsilyl)ethynyl)pyridine (6)

In a 250-mL round-bottomed flask, 4-iodopyridine (2.50 g, 12.20 mmol, 1 equiv.) and triphenylphosphine (255.9 mg, 0.98 mmol, 8 mol%) were suspended in 75 mL of triethylamine. It was degassed by bubbling dinitrogen for 30 minutes, and bis(triphenylphosphine)palladium(II) dichloride (342.4 mg, 0.49 mmol, 4 mol%), copper(I) iodide (92.9 mg, 0.49 mmol, 4 mol%) and trimethylsilylacetylene (2.57 mL, 18.29 mmol, 1.5 equiv.) were added. The reaction flask was fitted to a water-jacketed condenser, cooled to −78 °C, subjected to a brief vacuum/backfill cycle and stirred at 80 °C for 20 hours under nitrogen atmosphere. After removing volatile materials *in vacuo*, the residue was re-dissolved in 100 mL of chloroform and filtered through a pad of Celite, using an extra 25 mL portion of chloroform to wash the filter pad. The combined filtrate was then washed with distilled water (2 × 25 mL) and brine (25 mL), dried over anhydrous magnesium sulfate, and evaporated to dryness under vacuum. The resulting dark color product was purified by column chromatography (silica gel, hexanes/ethyl acetate = 1:1) which afforded 4-((trimethylsilyl)ethynyl)pyridine as a yellow/orange oil. Yield: 1.82 g (10.4 mmol, 85%). ^{1}H NMR (400 MHz, $CDCl_3$) δ (ppm): 8.55 (d, 2H), 7.29 (d, 2H), 0.26 (s, 9H).

3.2.9 Synthesis of 4-ethynylpyridine (7)

In a nitrogen-flushed, 100-mL round-bottom flask, 4-((trimethylsilyl)ethynyl)pyridine (1.04 g, 5.93 mmol, 1 equiv.) and potassium carbonate (1.64 g, 11.9 mmol, 2 equiv.) were suspended in 25 mL of methanol. After stirring vigorously at room temperature for two hours, the

reaction mixture was diluted with 75 mL of diethyl ether and filtered through a pad of Celite, using an extra 25 mL portion of diethyl ether to wash the filter pad. Solvents were removed under reduced pressure to yield an oil, which quickly solidified to give 4-ethynylpyridine as a pale-yellow solid. It was used directly in the next step without further purification. Yield: 0.57 g (5.53 mmol, 93%). ^{1}H NMR (400 MHz, $CDCl_3$) δ (ppm): 8.60 (d, 2H), 7.35 (d, 2H), 3.29 (s, 1H).

3.2.10 Synthesis of 4-hydroxy-3-(4-(pyridin-4-ylethynyl)phenyl)pent-3-en-2-one (L2)

4-Hydroxy-3-(4-iodophenyl)pent-3-en-2-one (1.00 g, 3.31 mmol, 1 equiv.) and triphenylphosphine (69.5 mg, 0.26 mmol, 8 mol%) were placed in a 100-mL round-bottomed flask. Triethylamine (50 mL) was added and the resulting solution was purged with dinitrogen gas for 30 minutes. Then, bis(triphenylphosphine)palladium(II) dichloride (92.9 mg, 0.13 mmol, 4 mol%), copper(I) iodide (25.2 mg, 0.13 mmol, 4 mol%) and 4-ethynylpyridine (0.51 g, 4.96 mmol, 1.5 equiv.) were added. The reaction mixture was cooled to −78 °C, subjected to a brief vacuum/backfill cycle and stirred at 75 °C under nitrogen atmosphere. The progress of the reaction was monitored by TLC for disappearance of 4-hydroxy-3-(4-iodophenyl)pent-3-en-2-one and, upon completion (after 24 hours), volatile materials were removed *in vacuo*. The residue was re-dissolved in 100 mL of methylene chloride and filtered through a pad of Celite, using an extra 25 mL portion of solvent to wash the filter pad. The combined filtrate was washed with saturated ammonium chloride (25 mL), distilled water (25 mL) and brine (25 mL), dried over anhydrous magnesium sulfate, and evaporated to dryness under vacuum. The crude product was chromatographed on silica gel using pure hexanes followed by hexanes/ethyl acetate (1:3) mixture to obtain the title compound, **L2**, as a pale-yellow solid. Single crystals were grown by slow evaporation of a diethyl ether solution. Yield: 0.63 g (2.27 mmol, 69%). ^{1}H NMR (400 MHz, $CDCl_3$) δ (ppm): 16.69 (s, 1H), 8.62 (dd, 2H), 7.58 (d, 2H), 7.39 (dd, 2H), 7.21 (d, 2H), 1.91 (s,

6H). ^{13}C NMR (100 MHz, $CDCl_3$) δ (ppm): 190.91, 149.87, 138.21, 132.65, 132.32, 131.76, 131.32, 121.55, 114.77, 93.60, 87.59, 24.42.

3.2.11 Synthesis of 4-hydroxy-3-(4-(pyridin-3-ylethynyl)phenyl)pent-3-en-2-one (L3)

L3 was obtained as a yellow solid by following the same synthetic pathway as described for **L2** (see Figure 3.9). 3-Ethynylpyridine was synthesized from 3-iodopyridine and then subjected to cross-coupling with **5**. Reaction conditions were similar to those employed in the synthesis of **6**, **7** and **L2**. Crystals suitable for single-crystal X-ray diffraction were grown from a diethyl ether solution by slow evaporation. Yield: 78%. ^1H NMR (400 MHz, $CDCl_3$) δ (ppm): 16.69 (s, 1H), 8.78 (d, 1H), 8.56 (dd, 1H), 7.82 (dt, 1H), 7.58 (d, 2H), 7.30 (dd, 1H), 7.20 (d, 2H), 1.91 (s, 6H).

3.2.12 Synthesis of 4-hydroxy-3-(4-(pyridin-2-ylethynyl)phenyl)pent-3-en-2-one (L4)

L4 was obtained as a yellow solid by following the same synthetic pathway as described for **L2** (see Figure 3.9). 2-Ethynylpyridine was synthesized from 2-iodopyridine and then subjected to cross-coupling with **5**. Reaction conditions were similar to those employed in the synthesis of **6**, **7** and **L2**. Yield: 86%. ^1H NMR (400 MHz, $CDCl_3$) δ (ppm): 16.69 (s, 1H), 8.64 (d, 1H), 7.70 (td, 1H), 7.63 (d, 2H), 7.54 (d, 1H), 7.26 (t, 1H), 7.19 (d, 2H), 1.91 (s, 6H).

3.2.13 Synthesis of 4-hydroxy-3-(4-(thiophen-3-ylethynyl)phenyl)pent-3-en-2-one (L5)

L5 was obtained as a yellow solid by following the same synthetic pathway as described for **L2** (see Figure 3.9). 3-Ethynylthiophene was synthesized from 3-bromothiophene and then subjected to cross-coupling with **5**. Reaction conditions were similar to those employed in the synthesis of **6**, **7** and **L2**. Crystals suitable for single-crystal X-ray diffraction were grown by slow

evaporation of an acetone solution. Yield: 89%. ^{1}H NMR (400 MHz, $CDCl_3$) δ (ppm): 16.68 (s, 1H), 7.54 (m, 3H), 7.32 (dd, 1H), 7.20 (d, 1H), 7.16 (d, 2H), 1.90 (s, 6H).

3.2.14 Synthesis of 4-hydroxy-3-(4-(thiophen-2-ylethynyl)phenyl)pent-3-en-2-one (L6)

L6 was obtained as a yellow solid by following the same synthetic pathway as described for **L2** (see Figure 3.9). 2-Ethynylthiophene was synthesized from 2-bromothiophene and then subjected to cross-coupling with **5**. Reaction conditions were similar to those employed in the synthesis of **6**, **7** and **L2**. Yield: 64%. ^{1}H NMR (400 MHz, $CDCl_3$) δ (ppm): 16.70 (s, 1H), 7.54 (d, 2H), 7.31 (m, 2H), 7.17 (d, 2H), 7.03 (dd, 1H), 1.90 (s, 6H).

3.2.15 Synthesis of 3-(4-((6-aminopyridin-3-yl)ethynyl)phenyl)-4-hydroxypent-3-en-2-one (L7)

L7 was obtained as a yellow solid by following the same synthetic pathway as described for **L2** (see Figure 3.9). 5-Ethynylpyridin-2-amine was synthesized from 5-bromopyridin-2-amine and then subjected to cross-coupling with **5**. Reaction conditions were similar to those employed in the synthesis of **6**, **7** and **L2**. Yield: 70%. ^{1}H NMR (400 MHz, $CDCl_3$) δ (ppm): 16.69 (s, 1H), 8.28 (d, 1H), 7.56 (dd, 1H), 7.52 (d, 2H), 7.15 (d, 2H), 6.49 (d, 1H), 4.63 (s, br, 2H), 1.90 (s, 6H).

3.2.16 Synthesis of *N*-(5-((4-(2-hydroxy-4-oxopent-2-en-3-yl)phenyl)ethynyl)pyridin-2-yl)acetamide (L8)

To a solution of **L7** (112 mg, 0.38 mmol, 1 equiv.) and triethylamine (80 µL, 0.57 mmol, 1.5 equiv.) in dry methylene chloride (10 mL) in a 50-mL round-bottomed flask, a solution of acetic anhydride (54 µL, 0.57 mmol, 1.5 equiv.) in dry methylene chloride (10 mL) was added dropwise at 5 °C with stirring. The reaction mixture was allowed to reach to room temperature and stirred for an additional three-hour period. Water (20 mL) was then added, the organic layer was

separated, and the aqueous layer was extracted once more with methylene chloride (20 mL). The organic layers were combined, dried over anhydrous magnesium sulfate, and concentrated to get the title compound as a light brown solid. Yield: 98%. ^{1}H NMR (400 MHz, $CDCl_3$) δ (ppm): 16.70 (s, 1H), 8.43 (d, 1H), 8.32 (s, br, 1H), 8.23 (d, 1H), 7.83 (dd, 1H), 7.55 (d, 2H), 7.18 (d, 2H), 2.23 (s, 3H), 1.90 (s, 6H).

3.2.17 Synthesis of 4-hydroxy-3-(4-(pyridin-3-yl)phenyl)pent-3-en-2-one (L0)

To a 50-mL round-bottom flask with **5** (152 mg, 0.50 mmol, 1 equiv.) was added 1,2-dimethoxyethane (20 mL) and *tert*-butyl alcohol (2 mL), and the resulting mixture was degassed by bubbling nitrogen gas for 20 minutes. Potassium *tert*-butoxide (168 mg, 1.50 mmol, 3 equiv.), pyridine-3-boronic acid (154 mg, 1.25 mmol, 2.5 equiv.) and tetrakis(triphenylphosphine)palladium(0) catalyst (46 mg, 0.04 mmol, 8 mol%) were charged, and nitrogen was bubbled again for additional 10 minutes. It was then refluxed under nitrogen for four hours, after which the solvents were removed *in vacuo*. The residue was re-dissolved in 50 mL of methylene chloride and filtered through a pad of Celite. The filtrate was washed with distilled water (2 × 15 mL) and brine (15 mL), dried over anhydrous magnesium sulfate, and evaporated to dryness under vacuum. Further purification was carried out by gradient elution with hexanes/ethyl acetate mixtures on a silica gel column, affording **L0** as a yellow-colored solid. Yield: 53 mg (0.21 mmol, 42%). ^{1}H NMR (400 MHz, $CDCl_3$) δ (ppm): 16.74 (s, 1H), 8.89 (d, 1H), 8.61 (dd, 1H), 7.91 (dt, 1H), 7.61 (d, 2H), 7.39 (dd, 1H), 7.29 (d, 2H), 1.94 (s, 6H).

3.2.18 Synthesis of $[Cu(L1)_2(MeOH)_2]_n$

In a glass vial, **L1** (6 mg, *ca.* 2 equiv.) was dissolved in 5 mL of methanol. Then, copper(II) perchlorate hexahydrate (4 mg, 10.8 μmol, 1 equiv.) dissolved in 1 mL of methanol was added and mixed well. After careful addition of two drops of triethylamine/methanol (1:5 v/v) solution with

minimal agitation, the vial was sealed and left undisturbed at ambient conditions to allow triethylamine to diffuse into the solution slowly. Dark green crystals suitable for single-crystal X-ray diffraction were observed after 24 hours. ATR-FTIR (cm^{-1}): 3019.70, 1571.52, 1484.91, 1419.24, 1372.14, 1313.84, 1219.60, 1109.67, 1005.42, 975.38, 920.54, 858.38, 812.74, 765.02, 736.84.

3.2.19 Synthesis of [Fe(L2)$_3$]

In a glass vial, **L2** (6 mg, 21.6 µmol, 3 equiv.) was dissolved in 4 mL of acetonitrile. Then, iron(III) perchlorate hydrate, $Fe(ClO_4)_3 \cdot xH_2O$ (4 mg, *ca.* 1 equiv.) dissolved in 1 mL of acetonitrile was added and mixed well. After careful addition of two drops of triethylamine/acetonitrile (1:5 v/v) solution with minimal agitation, the vial was sealed and left undisturbed at ambient conditions to allow triethylamine to diffuse into the solution slowly. Red/orange crystals suitable for single-crystal X-ray diffraction were harvested after three days. ATR-FTIR (cm^{-1}): 2919.69, 2819.41, 2216.89, 1574.14, 1541.06, 1421.62, 1359.28, 1319.34, 1213.75, 1099.78, 1039.10, 1009.70, 978.55, 917.92, 838.32, 817.46, 730.19.

3.2.20 Synthesis of [Cu(L2)$_2$(MeOH)$_2$]

In a glass vial, **L2** (6 mg, 21.6 µmol, 2 equiv.) was dissolved in 2 mL of dimethylformamide. Then, copper(II) perchlorate hexahydrate (4 mg, 10.8 µmol, 1 equiv.) dissolved in 1 mL of methanol was added and mixed well. After careful addition of two drops of triethylamine/methanol (1:5 v/v) solution with minimal agitation, the vial was sealed and left undisturbed at ambient conditions to allow triethylamine to diffuse into the solution slowly. Dark green crystals suitable for single-crystal X-ray diffraction were observed after 24 hours. ATR-FTIR (cm^{-1}): 3556.17, 3412.72, 3234.91, 2934.10, 2876.18, 2219.07, 1664.48, 1568.79, 1502.89,

1405.21, 1342.64, 1315.15, 1258.06, 1214.92, 1092.75, 1068.96, 1003.09, 916.19, 834.59, 812.88, 728.28.

3.2.21 Synthesis of $[Zn(L2)_2(MeOH)_2]$

Pale yellow crystals suitable for single-crystal X-ray diffraction were obtained within 24 hours by following the same method mentioned as for $[Cu(\mathbf{L2})_2(MeOH)_2]$, but using zinc(II) perchlorate hexahydrate as the metal source. ATR-FTIR (cm^{-1}): 3025.67, 2923.55, 2801.53, 2218.52, 1662.77, 1577.47, 1506.86, 1420.72, 1380.55, 1342.62, 1311.32, 1256.86, 1214.64, 1100.02, 1031.19, 1001.10, 909.05, 827.49, 729.92.

3.2.22 Synthesis of $[Co(L2)_2]_n$

To grow crystals *via* layering technique, **L2** (6 mg, 21.6 µmol, 2 equiv.) was dissolved in 1 mL of dimethylformamide, basified by adding two drops of triethylamine/methanol (1:5 v/v) solution and transferred into a narrow glass tube. After careful layering of 1 mL of neat methanol, cobalt(II) perchlorate hexahydrate (4 mg, 10.8 µmol, 1 equiv.) dissolved in 1 mL of methanol was slowly added on top without disturbing it. The tube was then sealed and allowed to stand at room temperature for one week, during which time reddish orange crystals suitable for single-crystal X-ray diffraction were appeared. ATR-FTIR (cm^{-1}): 2925.20, 2362.33, 2331.66, 2218.40, 1673.24, 1578.07, 1507.53, 1379.15, 1342.97, 1310.59, 1213.52, 1086.62, 1004.12, 970.51, 909.78, 831.42, 791.53, 729.05.

3.2.23 Synthesis of $[Cu(L3)_2]$

In a glass vial, **L3** (6 mg, 21.6 µmol, 2 equiv.) was dissolved in 2 mL of dimethyl sulfoxide. Then, copper(II) perchlorate hexahydrate (4 mg, 10.8 µmol, 1 equiv.) dissolved in 1 mL of methanol was added and mixed well. After careful addition of two drops of triethylamine/methanol (1:10 v/v) solution with minimal agitation, the vial was sealed and left undisturbed at ambient

conditions to allow triethylamine to diffuse into the solution slowly. Dark green crystals suitable for single-crystal X-ray diffraction were observed after two days. ATR-FTIR (cm^{-1}): 3025.91, 2220.79, 1571.79, 1505.25, 1421.83, 1369.19, 1345.36, 1312.43, 1185.89, 1101.72, 1008.01, 974.56, 954.05, 919.65, 836.49, 801.16, 739.39, 698.28.

3.2.24 Synthesis of $[Cu(L4)_2]$

In a glass vial, **L4** (6 mg, 21.6 µmol, 2 equiv.) was dissolved in 1 mL of acetonitrile. Then, copper(II) perchlorate hexahydrate (4 mg, 10.8 µmol, 1 equiv.) dissolved in 1 mL of methanol was added and mixed well. After careful addition of two drops of triethylamine/methanol (1:5 v/v) solution with minimal agitation, the vial was sealed and left undisturbed at ambient conditions to allow triethylamine to diffuse into the solution slowly. Dark green crystals suitable for single-crystal X-ray diffraction were observed after 24 hours. ATR-FTIR (cm^{-1}): 2217.95, 1558.45, 1421.15, 1355.60, 1314.27, 1146.57, 1099.04, 1013.49, 981.90, 922.89, 833.71, 778.61, 738.08, 709.79.

3.2.25 Synthesis of $[Cu(L5)_2]$

In a glass vial, **L5** (6.1 mg, 21.6 µmol, 2 equiv.) was dissolved in 3 mL of acetonitrile. Then, copper(II) perchlorate hexahydrate (4 mg, 10.8 µmol, 1 equiv.) dissolved in 1 mL of acetonitrile was added and mixed well. After careful addition of two drops of triethylamine/ acetonitrile (1:5 v/v) solution with minimal agitation, the vial was sealed and left undisturbed at ambient conditions to allow triethylamine to diffuse into the solution slowly. Yellowish green crystals suitable for single-crystal X-ray diffraction were observed after two days. ATR-FTIR (cm^{-1}): 3092.20, 1563.58, 1418.61, 1367.59, 1103.00, 1019.84, 921.77, 833.72, 782.64.

3.2.26 Synthesis of $[Cu(L5)(OMe)]_2$

In a glass vial, **L5** (6.1 mg, 21.6 µmol, 2 equiv.) was dissolved in 2 mL of dimethyl sulfoxide. Then, copper(II) perchlorate hexahydrate (4 mg, 10.8 µmol, 1 equiv.) dissolved in 1 mL of methanol was added and mixed well. After adding two drops of triethylamine/methanol (1:5 v/v) mixture, the vial was sealed and heated to obtain a clear, dark green solution. Dark green crystals suitable for single-crystal X-ray diffraction were observed after one week. ATR-FTIR (cm^{-1}): 3393.91, 2917.09, 2809.74, 1572.62, 1420.17, 1354.13, 1102.25, 1016.92, 917.51, 836.01, 774.76.

3.2.27 Single-crystal X-ray crystallography

Detailed crystallographic information about the data collections, solutions and refinements can be found in the Appendix B. Underlying topologies of the crystal structures were determined with ToposPro,[20] and all structural images were generated using Mercury.[21]

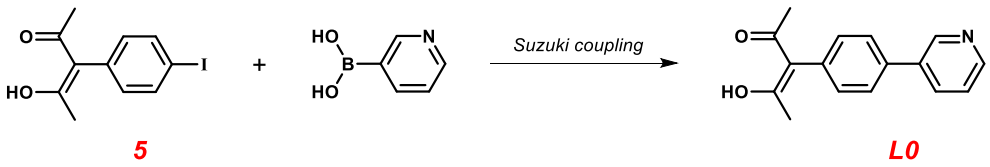

5 *L0*

Figure 3.7 Synthetic route to **L0**.

3.3 Results and discussion

Our initial attempts at preparing **L0** and **L1** through direct cross-coupling of 4-hydroxy-3-(4-iodophenyl)pent-3-en-2-one (**5**) and the appropriate pyridinylboronic acid were not successful because the acac functionality could not withstand the conventional Suzuki coupling conditions and hydrolyzed into the corresponding phenylacetone. We re-attempted their synthesis by employing non-nucleophilic reaction conditions and managed to obtain **L0** (Figure 3.7). However,

we had to follow an alternative, multistep pathway for **L1** where 4-(pyridin-4-yl)benzaldehyde was reacted with the biacetyl-trimethyl phosphite (1:1) adduct to yield the corresponding oxyphosphorane intermediate which, in turn, gave the desired product upon methanolysis (Figure 3.8, see Experimental section for details).[22] On the other hand, **L2** was obtained relatively easily in moderate yields according to the synthetic route given in Figure 3.9, and the same method was adopted for the preparation of **L3**–**L7**. Finally, acylation of **L7** with acetic anhydride readily afforded **L8** in quantitative yields (Figure 3.10).

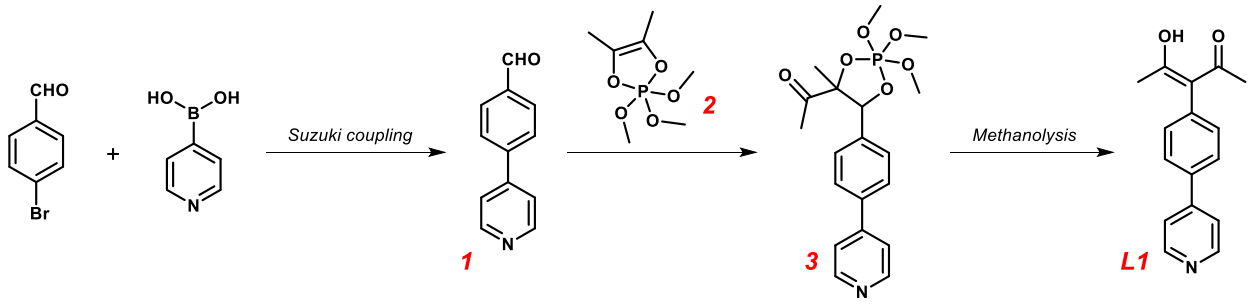

Figure 3.8 Synthetic route to **L1**.

Even though β-diketones can undergo keto-enol tautomerism and exist as a mixture of diketo and keto-enol forms, solution NMR suggests that all acac species (**5**, **L0**–**L8**) stay exclusively in their keto-enolic form. This can be ascribed to the conjugation and intramolecular hydrogen bonding that shift this dynamic equilibrium in favor of keto-enol tautomer.

As evidenced from the single-crystal structural data of **L2**, **L3** and **L5**, the keto-enolic form is persistent in the solid-state as well, with an intramolecular O–H···O hydrogen bond (Figure 3.11), indicated by a short O···O separation (2.436 Å in **L2**, 2.461 Å and 2.470 Å in **L3**, 2.433 Å in **L5**). In **L2**, the acetylacetone segment is coplanar with the apical pyridyl ring and perpendicular to the central phenyl ring. And the ligand is slightly bent along the plane defined by acetylacetone

and pyridine. In **L3**, there are two crystallographically independent molecules in the lattice. In **L5**, both the thiophene segment and the enol hydrogen have 50% occupancy. Because of the enol disorder, the exact position of the hydrogen atom cannot be determined accurately. Having said this, the hydrogen bonding looks reasonable. There are no obvious structure-directing intermolecular interactions in the overall packing of any of these three ligands.

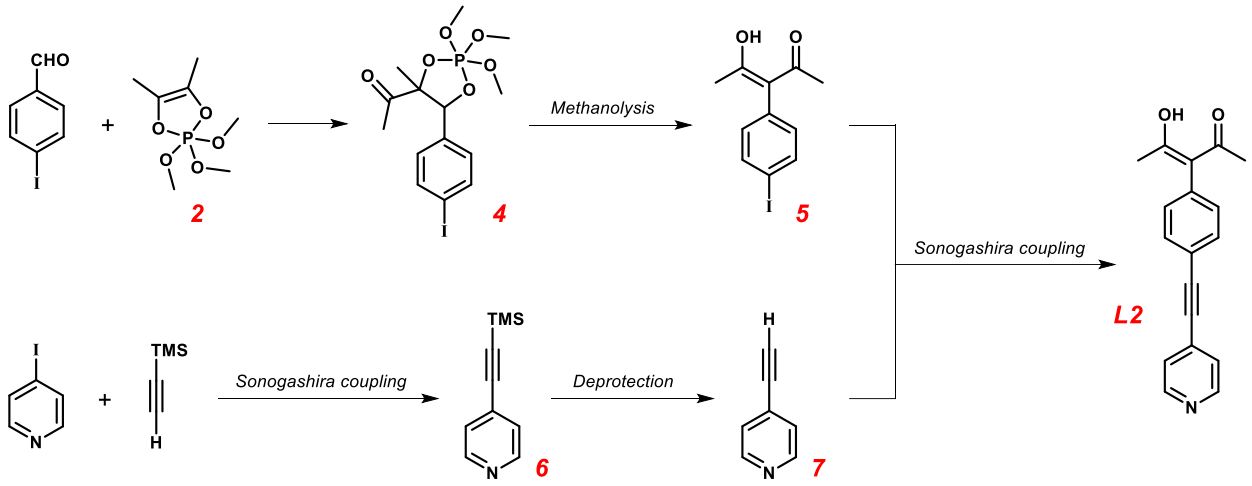

Figure 3.9 Synthetic route to **L2**.

For metal binding studies, we used divalent Mn(II), Co(II), Ni(II), Cu(II) and Zn(II) and trivalent Fe(III) salts (associated with weakly-coordinating anions). In most cases, the reactions led to instant precipitates or microcrystalline material which are insoluble in common organic solvents. To harvest single-crystals suitable for X-ray structural analysis, we therefore employed diluted solutions (mM) along with controlled diffusion of the base, triethylamine. In that way, we were able to obtain nine good-quality crystalline products. Unfortunately, with **L0** and **L6**–**L8**, every attempt failed.

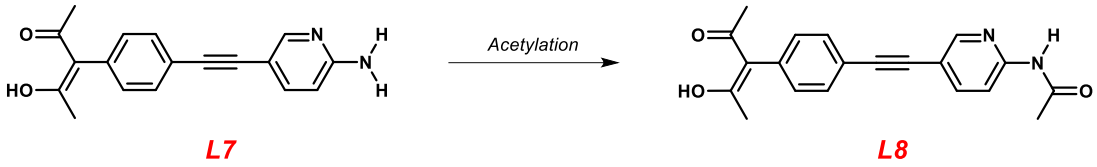

Figure 3.10 Synthetic route to **L8**.

The reaction of **L1** with copper(II) perchlorate yielded blue-green rod-shaped crystals. Their single-crystal X-ray crystallographic structural analysis revealed that two acac units coordinate to each copper ion in a square-planar arrangement, with Cu–O distances in the range of 1.9339(10)–1.9468(10) Å. The intermolecular Cu–N coordination fills up vacant axial positions and results in an octahedral geometry around the metal center. However, as envisaged by the Jahn-Teller theorem, it undergoes tetragonal elongation (Z-out distortion) and weakens the two Cu–N bonds significantly (Cu–N distance = 2.5214(13) Å).

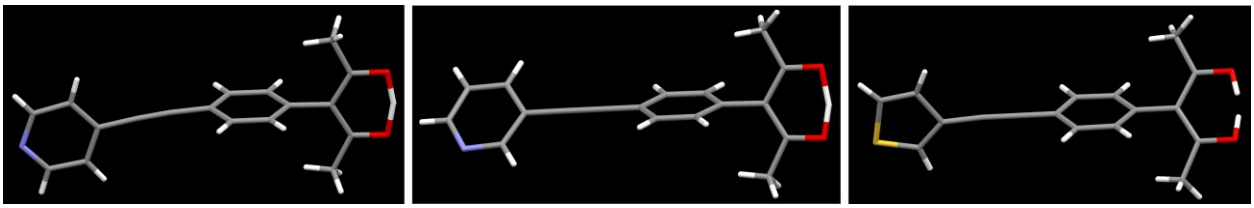

Figure 3.11 Structures of (from left) **L2**, **L3** and **L5**.

As shown in Figure 3.12a, the hexa-coordinated copper ions act as four-connecting square-planar nodes and build a two-dimensional coordination polymer having a 4^4 square lattice (**sql**) topology. Adjacent square grids are stacked in a staggered manner, but every other layer is superimposed (staggered ···ABAB··· stacking, see Figure 3.12 b and c). This layered arrangement creates isolated cavities (12.8% "free" volume when calculated using contact surface and 1.2 Å probe radius), which are taken up by methanol molecules (Figure 3.13a). In fact, each Cu(**L1**)$_2$

unit has two closely-associated methanol molecules linked by O–H(methanol)···O(acac) hydrogen bonds (Figure 3.13b).

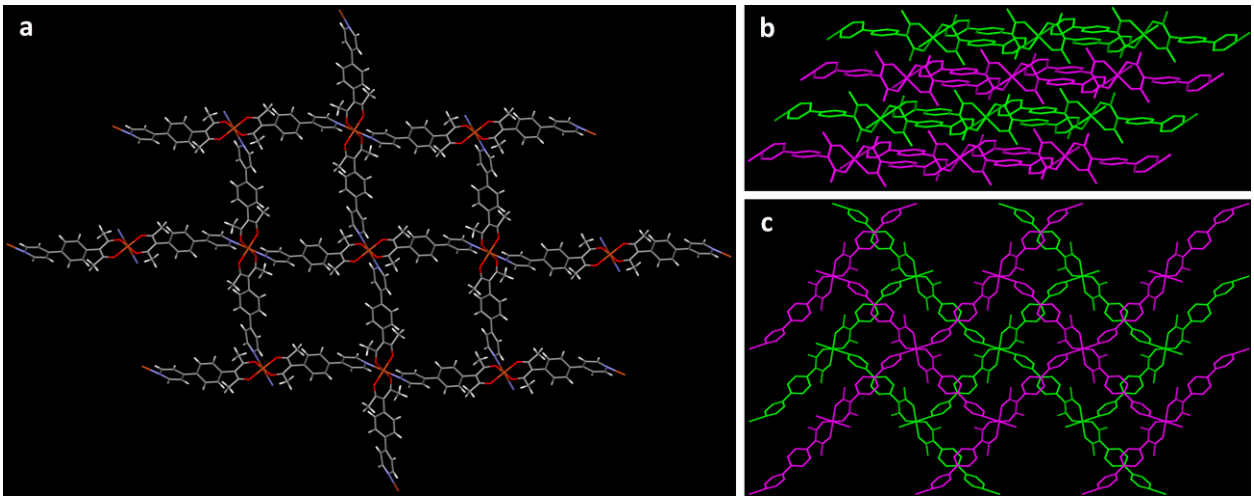

Figure 3.12 *a)* Structure of $[Cu(\mathbf{L1})_2]_n$; *b)* side-on view of layered packing motif as seen down b axis; *c)* interlayer relationship within the crystal packing scheme when viewed down c axis.

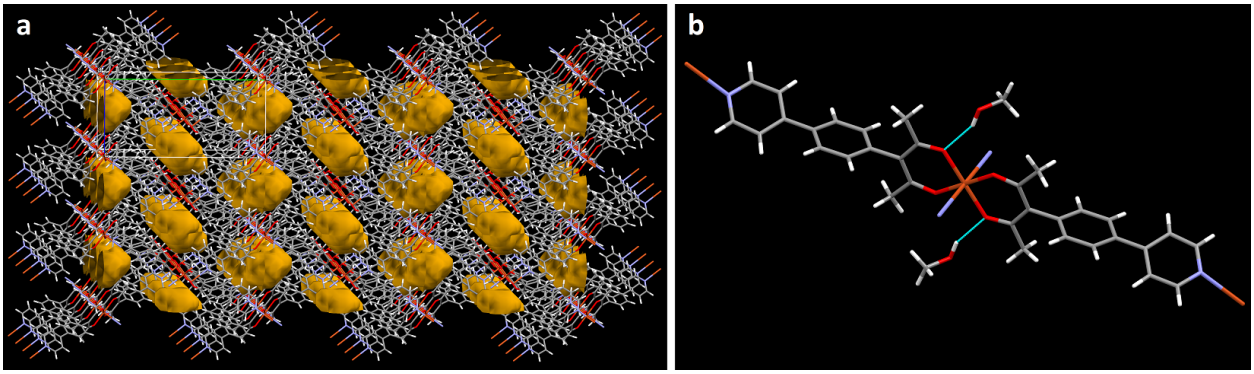

Figure 3.13 *a)* Segregated voids and *b)* accommodation of methanol molecules in $[Cu(\mathbf{L1})_2]_n$ lattice.

The reaction between **L2** and copper(II) perchlorate offered dark blue-green crystalline material. The structural examination revealed that the copper ion is tetracoordinated (chelated by two acac-moieties) and sits in a distorted square planar geometry (Cu–O_{acac} distance = 1.9397(16)–

1.9445(17) Å). The fifth and sixth coordination sites are occupied by apically-bound methanol molecules (Cu–O_{MeOH} distance = 2.444(2) Å). Any given [Cu(**L2**)$_2$(MeOH)$_2$] entity subsequently participates in four O–H(methanol)···N(pyridine) hydrogen-bonds with two neighboring molecules, thereby creating a one-dimensional supramolecular chain (Figure 3.14a).

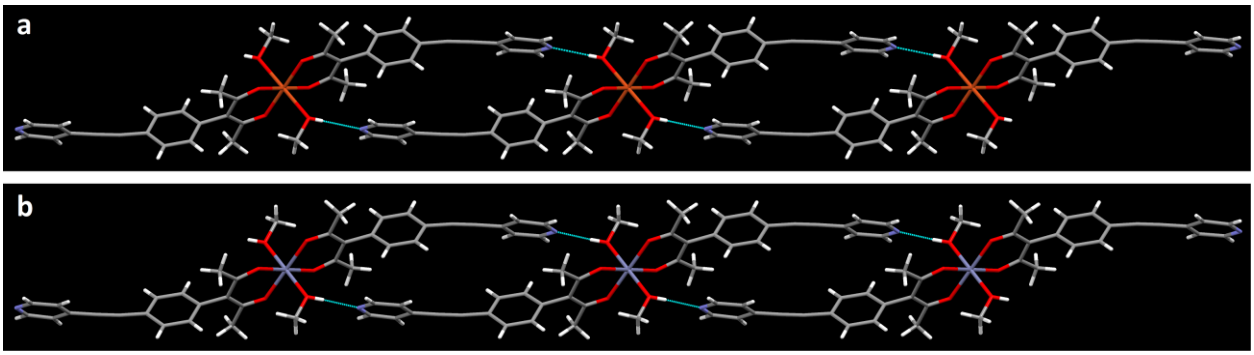

Figure 3.14 Structures of *a)* [Cu(**L2**)$_2$(MeOH)$_2$] and *b)* [Zn(**L2**)$_2$(MeOH)$_2$], showing the formation of ribbon-like supramolecular polymers through O–H(methanol)···N(pyridine) interactions.

The reaction of **L2** with zinc(II) perchlorate produced colorless/light yellow crystals. The crystal structure shows identical features to those displayed by [Cu(**L2**)$_2$(MeOH)$_2$], with two acac moieties occupying the equatorial plane, leaving room for methanol molecules to coordinate in the axial positions (Zn–O_{acac} distance = 2.0285(13)–2.0330(14) Å, Zn–O_{MeOH} distance = 2.1977(16) Å). Once again, intermolecular hydrogen bonding organizes these discrete [Zn(**L2**)$_2$(MeOH)$_2$] units into a one-dimensional infinite assembly (Figure 3.14b). Thermogravimetric studies show that both [Cu(**L2**)$_2$(MeOH)$_2$] and [Zn(**L2**)$_2$(MeOH)$_2$] start losing their coordinated solvent molecules at around 100 °C.

The structural determination of the product from **L2** and cobalt(II) perchlorate (orange crystals) shows that it has a very similar metal-ligand connectivity to that of [Cu(**L1**)$_2$]$_n$. That is, two acac and two pyridyl moieties respectively occupy the equatorial and axial positions, again

with some tetragonal distortion. The Cu–O bond lengths lie between 2.013(3) Å and 2.021(3) Å while each Cu–N bond has a length of 2.222(4) Å. This time, in contrast to what we observed in $[Cu(\mathbf{L1})_2]_n$, the resulting four-connected square-planar nodes devise a three-dimensional network (Figure 3.15). On closer inspection, half of the adjacent nodes are coplanar whereas the other half is perpendicular, giving rise to a $6^5.8$ $CdSO_4$-like (**cds**) topology.

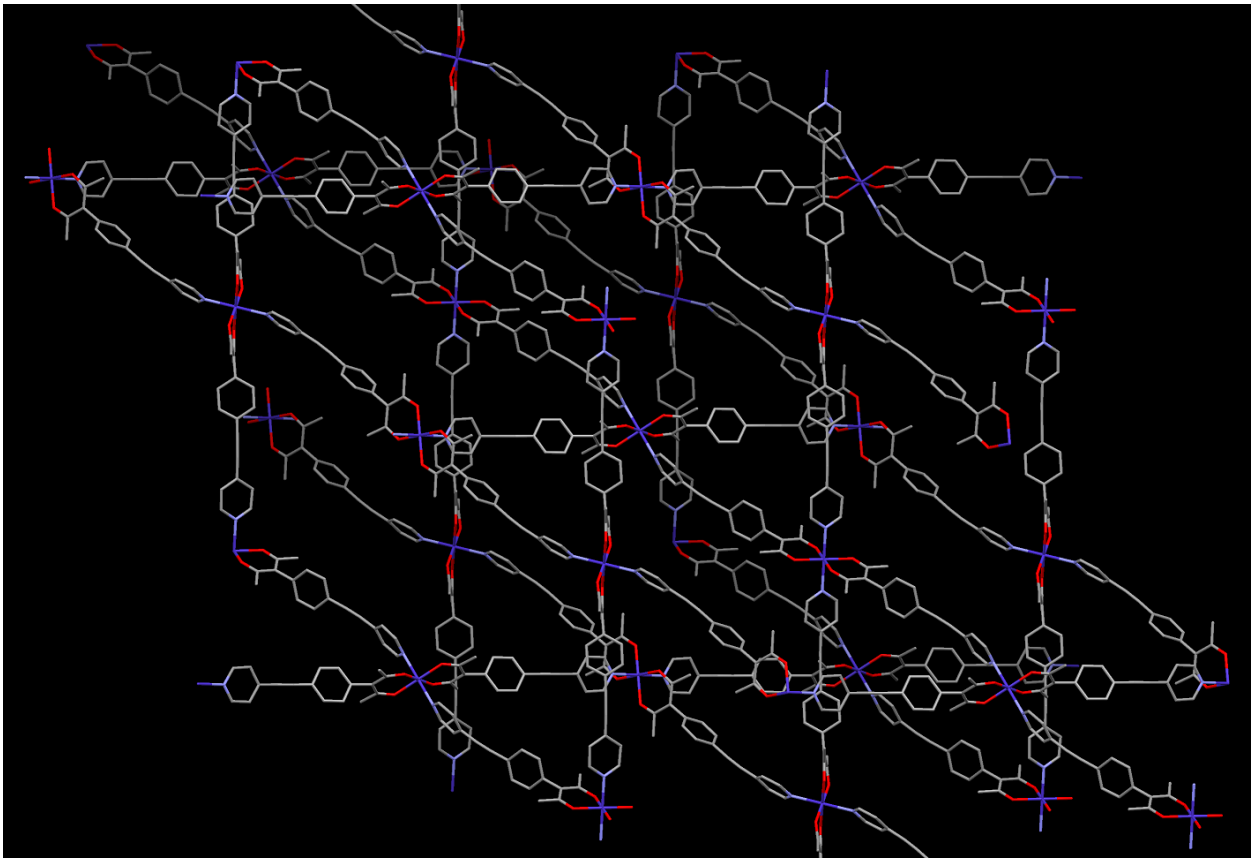

Figure 3.15 Structure of $[Co(\mathbf{L2})_2]_n$ (only a single subnet is shown, hydrogen atoms have been omitted for clarity).

There are three interpenetrating nets in the overall $[Co(\mathbf{L2})_2]_n$ structure (Figure 3.16a). Those individual nets are related purely by translations and, in fact, the whole entangled array can be generated by translating a single net along the full interpenetration vector (class Ia).[23]

Irrespective of this three-fold interpenetration, it is still quite open and makes one-dimensional channels parallel to the crystallographic *c* axis (Figure 3.16b). When guest solvent molecules are removed, the total void volume becomes 30.6% of the unit cell (calculated with Mercury software using contact surface and 1.2 Å probe radius).

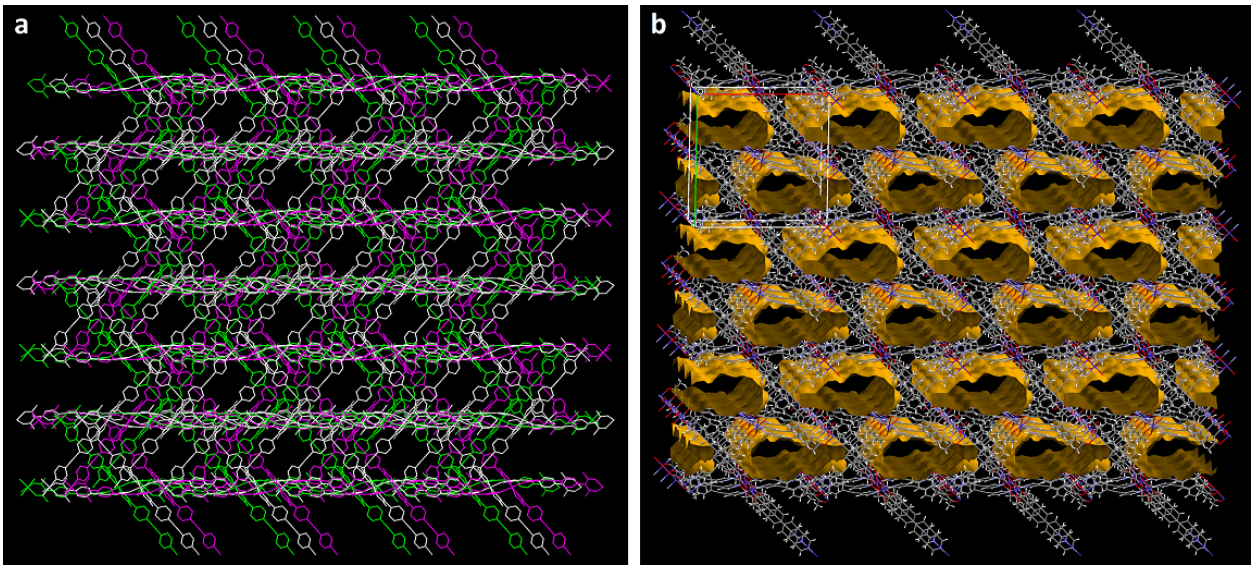

Figure 3.16 *a)* Three-fold interpenetration and *b)* one-dimensional channels present in $[Co(\mathbf{L2})_2]_n$.

The reaction of **L2** with iron(III) perchlorate produced red-orange crystals. As expected for a trivalent metal ion, it is a tris-chelated acac complex, $[Fe(\mathbf{L2})_3]$, with a slightly distorted octahedral coordination sphere. The Fe–O distances span from 1.984(2) to 1.997(3) Å, and the angles between equatorial and axial O–Fe–O bonds fall within the ranges of 85.24(10)–94.42(11) and 173.98(10)–175.60(11)°, respectively. Another interesting feature is that, like in other known metal tris-diketonates with large aromatic groups attached centrally to the ligand, two chelate rings have been bent along their O···O line in order to bring the remainder of those two ligands closer to each other, thereby reducing the steric volume of the overall complex to some extent. As a consequence of this collapsed and more compact configuration, it shows a substantial deviation

from the perfect trigonal symmetry (N···Fe···N angles are 100.41, 124.36 and 134.25°, N···N separations are 22.38, 25.76 and 26.81 Å). Rather surprisingly, the pyridyl sites remain essentially "idle" and fail to produce extended structures. Nevertheless, one arm of each complex seems to have a very weak, two-point N···H link with an adjacent complex, thereby forming dimeric aggregates (Figure 3.17).

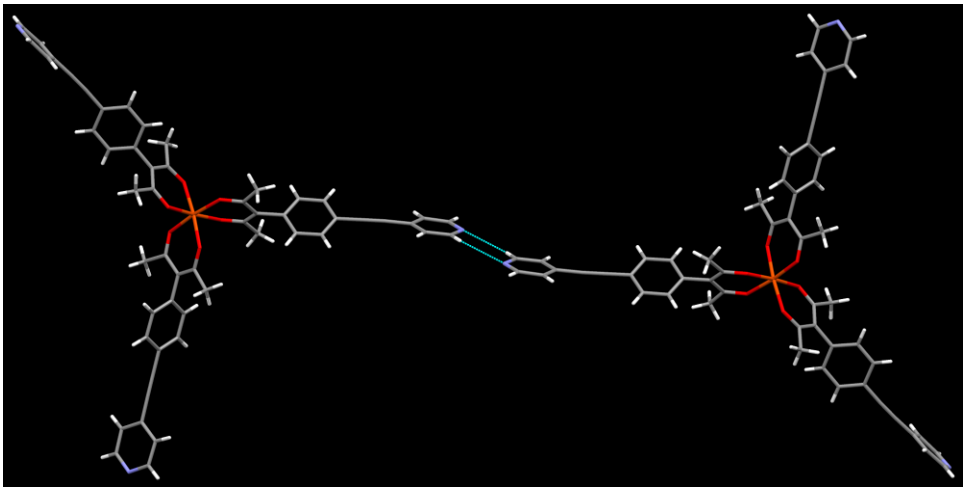

Figure 3.17 Structure of [Fe(**L2**)$_3$], showing the formation of dimers through pairwise N···H interactions.

The reaction between **L3** and copper(II) perchlorate offered dark blue-green crystals. Interestingly, the structure contains both monomeric and dimeric complexes (Figure 3.18). The former is a typical bis-acac derivative with square-planar coordination sphere (Cu–O distance = 1.8885(16)–1.8934(17) Å). The latter is formed by mutual Cu–N coordination of two adjacent monomeric [Cu(**L3**)$_2$] units. That means, each metal center in the dimer is penta-coordinated by four O atoms from acac moieties at the equatorial plane and one N atom from a pyridyl moiety at the axial position (Cu–O distance = 1.9167(16)–1.9427(16) Å, Cu–N distance = 2.314(2) Å). The cyclic rhomboidal segment of resulting dimers, made up of two square-pyramidal metal centers

and two ligands, has a 13.9 Å intermetallic distance. Intramolecular N–N separation is 41.2 Å. It is not completely clear as to why this bonding pattern is not propagated to build a one-dimensional coordination polymer. This is probably a kinetic product or a supramolecular isomer.

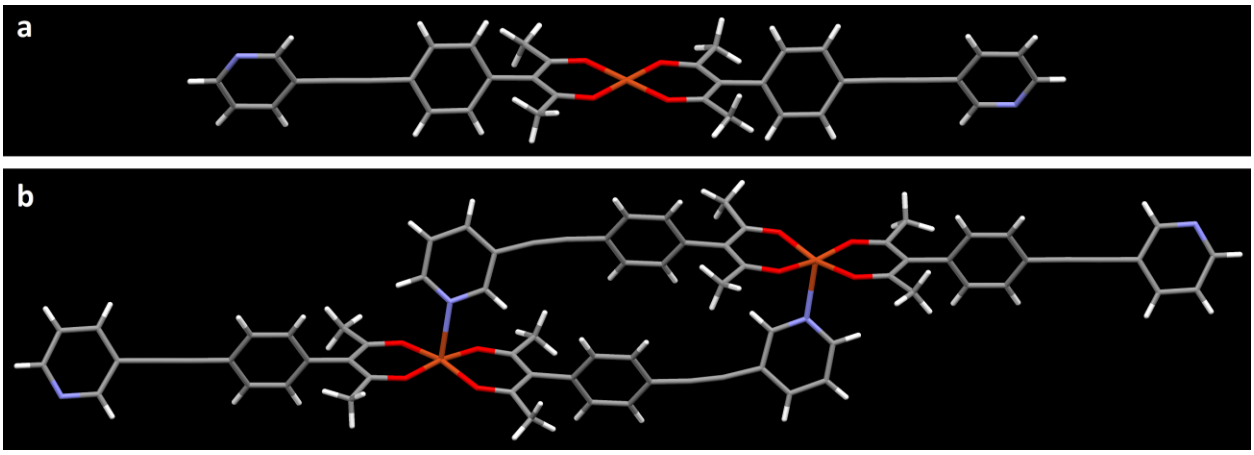

Figure 3.18 Structure of [Cu(**L3**)$_2$] in which both mono- and di-nuclear complexes are coexistent.

The reaction between **L4** and copper(II) perchlorate offered dark blue-green crystals. As usual, the copper ion is chelated by two acac moieties, furnishing a square-planar complex (Cu–O distance = 1.893(3)–1.910(3) Å). The 2-pyridinyl domains are not involved in any noticeable supramolecular binding events, and the complex remains monomeric and discrete (Figure 3.19).

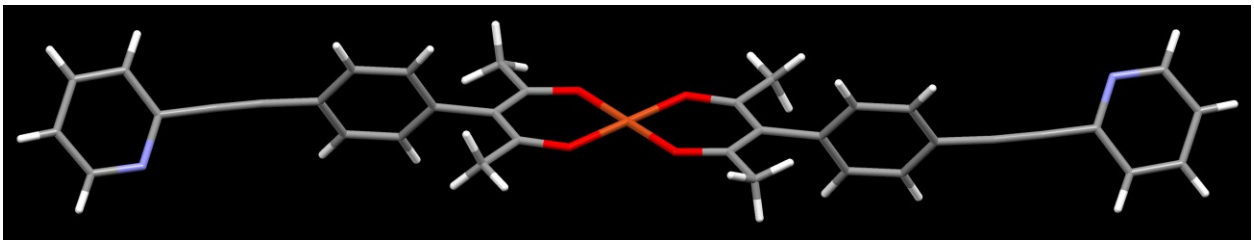

Figure 3.19 Structure of [Cu(**L4**)$_2$].

The reaction between **L5** and copper(II) perchlorate offered yellowish-green crystals. It turned out that the structure was distinct from the rest and have 1:1 metal/ligand ratio. The unique composition is a consequence of di-methoxy bridging (Cu–O_{acac} distance = 1.882(2)–1.889(3) Å, Cu–O_{MeO} distance = 1.916(2)–1.923(3) Å, Cu–Cu separation = 2.9978(10) Å). Methoxy-bridged dinuclear acac complexes are not uncommon in literature, and are normally synthesized by treating the acac complex in methanol with a strong base followed by refluxing.

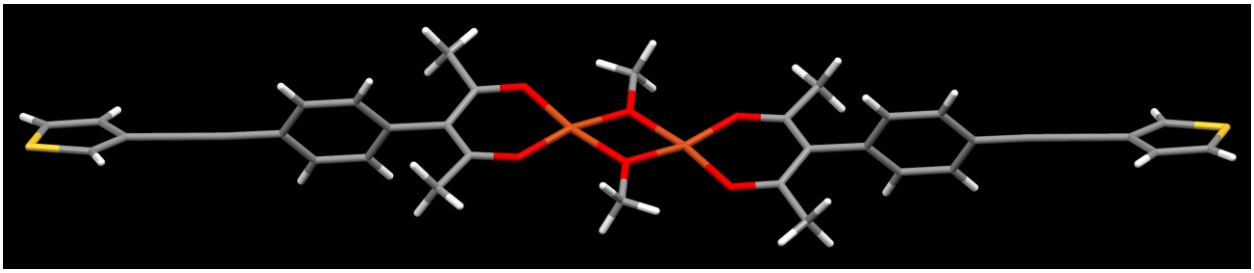

Figure 3.20 Structure of [Cu(**L5**)(μ_2-OMe)]$_2$.

We then allowed **L5** and copper(II) perchlorate to react in a methanol-free medium and were able to obtain yellowish-green crystalline product. This time, the structure was found to be the expected bis-chelated acac complex (Cu–O distance = 1.8954(16)–1.9048(17) Å). As seen/discussed above, metal centers in [Cu(**L3**)$_2$], [Cu(**L4**)$_2$] and [Cu(**L5**)(μ_2-OMe)]$_2$ are coordinatively not fully saturated. In the structure of [Cu(**L5**)$_2$], however, two thiophene residues above and below the equatorial plane defined by CuO_4 create a pseudo-octahedral environment around each Cu^{2+} ion (Cu···S distance = 3.1 Å). This offset parallel stacking of discrete bis-acac complexes leads to a formation of a supramolecular "stair chain" (Figure 3.21).

Out of nine structures presented here, only two products, namely [Cu(**L1**)$_2$]$_n$ and [Co(**L2**)$_2$]$_n$, can be considered as coordination networks. They have 4^4 square lattice (**sql**) and $6^5.8$ $CdSO_4$ (**cds**) net topologies, respectively. In theory, uninodal nets made up of square-planar nodes

can adopt a wide variety of other topologies such as $6^4.8^2$ NbO (**nbo**), $7^5.9$ quartz dual (**qzd**), $4^2.8^4$ (**lvt**), *etc*. Moreover, coordination polymers made from pyridyl-acetylacetonate ligands are relatively labile due to rather weak metal-pyridine coordination and if there is Jahn-Teller effect, they become even weaker. This means that, even a slight variation in the reaction conditions would have a profound effect on the end product. Hence, it is quite conceivable that we can build other supramolecular isomers if we try out different conditions.

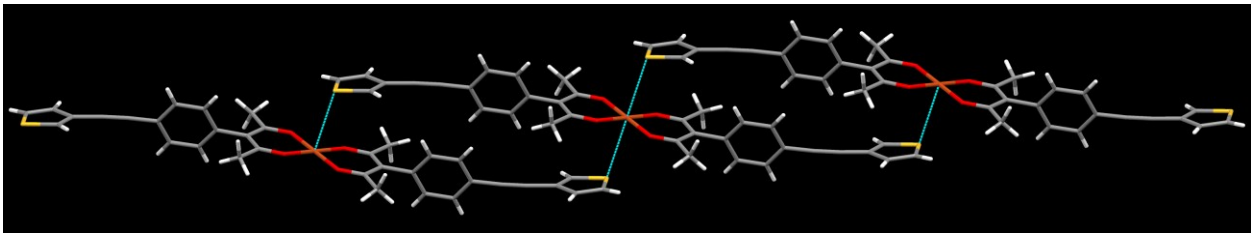

Figure 3.21 Structure of [Cu(**L5**)$_2$], showing the formation of one-dimensional stair motif by means of parallel-displaced stacking.

3.4 Conclusions

Complexes formed with metal dications are identical with respect to the coordination geometry around the metal center. In each of the complexes, the metal is four-coordinate and resides in a square planar environment. Differences in the overall architectures stem basically from the role played by the terminal heterocycles. The choice of solvent(s) is also critical. In almost all of our reactions, we had to use a "non-innocent" solvent, methanol. In some cases, it directly binds to the primary coordination sphere of the metal. In other cases, it makes hydrogen-bonding interactions with ligand Lewis basic sites. It can get deprotonated and act as a bridging ligand as well.

It should be noted that the structures obtained in this study are by no means exhaustive, but they do demonstrate the viability of **L0**–**L8** in the fabrication of exotic metallo-supramolecular architectures. All these ligands are attainable with decent yields except **L0** and **L1**, of which the synthetic methods need to be optimized. Moreover, they are readily soluble in common organic solvents and exhibit good stability for trouble-free handling. **L1** and **L2**, which have a tendency to behave as linear *exo*-ditopic ligands, are particularly promising towards the construction of coordination networks with interesting topologies and extended metrices.

As each ligand furnish two inequivalent metal binding domains, metal-acetylacetonates derived from them have the potential to act as preconstructed building blocks or metalloligands for the construction of mixed metal-organic frameworks (MMOFs). One can also utilize other types of interactions to translate the inherent geometry and dimensionality of these metal-acetylacetonates into extended architectures. However, we found that these metallo species are nearly insoluble in common solvents, so such endeavors should rely on one-pot synthetic approaches.

3.5 References

1. M. D. Allendorf and V. Stavila, *CrystEngComm*, 2015, **17**, 229-246; L. Nicole, C. Laberty-Robert, L. Rozes and C. Sanchez, *Nanoscale*, 2014, **6**, 6267-6292; H. Furukawa, K. E. Cordova, M. O'Keeffe and O. M. Yaghi, *Science*, 2013, **341**, 974-986.
2. Y. B. He, B. Li, M. O'Keeffe and B. L. Chen, *Chem. Soc. Rev.*, 2014, **43**, 5618-5656; U. Schubert, *Chem. Soc. Rev.*, 2011, **40**, 575-582; O. M. Yaghi, M. O'Keeffe, N. W. Ockwig, H. K. Chae, M. Eddaoudi and J. Kim, *Nature*, 2003, **423**, 705-714; D. J. Tranchemontagne, J. L. Mendoza-Cortes, M. O'Keeffe and O. M. Yaghi, *Chem. Soc. Rev.*, 2009, **38**, 1257-1283; M. Eddaoudi, D. B. Moler, H. L. Li, B. L. Chen, T. M. Reineke, M. O'Keeffe and O. M. Yaghi, *Acc. Chem. Res.*, 2001, **34**, 319-330.
3. S. S. Chen, *CrystEngComm*, 2016, **18**, 6543-6565; C. Pettinari, A. Tabacaru and S. Galli, *Coord. Chem. Rev.*, 2016, **307**, 1-31; G. Aromi, L. A. Barrios, O. Roubeau and P. Gamez, *Coord. Chem. Rev.*, 2011, **255**, 485-546; J. G. Haasnoot, *Coord. Chem. Rev.*, 2000, **200**, 131-185; R. Contreras, A. Flores-Parra, E. Mijangos, F. Tellez, H. Lopez-Sandoval and N. Barba-Behrens, *Coord. Chem. Rev.*, 2009, **253**, 1979-1999; S. Q. Bai, D. J. Young and T.

S. A. Hor, *Chem-Asian J*, 2011, **6**, 292-304; C. Kaes, A. Katz and M. W. Hosseini, *Chem. Rev.*, 2000, **100**, 3553-3590; B. H. Ye, M. L. Tong and X. M. Chen, *Coord. Chem. Rev.*, 2005, **249**, 545-565.

4. D. F. Martin and B. B. Martin, *Inorg. Chem.*, 1962, **1**, 404-408; M. Calvin and K. W. Wilson, *J. Am. Chem. Soc.*, 1945, **67**, 2003-2007.
5. J. H. Olivier, J. Harrowfield and R. Ziessel, *Chem. Commun.*, 2011, **47**, 11176-11188.
6. Y. S. Zhang, S. R. Breeze, S. N. Wang, J. E. Greedan, N. P. Raju and L. J. Li, *Canadian Journal of Chemistry-Revue Canadienne De Chimie*, 1999, **77**, 1424-1435; Y. S. Zhang, S. N. Wang, G. D. Enright and S. R. Breeze, *J. Am. Chem. Soc.*, 1998, **120**, 9398-9399.
7. L. Y. Yao, L. Qin and S. Y. Yu, *Chem-Asian J*, 2012, **7**, 2555-2558; G. J. E. Davidson, A. J. Baer, A. P. Cote, N. J. Taylor, G. S. Hanan, Y. Tanaka and M. Watanabe, *Canadian Journal of Chemistry-Revue Canadienne De Chimie*, 2002, **80**, 496-498; J. K. Cherutoi, J. D. Sandifer, U. R. Pokharel, F. R. Fronczek, S. Pakhomova and A. W. Maverick, *Inorg. Chem.*, 2015, **54**, 7791-7802; C. Pariya, F. R. Fronczek and A. W. Maverick, *Inorg. Chem.*, 2011, **50**, 2748-2753; C. Pariya, C. R. Sparrow, C. K. Back, G. Sandi, F. R. Fronczek and A. W. Maverick, *Angew Chem Int Edit*, 2007, **46**, 6305-6308; A. W. Maverick, D. R. Billodeaux, M. L. Ivie, F. R. Fronczek and E. F. Maverick, *J Incl Phenom Macro*, 2001, **39**, 19-26; M. Rancan, J. Tessarolo, M. Casarin, P. L. Zanonato, S. Quici and L. Armelao, *Inorg. Chem.*, 2014, **53**, 7276-7287; M. Rancan, J. Tessarolo, P. L. Zanonato, R. Seraglia, S. Quici and L. Armelao, *Dalton T*, 2013, **42**, 7534-7538; M. Rancan, A. Dolmella, R. Seraglia, S. Orlandi, S. Quici, L. Sorace, D. Gatteschi and L. Armelao, *Inorg. Chem.*, 2012, **51**, 5409-5416; M. Rancan, A. Dolmella, R. Seraglia, S. Orlandi, S. Quici and L. Armelao, *Chem. Commun.*, 2012, **48**, 3115-3117; J. B. Lambert and Z. Q. Liu, *J. Chem. Crystallogr.*, 2007, **37**, 629-639.
8. J. H. Olivier, A. Haefele, P. Retailleau and R. Ziessel, *Org. Lett.*, 2010, **12**, 408-411; L. G. Mackay, H. L. Anderson and J. K. M. Sanders, *J. Chem. Soc., Perkin Trans. 1*, 1995, 2269-2273.
9. A. D. Burrows, M. F. Mahon, C. L. Renouf, C. Richardson, A. J. Warren and J. E. Warren, *Dalton T*, 2012, **41**, 4153-4163; A. D. Burrows, C. G. Frost, M. F. Mahon, P. R. Raithby, C. L. Renouf, C. Richardson and A. J. Stevenson, *Chem. Commun.*, 2010, **46**, 5067-5069; L. Carlucci, G. Ciani, D. M. Proserpio and M. Visconti, *CrystEngComm*, 2011, **13**, 5891-5902; P. C. Andrews, G. B. Deacon, R. Frank, B. H. Fraser, P. C. Junk, J. G. MacLellan, M. Massi, B. Moubaraki, K. S. Murray and M. Silberstein, *Eur. J. Inorg. Chem.*, 2009, 744-751; M. Dudek, J. K. Clegg, C. R. K. Glasson, N. Kelly, K. Gloe, K. Gloe, A. Kelling, H. J. Buschmann, K. A. Jolliffe, L. F. Lindoy and G. V. Meehan, *Crystal Growth & Design*, 2011, **11**, 1697-1704; L. Carlucci, G. Ciani, S. Maggini, D. M. Proserpio and M. Visconti, *Chem-Eur J*, 2010, **16**, 12328-12341.
10. Y. X. Zhang, B. L. Chen, F. R. Fronczek and A. W. Maverick, *Inorg. Chem.*, 2008, **47**, 4433-4435; B. L. Chen, F. R. Fronczek and A. W. Maverick, *Inorg. Chem.*, 2004, **43**, 8209-8211.
11. V. D. Vreshch, A. B. Lysenko, A. N. Chernega, J. A. K. Howard, H. Krautscheid, J. Sieler and K. V. Domasevitch, *Dalton T*, 2004, 2899-2903; V. D. Vreshch, A. N. Chernega, J. A. K. Howard, J. Sieler and K. V. Domasevitch, *Dalton T*, 2003, 1707-1711.
12. V. D. Vreshch, A. B. Lysenko, A. N. Chernega, J. Sieler and K. V. Domasevitch, *Polyhedron*, 2005, **24**, 917-926.

13. J. Yoshida, S. Nishikiori, R. Kuroda and H. Yuge, *Chem-Eur J*, 2013, **19**, 3451-3457; R. Kuroda, J. Yoshida, A. Nakamura and S. Nishikiori, *CrystEngComm*, 2009, **11**, 427-432; J. Yoshida, S. Nishikiori and R. Kuroda, *Chem-Eur J*, 2008, **14**, 10570-10578.
14. K. N. Truong, C. Merkens and U. Englert, *Acta Crystallogr B*, 2017, **73**, 981-991; Q. Q. Guo and U. Englert, *Dalton T*, 2017, **46**, 8514-8523; Q. Q. Guo, C. Merkens, R. Z. Si and U. Englert, *CrystEngComm*, 2015, **17**, 4383-4393; C. Merkens, K. N. Truong and U. Englert, *Acta Crystallogr B*, 2014, **70**, 705-713; C. Merkens, N. Becker, K. Lamberts and U. Englert, *Dalton T*, 2012, **41**, 8594-8599; C. Merkens and U. Englert, *Dalton T*, 2012, **41**, 4664-4673; M. Kondracka and U. Englert, *Inorg. Chem.*, 2008, **47**, 10246-10257.
15. D. J. Li, L. Q. Mo and Q. M. Wang, *Inorg. Chem. Commun.*, 2011, **14**, 1128-1131; A. D. Burrows, K. Cassar, M. F. Mahon and J. E. Warren, *Dalton T*, 2007, 2499-2509.
16. D. Simond, S. E. Clifford, A. F. Vieira, C. Besnard and A. F. Williams, *RSC Adv.*, 2014, **4**, 16686-16693.
17. Z. M. Chen, Y. Cui, X. F. Jiang, J. Tong and S. Y. Yu, *Chem. Commun.*, 2017, **53**, 4238-4241; Q. Q. Guo and U. Englert, *Crystal Growth & Design*, 2016, **16**, 5127-5135.
18. C. Merkens, F. F. Pan and U. Englert, *CrystEngComm*, 2013, **15**, 8153-8158.
19. J. C. Gamekkanda, A. S. Sinha, J. Desper, M. Dakovic and C. B. Aakeroy, *Crystals*, 2017, **7**; C. B. Aakeroy, A. S. Sinha, P. D. Chopade and J. Desper, *Dalton T*, 2011, **40**, 12160-12168.
20. V. A. Blatov, A. P. Shevchenko and D. M. Proserpio, *Crystal Growth & Design*, 2014, **14**, 3576-3586.
21. C. F. Macrae, I. J. Bruno, J. A. Chisholm, P. R. Edgington, P. McCabe, E. Pidcock, L. Rodriguez-Monge, R. Taylor, J. van de Streek and P. A. Wood, *J. Appl. Crystallogr.*, 2008, **41**, 466-470.
22. F. Ramirez, S. B. Bhatia, A. V. Patwardhan and C. P. Smith, *The Journal of Organic Chemistry*, 1967, **32**, 3547-3553; F. Ramirez, A. V. Patwardhan, N. Ramanathan, N. B. Desai, C. V. Greco and S. R. Heller, *J. Am. Chem. Soc.*, 1965, **87**, 543-548.
23. V. A. Blatov, L. Carlucci, G. Ciani and D. M. Proserpio, *CrystEngComm*, 2004, **6**, 377-395.

Chapter 4 - Porous unary and binary solids

4.1 Introduction

Molecules in crystals tend to fill space as efficiently as possible in order to maximize attractive dispersion forces and to minimize free energy.[1] However, when the molecules are specifically designed to bear sufficiently large and dimensionally fixed inner cavities or clefts, their packing in the solid state can lead to porous structures.[2] Molecular cages and bowl-shaped compounds, for instance, have the potential to create such molecular porous materials (MPMs). Since the porosity in the bulk solid arises from the interconnection of voids that are present in the molecules themselves, they are more precisely referred to as intrinsically porous molecular materials.

Another viable strategy towards MPMs is to employ molecules with bulky, divergent and/or awkward shapes that cannot pack tightly. 4-*p*-Hydroxyphenyl-2,2,4-trimethylchroman (Dianin's compound),[3] tris(*o*-phenylenedioxy)cyclotriphosphazene (TPP)[4] and 3,3′,4,4′-tetrakis(trimethylsilylethynyl)biphenyl (TTEB)[5] are among the representative examples. As they do not have pre-fabricated molecular free volumes, they are known as extrinsically porous molecular materials. Their porosity is merely a consequence of frustrated packing.

We have now expanded this idea to a family of tetrahedral molecules substituted at the four vertices with bulky groups. Here we report the synthesis and crystallographic study of two such species; tetrakis(4-((trimethylsilyl)ethynyl)phenyl)methane [**TMS$_4$TEPM**] and 1,3,5,7-tetrakis(4-((trimethylsilyl)ethynyl)phenyl)adamantane [**TMS$_4$TEPA**] (Figure 4.1 top). By affixing large (trimethylsilyl)ethynyl moieties to the pristine tetraphenylmethane (TPM) and 1,3,5,7-tetraphenyladamantane (TPA) core units, our aim was to disturb close-packing and to realize more open crystalline solids.

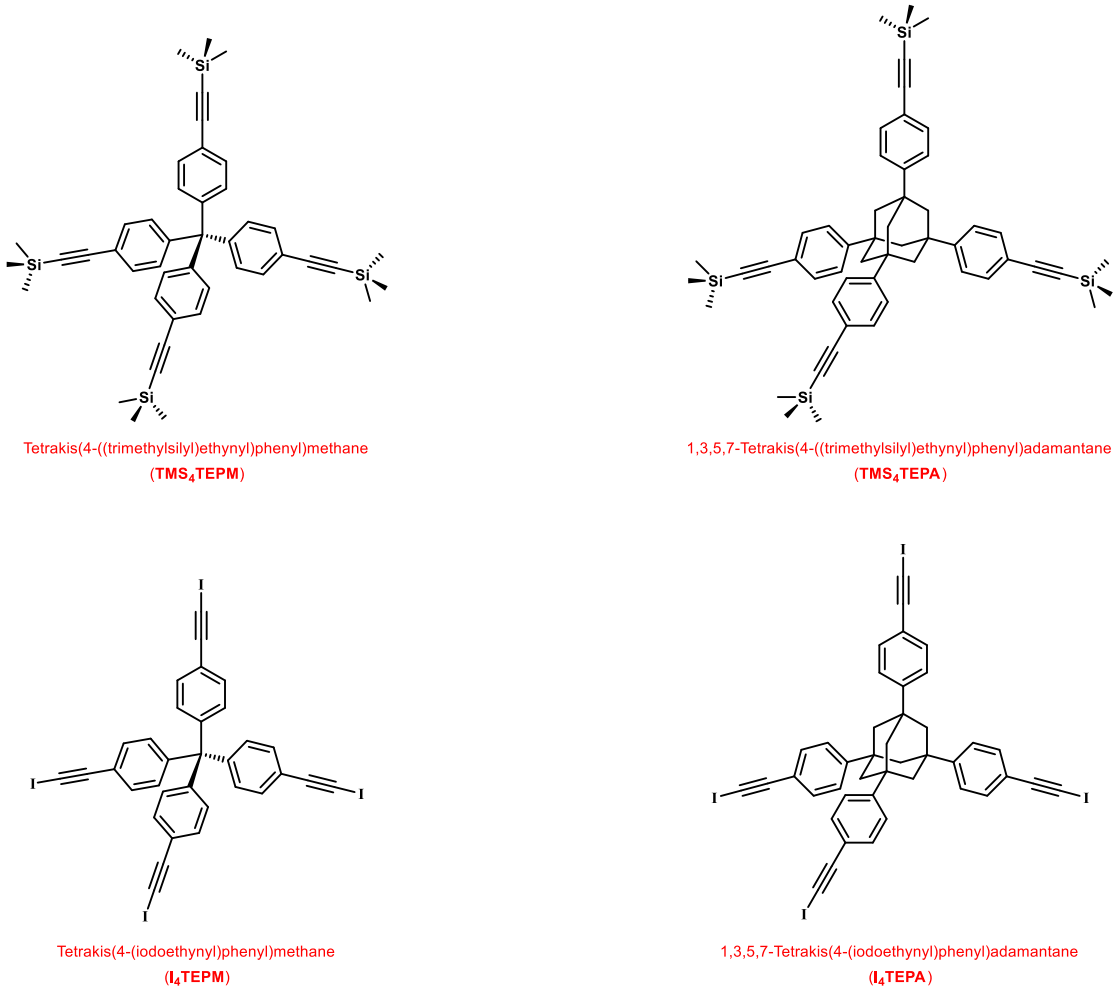

Figure 4.1 Structural formulas of the molecules used in this study.

Even though molecular shape is of primary importance in crystal packing, it is not the only structure-directing factor. The presence of functional units that can partake in directional and energetically significant non-covalent interactions has a major influence on molecular arrangement. Molecules featuring multiple peripheral binding sites have been given the name "tectons" to distinguish them from normal molecules.[6] With tectons, the structure is built up so as to saturate the maximum amount of interactions, which is usually accompanied by compromises regarding dense-packing. Their association induces the assembly of networks in which each molecule is positioned in a definite way with respect to its neighbors (molecular recognition).

Moreover, unlike van der Waals contacts, intermolecular point contacts consume only a little molecular surface, thereby leaving more usable surface. In this context, a great body of work has been done with hydrogen-bonding tectons. Some notable examples include triptycene equipped with imidazolone,[7] spirobifluorene equipped with triaminotriazine[8] and polyfluorinated triphenylbenzene equipped with pyrazole.[9]

We therefore decided to undertake some modifications to the TPM and TPA scaffolds and came up with two new tectons, tetrakis(4-(iodoethynyl)phenyl)methane (**I_4TEPM**) and 1,3,5,7-tetrakis(4-(iodoethynyl)phenyl)adamantane (**I_4TEPM**) (Figure 4.1 bottom). The iodoethynyl functionality is one of the strongest halogen-bond (XB) donors. It can direct the assembly of network structures through the C≡C–I···(C≡C) self-complementary XB motif (wherein the C≡C pi system acts as the XB acceptor). Above all, both these tetravalent tectons are readily accessible from the corresponding TMS derivatives, **TMS_4TEPM** and **TMS_4TEPA**. Although there are precedents demonstrating the versatility of iodoethynyl species as XB donors in supramolecular chemistry and crystal engineering, tetraiodoethynylarenes are very rare among them.[10]

Finally, in addition to tectonic construction, we also wanted to try out the suitability of these tetrahedral tetraiodoethynyl compounds in modular construction by co-crystallizing them with appropriate Lewis basic (*i.e.* XB-accepting) co-formers, in order to realize multicomponent porous assemblies.

4.2 Experimental

4.2.1 Materials and methods

All reagents, solvents and precursors (tetraphenylmethane and 1-bromoadamantane) were purchased from commercial sources, and were used as received without further purification.

Nuclear magnetic resonance spectra were recorded on a Varian Unity Plus (400 MHz) NMR spectrometer. A Nicolet 380 FT-IR system was used for the infrared spectroscopic analysis. Differential scanning calorimetry (DSC) and thermogravimetric analysis (TGA) were performed on TA Instruments TA Q20 and TA Q50, respectively.

4.2.2 Synthesis of tetrakis(4-bromophenyl)methane, Br_4TPM

The bromination of tetraphenylmethane was performed neat using an excess of molecular bromine. To a 100-mL round-bottom flask containing tetraphenylmethane (2.00 g, 6.24 mmol, 1 equiv.), bromine liquid (6.4 mL, 124.8 mmol, 20 equiv.) was added carefully at 0 °C. After attaching a water-cooled reflux condenser, the resultant dark reddish slurry was stirred vigorously at room temperature for one hour, and then cooled to −78 °C by using a dry ice/acetone bath. Ethanol (25 mL) was added slowly and the reaction mixture was allowed to warm to room temperature overnight. Then, to destroy excess/unreacted bromine, it was treated with 40% aqueous solution of sodium bisulfite (approximately 75 mL) and stirred for additional 30 minutes until the orange color disappeared. The tan colored solid was collected by filtration, washed well with distilled water (100 mL) and oven-dried at 60 °C for five hours. This solid was further purified by re-crystallization from chloroform/ethanol (2:1), affording tetrakis(4-bromophenyl)methane, **Br_4TPM** as an off-white crystalline material. Yield: 3.65 g (5.74 mmol, 92%). ^{1}H NMR (400 MHz, $CDCl_3$) δ (ppm): 7.39 (d, 8H), 7.01 (d, 8H). ^{13}C NMR (100 MHz, $CDCl_3$) δ (ppm): 144.64, 132.57, 131.30, 121.02, 63.84.

4.2.3 Synthesis of tetrakis(4-((trimethylsilyl)ethynyl)phenyl)methane, TMS_4TEPM

Tetrakis(4-bromophenyl)methane (3.50 g, 5.50 mmol, 1 equiv.) and triphenylphosphine (462 mg, 1.76 mmol, 32 mol%) were placed in a 250-mL round-bottomed flask. Diisopropyl amine (100 mL) was added and the resulting solution was purged with dinitrogen gas for 30 minutes.

Then, bis(triphenylphosphine)palladium(II) dichloride (618 mg, 0.88 mmol, 16 mol%), copper(I) iodide (168 mg, 0.88 mmol, 16 mol%) and trimethylsilylacetylene (6.2 mL, 44.0 mmol, 8 equiv.) were added. The reaction flask was fitted to a water-jacketed condenser, cooled to −78 °C, subjected to a brief vacuum/backfill cycle and refluxed for 24 hours under nitrogen atmosphere. After removing volatile materials *in vacuo*, the residue was re-dissolved in chloroform (100 mL) and filtered through a pad of Celite, using an extra 50 mL portion of chloroform to wash the filter pad. The combined filtrate was then washed with distilled water (2 × 25 mL) and brine (25 mL), dried over anhydrous magnesium sulfate, and evaporated to dryness under vacuum. Crude product was flash-column-chromatographed on silica gel using pure hexanes followed by hexanes/ethyl acetate (4:1) as eluents to obtain the title compound, **TMS$_4$TEPM** as a pale yellowish solid. Yield: 3.30 g (4.68 mmol, 85%). ^{1}H NMR (400 MHz, $CDCl_3$) δ (ppm): 7.33 (d, 8H), 7.05 (d, 8H), 0.24 (s, 36H). ^{13}C NMR (100 MHz, $CDCl_3$) δ (ppm): 146.21, 131.59, 130.95, 121.42, 104.82, 95.00, 64.98, 0.18.

4.2.4 Synthesis of tetrakis(4-(iodoethynyl)phenyl)methane, I$_4$TEPM

Acetonitrile (150 mL) was transferred into a 250-mL round-bottom flask that contained tetrakis(4-((trimethylsilyl)ethynyl)phenyl)methane (2.50 g, 3.54 mmol, 1 equiv.). The flask was wrapped in aluminium foil, and then silver(I) fluoride (2.70 g, 21.3 mmol, 6 equiv.) and *N*-iodosuccinimide (4.78 g, 21.3 mmol, 6 equiv.) were added. It was evacuated (while stirring), refilled with nitrogen and stirred at room temperature for 24 hours. Distilled water (200 mL) was added and the resulting mixture was extracted with diethyl ether (4 × 50 mL). The combined organic layers were washed with saturated sodium bisulfite (40 mL), distilled water (40 mL) and brine (40 mL), and dried over anhydrous magnesium sulfate. Evaporation of the solvent under reduced pressure resulted in an orange colored residue. Additional cleanup by column

chromatography (silica gel, hexanes/ethyl acetate = 9:1) gave the desired compound, **I_4TEPM**, as a yellow solid. Yield: 1.83 g (1.98 mmol, 56%). ^{1}H NMR (400 MHz, $CDCl_3$) δ (ppm): 7.32 (d, 8H), 7.06 (d, 8H). ^{13}C NMR (100 MHz, $CDCl_3$) δ (ppm): 146.34, 132.04, 130.87, 121.81, 93.87, 65.02, 7.03. ^{1}H NMR (400 MHz, DMSO-d6) δ (ppm): 7.37 (d, 8H), 7.04 (d, 8H). ^{13}C NMR (100 MHz, DMSO-d6) δ (ppm): 145.68, 131.66, 130.36, 121.08, 92.11, 64.26, 18.41.

4.2.5 Synthesis of 1,3,5,7-tetraphenyladamantane (TPA)

In a 250-mL round-bottom flask, *tert*-butyl bromide (3.9 mL, 34.9 mmol, 2.5 equiv.) was added to a solution of 1-bromoadamantane (3.00 g, 13.9 mmol, 1 equiv.) in anhydrous benzene (30 mL). The flask was placed in an ice bath and aluminium chloride (186 mg, 1.39 mmol, 10 mol%) was carefully charged to the chilled, stirring solution. The mixture was then heated under reflux until the evolution of hydrogen bromide ceased (the top of the condenser was connected to a gas absorption trap containing 30% aqueous sodium hydroxide). The resultant heterogeneous mixture was allowed to cool to room temperature and filtered, and the residue was washed sequentially with chloroform (30 mL), water (50 mL) and chloroform (30 mL). The off-white solid was further purified by washing overnight with refluxing chloroform in a Soxhlet apparatus, which gave 1,3,5,7-tetraphenyladamantane as a fine white powder. Yield: 5.04 g (11.4 mmol, 82%). Mp: > 300 °C. ATR-FTIR (cm^{-1}): 3054.63, 3020.15, 2918.35, 2848.84, 1596.64, 1492.55, 1441.99, 1354.80, 1262.69, 1078.06, 1030.47, 918.30, 889.35, 843.99, 788.04, 759.64, 745.85, 699.26.

4.2.6 Synthesis of 1,3,5,7-tetrakis(4-iodophenyl)adamantane (I_4TPA)

To a 250-mL round-bottom flask containing a suspension of 1,3,5,7-tetraphenyladamantane (4.00 g, 9.08 mmol, 1 equiv.) in chloroform (100 mL) was added iodine (5.76 g, 22.7 mmol, 2.5 equiv.). This mixture was stirred vigorously at room temperature until iodine fully dissolved. The flask was flushed with nitrogen gas and

(bis(trifluoroacetoxy)iodo)benzene (9.76 g, 22.7 mmol, 2.5 equiv.) was added. The resulting mixture was stirred at room temperature for 12 hours. It was then filtered off, and the collected solid was washed with excess amount of chloroform (200 mL). The combined dark purple filtrate was washed with 5% sodium bisulfite solution twice (2 × 50 mL), followed by distilled water (100 mL) and saturated sodium chloride solution (100 mL). It was dried with anhydrous magnesium sulfate and the solvent was removed under reduced pressure, which resulted in a pale-yellow solid. After refluxing in methanol (200 mL) for 12 hours, the pure compound was isolated as a white solid by filtration and air-drying. Yield: 5.91 g (6.26 mmol, 69%). ^{1}H NMR (400 MHz, CDCl3) δ (ppm): ^{1}H NMR (400 MHz, $CDCl_3$) δ (ppm): 7.67 (d, 8H), 7.18 (d, 8H), 2.06 (s, 12H).

4.2.7 Synthesis of 1,3,5,7-tetrakis(4-((trimethylsilyl)ethynyl)phenyl)adamantane (TMS$_4$TEPA)

As in the synthesis of **TMS$_4$TEPM**, this step involved a four-fold Sonogashira cross-coupling reaction of 1,3,5,7-tetrakis(4-iodophenyl)adamantane (**I$_4$TPA**) with trimethylsilylacetylene. Yield: 88%. ^{1}H NMR (400 MHz, CDCl3) δ (ppm): ^{1}H NMR (400 MHz, $CDCl_3$) δ (ppm): 7.45 (d, 8H), 7.38 (d, 8H), 2.09 (s, 12H), 0.24 (s, 36H). ^{13}C NMR (100 MHz, $CDCl_3$) δ (ppm): 149.63, 132.29, 125.13, 121.32, 105.19, 94.20, 46.97, 39.53, 0.25.

4.2.8 Synthesis of 1,3,5,7-tetrakis(4-(iodoethynyl)phenyl)adamantane (I$_4$TEPA)

The same one-pot desilylative iodination method described above for the synthesis of **I$_4$TEPM** was employed. Yield: 63%. ^{1}H NMR (400 MHz, CDCl3) δ (ppm): 7.42 (d, 8H), 7.39 (d, 8H), 2.09 (s, 12H). ^{13}C NMR (100 MHz, $CDCl_3$) δ (ppm): 149.82, 132.64, 125.16, 121.57, 94.16, 46.88, 39.50, 6.18. ^{1}H NMR (400 MHz, DMSO-d6) δ (ppm): 7.51 (d, 8H), 7.37 (d, 8H), 2.00 (s, 12H). ^{13}C NMR (100 MHz, DMSO-d6) δ (ppm): 150.14, 131.74, 125.48, 120.50, 92.59, 45.48, 38.95, 17.02.

4.2.9 Synthesis of I_4TEPM·4pyridine

In a 2-dram glass vial, **I_4TEPM** (10 mg, 0.011 mmol) was dissolved in 0.5 mL of pyridine. This open vial was placed in a second larger container (50-mL glass jar) having 10 mL of pyridine/methanol (1:4) mixture. The outer container was then closed/sealed, and the apparatus was kept at ambient conditions to allow the vapor from methanol (anti-solvent) to diffuse into the sample solution. When the total volume of the inner vial became ~3 mL, it was taken out and, after partially tightening the lid, left undisturbed at ambient conditions to allow the solvents to evaporate slowly. Colorless/pale-yellow crystals were observed after few days.

4.2.10 Synthesis of I_4TEPM·2THF

In a 2-dram glass vial, **I_4TEPM** (10 mg, 0.011 mmol) was dissolved in 1 mL of tetrahydrofuran. After adding 1 mL of methanol, the vial (with partially-tightened screw cap) was left undisturbed at ambient conditions to allow the solvents to evaporate slowly. Colorless/pale-yellow crystals suitable for single-crystal X-ray diffraction were observed after few days. ATR-FTIR (cm^{-1}): 2973.60, 2865.19, 2165.12, 1683.63, 1588.39, 1493.96, 1422.65, 1403.51, 1364.97, 1189.71, 1114.95, 1044.48, 1017.57, 883.88, 830.44, 809.10.

4.2.11 Synthesis of I_4TEPM·2DMSO

In a 2-dram glass vial, **I_4TEPM** (10 mg, 0.011 mmol) was dissolved in 0.5 mL of dimethyl sulfoxide. The vial (with partially-tightened screw cap) was then allowed to stand at room temperature for one week, during which time colorless/pale-yellow crystals suitable for single-crystal X-ray diffraction were appeared. ATR-FTIR (cm^{-1}): 3031.61, 2986.12, 2908.50, 2159.57, 1493.63, 1428.95, 1398.06, 1307.76, 1186.14, 1113.34, 1039.17, 1014.16, 945.19, 825.81, 697.29.

4.2.12 Synthesis of I_4TEPM·2dioxane

In a 2-dram glass vial, **I_4TEPM** (10 mg, 0.011 mmol) was suspended in 0.5 mL 1,4-dioxane. After adding a few drops of methylene chloride, the vial was sealed and heated to obtain a clear solution. Colorless/pale-yellow crystals suitable for single-crystal X-ray diffraction were harvested by slow evaporation. ATR-FTIR (cm^{-1}): 2957.75, 2906.36, 2850.52, 2170.96, 1490.46, 1448.06, 1400.59, 1369.35, 1288.08, 1251.61, 1186.43, 1112.87, 1077.44, 1016.07, 975.67, 865.59, 828.77, 735.16.

4.2.13 Electrostatic potential calculations

In order to calculate the molecular electrostatic potentials (MEPs) of tetra-halogenated species, first, their geometries were optimized using Spartan '14 software. Geometry optimizations of TPM derivatives were carried out at hybrid functional B3LYP/6-311+G** level of theory. For TPM derivatives, B3LYP/6-311++G** level was used. The visualization of MEPs was subsequently attained through mapping its values onto 0.002 au isosurface, determined with a positive point charge in the vacuum as a probe. The numbers, now termed surface potentials, indicate the Coulombic interaction energies (expressed in kJ/mol) between the probe and this isodensity surface at different points.

4.2.14 Single-crystal X-ray diffraction

Detailed crystallographic information about the data collections, solutions and refinements can be found in the Appendix C. Structural visualizations and void mapping were done using Mercury software.[11] For void volume calculations, default parameters (contact surface, 1.2 Å probe radius and 0.7 Å grid spacing) were used.

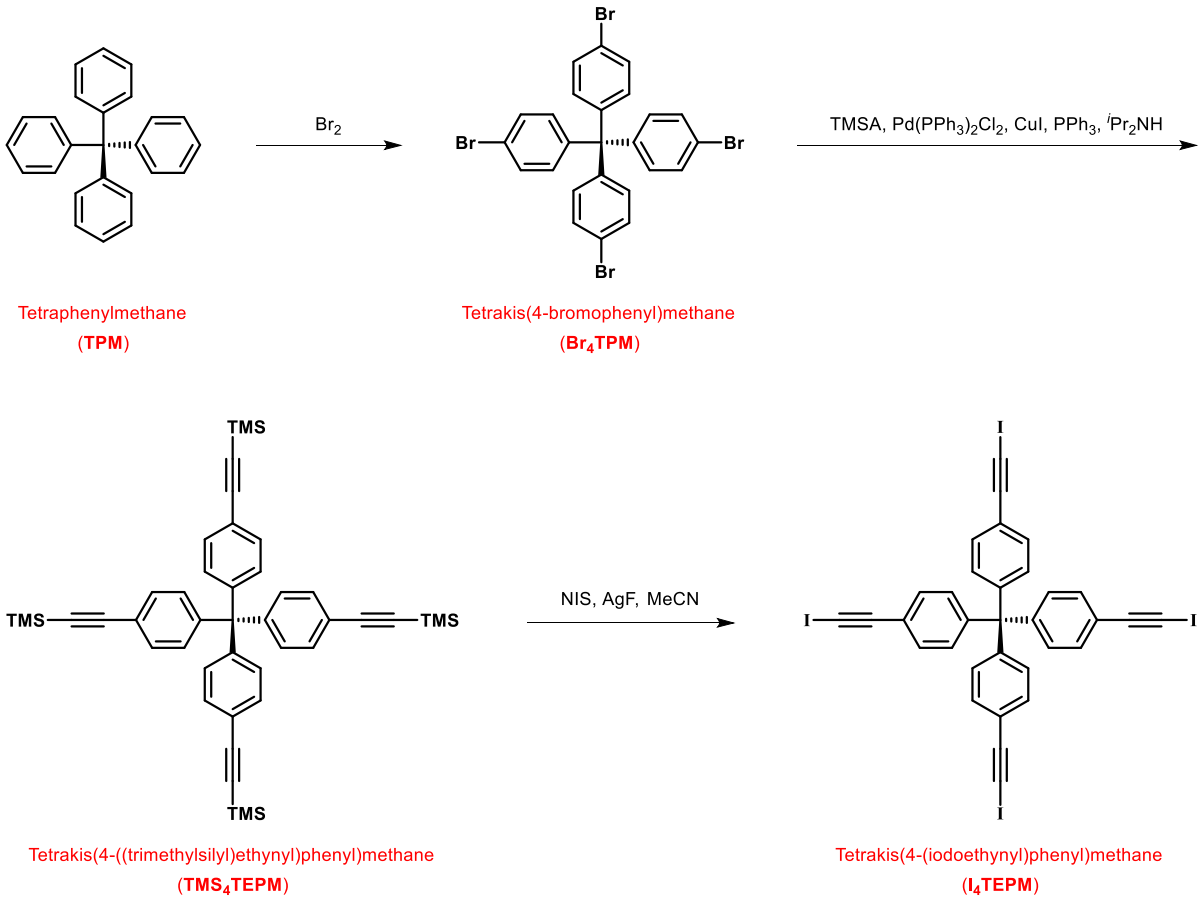

Figure 4.2 Synthetic route to **TMS$_4$TEPM** and **I$_4$TEPM**.

4.3 Results and discussion

Starting with commercially available tetraphenylmethane, **TMS$_4$TEPM** was prepared in two steps (*i.e.* tetra-*para*-bromination followed by coupling with trimethylsilylacetylene) with an overall yield of 78% (Figure 4.2). The synthesis of **TMS$_4$TEPA** required three steps; TPA was prepared through the Friedel-Crafts reaction of 1-bromoadamantane and benzene in the presence of tert-butyl bromide and aluminium chloride, and was then subjected to tetra-*para*-iodination followed by coupling with trimethylsilylacetylene (Figure 4.3). The overall yield was 50%.

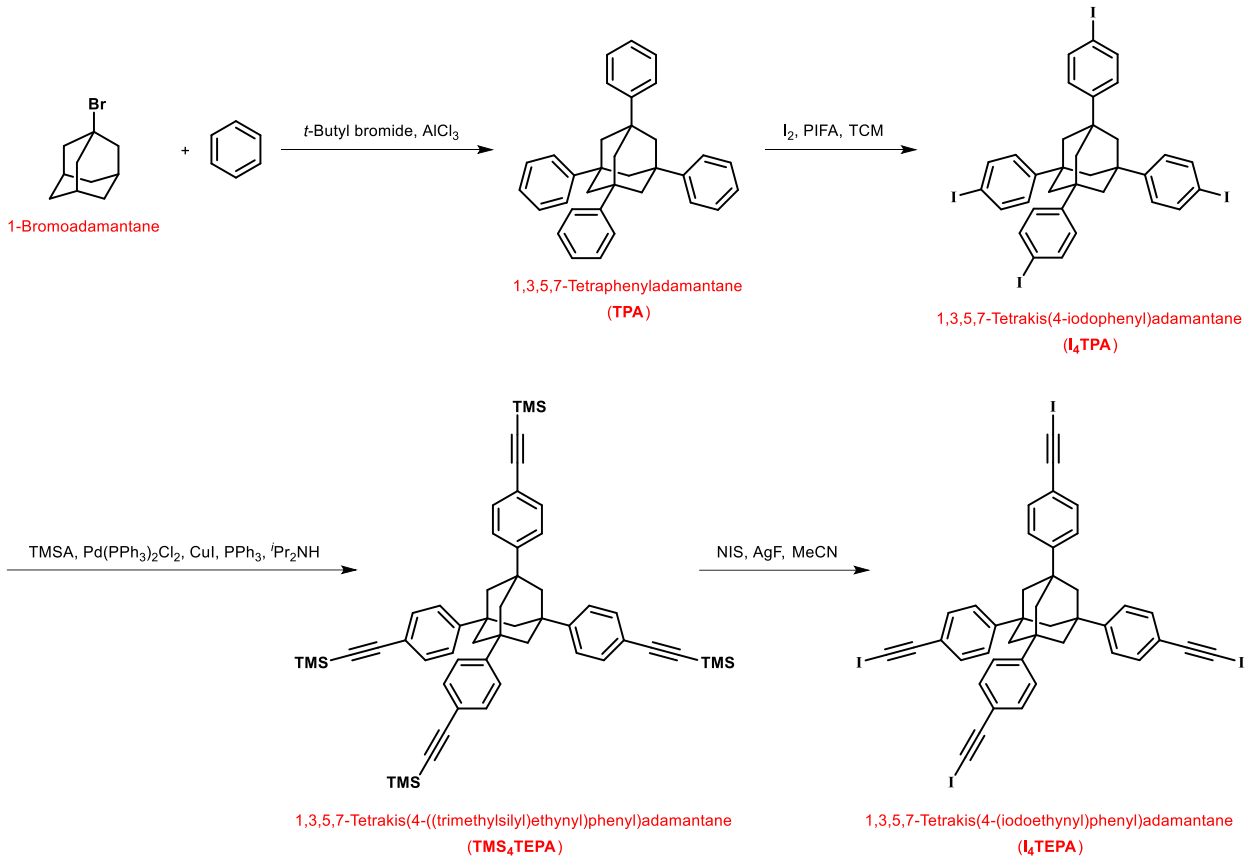

Figure 4.3 Synthetic route to **TMS$_4$TEPA** and **I$_4$TEPA**.

Single crystals of **TMS$_4$TEPM** suitable for single-crystal X-ray crystallography were obtained by slow evaporation of either tetrahydrofuran/ethanol or chloroform/ethanol solution. For **TMS$_4$TEPA**, X-ray quality crystals could be harvested from hexanes, heptane, heptane/dichloromethane or chloroform/ethanol. As anticipated, structural determination revealed that both are porous in nature (12.8% and 10.7%, respectively). They, however, do not form empty-channel structures; instead, they have disconnected spatial voids or "porosity without pores" as denominated by Barbour (Figure 4.4).[12] The overall packing is mainly mediated by extensive phenyl embraces.[13]

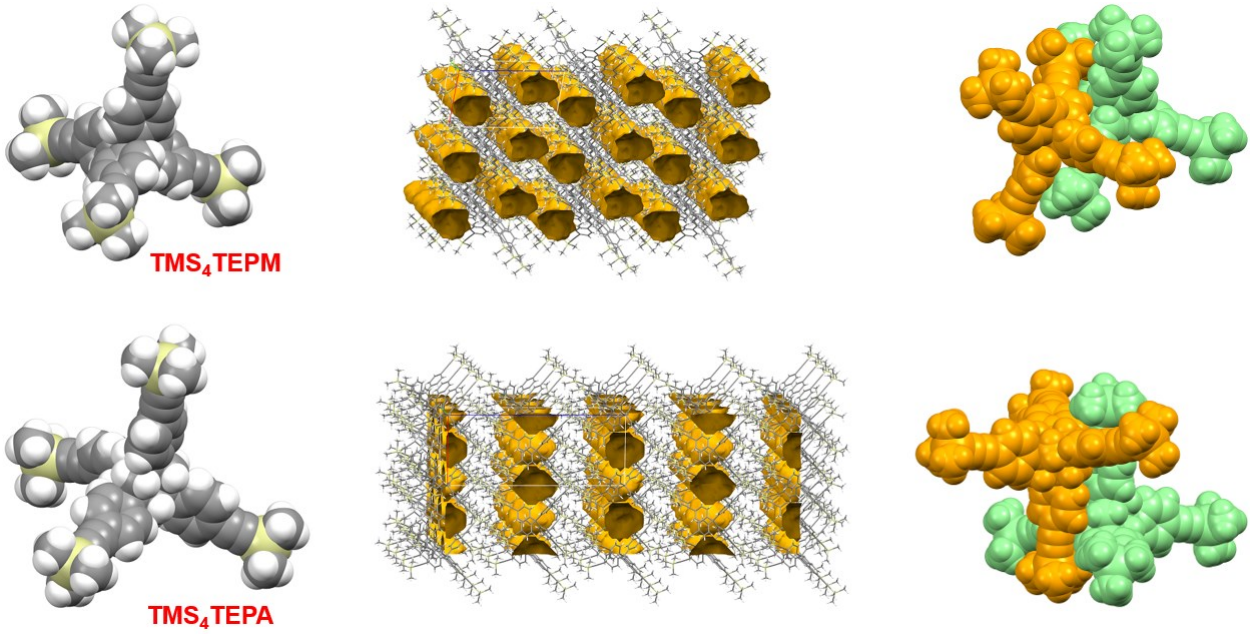

Figure 4.4 Structures of **TMS$_4$TEPM** and **TMS$_4$TEPA**.

Tetraiodoethynyl derivatives, **I$_4$TEPM** and **I$_4$TEPA**, were synthesized *via* one-pot/*in-situ* desilylative iodination of tetraTMS-acetylenyl species using silver(I) fluoride and *N*-iodosuccinimide (see Figures 4.2 and 4.3). This direct trimethylsilyl-to-iodo transformation allowed us to avoid potentially unstable ethynyl intermediates and to achieve the target compounds in moderate yields (56% and 63%, respectively).

Owing to the four-fold symmetry, the ^{1}H and ^{13}C NMR spectra of these tetraTMSethynyl and tetraiodoethynyl species are quite simple. However, the signals of **I$_4$TEPM** and **I$_4$TEPA** display appreciable solvent dependency, with the alkynyl carbon bonded to iodine being most strongly affected (**I$_4$TEPM**: 7.0 ppm in $CDCl_3$ *versus* 18.4 ppm in DMSO-*d6*, **I$_4$TEPA**: 6.2 ppm in $CDCl_3$ *versus* 17.0 ppm in DMSO-*d6*). This change in chemical shifts is a direct consequence of XB-based complexation; when the iodine atom interacts with a Lewis basic solvent, it leads to a paramagnetic deshielding at the carbon atom bearing that iodine which, in turn, moves its NMR

resonance frequency downfield.[14] It is also worth mentioning that the ^{1}H NMR spectra of two adamantane species exhibit conspicuous second order effects (leaning/roofing effect).

In order to quantify the electron density distribution over the free tetraiodoethynyl tectons, and especially to get some insight about the degree of activation/electronic polarization on iodine atoms caused by *sp*-hybridized carbons, their molecular electrostatic potential surfaces (MEPS)[15] were calculated. As expected, both **I$_4$TEPM** and **I$_4$TEPA** were found to have more pronounced electron-deficient regions (*i.e.* σ-holes) on each iodine atom. Indeed, these σ-hole potential values are significantly higher than those of other closely-related tetra-halogenated molecules (Figure 4.5). Note that the structures of tetrakis(4-bromophenyl)methane (**Br$_4$TPM**), tetrakis(4-iodophenyl)methane (**I$_4$TPM**), tetrakis(4-(bromoethynyl)phenyl)methane (**Br$_4$TEPM**) and tetrakis(4-iodophenyl)adamantane (**I$_4$TPA**) have previously been reported.[16]

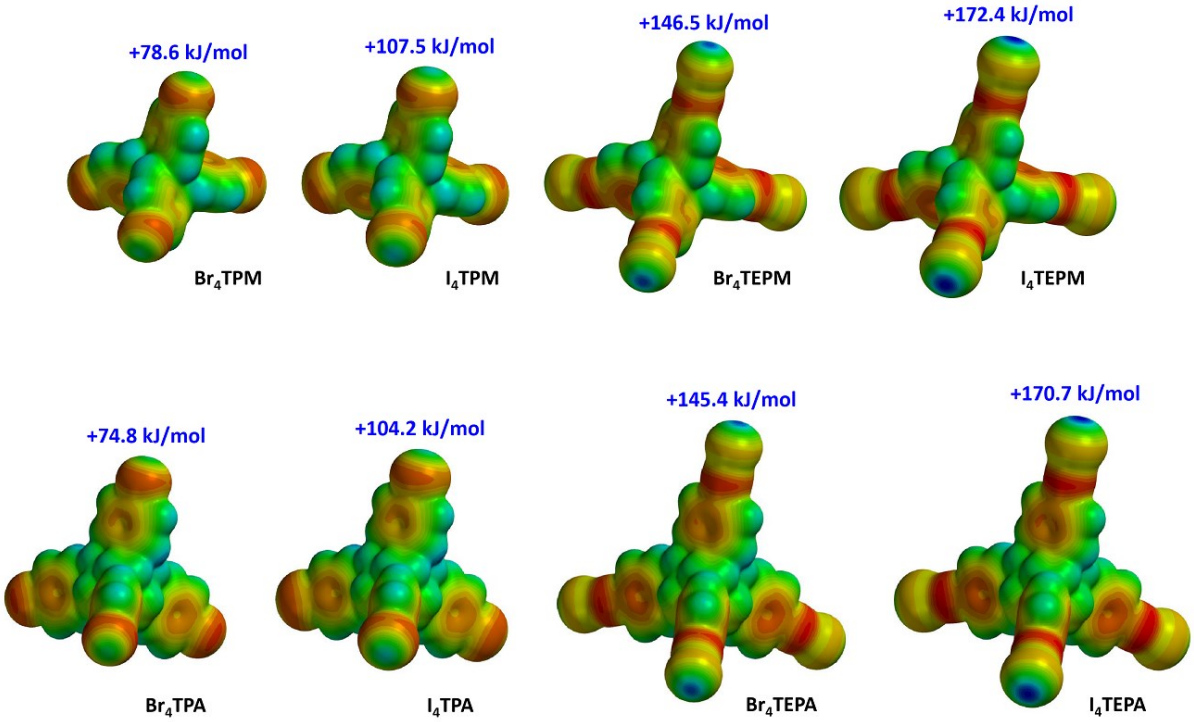

Figure 4.5 MEP surfaces of tetrahalogenated TPM and TPA species. Range: from −80 kJ/mol (red) to +175 kJ/mol (blue).

We then tried to grow good quality crystals of **I$_4$TEPM** and **I$_4$TEPA** but were successful only with the former. The single-crystal X-ray analysis of **I$_4$TEPM** shows that the molecules are ordered in rows which, in turn, are linked together by relatively rare C≡C–I···(C≡C) halogen-bonding interactions. The approach of iodine is almost perpendicular to the C≡C triple bond with 3.261 and 3.404 Å close contacts to the alkyne carbons. These T-shaped contacts ultimately result in zigzag ladder motifs between individual molecular rows, leading to an infinite two-dimensional network (Figure 4.6 left).

In contrast to the structure of **TMS$_4$TEPM** with isolated voids, **I$_4$TEPM** possesses one-dimensional channels along the crystallographic *b* axis (Figure 4.6 right). These channels account for 24.3% of the crystal volume which is roughly twice as high as that of **TMS$_4$TEPM**. Most importantly, **I$_4$TEPM** can maintain its structural integrity upon guest solvent loss, indicating its ability to exhibit permanent porosity. Another point worth stressing here is that the precursor molecules, namely tetraphenylmethane, tetrakis(4-bromophenyl)methane and tetrakis(4-iodophenyl)methane, all form non-porous structures, highlighting the effectiveness of our strategy (Figure 4.7).

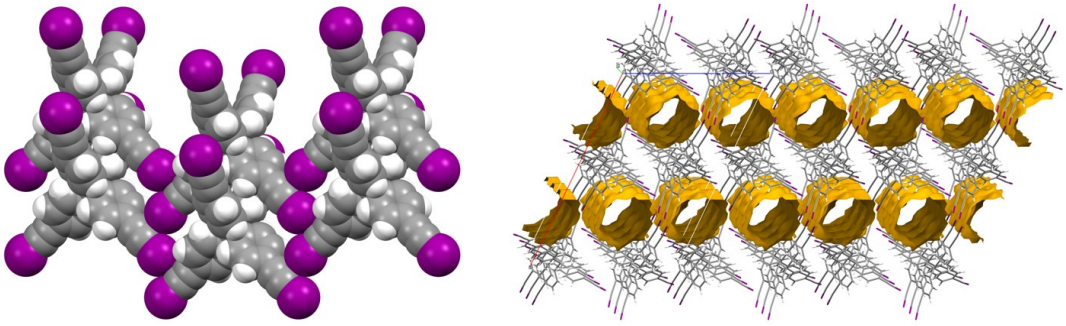

Figure 4.6 (left) Molecular association in the structure of **I$_4$TEPM** and (right) 1D channels when viewed perpendicular to the *ac* plane.

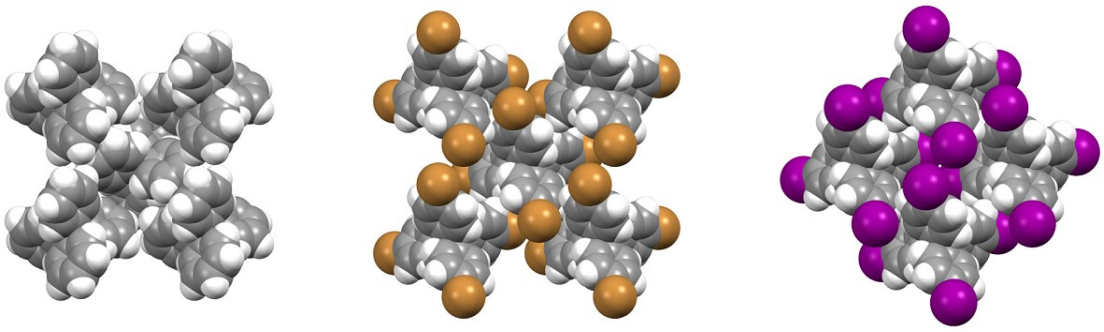

Figure 4.7 Densely-packed structures of (from left) **TPM**, **Br$_4$TPM** and **I$_4$TPM**.

After knowing motif-forming characteristics of **I$_4$TEPM** by itself, we wanted to incorporate it within two-component solid forms. As a co-crystallizing partner, our first choice was pyridine, one of the simplest XB acceptors, even though it cannot lead **I$_4$TEPM** to a polymeric assembly. We managed to get a binary crystalline material (confirmed by NMR and TGA) but the structural characterization was not successful as those crystals rapidly deteriorated during data collection. This intrigued us to try out other Lewis basic/coordinating solvents with multiple bond forming ability. In three cases, with tetrahydrofuran (THF), dimethyl sulfoxide (DMSO) and dioxane, **I$_4$TEPM** afforded crystalline solids. After confirming the binary nature of each of these three products by IR, NMR and TGA analyses (Figure 4.8), they were subjected to single-crystal X-ray structure determination.

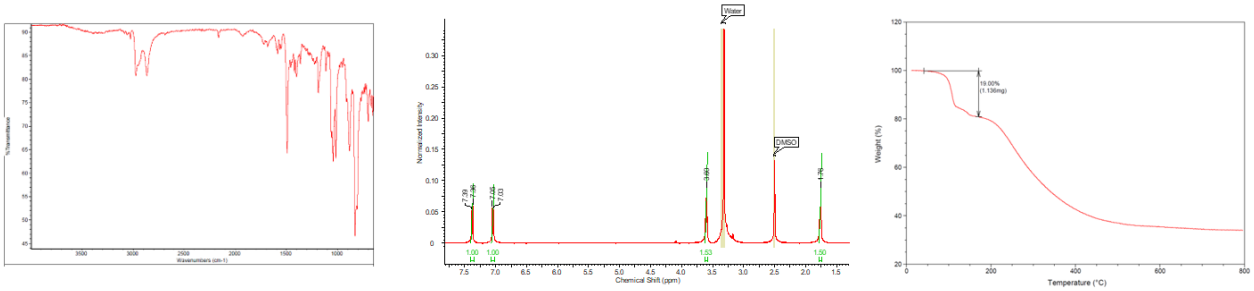

Figure 4.8 Preliminary analysis of **I$_4$TEPM** crystals grown from THF/MeOH. (from left) IR, NMR and TGA.

Crystallization of **I$_4$TEPM** in tetrahydrofuran/methanol resulted in crystals of **I$_4$TEPM**·2THF where each THF molecule forms two halogen bonds in a bifurcated manner and connect adjacent **I$_4$TEPM** molecules together, thereby forming a one-dimensional twisted ribbon-like architecture (Figure 4.9 left). And the lattice comprises isolated voids that account for 10.3% of unit cell volume (Figure 4.9 right).

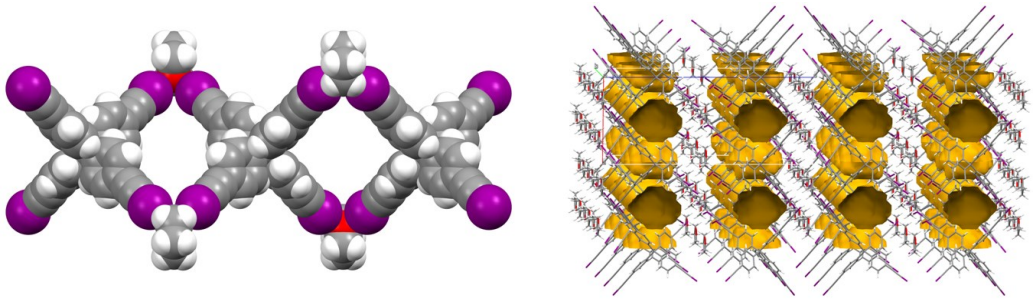

Figure 4.9 (left) 1D chain/twisted ribbon structure of **I$_4$TEPM**·2THF and (right) isolated voids when viewed perpendicular to the *ac* plane.

Crystallization of **I$_4$TEPM** from dimethyl sulfoxide yielded crystals of t **I$_4$TEPM**·2DMSO which has XB interactions analogous to the ones observed in **I$_4$TEPM**·2THF. Once again, the coordinating solvent acts as a bridging ligand and gives rise to a one-dimensional twisted-ribbon supramolecular chain, with 1D channels of 19.0% free volume in the overall packing (Figure 4.10).

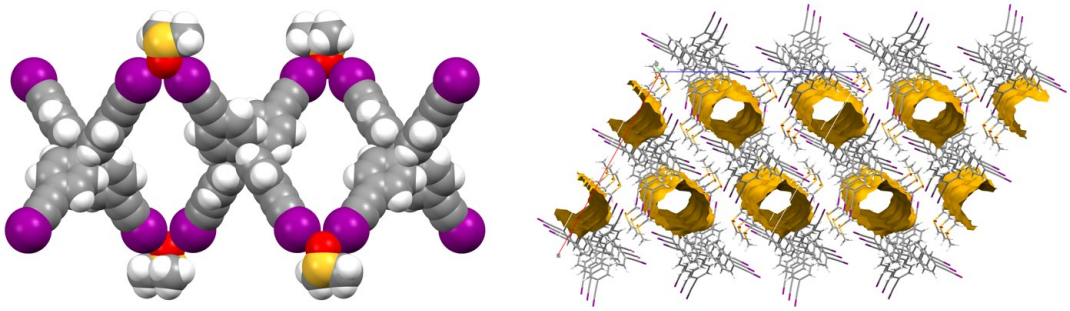

Figure 4.10 (left) 1D chain/twisted ribbon structure of **I$_4$TEPM**·2DMSO and (right) 1D channels when viewed perpendicular to the *ac* plane.

Crystallization of **I4TEPM** in 1,4-dioxane/dichloromethane resulted in crystals of **I4TEPM**·2Dioxane. This time, the solvent molecule serves as a linear ditopic ligand, so the structure propagates into two dimensions (Figure 4.11 left). As in **I4TEPM**·2DMSO, the structure creates 1D channels parallel to the crystallographic *c* axis, holding 18.7% free volume (Figure 4.11 right)

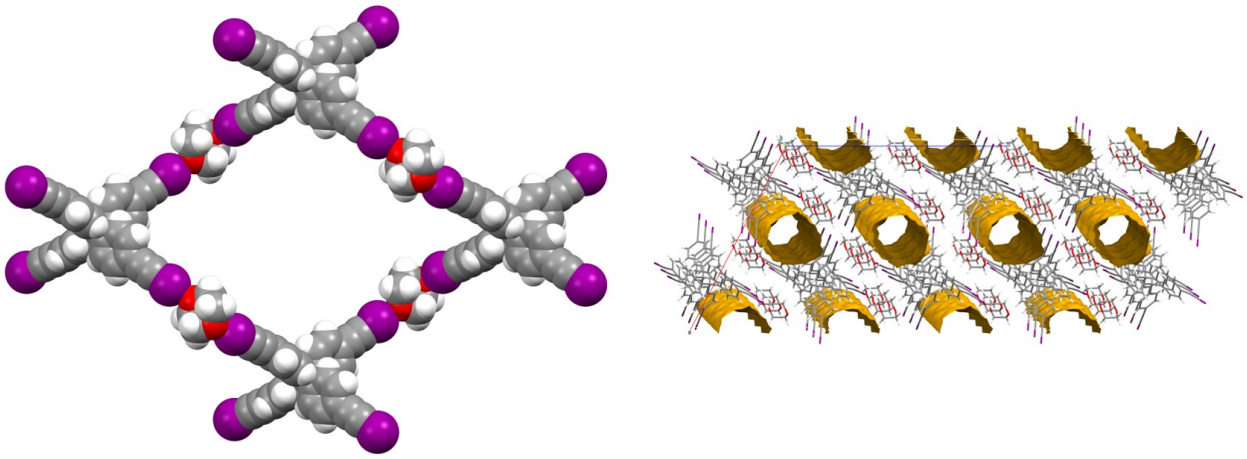

Figure 4.11 (left) 2D sheet structure of **I4TEPM**·2Dioxane and (right) 1D channels when viewed perpendicular to the *ac* plane.

The normalized distance (*ND*) and the percent radii reduction (%*RR*) are two common indicators that can be used as rough measures of the strength of XBs [$ND = d_{xy}/(r_x + r_y)$ where d_{xy} is the crystallographically determined XB distance, and r_x and r_y are the van der Waals radii for the two involved atoms (I = 1.98 Å, O = 1.52 Å), $\%RR = (1 - ND) \times 100$]. As can be seen in Table 4.1, the %*RR* values calculated for XBs observed in our three solvates are greater than 15% (except in one case) that mirror the moderate strength of those interactions. Moreover, all bonds have near-linear (> 170° angles, again one exception) arrangements that reflect the high directionality of those interactions.

Table 4.1 XB interaction parameters in the studied complexes.

Complex	C–I···O	*d*(I···O)/Å	*ND*	*RR*/%	∠(C–I···O)/°
I4TEPM·THF	C9–I10···O11	2.965(5)	0.85	15.3	170.1(3)
I4TEPM·DMSO	C9–I10···O23	3.013(3)	0.86	13.9	162.04(14)
	C18–I19···O23	2.797(3)	0.80	20.1	170.00(14)
I4TEPM·Dioxane	CG–I1···O4	2.774	0.79	20.7	174.23
	CH–I2···O3	2.818	0.80	19.5	174.41

The DSC and TGA thermograms show that the solvents are strongly attached to the crystal lattice; the removal temperatures are noticeably higher than their respective boiling points (Figure 4.12). However, once removed from the mother liquor, the crystals gradually become opaque because of the partial loss of halogen-bonded and freely-occupying solvent molecules.

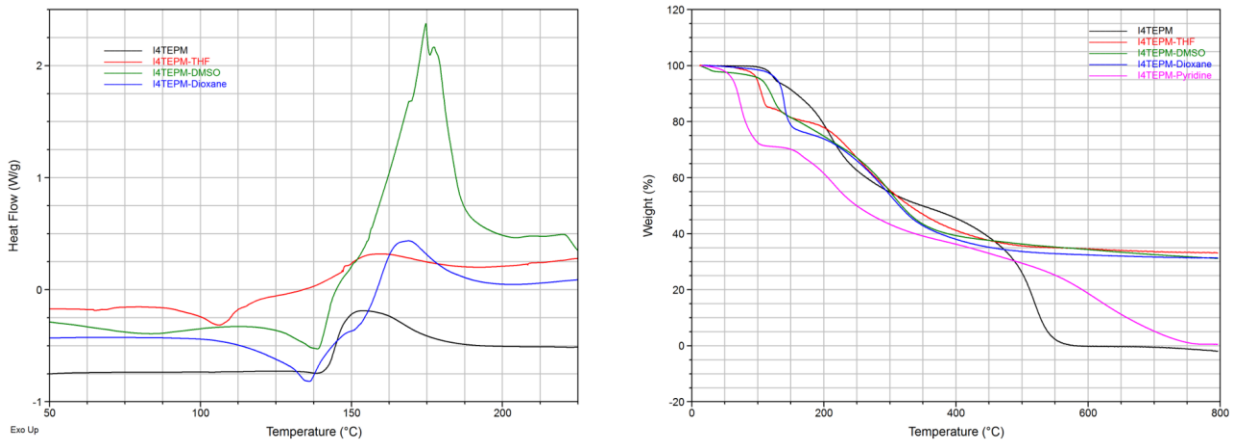

Figure 4.12 (left) DSC traces (Tzero aluminum pan, 1–2 mg sample size, 5 °C·min^{-1} heating rate, nitrogen atmosphere) and (right) TGA traces (platinum pan, 5–10 mg sample size, 10 °C·min^{-1} heating rate, nitrogen atmosphere).

4.4 Conclusions

The solid-state packing behavior of tetrakis(4-((trimethylsilyl)ethynyl)phenyl)methane [**TMS4TEPM**] and 1,3,5,7-tetrakis(4-((trimethylsilyl)ethynyl)phenyl)adamantane [**TMS4TEPA**]

shows that they have some degree of extrinsic porosity. By converting these two molecules into tecton-like derivatives with XB capability, **I_4TEPM** and **I_4TEPA**, the porosity can be increased significantly. Even though the latter tends to form disordered or fragile crystals, the former crystallizes into porous solids in its neat form as well as with suitable co-formers. Binary crystals formed with THF, DMSO and 1,4-dioxane show considerable free volume but are quite unstable; attempts to remove the trapped solvents destroy the crystal lattice.

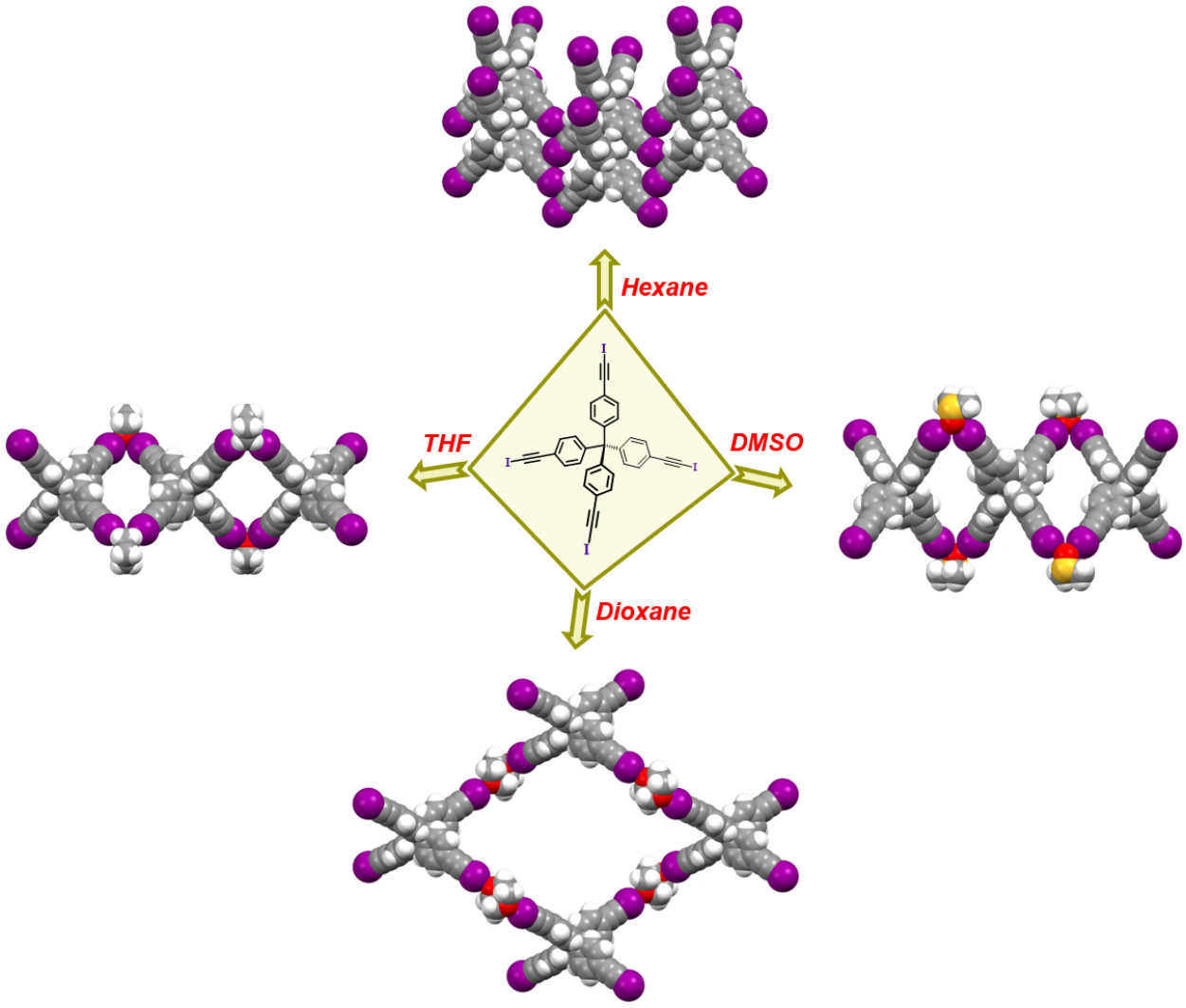

Figure 4.13 XB-directed unary and binary structures resulted from **I_4TEPM**.

Our results demonstrate that iodoethynyl-functionalized tectons are good at making molecular analogues of zeolites not only *via* the molecular tectonics approach but also *via* the modular approach. We are hopeful that such halogen-bonding tectons can be exploited to make single- and multi-component crystals with even higher porosity and stability that would find useful applications in sensing, separation, catalysis, storage, delivery, *etc.*

4.5 References

1. J. D. Dunitz, G. Filippini and A. Gavezzotti, *Tetrahedron*, 2000, **56**, 6595-6601; C. P. Brock and J. D. Dunitz, *Chem. Mater.*, 1994, **6**, 1118-1127; A. I. Kitaigorodskii, *Molecular Crystals and Molecules*, Academic Press, New York, 1973; A. I. Kitaigorodskii, *Organic Chemical Crystallography*, Consultants Bureau, New York, 1961; A. I. Kitaigorodskii, *Chem. Soc. Rev.*, 1978, **7**, 133-163; A. I. Kitaigorodskii, *Acta Crystallographica*, 1965, **18**, 585-590; A. I. Kitaigorodskii, *J. Phys. (USSR)*, 1945, **9**, 351-352.
2. J. R. Holst, A. Trewin and A. I. Cooper, *Nat. Chem.*, 2010, **2**, 915-920; M. I. Hashim, C. W. Hsu, H. T. M. Le and O. S. Miljanic, *Synlett*, 2016, **27**, 1907-1918; J. Tian, P. K. Thallapally and B. P. McGrail, *CrystEngComm*, 2012, **14**, 1909-1919; J. D. Evans, K. E. Jelfs, G. M. Day and C. J. Doonan, *Chem. Soc. Rev.*, 2017, **46**, 3286-3301; M. Mastalerz, *Chem-Eur J*, 2012, **18**, 10082-10091.
3. F. Imashiro, M. Yoshimura and T. Fujiwara, *Acta Crystallographica Section C*, 1998, **54**, 1357-1360; R. M. Barrer and V. H. Shanson, *J. Chem. Soc., Chem. Commun.*, 1976, 333-334.
4. G. Couderc, T. Hertzsch, N. R. Behrnd, K. Krämer and J. Hulliger, *Microporous Mesoporous Mater.*, 2006, **88**, 170-175; T. Hertzsch, C. Gervais, J. Hulliger, B. Jaeckel, S. Guentay, H. Bruchertseifer and A. Neels, *Adv. Funct. Mater.*, 2006, **16**, 268-272; A. Comotti, S. Bracco, L. Ferretti, M. Mauri, R. Simonutti and P. Sozzani, *Chem. Commun.*, 2007, 350-352; P. Sozzani, S. Bracco, A. Comotti, L. Ferretti and R. Simonutti, *Angew. Chem. Int. Ed.*, 2005, **44**, 1816-1820; P. Sozzani, A. Comotti, R. Simonutti, T. Meersmann, J. W. Logan and A. Pines, *Angew. Chem. Int. Ed.*, 2000, **39**, 2695-2699; H. R. Allcock, *Acc. Chem. Res.*, 1978, **11**, 81-87; H. R. Allcock and L. A. Siegel, *J. Am. Chem. Soc.*, 1964, **86**, 5140-5144.
5. K. J. Msayib, D. Book, P. M. Budd, N. Chaukura, K. D. M. Harris, M. Helliwell, S. Tedds, A. Walton, J. E. Warren, M. C. Xu and N. B. McKeown, *Angew Chem Int Edit*, 2009, **48**, 3273-3277.
6. J. D. Wuest, *Chem. Commun.*, 2005, 5830-5837; M. W. Hosseini, *Acc. Chem. Res.*, 2005, **38**, 313-323; M. W. Hosseini, *CrystEngComm*, 2004, **6**, 318-322; D. Su, X. Wang, M. Simard and J. D. Wuest, *Supramol. Chem.*, 1995, **6**, 171-178.
7. M. Mastalerz and I. M. Oppel, *Angew Chem Int Edit*, 2012, **51**, 5252-5255.
8. J. H. Fournier, T. Maris and J. D. Wuest, *J. Org. Chem.*, 2004, **69**, 1762-1775; E. Demers, T. Maris and J. D. Wuest, *Crystal Growth & Design*, 2005, **5**, 1227-1235.

9. T. H. Chen, I. Popov, W. Kaveevivitchai, Y. C. Chuang, Y. S. Chen, O. Daugulis, A. J. Jacobson and O. S. Miljanic, *Nat Commun*, 2014, **5**.
10. L. Turunen, F. F. Pan, N. K. Beyeh, M. Cetina, J. F. Trant, R. H. A. Ras and K. Rissanen, *CrystEngComm*, 2017, **19**, 5223-5229; L. Turunen, N. K. Beyeh, F. Pan, A. Valkonen and K. Rissanen, *Chem. Commun.*, 2014, **50**, 15920-15923; O. Dumele, B. Schreib, U. Warzok, N. Trapp, C. A. Schalley and F. Diederich, *Angew. Chem. Int. Ed.*, 2017, **56**, 1152-1157; J. Lieffrig, H. M. Yamamoto, T. Kusamoto, H. B. Cui, O. Jeannin, M. Fourmigue and R. Kato, *Cryst. Growth Des.*, 2011, **11**, 4267-4271.
11. C. F. Macrae, I. J. Bruno, J. A. Chisholm, P. R. Edgington, P. McCabe, E. Pidcock, L. Rodriguez-Monge, R. Taylor, J. van de Streek and P. A. Wood, *J. Appl. Crystallogr.*, 2008, **41**, 466-470.
12. L. J. Barbour, *Chem. Commun.*, 2006, **0**, 1163-1168.
13. I. Dance and M. Scudder, *CrystEngComm*, 2009, **11**, 2233-2247.
14. W. N. Moss and N. S. Goroff, *J. Org. Chem.*, 2005, **70**, 802-808.
15. P. Politzer, J. S. Murray and T. Clark, *PCCP*, 2010, **12**, 7748-7757.
16. W. Z. Guo, E. Galoppini, R. Gilardi, G. I. Rydja and Y. H. Chen, *Cryst. Growth Des.*, 2001, **1**, 231-237; R. Thaimattam, D. S. Reddy, F. Xue, T. C. W. Mak, A. Nangia and G. R. Desiraju, *New J. Chem.*, 1998, **22**, 143-148; D. S. Reddy, D. C. Craig and G. R. Desiraju, *J. Am. Chem. Soc.*, 1996, **118**, 4090-4093.

Chapter 5 - Diamondoid networks *via* halogen-bonding

5.1 Introduction

Crystalline solids with desirable structural features can be constructed with a significant degree of predictability as long as the participating tectons (i) are capable of retaining their required shapes and (ii) are "programmed" such that only the intended recognition event(s) can dominate their assembly.[1] Structurally divergent tectons tend to engender multidimensional architectures, and tetraphenylmethane (TPM) is an excellent platform for such building units because of its inherent tetrahedral/S_4-symmetric geometry (Figure 5.1 left).

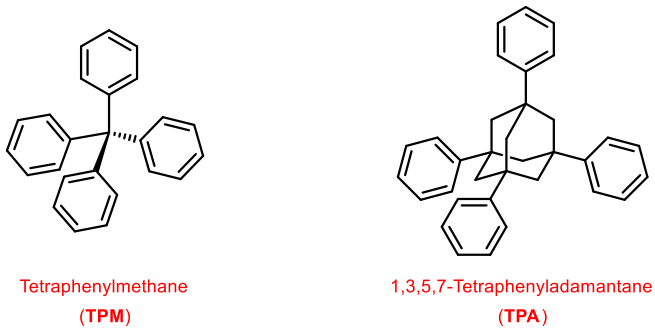

Figure 5.1 Structural formulas of tetraphenylmethane (TPM) and tetraphenyladamantane (TPA).

The TPM core can be derivatized (*e.g.* tetra-*para*-substitution) with a wide array of different functional groups suitable for metal-binding, dynamic covalent chemistry, hydrogen-bonding, *etc.* where all the attachment sites are naturally oriented towards the vertices of a tetrahedron.[2] It also presents other advantageous attributes such as high thermal stability and conformational rigidity. Furthermore, the bulky, windmill-like arrangement of the molecule often restricts it from efficient packing in the crystalline phase.[3] TPM derivatives are, therefore, well-suited for producing highly-symmetric, three-dimensional porous architectures, particularly 6^6

diamond-like (diamondoid, **dia**) networks.[4] Indeed, considerable efforts have been devoted to incorporating TPM-based tectons within metal-organic frameworks (MOFs),[5] covalent organic frameworks (COFs)[6,7] and hydrogen-bonded organic frameworks (HOFs).[8]

Another tetrahedral molecule which has generated a great deal of interest in the crystal engineering community is 1,3,5,7-tetraphenyladamantane (TPA) which holds four phenyl rings at the bridgehead positions of adamantane (Figure 5.1 right). TPA is isomorphous with TPM but has a slightly higher packing index (70.4 *versus* 69.9), probably because it is stabilized not only by C–H(phenyl)···π interactions but also by C–H(methylene)···π interactions.[9] The exceptionally high melting point (417–419 °C) and exceptionally low solubility of TPA may also be attributed to the concerted effects of those extensive C–H···π interactions. Thanks to the very strong resemblance between TPM and TPA nuclei, it has become common practice to use TPA counterparts as higher homologues/congeners of TPM-based modular units for isoreticular expansion of framework-type architectures, both MOFs and COFs.[7,10]

It has been shown that halogen bonding (XB) can be exploited in the deliberate synthesis of network structures, including **dia** nets.[11] Despite much activity in this area, only one XB-driven heteromeric system comprising a TPM-derived tecton (and none from TPA-derived tectons) has been reported to date.[12] We therefore set out to co-crystallize two tetravalent XB donors, tetrakis(4-(iodoethynyl)phenyl)methane (**I_4TEPM**) and 1,3,5,7-tetrakis(4-(iodoethynyl)phenyl)adamantane (**I_4TEPA**), with appropriate Lewis basic co-formers in order to realize multicomponent **dia** assemblies (Figure 5.2).

In this study, the real virtue of rigid, rod-like iodoethynyl arms, apart from their excellent XB donating capabilities,[13] is that they (i) greatly expand the original TPM/TPA scaffold without adding superfluous steric crowding or unwanted flexibility, and (ii) deliver fully accessible binding

sites. The increased size of XB-donating modules as a starting point is preferred because it allows the assembly of large **dia** nets, thereby opening the door to topologically more fascinating materials. Preserving the stiffness is crucial to suppress the formation of undesirable structural motifs which are possible with tetrahedral tectons.

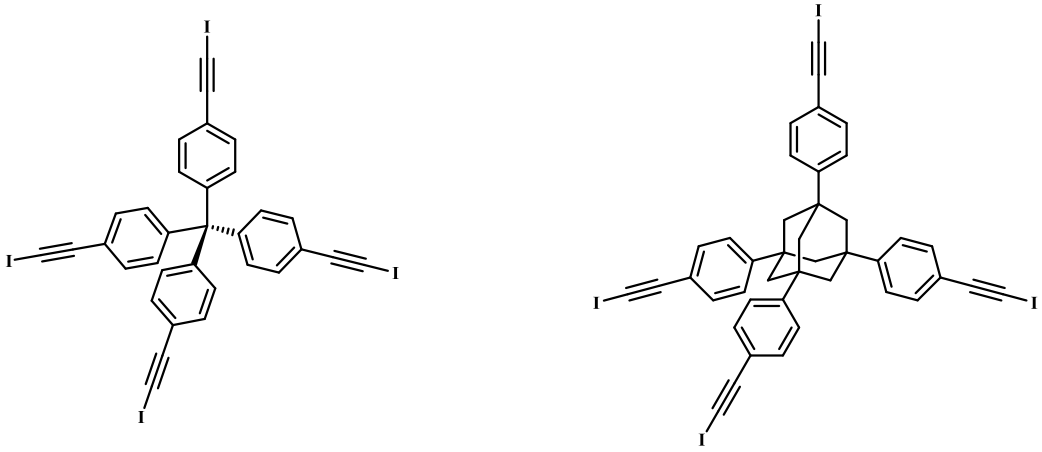

Tetrakis(4-(iodoethynyl)phenyl)methane
(**I_4TEPM**)

1,3,5,7-Tetrakis(4-(iodoethynyl)phenyl)adamantane
(**I_4TEPA**)

Figure 5.2 Two XB donating modules used in this study (see Chapter 4 for their synthesis and characterization).

Halide anions (chloride, bromide and iodide) were chosen as XB acceptors for **I_4TEPM** and **I_4TEPA** because their high charge concentrations will strengthen XB interactions (Figure 5.3). However, there is a real crystal engineering challenge associated with these electronically-saturated spherical entities as they hold little directional information. The flexibility of the coordination environment around the halide can lead to variable connectivities and hence, undesired structural outcomes. Fortunately, at the same time, they have the ability to ally their rich secondary valency with the co-crystallizing partner, and to undergo mutual-induced fitting of the actual bonding mode/topicity.[14] Such induced-binding phenomena and restricted coordination

profiles of halide anions, derived from a balance between the molecular structure of the interacting partners and general entropic reasons, are prominent in previous studies on multi-iodoethynyl species (Figure 5.4). It is, therefore, hypothesized that the tetrahedral, tetratopic **I$_4$TEPM**/**I$_4$TEPA** plus the directional XB linkages urge four-coordination on the halides, thereby ensuring the formation of **dia** frameworks (Figure 5.5).

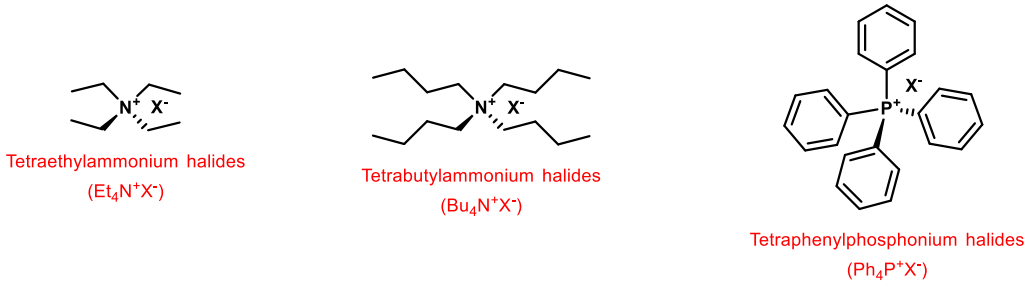

Figure 5.3 Halide salts used in this study (X^- = Cl^-, Br^-, I^-).

5.2 Experimental

5.2.1 Materials and methods

All the reagents, solvents, halide salts and tetraphenylmethane were purchased from commercial sources, and were used as received without further purification. Nuclear magnetic resonance spectra were recorded on a Varian Unity Plus (400 MHz) NMR spectrometer. A Nicolet 380 FT-IR system was used for the infrared spectroscopic analysis. Differential scanning calorimetry (DSC) and thermogravimetric analysis (TGA) were performed on TA Instruments TA Q20 and TA Q50, respectively.

5.2.2 Synthesis of I$_4$TEPM·[Et$_4$N]Cl (2:3) complex

In a 2-dram glass vial with a screw cap, **I$_4$TEPM** (10 mg, 0.011 mmol, 1 equiv.) was dissolved in 0.5 mL of tetrahydrofuran. Then, [Et$_4$N]Cl (8.0 mg, 0.044 mmol, 4 equiv.) in 0.5 mL of methanol

was added and the partially-tightened vial was left undisturbed at ambient conditions to allow the solvents to evaporate slowly. Colorless/pale-yellow crystals were observed after few days.

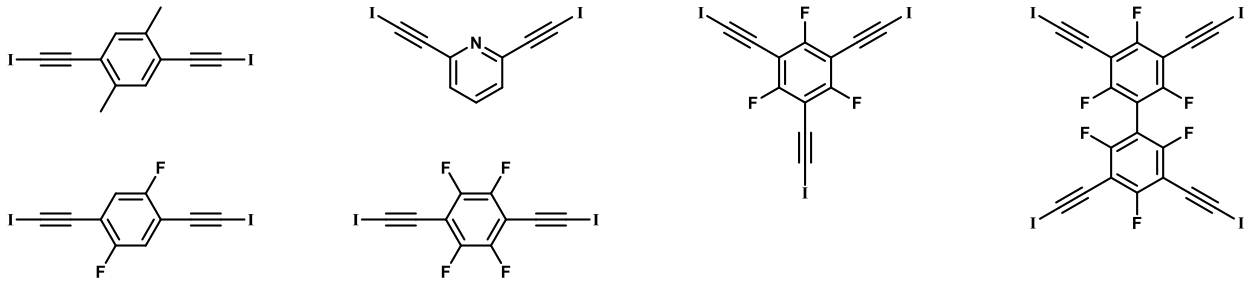

Figure 5.4 Iodoethynyl species successfully co-crystallized with halide ions.

5.2.3 Synthesis of I_4TEPM·[Et_4N]Br·THF (1:1:1) complex

In a 2-dram glass vial with a screw cap, **I_4TEPM** (10 mg, 0.011 mmol, 1 equiv.) was dissolved in 0.5 mL of tetrahydrofuran. Then, [Et_4N]Br (9.1 mg, 0.044 mmol, 4 equiv.) in 0.5 mL of methanol was added and the partially-tightened vial was left undisturbed at ambient conditions to allow the solvents to evaporate slowly. Colorless/pale-yellow crystals were observed after few days.

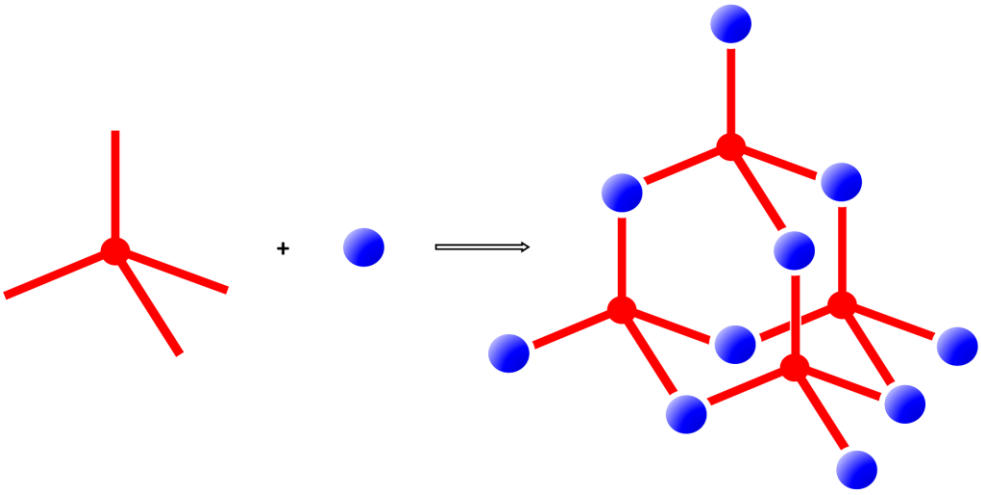

Figure 5.5 Schematic showing the formation of diamond-like skeleton from tetrahedrally-shaped XB donor and spherically-shaped halide ion.

5.2.4 Synthesis of I_4TEPM·[Et_4N]Br (1:1) complex

In a 2-dram glass vial with a screw cap, **I_4TEPM** (10 mg, 0.011 mmol, 1 equiv.) was dissolved in 0.5 mL of chloroform. Then, [Et_4N]Br (9.1 mg, 0.044 mmol, 4 equiv.) in 0.5 mL of methanol was added and the partially-tightened vial was left undisturbed at ambient conditions to allow the solvents to evaporate slowly. Colorless/pale-yellow crystals were observed after few days.

5.2.5 Synthesis of I_4TEPM·[Bu_4N]Cl (1:1) complex

Yellow color crystals were harvested in few days by following the same procedure stated above for **I_4TEPM**·[Et_4N]Br (1:1) complex, but using [Bu_4N]Cl (12.1 mg, 0.044 mmol, 4 equiv.) as the halide source.

5.2.6 Synthesis of I_4TEPM·[Bu_4N]Br (1:1) complex

Yellow color crystals were harvested in few days by following the same procedure stated above for **I_4TEPM**·[Et_4N]Br (1:1) complex, but using [Bu_4N]Br (14.0 mg, 0.044 mmol, 4 equiv.) as the halide source.

5.2.7 Synthesis of I_4TEPA·[Et_4N]I (3:2) complex

In a 2-dram glass vial with a screw cap, **I_4TEPA** (11.3 mg, 0.011 mmol, 1 equiv.) was dissolved in 1 mL of chloroform. Then, [Et_4N]I (11.2 mg, 0.044 mmol, 4 equiv.) in 0.5 mL of methanol was added and the partially-tightened vial was left undisturbed at ambient conditions to allow the solvents to evaporate slowly. Red/orange crystals were observed after 24 hours.

5.2.8 Synthesis of I_4TEPA·[Bu_4N]I (1:1) complex

Yellow/orange crystals were harvested within few hours by following the same procedure stated above for **I_4TEPA**·[Et_4N]I (3:2) complex, but using [Bu_4N]I (16.1 mg, 0.044 mmol, 4 equiv.) as the halide source.

5.2.9 Synthesis of I_4TEPM·[Ph_4P]Cl (1:1) complex

In a 2-dram glass vial with a screw cap, **I_4TEPM** (10 mg, 0.011 mmol, 1 equiv.) was dissolved in 0.5 mL of chloroform. Then, [Ph_4P]Cl (4.1 mg, 0.011 mmol, 1 equiv.) in 0.5 mL of methanol was carefully added on top, with minimal agitation to prevent the product from crashing out at the interface. The vial was sealed and left undisturbed at ambient conditions to allow the two solutions to diffuse together slowly. Yellowish orange crystals suitable for single-crystal X-ray diffraction were observed after two days. Decomposition temperature: 235–250 °C.

5.2.10 Synthesis of I_4TEPM·[Ph_4P]Br (1:1) complex

Our initial attempt of preparing single-crystals of title compound in the same way as **I_4TEPM**·[Ph_4P]Cl was failed due to instant product precipitation. Therefore, both starting solutions were subjected to two-fold dilution, and an intermediate buffer layer of methanol was placed between them to further decelerate their mixing. In a 2-dram glass vial with a screw cap, **I_4TEPM** (10 mg, 0.011 mmol, 1 equiv.) was dissolved in 1 mL of chloroform. After careful layering of 10 drops of neat methanol, [Ph_4P]Br (4.6 mg, 0.011 mmol, 1 equiv.) in 1 mL of methanol was slowly added on top without disturbing the interface. The vial was then sealed and allowed to stand at room temperature. Yellowish orange crystals suitable for single-crystal X-ray diffraction were appeared in 24 hours. Decomposition temperature: 230–250 °C.

5.2.11 Synthesis of I_4TEPM·[Ph_4P]I (1:1) complex

Yellowish orange crystals suitable for single-crystal X-ray diffraction were obtained within 10 hours by following the same solution layering (reactant diffusion) technique mentioned above for **I_4TEPM**·[Ph_4P]Br, but using an equimolar amount of [Ph_4P]I (5.1 mg, 0.011 mmol, 1 equiv.) as the halide salt. Decomposition temperature: 220–230 °C.

5.2.12 Powder X-ray diffraction

Experiments were performed on a Philips PW 1850 diffractometer, CuKα radiation, 40 kV voltage, and 40 mA current. The patterns were collected in the region of 5°–40° (2θ) with a step size of 0.02°, and 2.0 s counting per step for **I$_4$TEPM**·[Ph$_4$P]I and **I$_4$TEPM**·[Ph$_4$P]Br, and 6.0 s counting per step for **I$_4$TEPM**·[Ph$_4$P]Cl.

5.2.13 Single-crystal X-ray crystallography

Detailed crystallographic information about the data collections, solutions and refinements can be found in the Appendix D. Underlying topologies of the crystal structures were determined with ToposPro.[15] Structural images were generated using Mercury,[16] Olex2[17] and ToposPro.[15]

5.3 Results and discussion

Our initial attempts at constructing **dia** assemblies from **I$_4$TEPM** and **I$_4$TEPA** focused on the use of tetraalkyl ammonium halides as structural partners. Even though they did result in binary solid complexes (confirmed by NMR screening, see Appendix D), the necessary structural analysis was not possible due to their very poor crystallinity and stability. We surmised that this lack of stability had its origin in the structural flexibility of the countercations used. Since both XB donors possess elongated struts, the elementary units (*i.e.* the adamantane-like cages) of the ensuing **dia** nets would contain substantially larger voids. Tetraethylammonium and tetrabutylammonium cations are structurally "soft" which means that, even if they are capable of filling those cavities reasonably well, they may not be able to structurally support the remainder of the architecture.

We then decided to move our attention to tetraphenylphosphonium halides because, in terms of size, symmetry and shape persistency, the tetraphenylphosphonium cation would be a perfect fit with tetrahedral XB donating building blocks. Our hypotheses turned out to be accurate

because, when combined with **I$_4$TEPM**, each phosphonium salt readily produced stable and high-quality crystals. Their heteromeric nature was first established from preliminary FT-IR data, and a noticeable (> 9 cm^{-1}) red-shift of the C≡C triple-bond stretching band provided evidence for the occurrence of the intended XB interaction.[18] Subsequent ^{1}H NMR analysis suggested that all three complexes have a 1:1 stoichiometric ratio between **I$_4$TEPM** and the corresponding halide salt. According to DSC and TGA studies, they are endowed with decent thermal stabilities; no transitions or decompositions were observed below 200 °C (Figure 5.6).

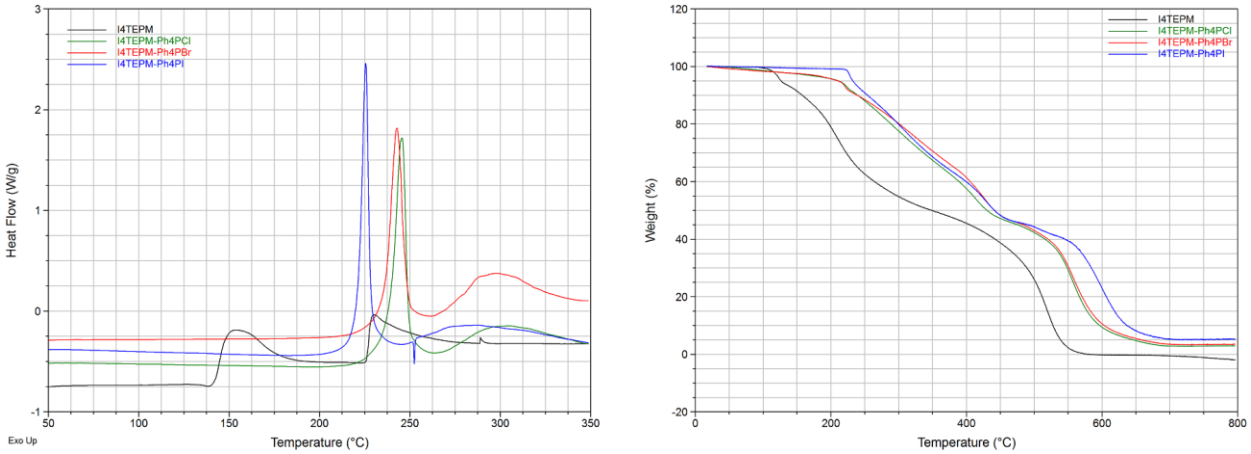

Figure 5.6 (left) DSC traces (Tzero aluminum pan, 1–2 mg sample size, 5 °C·min^{-1} heating rate, nitrogen atmosphere) and (right) TGA traces (platinum pan, 5–10 mg sample size, 10 °C·min^{-1} heating rate, nitrogen atmosphere).

The single-crystal X-ray crystallographic examination revealed that all three are isostructural and crystallize in a monoclinic system in the *I2/a* space group. They have a general formula of **I$_4$TEPM**·[Ph$_4$P]X (X = Cl, Br or I). **I$_4$TEPM** molecules are "coordinatively" saturated (*i.e.* all four donor sites are engaged in halogen-bonding) and function as tetra-directional linkers. As anticipated, the halide ions mimic both the topicity and the relative arrangement of XBs around **I$_4$TEPM**, and devise four-connecting tetrahedral nodes, thereby giving rise to the desired infinite

diamondoid architectures (Figure 5.7). Powder X-ray diffraction (PXRD) experiments showed a good agreement between measured diffraction patterns and those simulated from the corresponding single-crystal data, demonstrating the phase purities of the bulk solids (see Figure 5.8 and Appendix D).

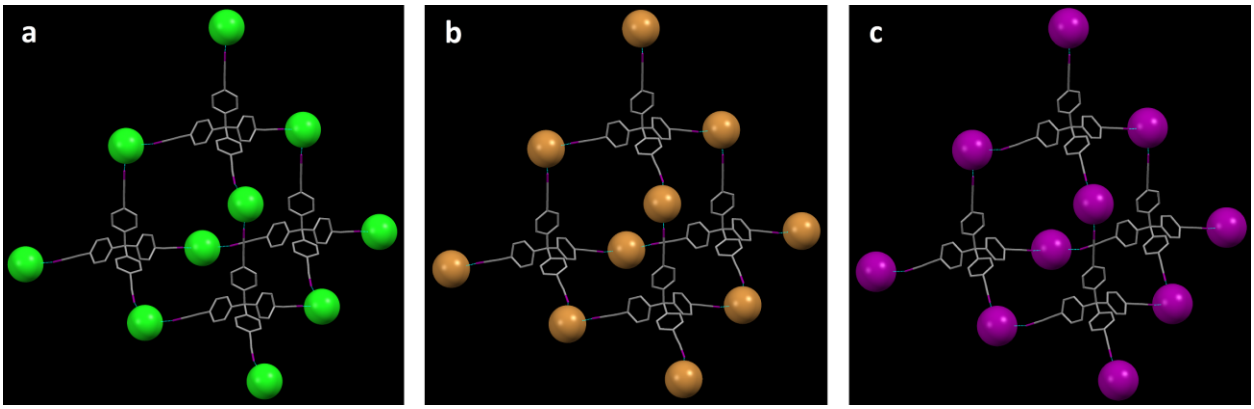

Figure 5.7 Structure of a) **I4TEPM**·[Ph4P]Cl, b) **I4TEPM**·[Ph4P]Br and c) **I4TEPM**·[Ph4P]I, emphasizing their diamondoid nature (hydrogen atoms and tetraphenylphosphonium cations have been omitted for clarity).

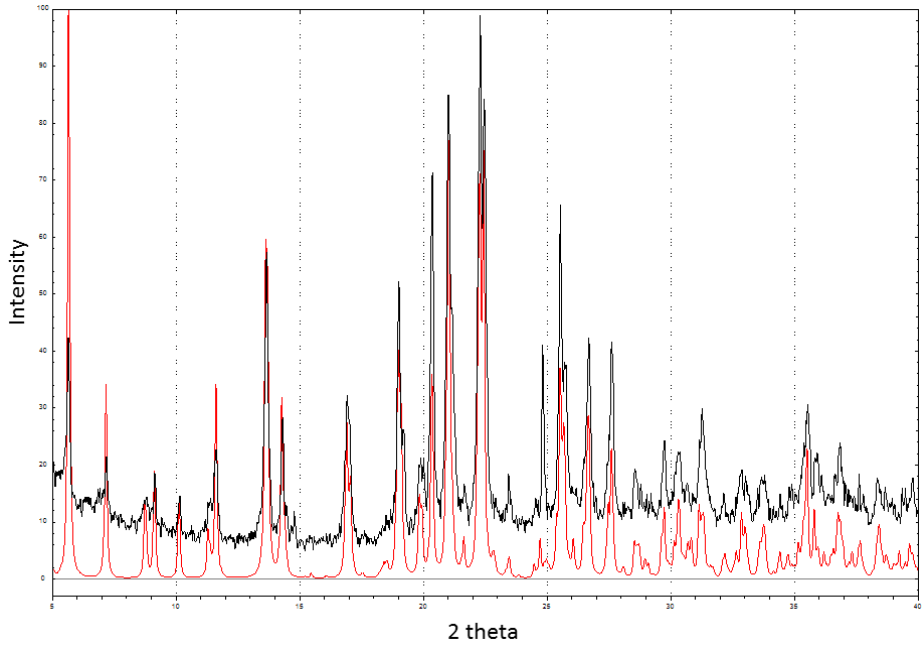

Figure 5.8 PXRD pattern of **I4TEPM**·[Ph4P]I (top - experimental, bottom - simulated).

Although each halide ion displays the same connectivity pattern, they show slight variations in I···X^- distances and I···X^-···I angles, even within the same structure. On account of this, the tetrahedral coordination geometry around halides is slightly distorted (Figure 5.9). Over the entire series, the C–I···X^- angles span from 165.7° to 177.5°, most of them being greater than 175°. And the normalized I···X^- distances fall within the range of 0.808–0.837, corresponding to 16.3–19.2% radii reduction (tabulated XB geometries can be found in Appendix D). These characteristics reflect moderately strong XB bonds.

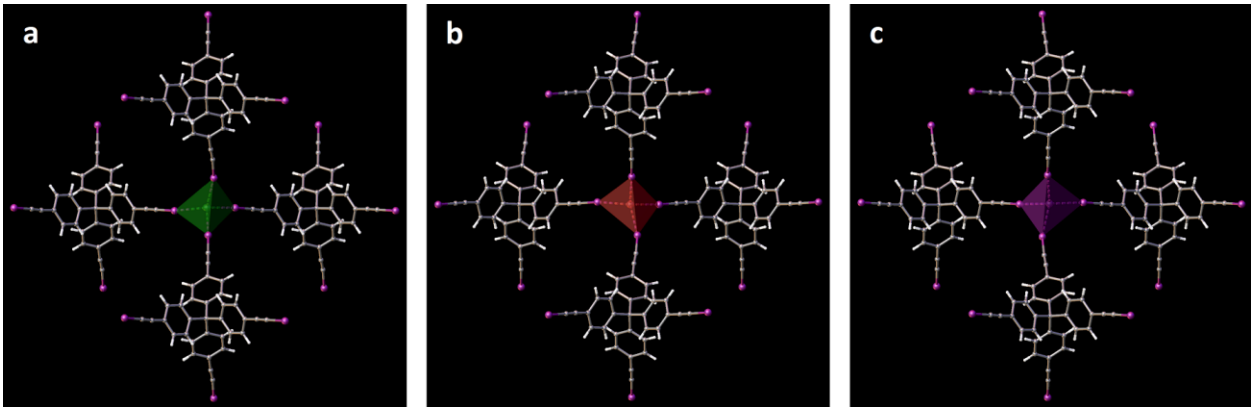

Figure 5.9 Coordination environment around a) chloride, b) bromide and c) iodide.

Even though, from a purely electrostatic point of view, the tendency to form strong interactions should decrease in the order $Cl^- > Br^- > I^-$, no such discrimination can be observed here. Indeed, they follow the opposite trend (in terms of the mean normalized contact), indicating the presence of other binding components such as charge-transfer contributions (Figure 5.10).

We also performed a CSD search in order to extract information about all reported iodoethynyl/halide halogen-bonds. The results are graphically represented in Figure 5.11, along with the twelve new data points we obtained in this work. Even though there is no obvious

correlation between the normalized distance and the angle, approximately 80% of them have angles greater than 170°, reaffirming XBs tendency towards linearity.

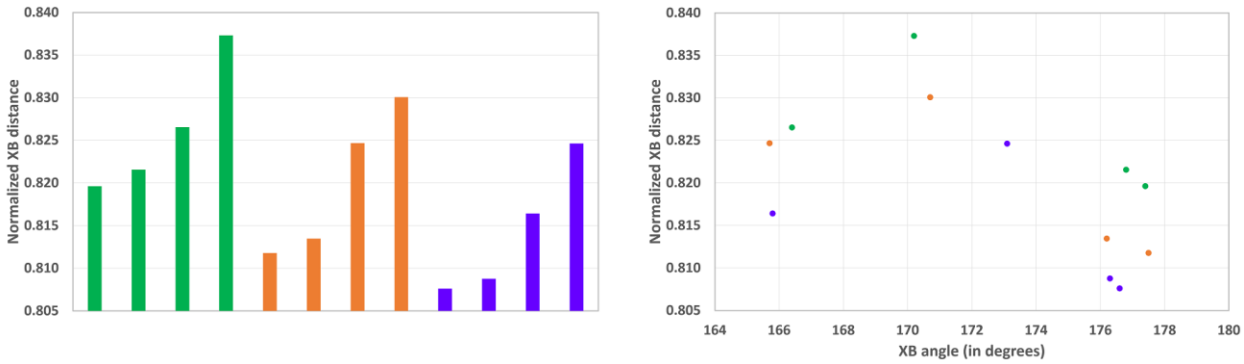

Figure 5.10 Varying of normalized XB lengths (left) across the three structures and (right) against the XB angles. In both graphical representations, different colors have been used to distinguish halide ions (chloride - green, bromide - orange and iodide - violet).

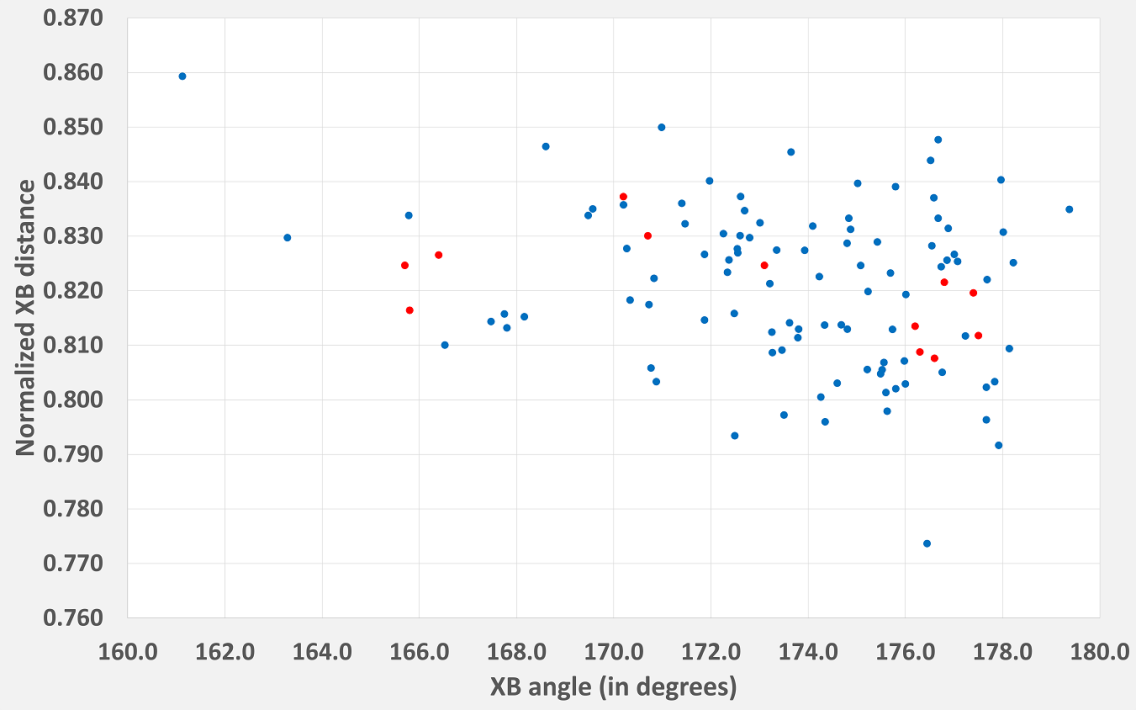

Figure 5.11 Normalized XB lengths of iodoethynyl/halide systems against their angles. Red circles represent data from this study, blue circles correspond to relevant data from CSD interrogation.

With **I$_4$TEPM** as the organic linker and negatively-charged halide as the node-forming component, these halogen-bonded anion-organic frameworks nicely conform to the node-and-linker principle which is popular in the field of MOFs. Figure 5.12 shows the propagation of the three-periodic **I$_4$TEPM**/chloride network when viewed down the crystallographic *b* axis. As can be seen, the overall structure contains four sub-lattices which are entangled to one another. This four-fold interpenetration (Z = 4) is true for the remaining two compounds as well, and belongs to class IIb.[19]

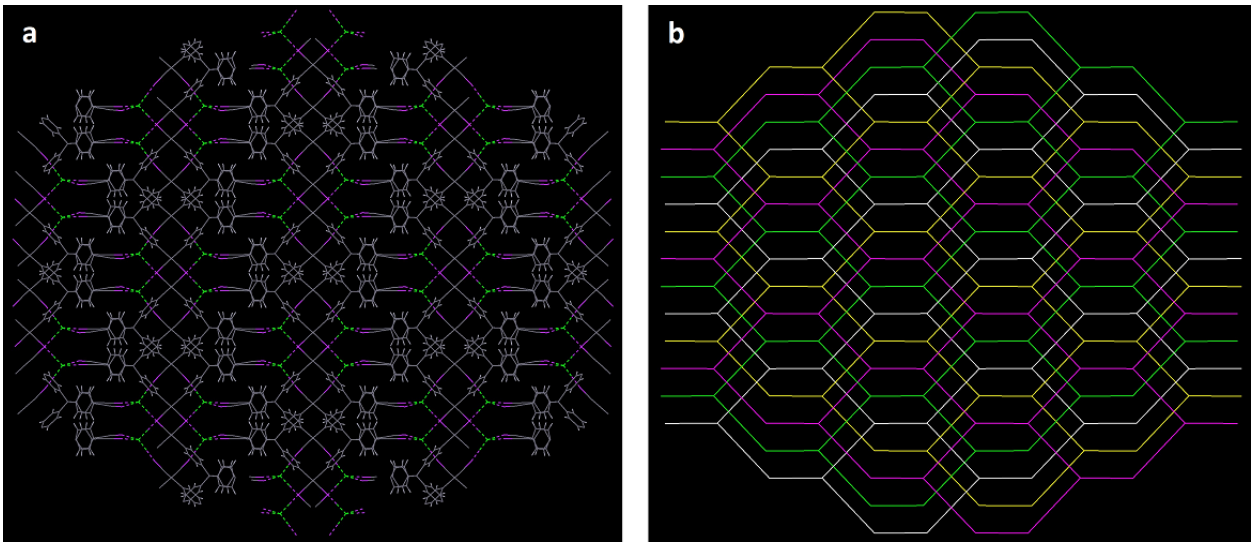

Figure 5.12 a) View down the *b* axis of **I$_4$TEPM**·[Ph$_4$P]Cl (associated tetraphenylphosphonium cations have been omitted for clarity); b) its simplified version.

At first look, the charge-balancing Ph_4P^+ cation seems to be a structurally innocent bystander entrapped within the independently formed anion-organic framework. However, it not only imposes constraints on the level of interpenetration but also boosts the mechanical strength of the lattice by effectively filling up the empty space. Indeed, with the inclusion of sterically demanding Ph_4P^+ cations, these interpenetrated halide-based networks result in a compact

arrangement which scarcely retains any conventional/usable porosity (Figure 5.13).[20] Moreover, the cation···anion attractive forces (which are absent in molecular co-crystals) impart extra stability to these structures.

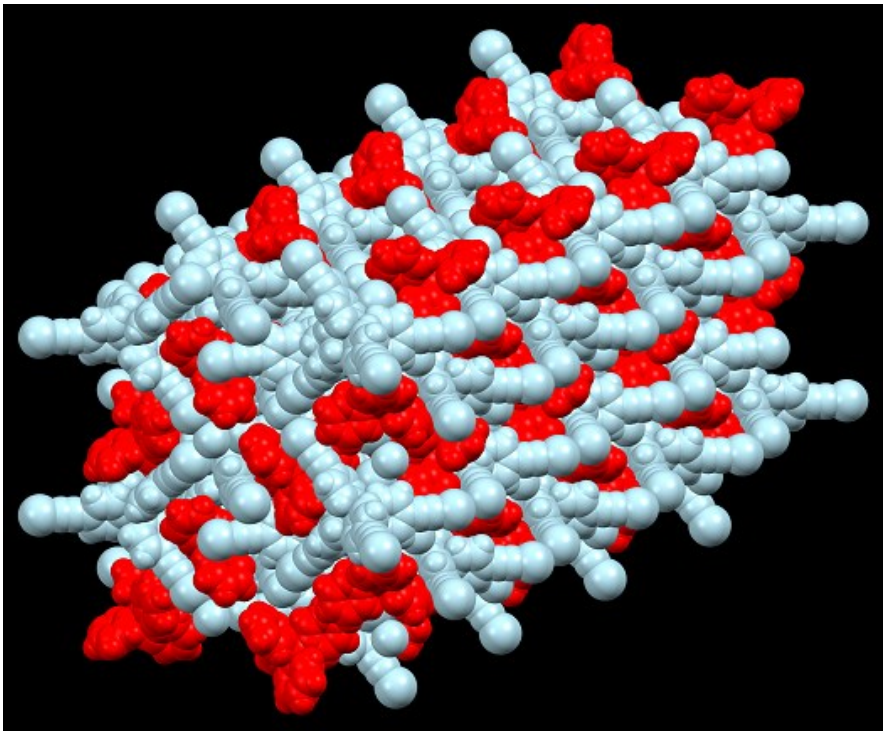

Figure 5.13 Close-packing achieved *via* interpenetration and cation enclathration (indicated in red are Ph_4P^+ cations).

A close inspection of the immediate vicinity of Ph_4P^+ cations reveals that each of them is surrounded by four **I$_4$TEPM** molecules, and *vice versa* (Figure 5.14). In other words, the cation brings together and organizes the assembly of **I$_4$TEPM** molecules around itself and guides their linking pattern in a way that leads to the observed topology, presumably with the aid of phenyl embraces.[21]

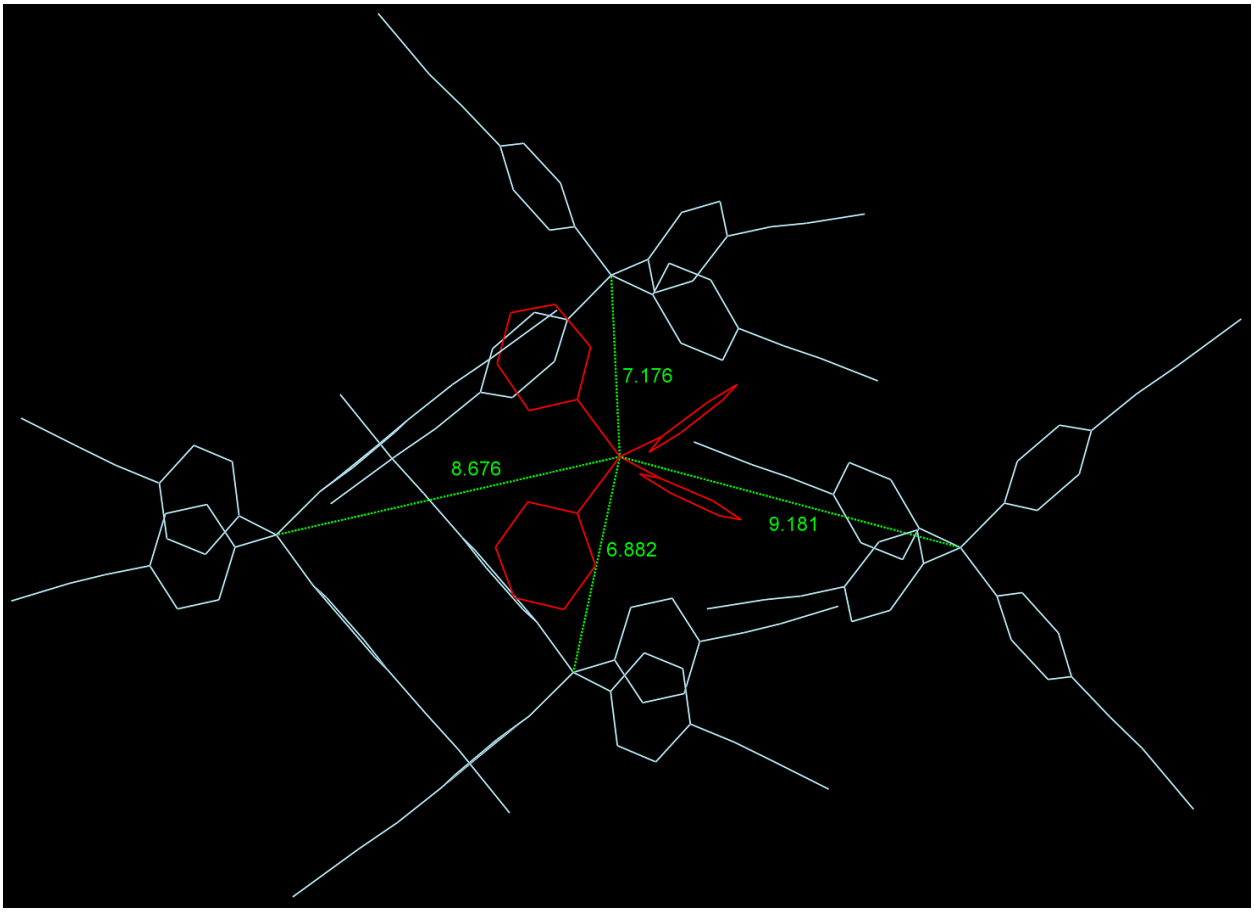

Figure 5.14 Tetraphenylphosphonium cation (red) and its nearest **I$_4$TEPM** neighbors.

In order to further verify and support this assertion, we tried to acquire at least some preliminary structural details of those "unstable" co-crystals prepared from tetraalkyl ammonium halides. Luckily, we were able to disclose the primary halogen-bonding interactions and the underlying net topology displayed by the **I$_4$TEPM**·[Bu$_4$N]Br system. The most peculiar difference in this structure is that bromide anions assume a four-connected square-planar arrangement and assemble a $4^2.8^4$ PtS-like (**pts**) net instead of a 6^6 **dia** net (Figure 5.15). In other words, the **I$_4$TEPM**/bromide dyad fails to build a diamondoid architecture when the counterion is tetrabutylammonium. Thus, it is clear that the cation has a profound impact on the final structural

outcome and the tetraphenylphosphonium cation serves as a template for the facile (and exclusive) synthesis and enhanced crystallizability of **dia** assemblies from **I$_4$TEPM** and halide ions.

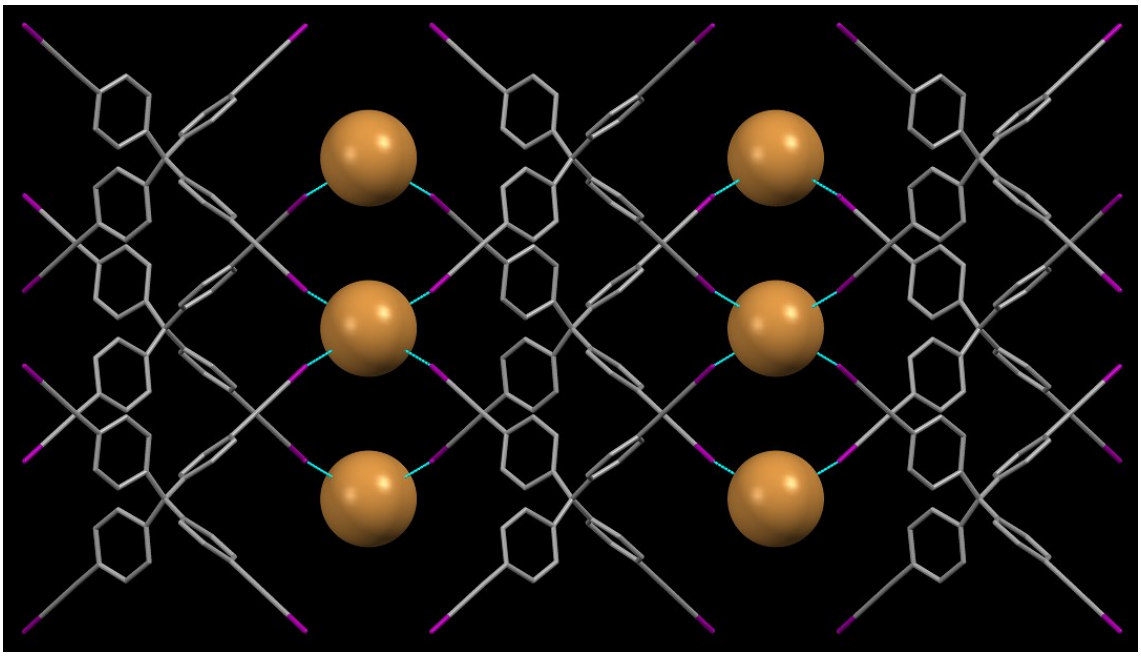

Figure 5.15 Preliminary structure of **I$_4$TEPM**·[Bu$_4$N]Br, highlighing the four-connected square-planar bromide nodes.

5.4 Conclusions

In summary, two tetrahedral tetratopic halogen-bond (XB) donors, tetrakis(4-(iodoethynyl)phenyl)methane, (**I$_4$TEPM**) and 1,3,5,7-tetrakis(4-(iodoethynyl)phenyl)adamantane (**I$_4$TEPA**) were subjected to a series of co-crystallization experiments with different halide salts. With tetraphenylphosphonium halide salts ([Ph$_4$P]X; X = Cl, Br, I), **I$_4$TEPM** readily yields robust diamondoid (**dia**) frameworks, where the assembly process is primarily governed by C–I···X$^-$ interactions.

The halide anions exhibit mutual-induced tetracoordination and provide four-connected tetrahedral nodes. This preferential tetra-coordinate behavior of halide anions is due to the balance

between the nature of the XB donor (number of donor sites/valency, the spatial arrangement of the donor sites, *etc.*), the inherent coordination profile of halide anions themselves, and the nature of the associated cation. The role of the charge-balancing Ph_4P^+ ions is multifaceted; they (i) hold templating information for the exclusive formation of quadruply interpenetrated **dia** nets, (ii) support structural integrity by residing in the void space, and (iii) add a stabilizing Coulombic term to the lattice energy.

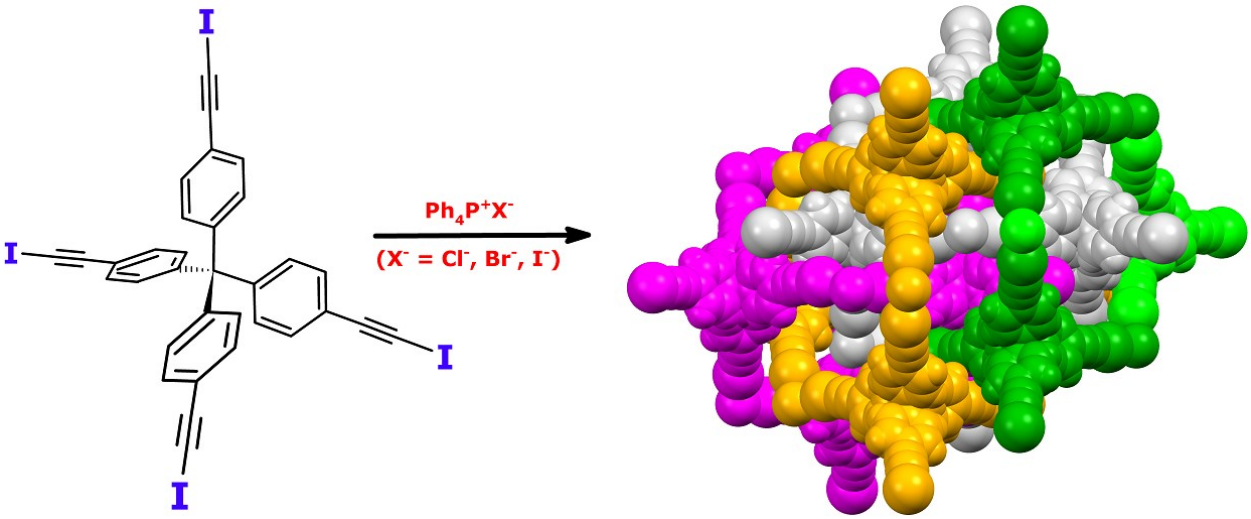

Figure 5.16 Explicit assembly of halide ions and tetraiodoethynyl-featured tetraphenylmethane into four-fold interpenetrated diamond-like networks in the presence of tetraphenylphosphonium cations.

We are currently exploring avenues for utilizing this XB-driven modular approach to fabricate permanently porous materials, by combining **I4TEPM** and **I4TEPA** with a variety of charge-neutral co-formers. As pointed out in Chapter 4, these tetravalent XB donors readily react with coordinating solvents, even though the resultant solids are prone to collapse upon guest solvent removal. It is therefore rational to think that they would offer relatively more stable binary systems if the co-formers employed are solids at ambient conditions. Few potential candidates are

shown in Figure 5.17. So far, the results look very promising and, by reacting **I$_4$TEPM** and tetraazaadamantane, we were able to produce a microcrystalline solid with the expected 1:1 composition (see Appendix D). We also synthesized tetrakis(4-pyridyl)cyclobutane through resorcinol-templated topochemical [2+2] photodimerization of bis(4-pyridyl)ethylene.

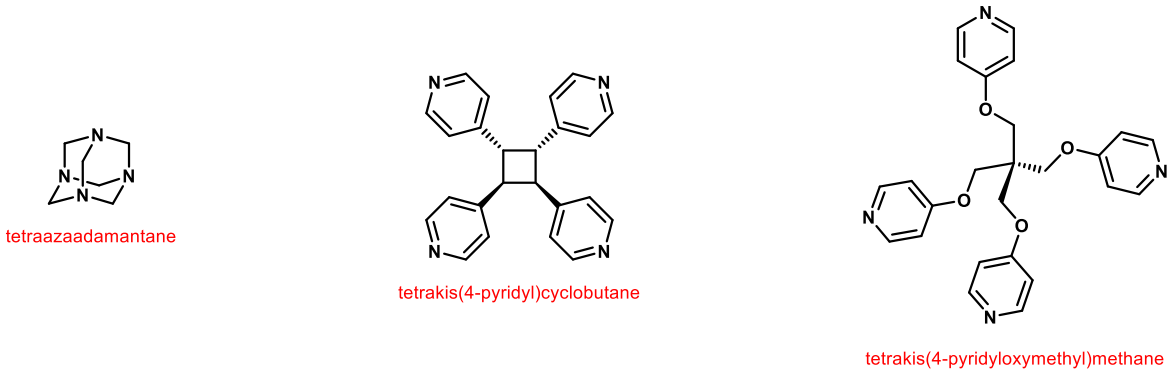

Figure 5.17 Neutral co-formers with tetrahedrally-disposed XB accepting sites.

5.5 References

1. J. D. Wuest, *Chem. Commun.*, 2005, **0**, 5830-5837; M. W. Hosseini, *CrystEngComm*, 2004, **6**, 318-322.
2. O. Plietzsch, C. I. Schilling, M. Tolev, M. Nieger, C. Richert, T. Muller and S. Brase, *Org. Biomol. Chem.*, 2009, **7**, 4734-4743; C. I. Schilling, O. Plietzsch, M. Nieger, T. Muller and S. Brase, *Eur. J. Org. Chem.*, 2011, 1743-1754; J. H. Fournier, X. Wang and J. D. Wuest, *Can. J. Chem.*, 2003, **81**, 376-380; T. Muller and S. Brase, *RSC Adv.*, 2014, **4**, 6886-6907.
3. O. Knop, K. N. Rankin, T. S. Cameron and R. J. Boyd, *Can. J. Chem.*, 2002, **80**, 1351-1366.
4. B. F. Hoskins and R. Robson, *J. Am. Chem. Soc.*, 1990, **112**, 1546-1554; B. F. Hoskins and R. Robson, *J. Am. Chem. Soc.*, 1989, **111**, 5962-5964.
5. D. M. Liu, Z. G. Xie, L. Q. Ma and W. B. Lin, *Inorg. Chem.*, 2010, **49**, 9107-9109; X. Zhang, X. Zhang, J. A. Johnson, Y. S. Chen and J. Zhang, *J. Am. Chem. Soc.*, 2016, **138**, 8380-8383; I. Boldog, K. Domasevitch, J. K. Maclaren, C. Heering, G. Makhloufi and C. Janiak, *CrystEngComm*, 2014, **16**, 148-151; C. B. Caputo, V. N. Vukotic, N. M. Sirizzotti and S. J. Loeb, *Chem. Commun.*, 2011, **47**, 8545-8547.
6. F. J. Uribe-Romo, J. R. Hunt, H. Furukawa, C. Klock, M. O'Keeffe and O. M. Yaghi, *J. Am. Chem. Soc.*, 2009, **131**, 4570-4571; H. M. El-Kaderi, J. R. Hunt, J. L. Mendoza-Cortes, A. P. Cote, R. E. Taylor, M. O'Keeffe and O. M. Yaghi, *Science*, 2007, **316**, 268-272.
7. D. Beaudoin, T. Maris and J. D. Wuest, *Nat. Chem.*, 2013, **5**, 830-834.

8. Y. B. He, S. C. Xiang and B. L. Chen, *J. Am. Chem. Soc.*, 2011, **133**, 14570-14573; P. Li, Y. B. He, H. D. Arman, R. Krishna, H. L. Wang, L. H. Weng and B. L. Chen, *Chem. Commun.*, 2014, **50**, 13081-13084; E. Le Fur, E. Demers, T. Maris and J. D. Wuest, *Chem. Commun.*, 2003, **0**, 2966-2967.
9. I. Boldog, A. B. Lysenko, E. B. Rusanov, A. N. Chernega and K. V. Domasevitch, *Acta Crystallogr C*, 2009, **65**, O248-O252.
10. N. C. Duncan, B. P. Hay, E. W. Hagaman and R. Custelcean, *Tetrahedron*, 2012, **68**, 53-64.
11. P. Metrangolo, F. Meyer, T. Pilati, D. M. Proserpio and G. Resnati, *Chem. Eur. J.*, 2007, **13**, 5765-5772; S. V. Lindeman, J. Hecht and J. K. Kochi, *J. Am. Chem. Soc.*, 2003, **125**, 11597-11606; D. S. Reddy, D. C. Craig, A. D. Rae and G. R. Desiraju, *J. Chem. Soc., Chem. Commun.*, 1993, **0**, 1737-1739.
12. S. Shankar, O. Chovnik, L. J. W. Shimon, M. Lahav and M. E. van der Boom, *Crystal Growth & Design*, 2018, **18**, 1967-1977.
13. C. B. Aakeröy, M. Baldrighi, J. Desper, P. Metrangolo and G. Resnati, *Chem. Eur. J.*, 2013, **19**, 16240-16247.
14. P. Metrangolo, F. Meyer, T. Pilati, G. Resnati and G. Terraneo, *Chem. Commun.*, 2008, **0**, 1635-1637; P. M. J. Szell, B. Gabidullin and D. L. Bryce, *Acta Cryst.*, 2017, **B73**, 153-162; D. E. Barry, C. S. Hawes, S. Blasco and T. Gunnlaugsson, *Cryst. Growth Des.*, 2016, **16**, 5194-5205; S. H. Jungbauer, S. Schindler, E. Herdtweck, S. Keller and S. M. Huber, *Chem. Eur. J.*, 2015, **21**, 13625-13636; M. C. Pfrunder, A. S. Micallef, L. Rintoul, D. P. Arnold, K. J. P. Davy and J. McMurtrie, *Cryst. Growth Des.*, 2014, **14**, 6041-6047; J. Lieffrig, O. Jeannin and M. Fourmigue, *J. Am. Chem. Soc.*, 2013, **135**, 6200-6210.
15. V. A. Blatov, A. P. Shevchenko and D. M. Proserpio, *Crystal Growth & Design*, 2014, **14**, 3576-3586.
16. C. F. Macrae, I. J. Bruno, J. A. Chisholm, P. R. Edgington, P. McCabe, E. Pidcock, L. Rodriguez-Monge, R. Taylor, J. van de Streek and P. A. Wood, *J. Appl. Crystallogr.*, 2008, **41**, 466-470.
17. O. V. Dolomanov, L. J. Bourhis, R. J. Gildea, J. A. K. Howard and H. Puschmann, *J. Appl. Crystallogr.*, 2009, **42**, 339-341.
18. C. W. Wang, D. Danovich, S. Shaik and Y. R. Mo, *J. Chem. Theory Comput.*, 2017, **13**, 1626-1637.
19. I. A. Baburin, V. A. Blatov, L. Carlucci, G. Ciani and D. M. Proserpio, *J. Solid State Chem.*, 2005, **178**, 2452-2474.
20. L. J. Barbour, *Chem. Commun.*, 2006, **0**, 1163-1168.
21. I. Dance and M. Scudder, *CrystEngComm*, 2009, **11**, 2233-2247.

Appendix A - Additional material for Chapter 2

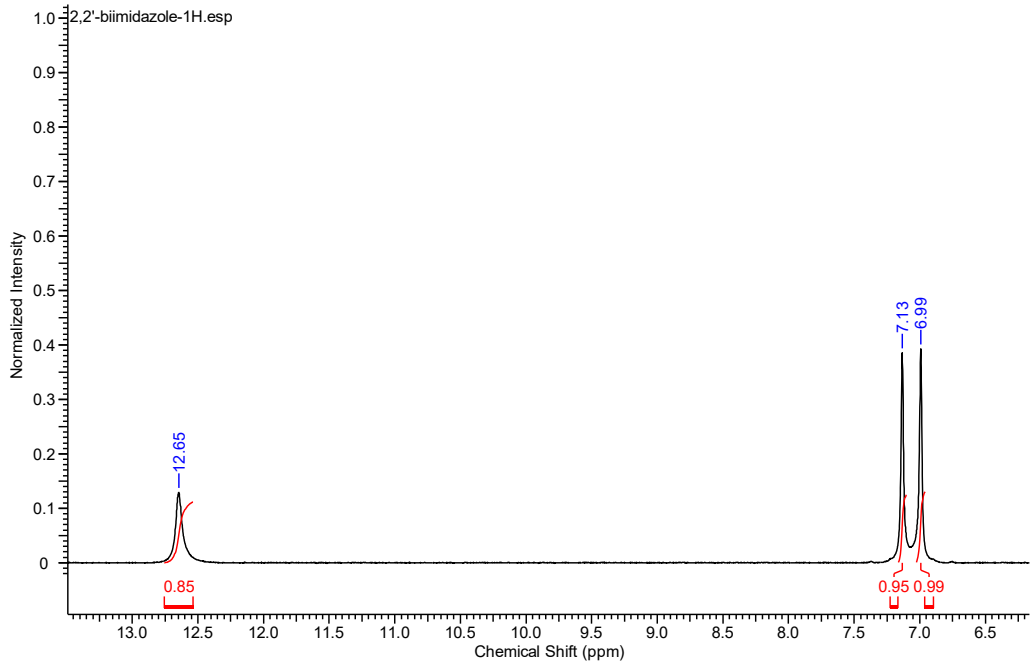

Figure A. 1 ^{1}H-NMR (400 MHz, DMSO-d6) spectrum of 2,2'-biimidazole.

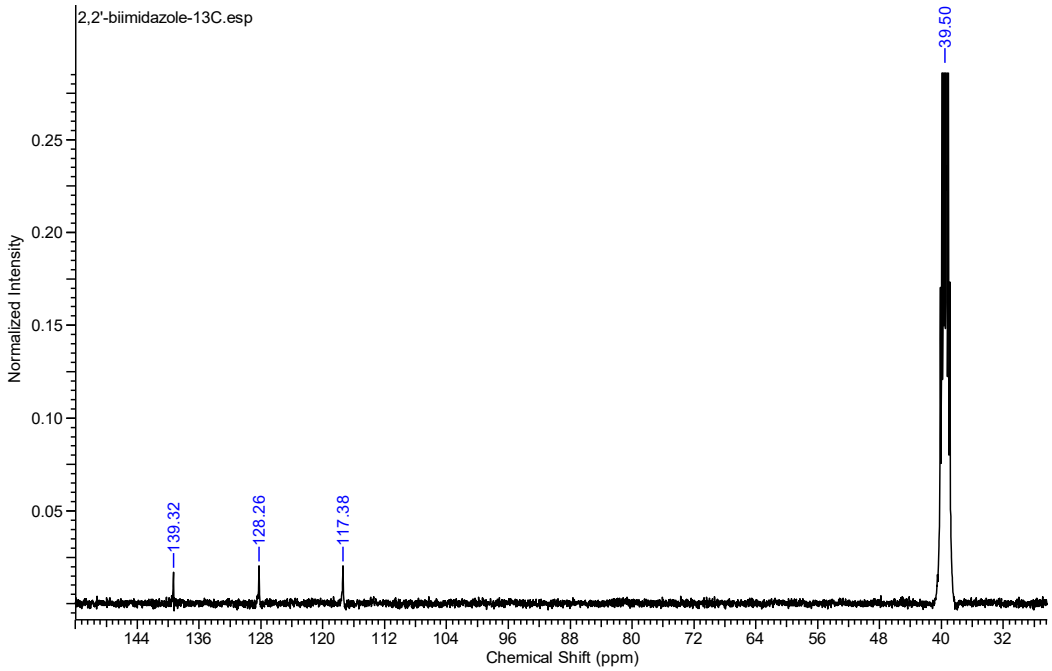

Figure A. 2 ^{13}C-NMR (100 MHz, DMSO-d6) spectrum of 2,2'-biimidazole.

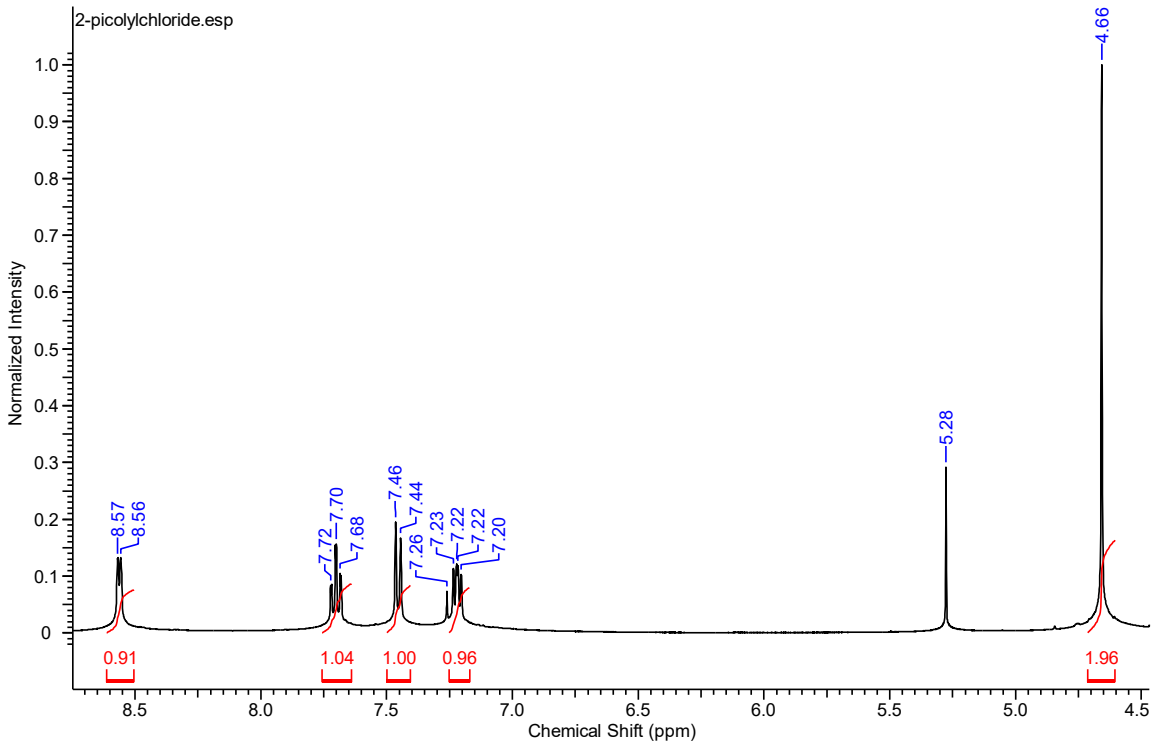

Figure A. 3 ^{1}H-NMR (400 MHz, $CDCl_3$) spectrum of 2-(chloromethyl)pyridine.

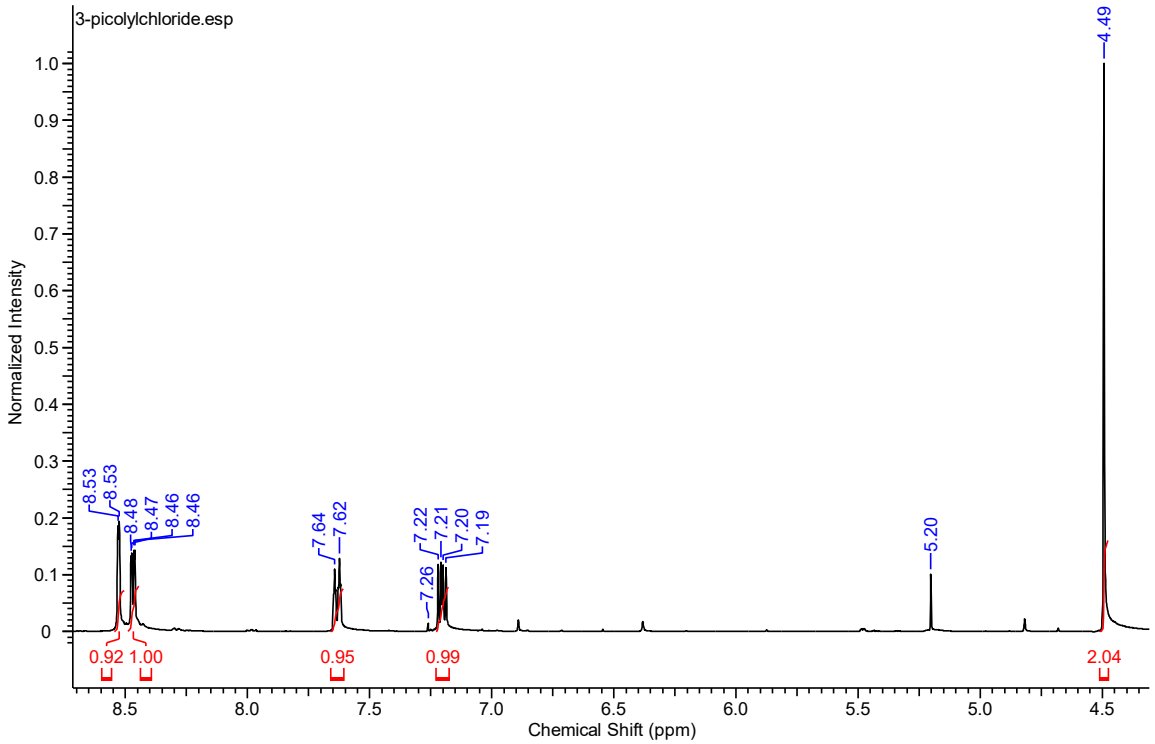

Figure A. 4 ^{1}H-NMR (400 MHz, $CDCl_3$) spectrum of 3-(chloromethyl)pyridine.

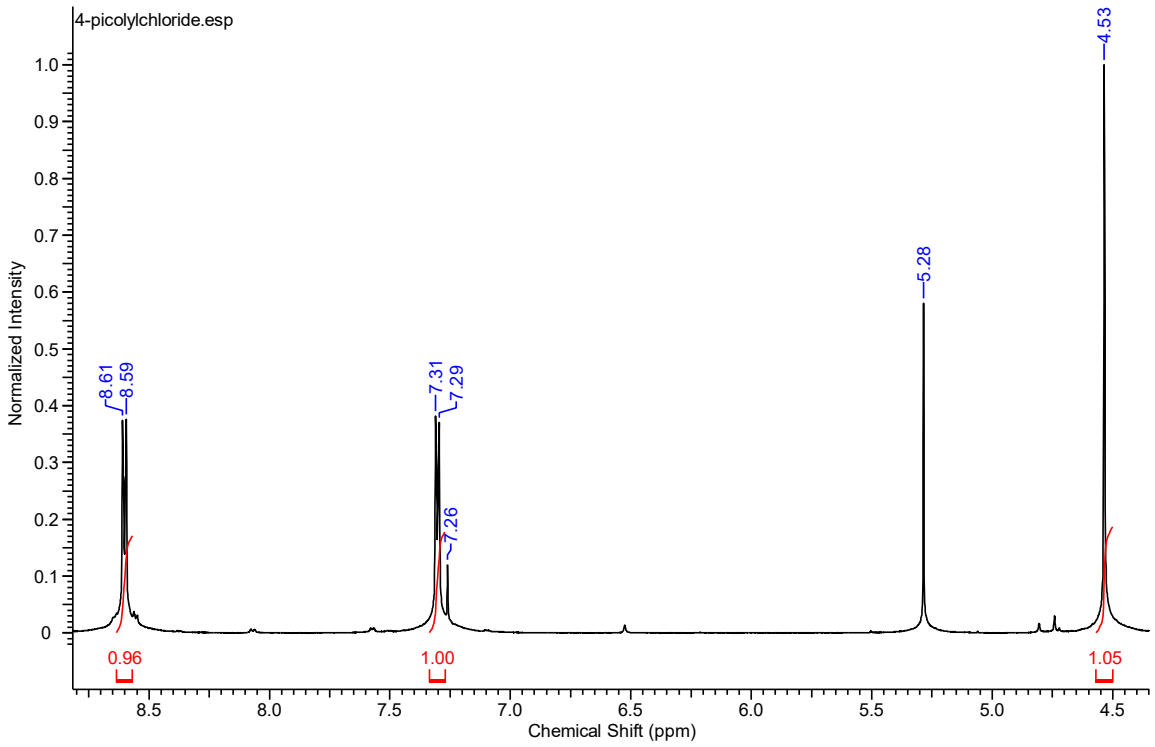

Figure A. 5 ^{1}H-NMR (400 MHz, $CDCl_3$) spectrum of 4-(chloromethyl)pyridine.

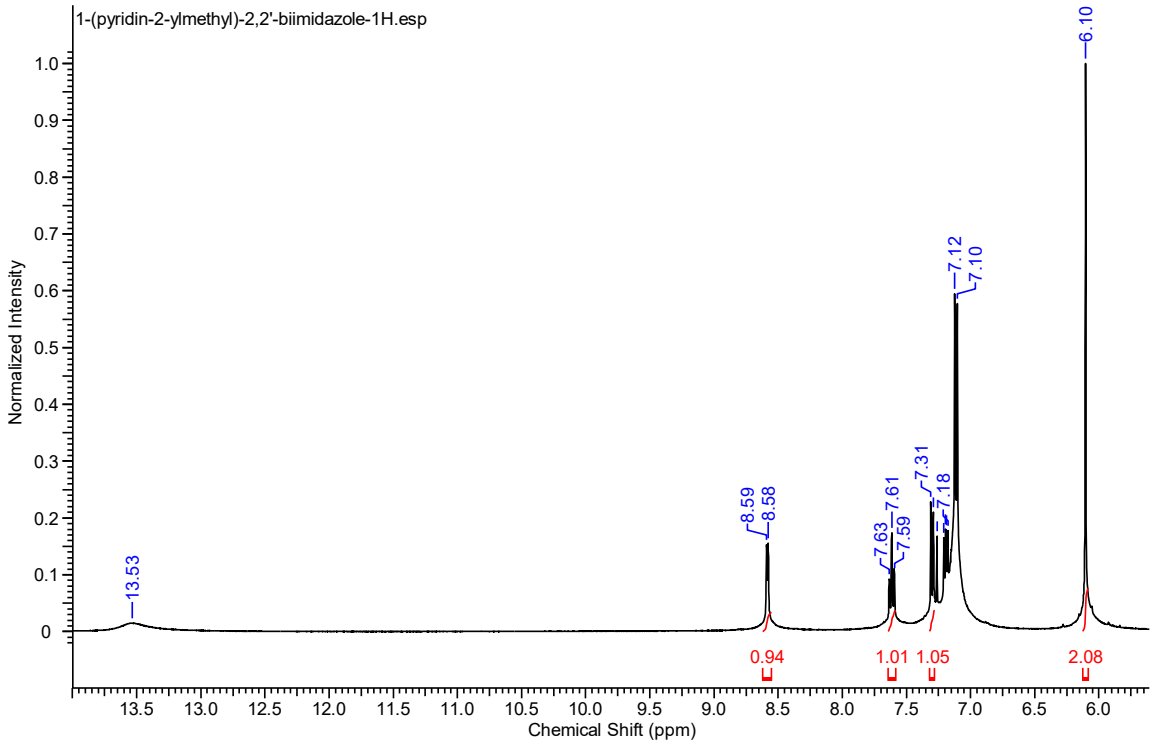

Figure A. 6 ^{1}H-NMR (400 MHz, $CDCl_3$) spectrum of 1-(pyridin-2-ylmethyl)-2,2'-biimidazole.

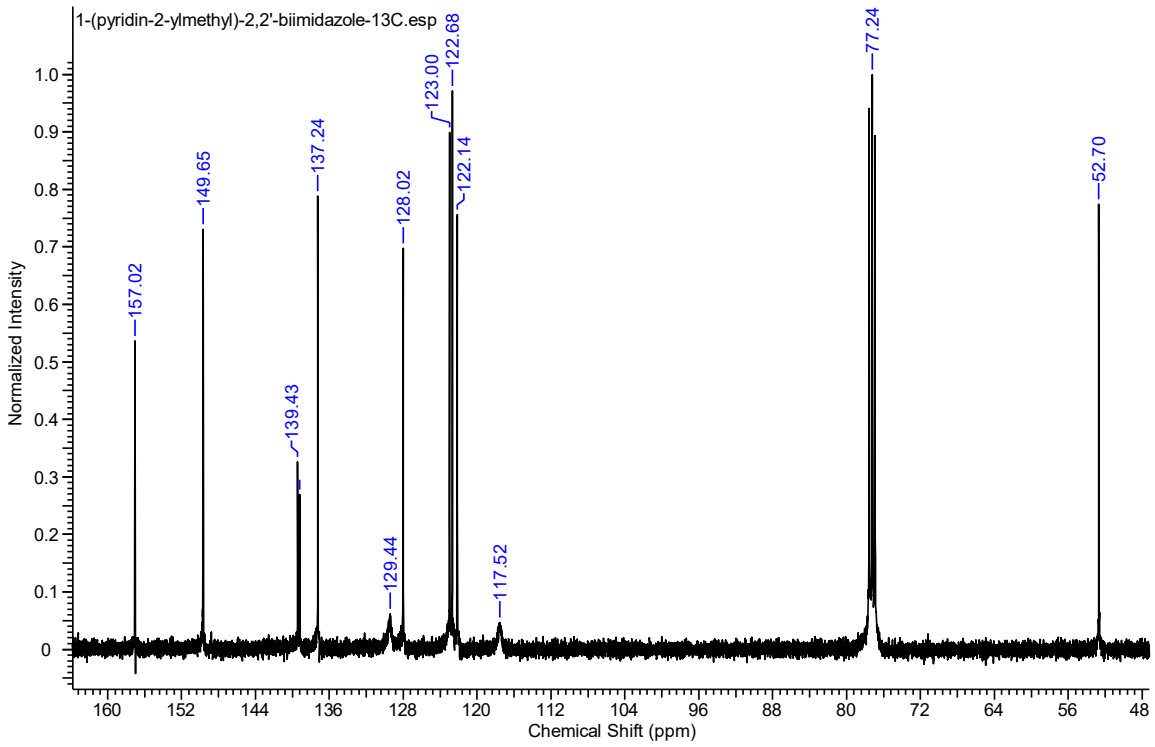

Figure A. 7 ^{13}C-NMR (100 MHz, $CDCl_3$) spectrum of 1-(pyridin-2-ylmethyl)-2,2'-biimidazole.

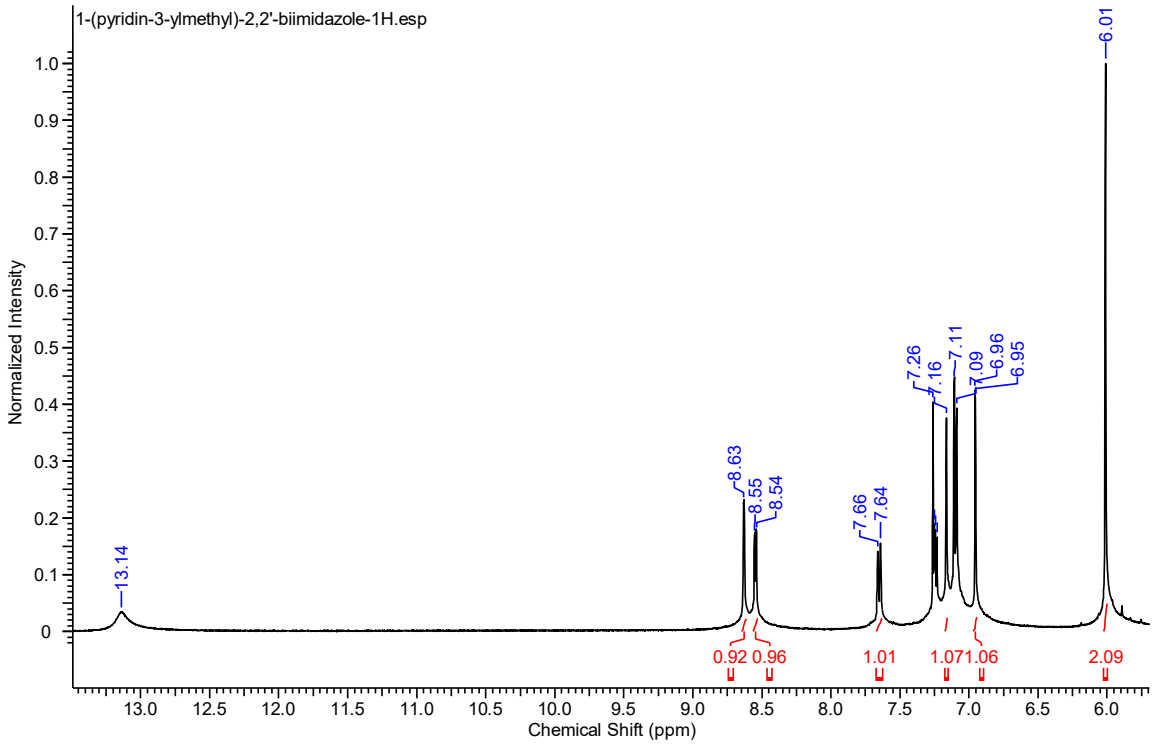

Figure A. 8 ^{1}H-NMR (400 MHz, $CDCl_3$) spectrum of 1-(pyridin-3-ylmethyl)-2,2'-biimidazole.

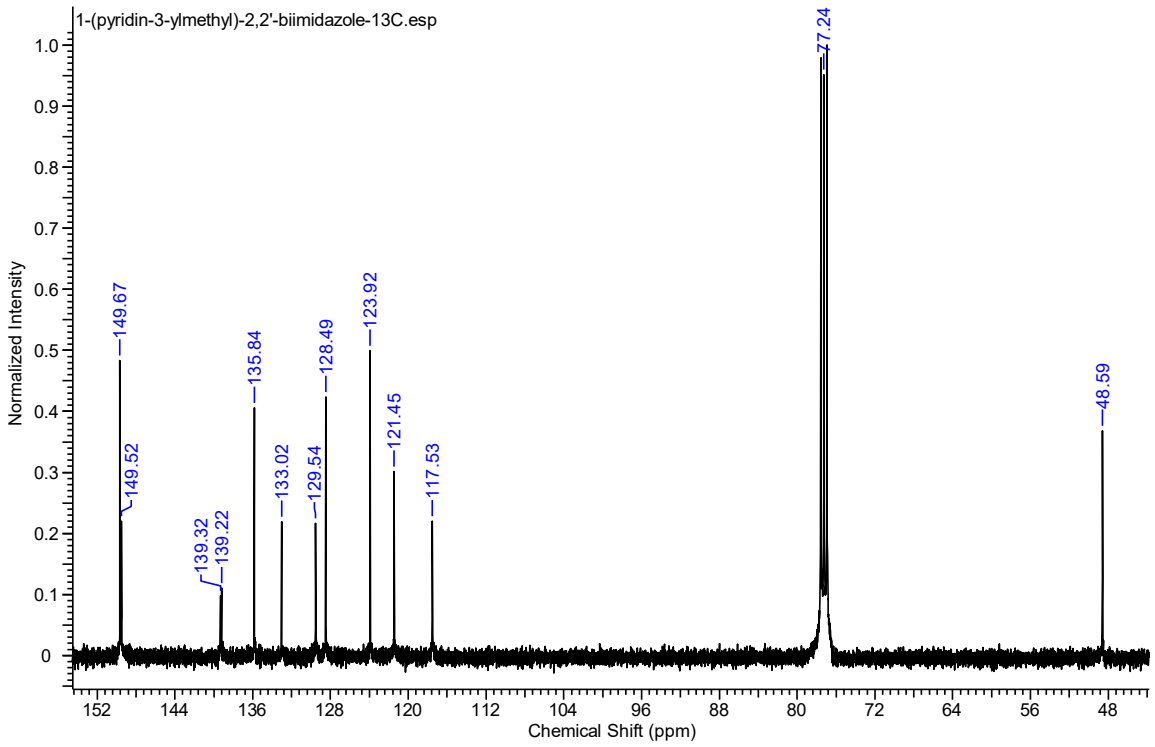

Figure A. 9 ^{13}C-NMR (100 MHz, $CDCl_3$) spectrum of 1-(pyridin-3-ylmethyl)-2,2'-biimidazole.

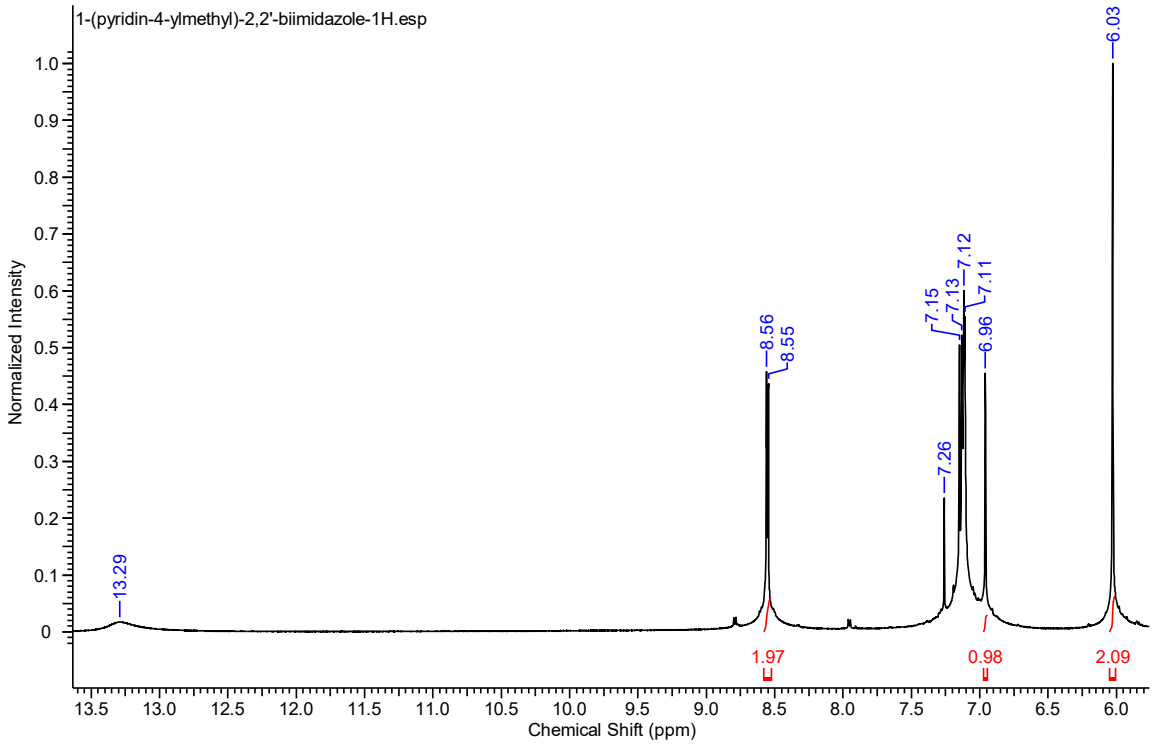

Figure A. 10 ^{1}H-NMR (400 MHz, $CDCl_3$) spectrum of 1-(pyridin-4-ylmethyl)-2,2'-biimidazole.

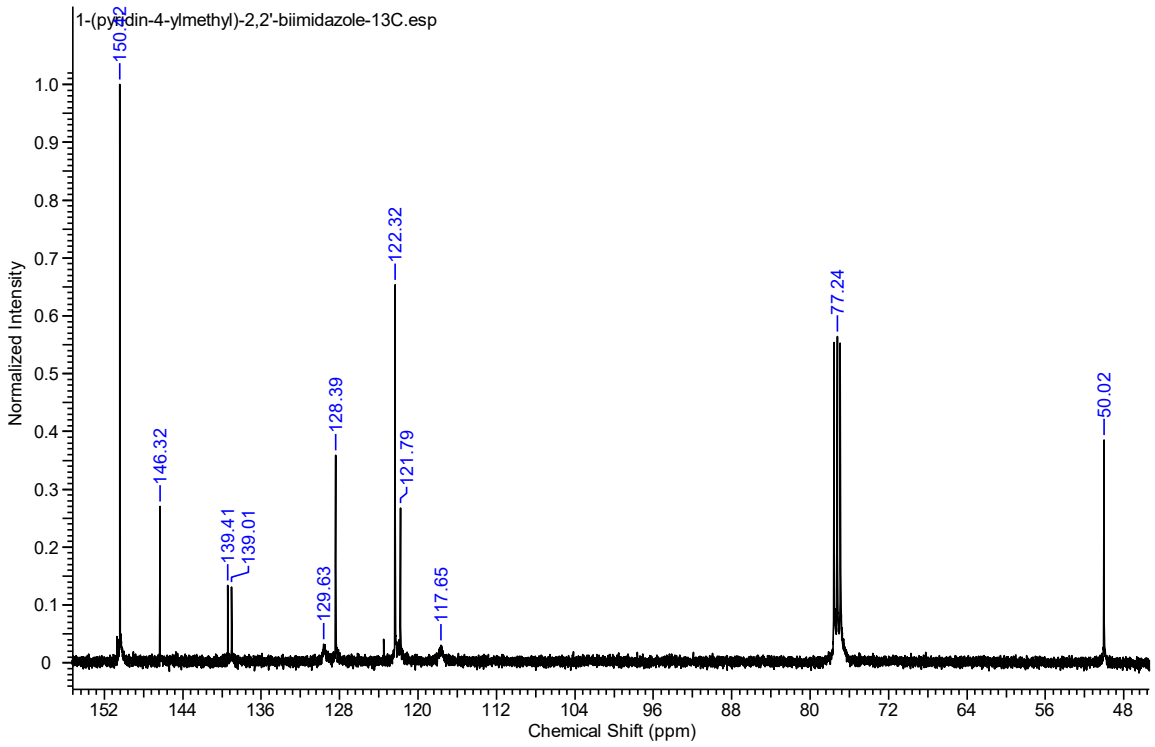

Figure A. 11 ^{13}C-NMR (100 MHz, $CDCl_3$) spectrum of 1-(pyridin-4-ylmethyl)-2,2'-biimidazole.

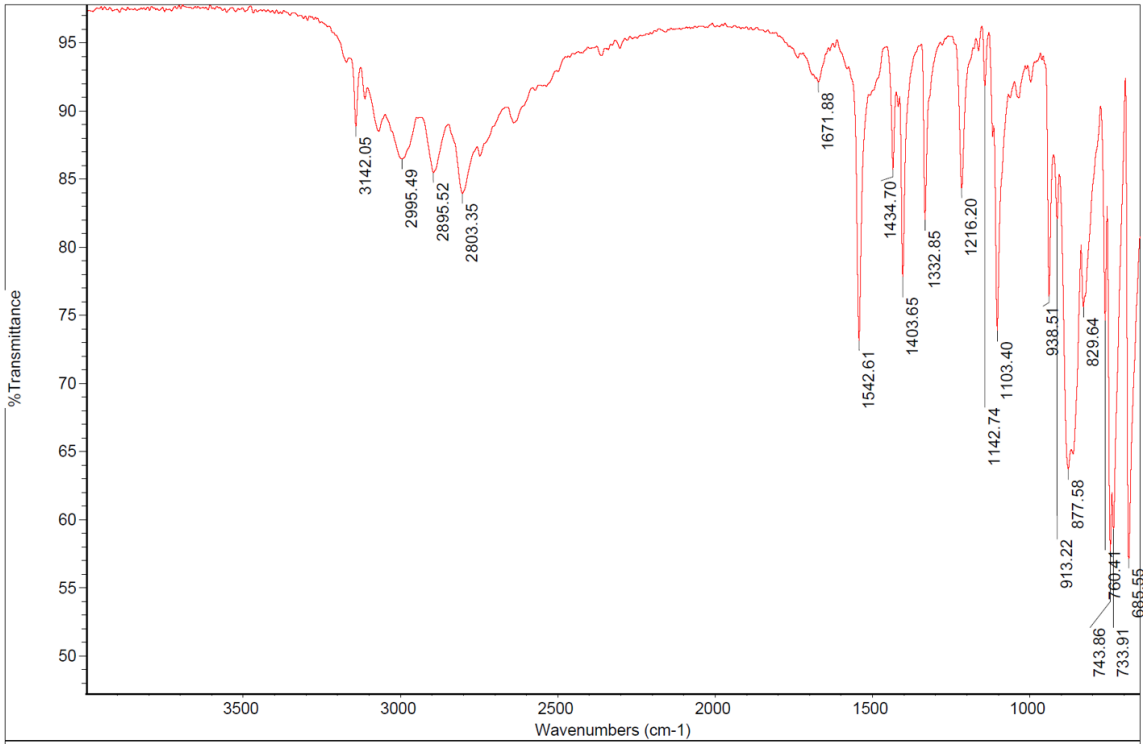

Figure A. 12 FT-IR spectrum of 2,2'-biimidazole.

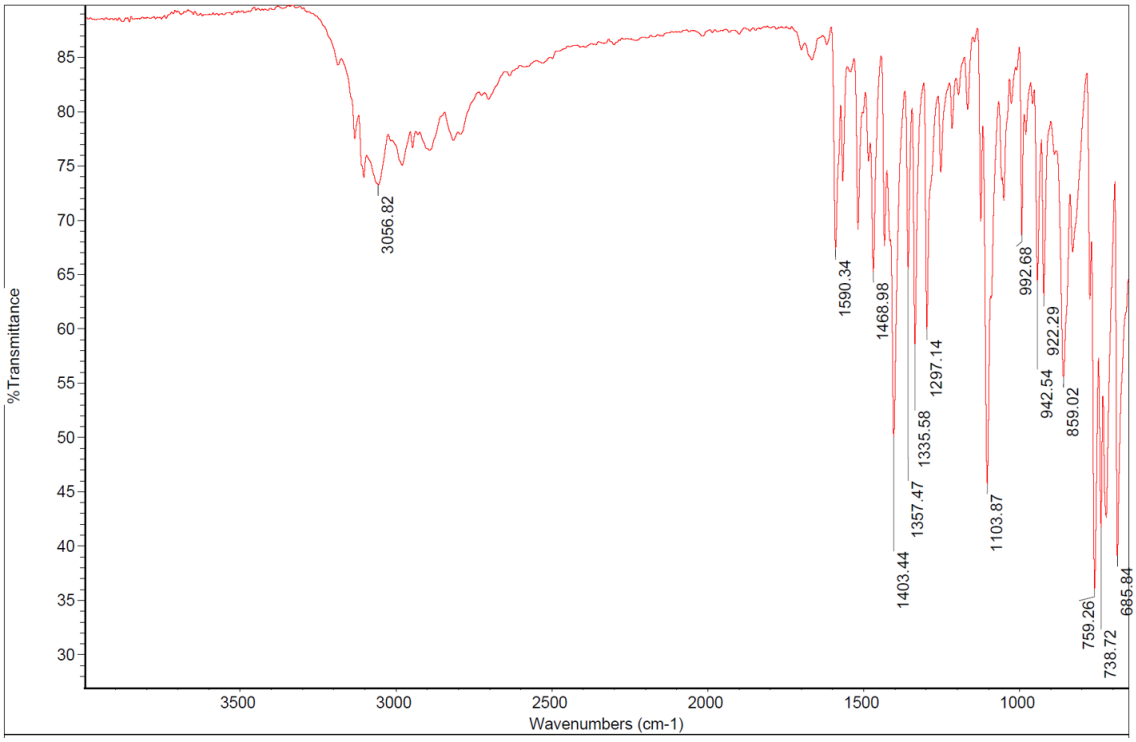

Figure A. 13 FT-IR spectrum of 1-(pyridin-2-ylmethyl)-2,2'-biimidazole.

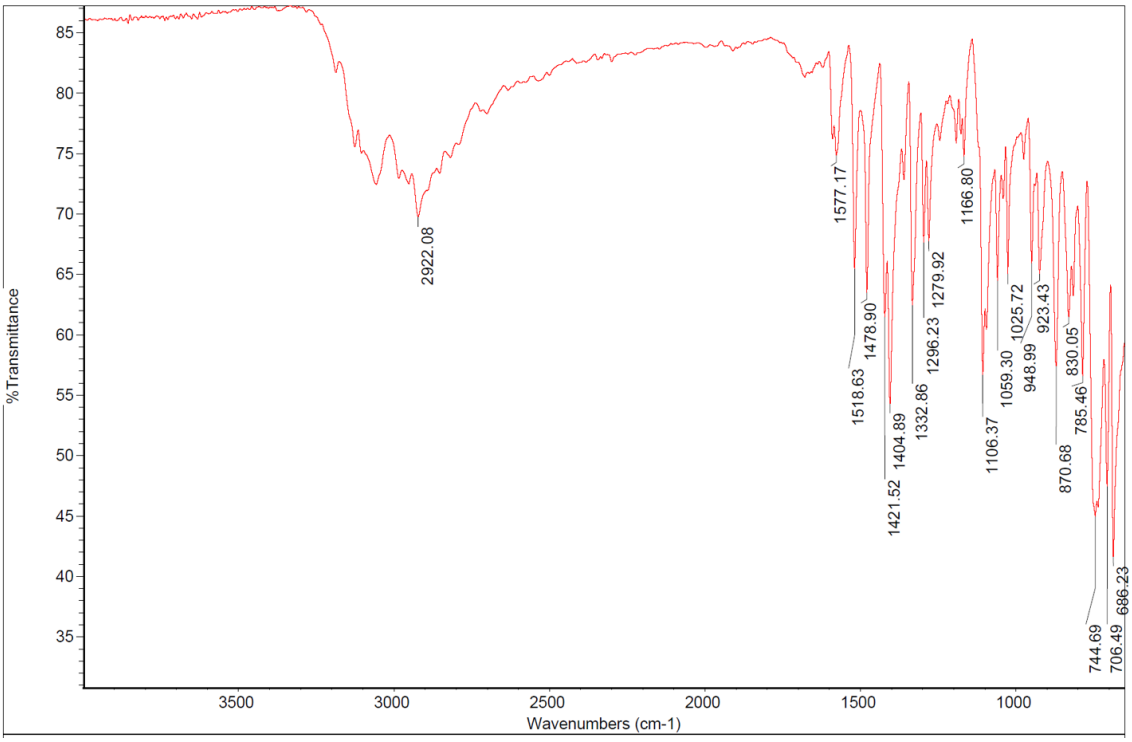

Figure A. 14 FT-IR spectrum of 1-(pyridin-3-ylmethyl)-2,2'-biimidazole.

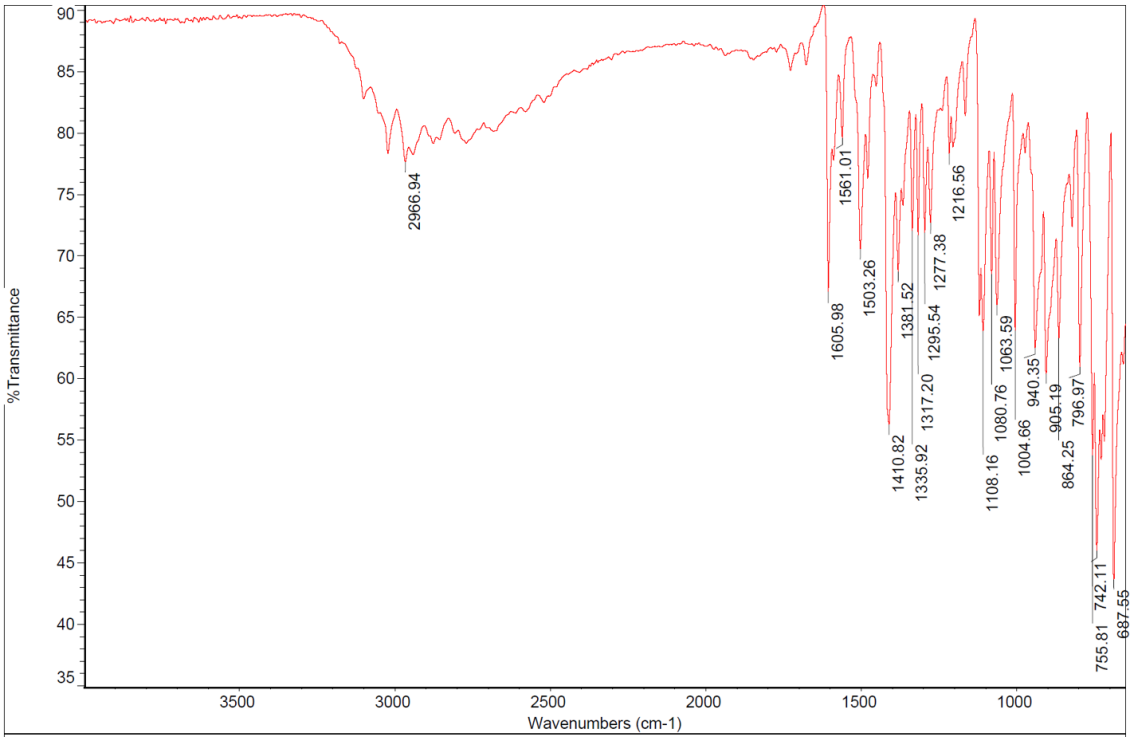

Figure A. 15 FT-IR spectrum of 1-(pyridin-4-ylmethyl)-2,2'-biimidazole.

Table A. 1 Crystallographic data for the acceptors and their co-crystals.

Code	**A1**	**A2**	**A3**	**A1:XBD2**	**A2:XBD2**
Formula moiety	$C_{12}H_{11}N_5$	$C_{12}H_{11}N_5$	$C_{12}H_{11}N_5$	$C_{12}H_{11}N_5$, $0.5(C_6F_4I_2)$	$C_{12}H_{11}N_5$, $0.5(C_6F_4I_2)$
Empirical formula	$C_{12}H_{11}N_5$	$C_{12}H_{11}N_5$	$C_{12}H_{11}N_5$	$C_{15}H_{11}F_2IN_5$	$C_{15}H_{11}F_2IN_5$
Molecular weight	225.26	225.26	225.26	426.19	426.19
Color, Habit	Pink, Prism	Colorless, Blocks	Orange, Blocks	Red, Plates	Red, Blocks
Crystal system	Monoclinic	Triclinic	Monoclinic	Triclinic	Triclinic
Space group, Z	$C2/c$, 8	$P\bar{1}$, 2	$P2(1)/n$, 4	$P\bar{1}$, 2	$P\bar{1}$, 2
a, Å	21.5686(12)	5.493(2)	7.490(3)	5.0691(14)	5.4649(17)
b, Å	5.8077(3)	10.339(4)	9.841(4)	8.055(2)	11.660(4)
c, Å	18.0356(10)	10.611(4)	15.253(5)	19.750(5)	12.493(4)
α, º	90	112.83(2)	90	93.952(13)	84.163(17)
β, º	110.1298(16)	99.24(3)	99.072(17)	93.442(12)	80.913(13)
γ, º	90	94.16(3)	90	105.938(16)	76.728(13)
Volume, Å^3	2121.2(2)	542.1(4)	1110.2(7)	771.0(4)	763.3(4)
Density, g/cm^3	1.411	1.380	1.348	1.836	1.854
T, ºK	120(2)	130(2)	130(2)	130(2)	130(2)
Crystal size, min x mid x max	0.280 x 0.340 x 0.440	0.080 x 0.160 x 0.240	0.132 x 0.238 x 0.316	0.110 x 0.185 x 0.220	0.232 x 0.328 x 0.578
X-ray wavelength, Å	0.71073	0.71073	0.71073	0.71073	0.71073
μ, mm^{-1}	0.092	0.090	0.088	2.104	2.125
Trans min / max	0.96 / 0.97	0.88 / 0.99	0.97 / 0.99	0.66 / 0.80	0.37 / 0.64
θ_{min}, º	2.01	2.13	2.47	1.04	1.80
θ_{max}, º	31.85	25.95	25.61	26.37	26.66
Reflections					
collected	19578	14694	19586	16067	18709
independent	3354	2078	2077	3140	2999

observed	2892	1341	1700	2891	2877
R_{int}	0.0292	0.0770	0.0489	0.0453	0.0413
Threshold expression	$> 2\sigma(I)$	$> 2\sigma(I)$	$> 2\sigma(I)$	$> 2\sigma(I)$	$> 2\sigma(I)$
No. parameters	157	159	158	212	212
No. restraints	0	0	0	0	0
R_1 (observed)	0.0421	0.0892	0.0393	0.0236	0.0189
wR_2 (all)	0.1188	0.2587	0.0919	0.0768	0.0508
Goodness of fit (all)	1.083	1.101	1.082	1.218	1.138
ρ_{max}, ρ_{min}, e Å^{-3}	0.358, -0.315	0.736, -0.575	0.157, -0.266	0.661, -0.512	0.395, -0.555
Completeness to 2θ limit	0.987	0.980	0.998	0.993	0.932

Code	**A2:XBD3**	**A3:XBD1**	**A3:XBD2**	**A1:HBD2**	**A1:HBD4**
Formula moiety	$(C_{12}H_{11}N_5)$, $(C_6F_3I_3)$	$(C_{12}H_{11}N_5)_2$, $(C_6F_4I_2)$	$(C_{12}H_{11}N_5)_2$, $(C_6F_4I_2)$, (C_1H_4O)	$(C_{12}H_{11}N_5)$, $(C_4H_6O_4)$	$C_{12}H_{12}N_5$, $C_8H_{13}O_4$
Empirical formula	$C_{18}H_{11}F_3I_3N_5$	$C_{30}H_{22}F_4I_2N_{10}$	$C_{31}H_{26}F_4I_2N_{10}O$	$C_{16}H_{17}N_5O_4$	$C_{20}H_{25}N_5O_4$
Molecular weight	735.02	852.38	225.26	343.34	399.45
Color, Habit	Colorless, Plates	Pink, Prism	Colorless, Plates	Colorless, Plates	Violet, Irregular
Crystal system	Monoclinic	Triclinic	Triclinic	Triclinic	Triclinic
Space group, Z	$P2(1)/c$, 4	$P\bar{1}$, 8	$P\bar{1}$, 4	$P\bar{1}$, 2	$P\bar{1}$, 2
a, Å	16.0707(15)	17.386(2)	13.4945(9)	5.0716(9)	5.1948(2)
b, Å	9.0666(8)	19.378(3)	14.8017(10)	11.314(2)	10.8967(3)
c, Å	14.8610(14)	19.435(3)	19.3714(13)	14.051(3)	18.2317(6)
α, º	90	92.996(5)	111.285(2)	90.818(7)	105.5790(10)
β, º	107.218(3)	106.710(5)	92.518(2)	99.190(6)	95.6070(10)
γ, º	90	106.560(4)	112.668(2)	99.925(6)	100.1040(10)
Volume, Å^3	2068.3(3)	5946.5(14)	3249.9(4)	783.2(3)	967.21(6)

Density, g/cm^3	2.360	1.904	1.808	1.456	1.372
T, ºK	120(2)	120(2)	120(2)	120(2)	296(2)
Crystal size, min x mid x max	0.120 x 0.360 x 0.440	0.180 x 0.260 x 0.360	0.120 x 0.280 x 0.340	0.120 x 0.380 x 0.420	0.055 x 0.090 x 0.250
X-ray wavelength, Å	0.71073	0.71073	0.71073	0.71073	1.54178
μ, mm^{-1}	4.575	2.182	2.002	0.108	0.805
Trans min / max	0.24 / 0.61	0.51 / 0.69	0.54 / 0.79	0.96 / 0.99	0.82 / 0.96
θ_{min}, º	1.33	1.41	1.566	1.469	2.55
θ_{max}, º	32.05	31.26	31.980	31.033	70.29
Reflections					
collected	36298	115429	73862	11896	17758
independent	7154	37450	20434	4628	3369
observed	6416	22954	17311	3897	3347
R_{int}	0.0296	0.0550	0.0242	0.0192	0.0475
Threshold expression	> 2σ(I)	> 2σ(I)	> 2σ(I)	> 2σ(I)	> 2σ(I)
No. parameters	265	1178	885	235	275
No. restraints	0	528	0	0	2
R_1 (observed)	0.0220	0.0621	0.0275	0.0418	0.0471
wR$_2$ (all)	0.0496	0.1994	0.0654	0.1226	0.1150
Goodness of fit (all)	1.030	1.174	1.039	1.034	1.097
ρ_{max}, ρ_{min}, e Å^{-3}	0.850, -1.301	2.706, -3.336	1.239, -0.526	0.371, -0.357	0.580, -0.371
Completeness to 2θ limit	0.994	0.984	0.991	0.970	0.908

Code	**A1:HBD6**	**A2:HBD1**	**A2:HBD3**	**A2:HBD5**	**A3:HBD1**
Formula moiety	$C_{12}H_{11}N_5$, 0.5($C_{12}H_{22}O_4$)	$C_{12}H_{11}N_5$, $C_7H_6O_2$	($C_{12}H_{11}N_5$)$_2$, ($C_6H_{10}O_4$)	($C_{12}H_{11}N_5$)$_2$, ($C_{10}H_{18}O_4$)	$C_{12}H_{11}N_5$, $C_7H_6O_2$
Empirical formula	$C_{18}H_{22}N_5O_2$	$C_{19}H_{17}N_5O_2$	$C_{30}H_{32}N_{10}O_4$	$C_{34}H_{40}N_{10}O_4$	$C_{19}H_{17}N_5O_2$

Molecular weight	340.40	347.38	596.65	652.76	347.38
Color, Habit	Red, Blocks	Red, Blocks	Pink, Prism	Red, Plates	Violet, Parallelepiped
Crystal system	Triclinic	Triclinic	Triclinic	Triclinic	Triclinic
Space group, Z	$P\bar{1}$, 2	$P\bar{1}$, 2	$P\bar{1}$, 2	$P\bar{1}$, 1	$P\bar{1}$, 2
a, Å	5.2936(3)	7.028(2)	8.0078(17)	5.7402(10)	6.42690(10)
b, Å	7.9437(5)	9.024(3)	10.167(2)	9.3514(16)	9.9656(2)
c, Å	22.8847(13)	13.602(4)	18.969(4)	14.973(3)	13.5194(3)
α, º	81.583(5)	90.229(19)	79.276(6)	97.467(5)	96.6910(10)
β, º	85.500(6)	91.564(17)	82.529(5)	91.771(6)	95.6860(10)
γ, º	70.615(5)	93.223(16)	70.640(5)	97.861(5)	100.6030(10)
Volume, Å^3	897.53(10)	860.9(4)	1427.8(5)	788.5(2)	838.84(3)
Density, g/cm^3	1.260	1.340	1.388	1.375	1.375
T, ºK	296(2)	130(2)	120(2)	120(2)	296(2)
Crystal size, min x mid x max	0.300 x 0.360 x 0.510	0.268 x 0.374 x 0.492	0.300 x 0.320 x 0.340	0.080 x 0.380 x 0.420	0.065 x 0.130 x 0.160
X-ray wavelength, Å	0.71073	0.71073	0.71073	0.71073	1.54178
μ, mm^{-1}	0.086	0.091	0.097	0.094	0.761
Trans min / max	0.95 / 1.00	0.96 / 0.98	0.86 / 0.97	0.76 / 0.99	0.89 / 0.95
θ_{min}, º	4.293	2.26	1.095	1.373	3.32
θ_{max}, º	24.999	25.73	31.509	31.023	69.93
Reflections					
collected	7915	18617	52300	14438	2977
independent	3140	3240	8898	4721	2977
observed	2254	2746	7471	3525	2905
R_{int}	0.0265	0.0398	0.0400	0.0338	0.6116
Threshold expression	$> 2\sigma(I)$	$> 2\sigma(I)$	$> 2\sigma(I)$	$> 2\sigma(I)$	$> 2\sigma(I)$
No. parameters	234	243	409	223	244

No. restraints	0	1	0	0	1
R_1 (observed)	0.0654	0.0360	0.0444	0.0484	0.0415
wR_2 (all)	0.1569	0.0980	0.1399	0.1436	0.1038
Goodness of fit (all)	1.095	1.049	1.083	1.115	1.136
ρ_{max}, ρ_{min}, e Å^{-3}	0.159, -0.172	0.176, -0.242	0.547, -0.322	0.335, -0.273	0.358, -0.289
Completeness to 2θ limit	0.994	0.984	0.995	0.970	0.937

Code	**A3:HBD2**	**A3:HBD3**
Formula moiety	$(C_{12}H_{11}N_5)$, $(C_4H_6O_4)$	$(C_{12}H_{11}N_5)$, $(C_6H_{10}O_4)$
Empirical formula	$C_{16}H_{17}N_5O_4$	$C_{18}H_{21}N_5O_4$
Molecular weight	343.34	371.40
Color, Habit	Red, Plates	Red, Blocks
Crystal system	Triclinic	Monoclinic
Space group, Z	$P\bar{1}$, 2	$P2(1)/n$, 4
a, Å	4.8081(7)	17.295(2)
b, Å	11.0210(17)	4.8014(7)
c, Å	14.819(2)	21.977(3)
α, º	97.881(6)	90
β, º	91.543(6)	90.912(11)
γ, º	90.181(6)	90
Volume, Å^3	777.5(2)	1824.7(4)
Density, g/cm^3	1.467	1.352
T, ºK	120(2)	296(2)
Crystal size, min x mid x max	0.080 x 0.340 x 0.400	0.280 x 0.310 x 0.530
X-ray wavelength, Å	0.71073	0.71073

μ, mm^{-1}	0.109	0.098
Trans min / max	0.77 / 0.99	0.95 / 1.00
θ_{min}, º	1.865	4.364
θ_{max}, º	30.567	26.999
Reflections		
collected	17051	9474
independent	4630	3958
observed	3399	2388
R_{int}	0.0441	0.0473
Threshold expression	> 2σ(I)	> 2σ(I)
No. parameters	235	257
No. restraints	0	0
R_1 (observed)	0.0519	0.0595
wR_2 (all)	0.1585	0.1791
Goodness of fit (all)	1.066	1.018
ρ_{max}, ρ_{min}, e Å^{-3}	0.402, -0.378	0.193, -0.179
Completeness to 2θ limit	0.985	0.997

Table A. 2 Selected halogen-bond distances and angles.

Compound	C–I···A	d(I···A)/Å	∠(C–I···A)/°
A2:XBD3	C41–I1···N31	2.8075(17)	179.16(7)
A3:XBD1	C71_1–I1_1···N31_1	3.443(11)	168.1(4)
	C71_2–I1_2···N31_2	3.469(11)	168.3(4)
	C71_3–I1_3···N31_3	3.247(11)	175.7(4)
	C71_4–I1_4···N31_4	3.250(11)	173.1(4)
A1:XBD2	C18–I21···N13	2.842(3)	179.26(11)
A2:XBD2	C18–I21···N14^a	2.839(2)	169.59(8)
A3:XBD2	C74_1–I2_1···O1S_1	2.8401(15)	171.86(6)
	C71_1–I1_1···N31_1	2.8887(18)	174.78(6)
	C74_2–I4_2···O1S_2	2.9005(16)	168.99(6)
	C71_2–I3_2···N31_2	2.9634(18)	165.58(6)

^{a}Symmetry transformations used to generate equivalent atoms: -1+x,y,z

Table A. 3 Selected hydrogen-bond distances and angles.

Compound	D–H···A	*d*(H···A)/Å	*d*(D···A)/Å	∠(D–H···A)/°	Symmetry operations used
A1	N21–H21···N13	2.015(14)	2.8810(12)	158.8(12)	-x,-y,-z
A2	N3–H3···N8	1.94(5)	2.905(5)	166.(4)	-x,1-y,-z
A3	N10–H10···N15	1.987(18)	2.8623(19)	163.2(16)	-1/2+x,1.5-y,1/2+z
A2:XBD3	N21–H21···N13	2.07(3)	2.871(2)	158(2)	-x,-1-y,1-z
A3:XBD1	N21_1–H21_1···N43_4	2.07	2.916(14)	162.2	x,y,1+z
	N51_1–H51_1···N43_2	2.11	2.955(14)	159.7	x,y,1+z
	N21_2–H21_2···N43_3	2.05	2.888(14)	159.2	x,1+y,z
	N51_2–H51_2···N43_1	2.07	2.906(15)	157.5	x,y,1+z
	N21_3–H21_3···N13_4	2.03	2.860(14)	156.2	x,y,1+z
	N51_3–H51_3···N13_2	2.05	2.888(14)	158.4	x,1+y,z
	N21_4–H21_4···N13_3	2.09	2.933(14)	160.7	x,y,1+z
	N51_4–H51_4···N13_1	2.09	2.938(14)	160.8	x,y,1+z
A1:XBD2	N10–H10···N5	2.10(4)	2.874(4)	156.(4)	2-x,2-y,-z
A2:XBD2	N10–H10···N5	2.08(3)	2.907(3)	156.(3)	1-x,-y,-z
A3:XBD2	N21_1–H21_1···N43_1	2.10(2)	2.903(2)	158(2)	x,2+y,1+z
	N21_2–H21_2···N43_2	2.13(2)	2.920(2)	163(2)	x,2+y,1+z
	N51_1–H51_1···N13_1	2.10(3)	2.896(2)	160(2)	x,2+y,1+z
	N51_2–H51_2···N13_2	2.05(2)	2.874(2)	160(2)	x,2+y,1+z
	O1S_1–H1_1···N61_1	1.81(3)	2.667(2)	173(2)	
	O1S_2–H1_2···N61_2	1.84(3)	2.721(2)	171(3)	
A2:HBD1	N6–H6···N3	2.038(16)	2.9010(17)	159.4(14)	2-x,1-y,-z
	O25–H25···N14	1.750(19)	2.6787(16)	177.(2)	x,-1+y,z
A3:HBD1	N14–H14···N2	2.080(17)	2.9136(14)	159.4(14)	-x,1-y,-z
	O25–H25···N10	1.660(19)	2.6082(13)	177.(2)	1+x,y,z
A2:HBD3	N21–H21···N43	1.974(14)	2.8715(12)	158.2(12)	3+x,y,-1+z
	N51–H51···N13	1.995(14)	2.8710(12)	158.3(12)	3+x,y,-1+z
	O71–H71···N31	1.755(15)	2.6977(11)	175.2(13)	
	O76–H76···N61	1.806(15)	2.7013(11)	174.9(13)	
A2:HBD5	N21–H21···N13	2.012(16)	2.8749(15)	158.8(14)	2-x,1-y,2-z
	O41–H41···N31	1.707(18)	2.6774(14)	171.3(15)	
A1:HBD6	N4–H1N···N2	2.09(3)	2.898(4)	158(3)	-x,2-y,1-z
	O2–H1O···N5	1.75(4)	2.732(3)	173(3)	
A3:HBD2	N21–H21···O42	1.97(2)	2.8616(17)	167.7(16)	
	O41–H41···N13	1.57(2)	2.5893(16)	167.4(17)	
	O44–H44···N31	1.68(2)	2.6431(17)	175.0(17)	1+x,y,1+z
A3:HBD3	O1–H1O···N2	1.70(4)	2.630(3)	158(3)	
	N4–H1N···O2	1.98(3)	2.859(3)	163(3)	
	O4–H20···N5	1.66(4)	2.649(3)	171(3)	1+x,-1+y,z
A1:HBD4	O29–H29···O19	1.78(2)	2.6963(18)	178.(3)	x,-1+y,z
	N14–H14···O19	1.81(2)	2.6980(18)	164.(2)	-1+x,y,z
	N2–H2···O18	1.65(2)	2.5930(18)	165.(3)	-1+x,y,z
A1:HBD2	N13–H13···O41	1.545(14)	2.5427(12)	163.9(13)	
	N21–H21···O42	1.781(15)	2.7129(12)	165.8(13)	
	O51–H51···O42	1.634(19)	2.6128(13)	169.9(16)	

Appendix B - Additional material for Chapter 3

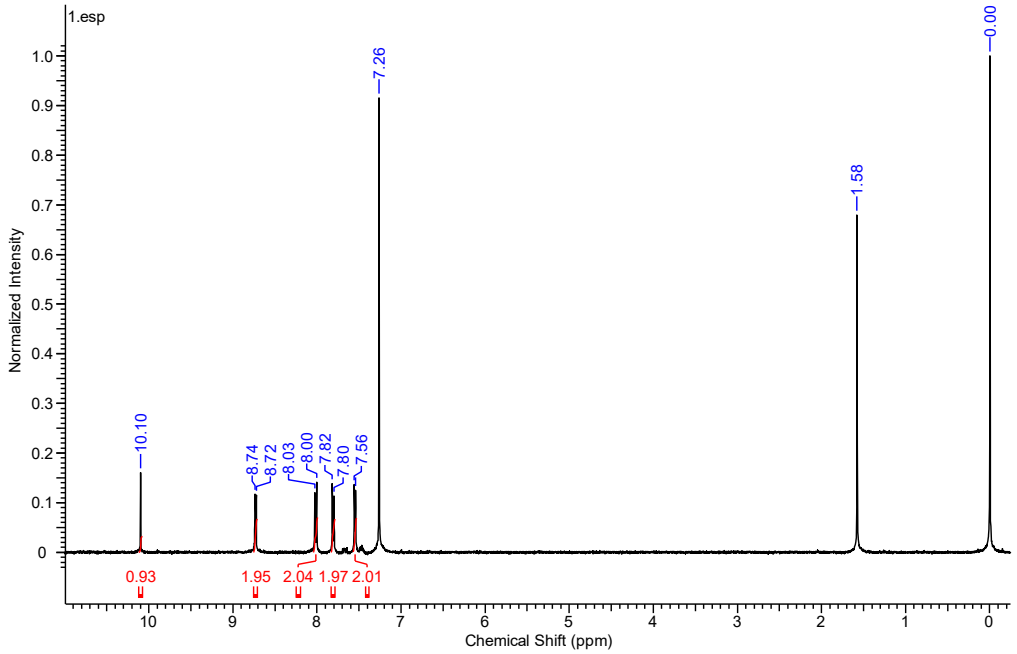

Figure B. 1 ^{1}H-NMR (400 MHz, $CDCl_3$) spectrum of 4-(pyridin-4-yl)benzaldehyde.

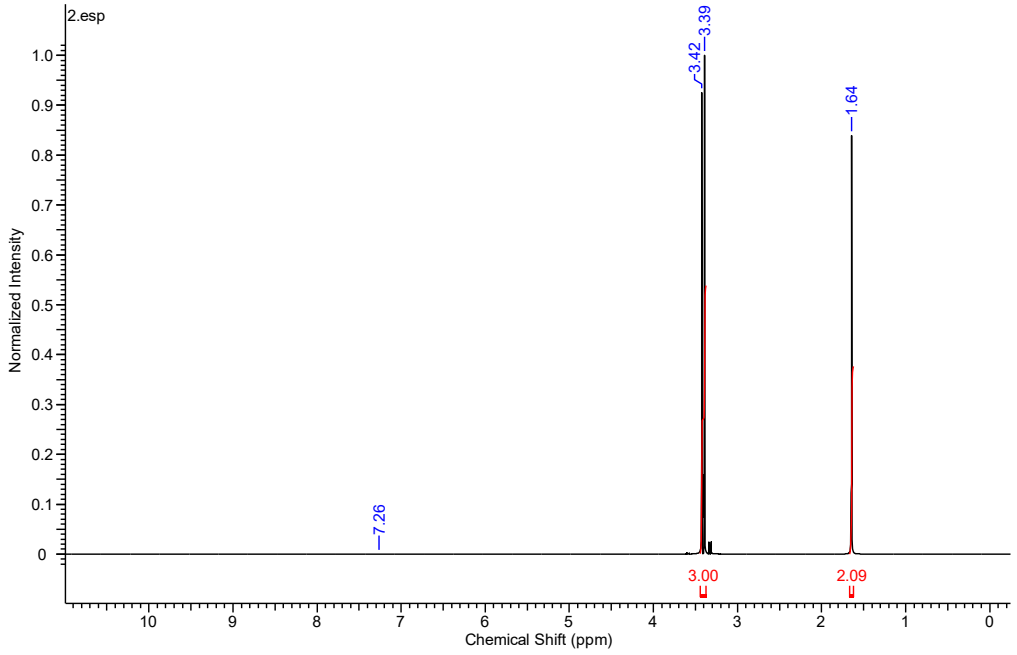

Figure B. 2 ^{1}H-NMR (400 MHz, $CDCl_3$) spectrum of 2,2,2-trimethoxy-4,5-dimethyl-1,3,2λ^5-dioxaphosphole.

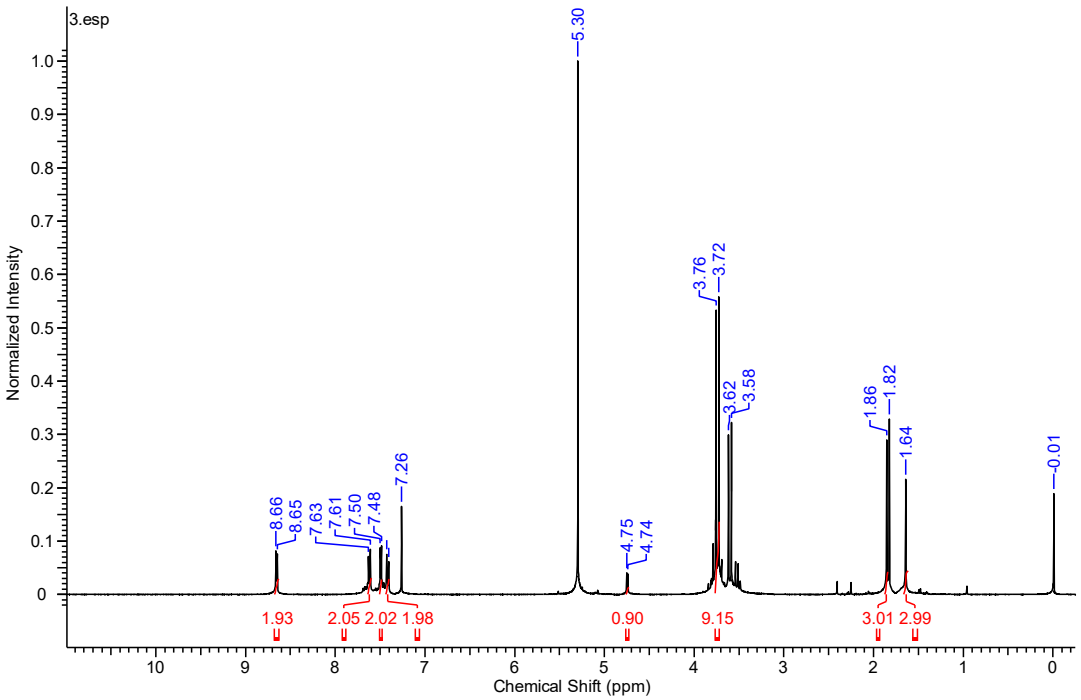

Figure B. 3 ^{1}H-NMR (400 MHz, $CDCl_3$) spectrum of 1-(2,2,2-trimethoxy-4-methyl-5-(4-(pyridin-4-yl)phenyl)-1,3,2λ^5-dioxaphospholan-4-yl)ethan-1-one.

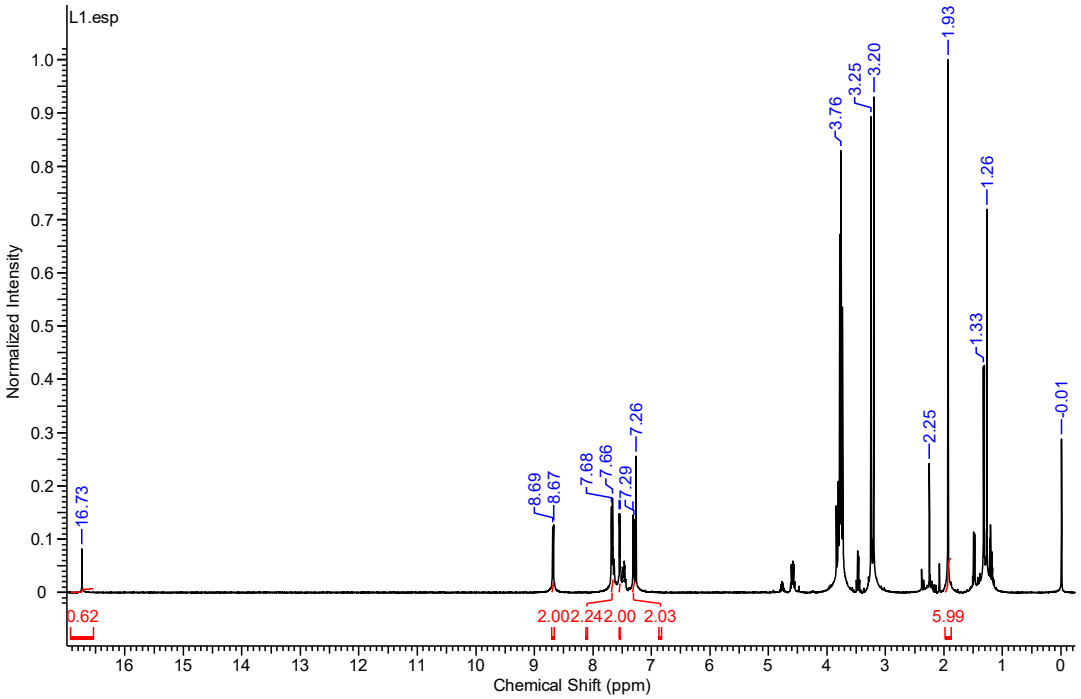

Figure B. 4 ^{1}H-NMR (400 MHz, $CDCl_3$) spectrum of 4-hydroxy-3-(4-(pyridin-4-yl)phenyl)pent-3-en-2-one [**L1**].

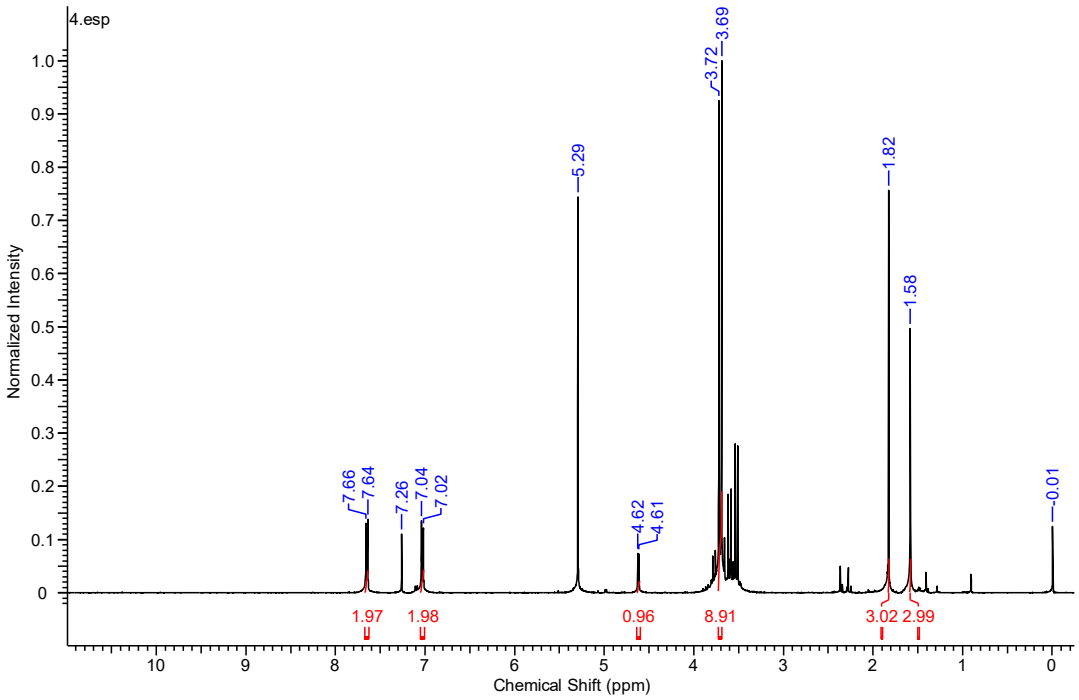

Figure B. 5 ^{1}H-NMR (400 MHz, $CDCl_3$) spectrum of 1-(5-(4-iodophenyl)-2,2,2-trimethoxy-4-methyl-1,3,2λ^5-dioxaphospholan-4-yl)ethan-1-one.

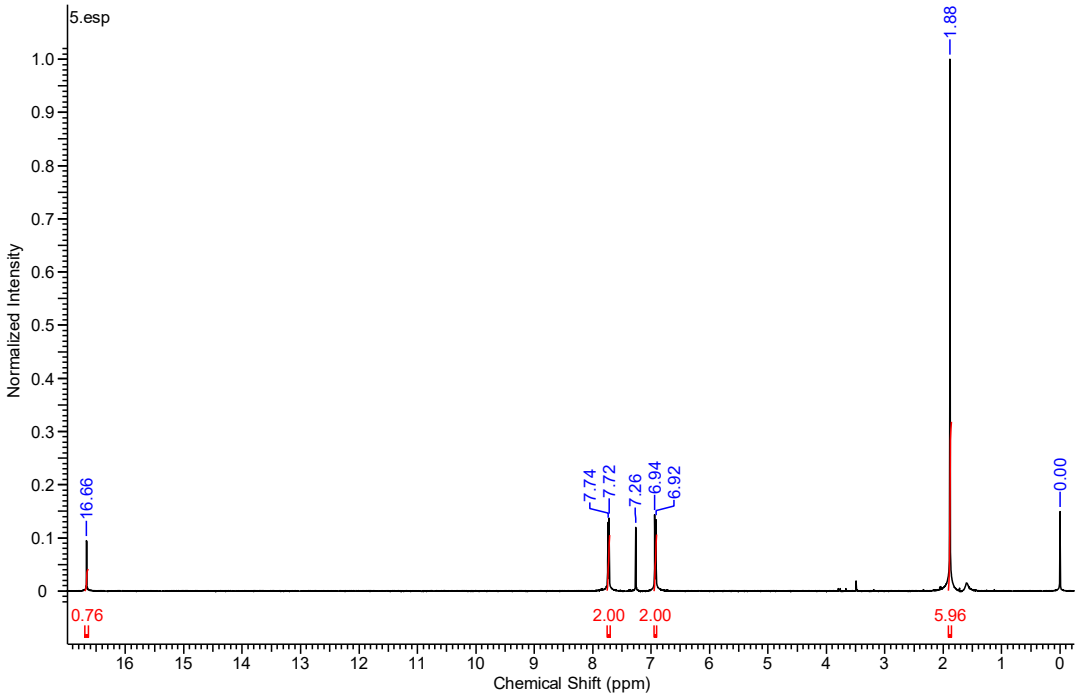

Figure B. 6 ^{1}H-NMR (400 MHz, $CDCl_3$) spectrum of 4-hydroxy-3-(4-iodophenyl)pent-3-en-2-one.

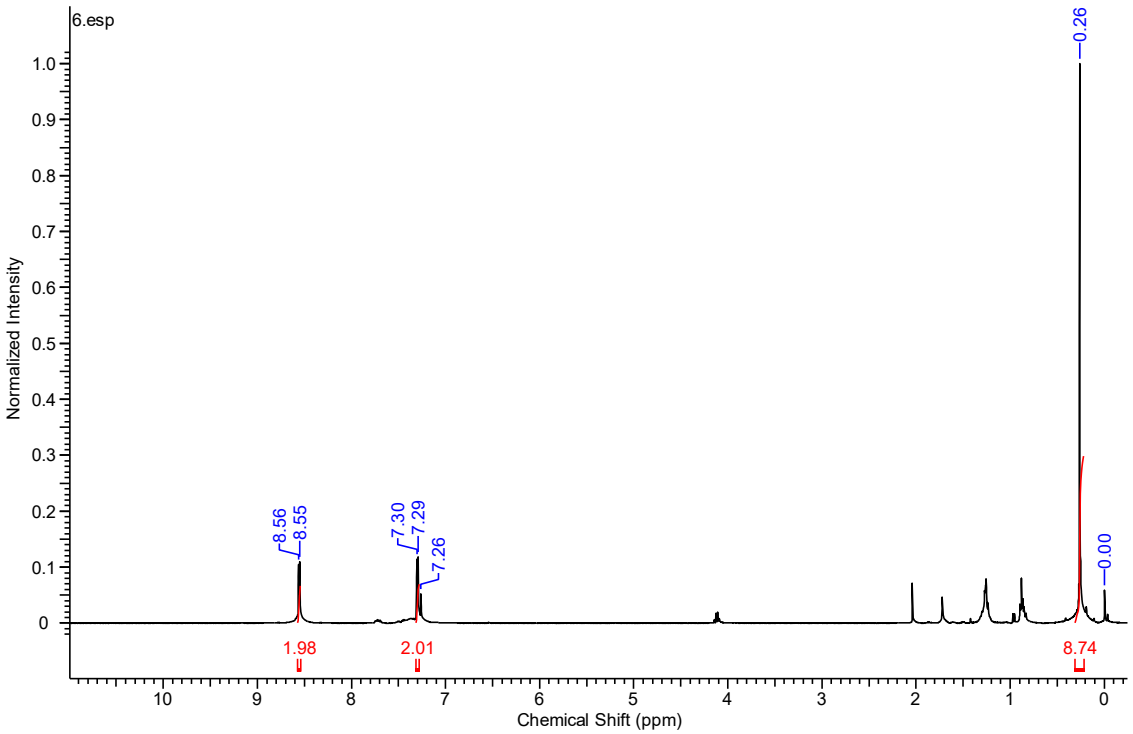

Figure B. 7 ^{1}H-NMR (400 MHz, $CDCl_3$) spectrum of 4-((trimethylsilyl)ethynyl)pyridine.

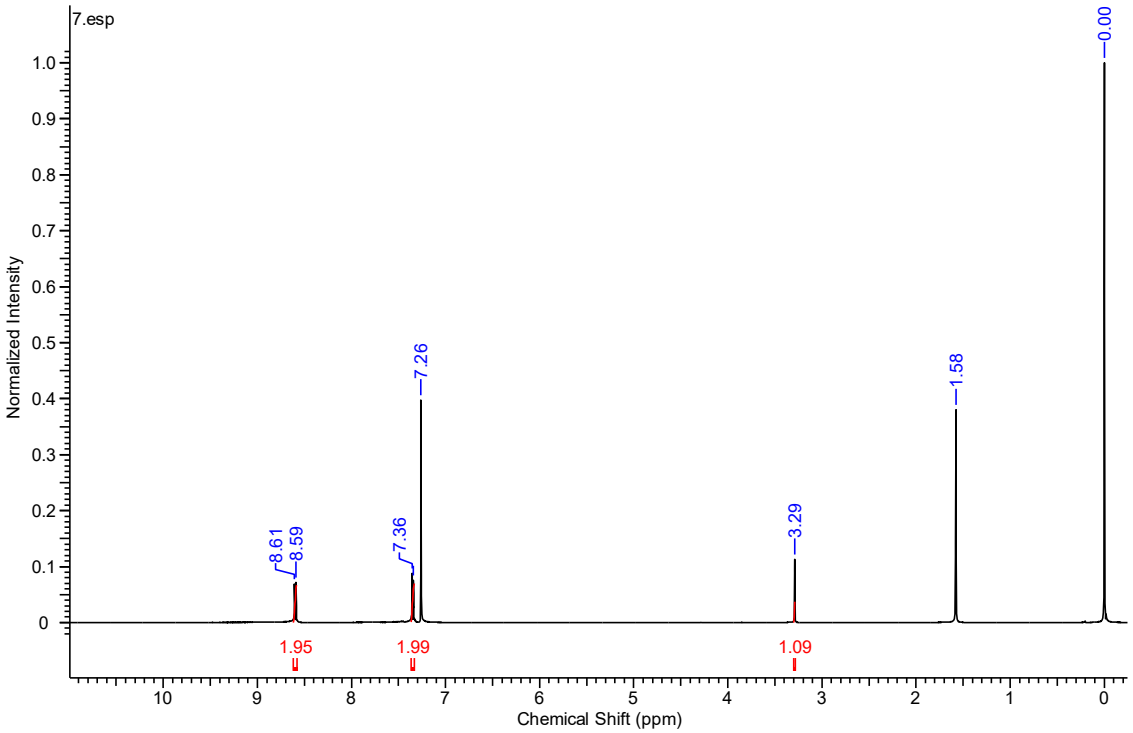

Figure B. 8 ^{1}H-NMR (400 MHz, $CDCl_3$) spectrum of 4-ethynylpyridine.

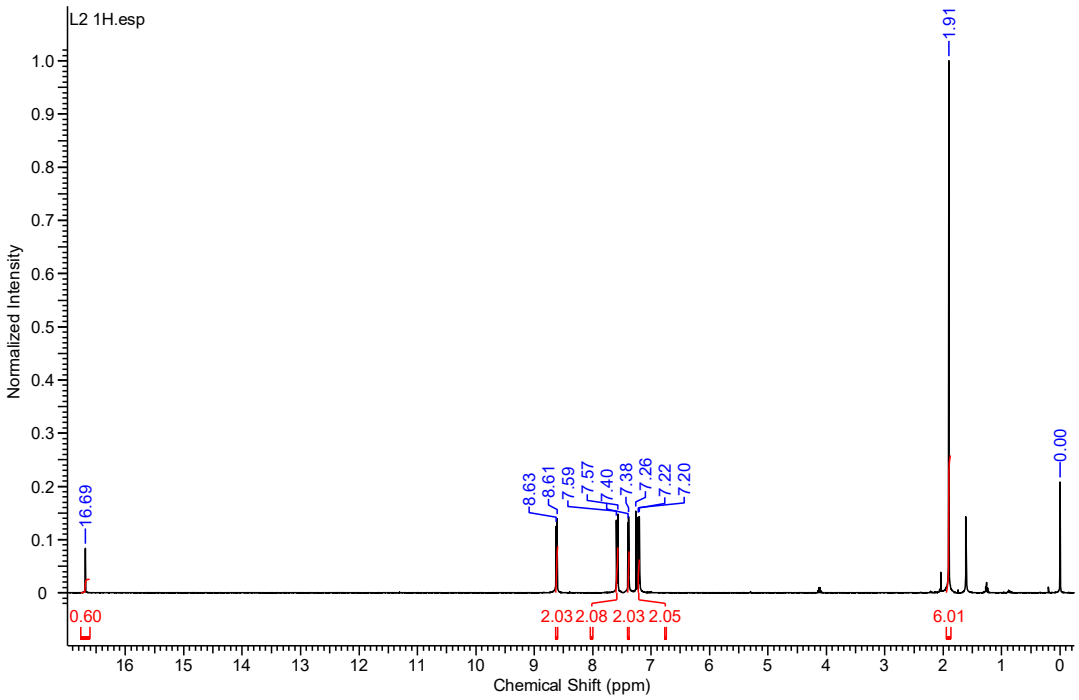

Figure B. 9 ^{1}H-NMR (400 MHz, $CDCl_3$) spectrum of 4-hydroxy-3-(4-(pyridin-4-ylethynyl)phenyl)pent-3-en-2-one [**L2**].

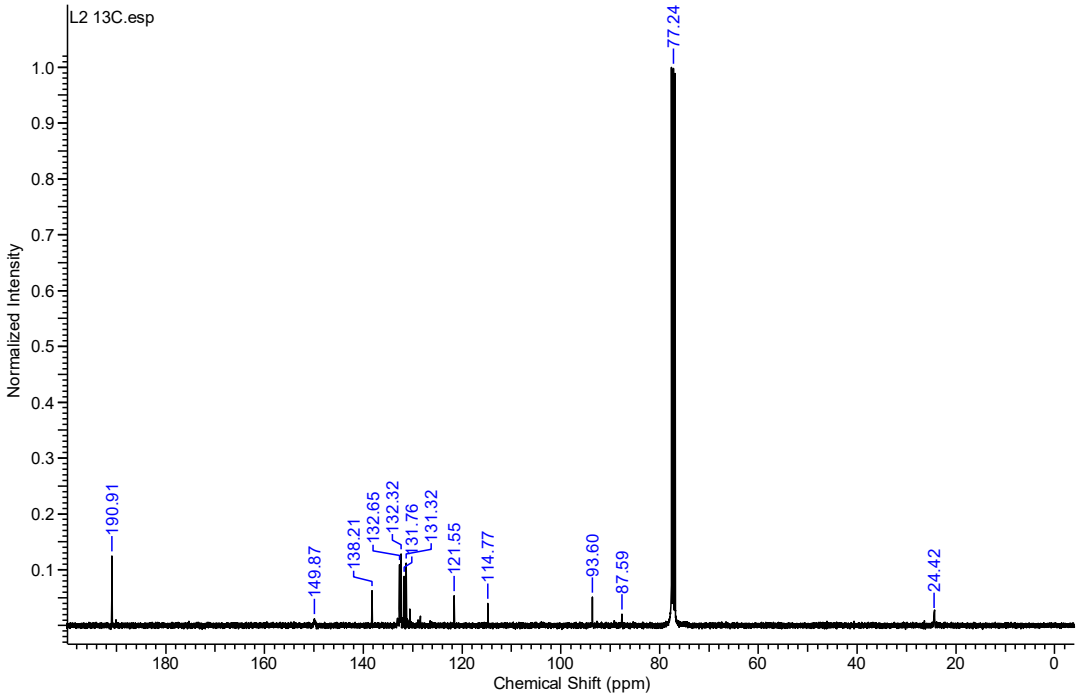

Figure B. 10 ^{13}C-NMR (100 MHz, $CDCl_3$) spectrum of 4-hydroxy-3-(4-(pyridin-4-ylethynyl)phenyl)pent-3-en-2-one [**L2**].

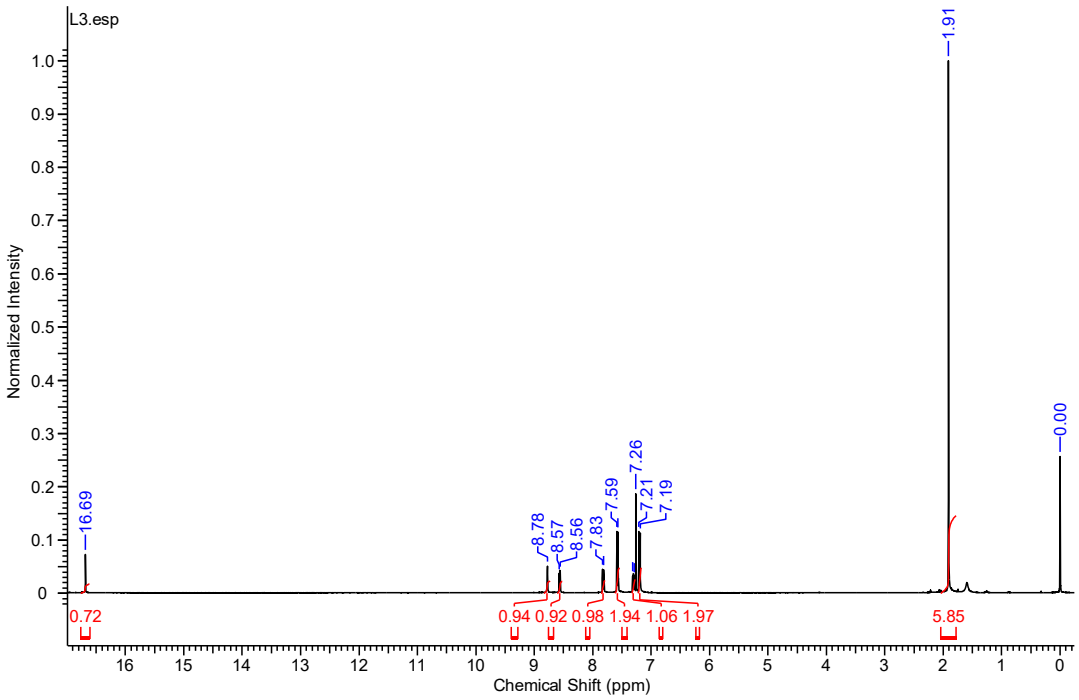

Figure B. 11 ^{1}H-NMR (400 MHz, $CDCl_3$) spectrum of 4-hydroxy-3-(4-(pyridin-3-ylethynyl)phenyl)pent-3-en-2-one [**L3**].

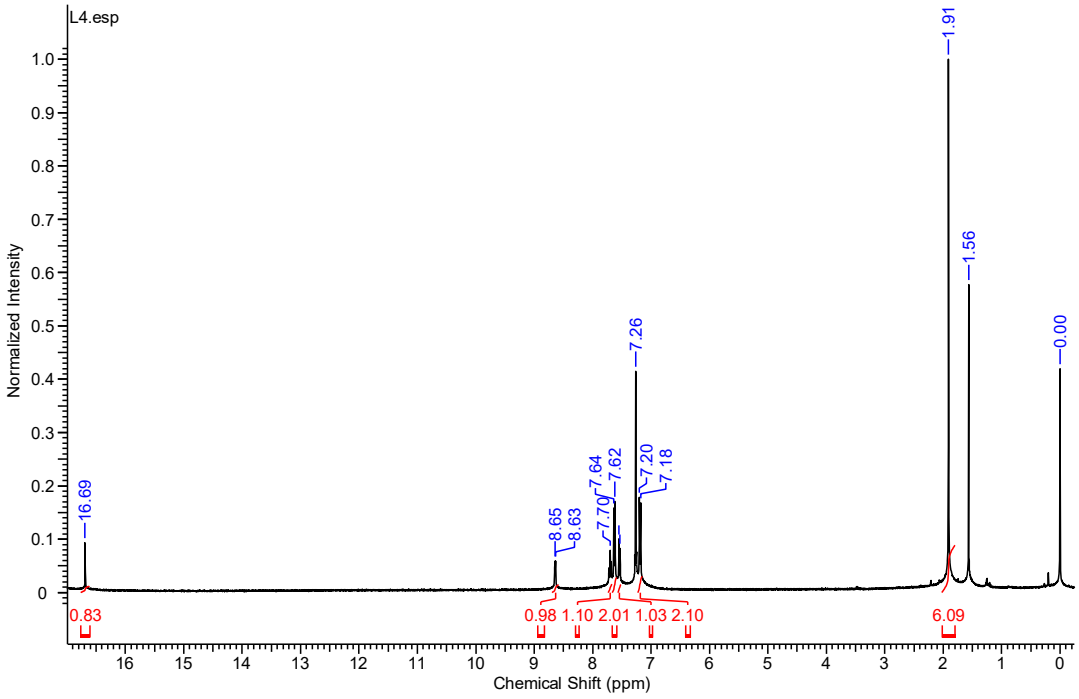

Figure B. 12 ^{1}H-NMR (400 MHz, $CDCl_3$) spectrum of 4-hydroxy-3-(4-(pyridin-2-ylethynyl)phenyl)pent-3-en-2-one [**L4**].

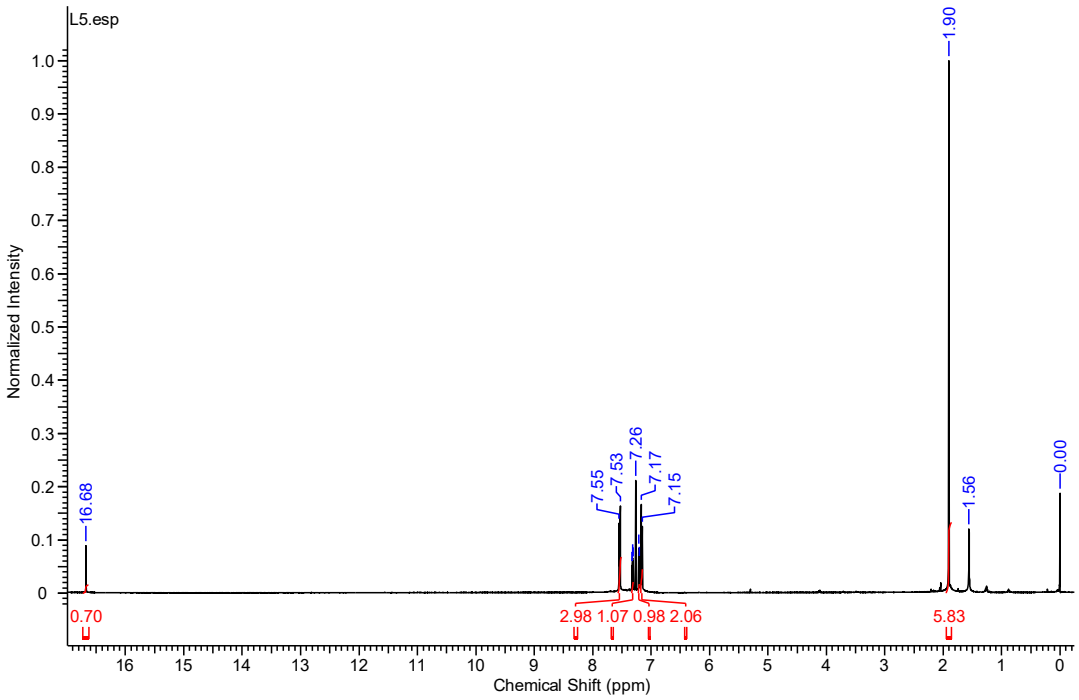

Figure B. 13 ^{1}H-NMR (400 MHz, $CDCl_3$) spectrum of 4-hydroxy-3-(4-(thiophen-3-ylethynyl)phenyl)pent-3-en-2-one [**L5**].

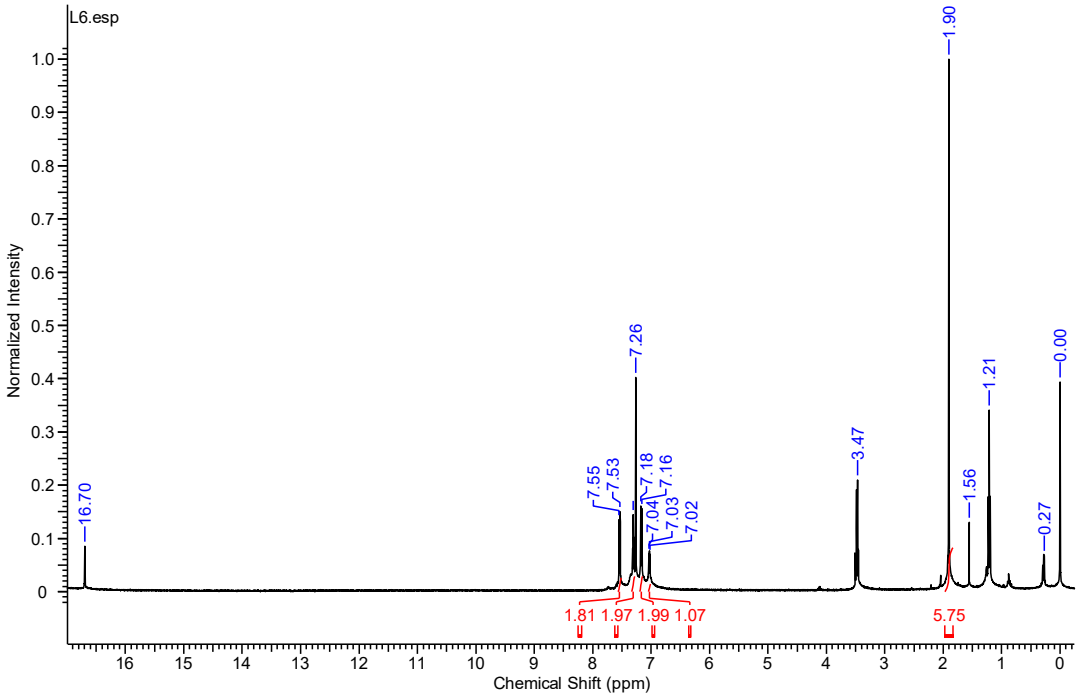

Figure B. 14 ^{1}H-NMR (400 MHz, $CDCl_3$) spectrum of 4-hydroxy-3-(4-(thiophen-2-ylethynyl)phenyl)pent-3-en-2-one [**L6**].

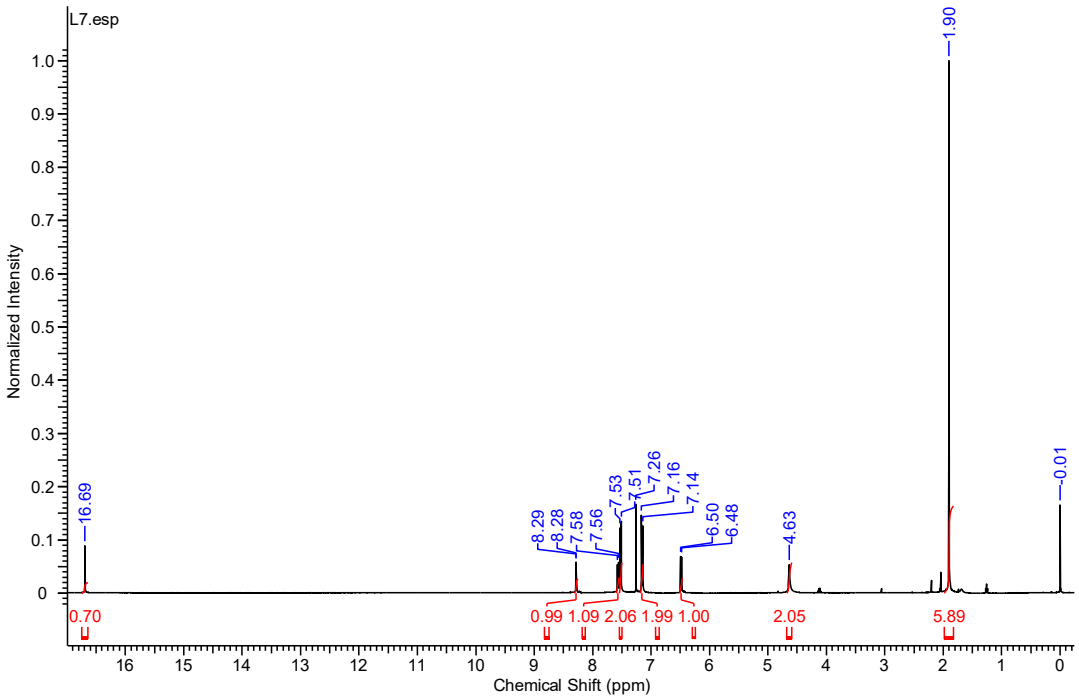

Figure B. 15 ^{1}H-NMR (400 MHz, $CDCl_3$) spectrum of 3-(4-((6-aminopyridin-3-yl)ethynyl)phenyl)-4-hydroxypent-3-en-2-one (**L7**).

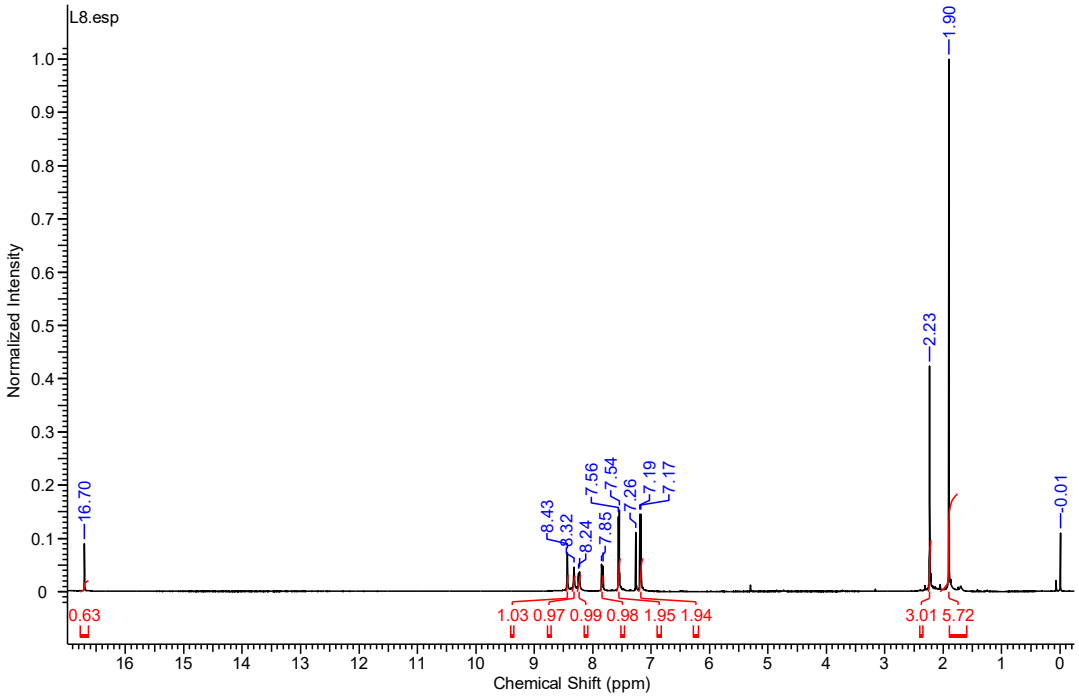

Figure B. 16 ^{1}H-NMR (400 MHz, $CDCl_3$) spectrum of *N*-(5-((4-(2-hydroxy-4-oxopent-2-en-3-yl)phenyl)ethynyl)pyridin-2-yl)acetamide (**L8**).

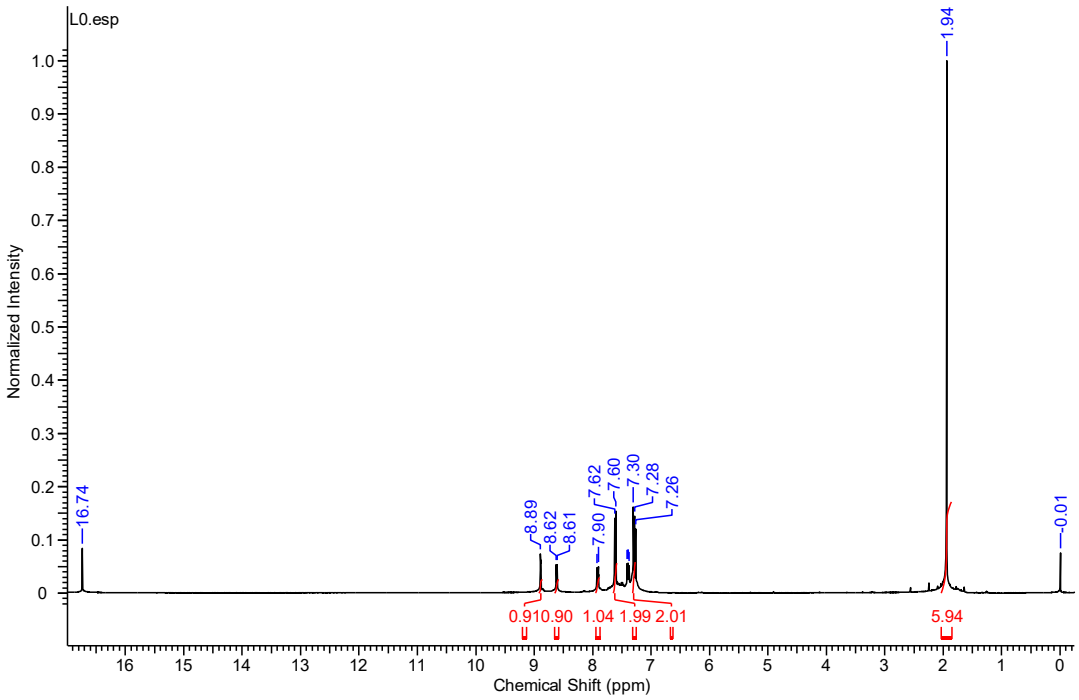

Figure B. 17 ^{1}H-NMR (400 MHz, $CDCl_3$) spectrum of 4-hydroxy-3-(4-(pyridin-3-yl)phenyl)pent-3-en-2-one (**L0**).

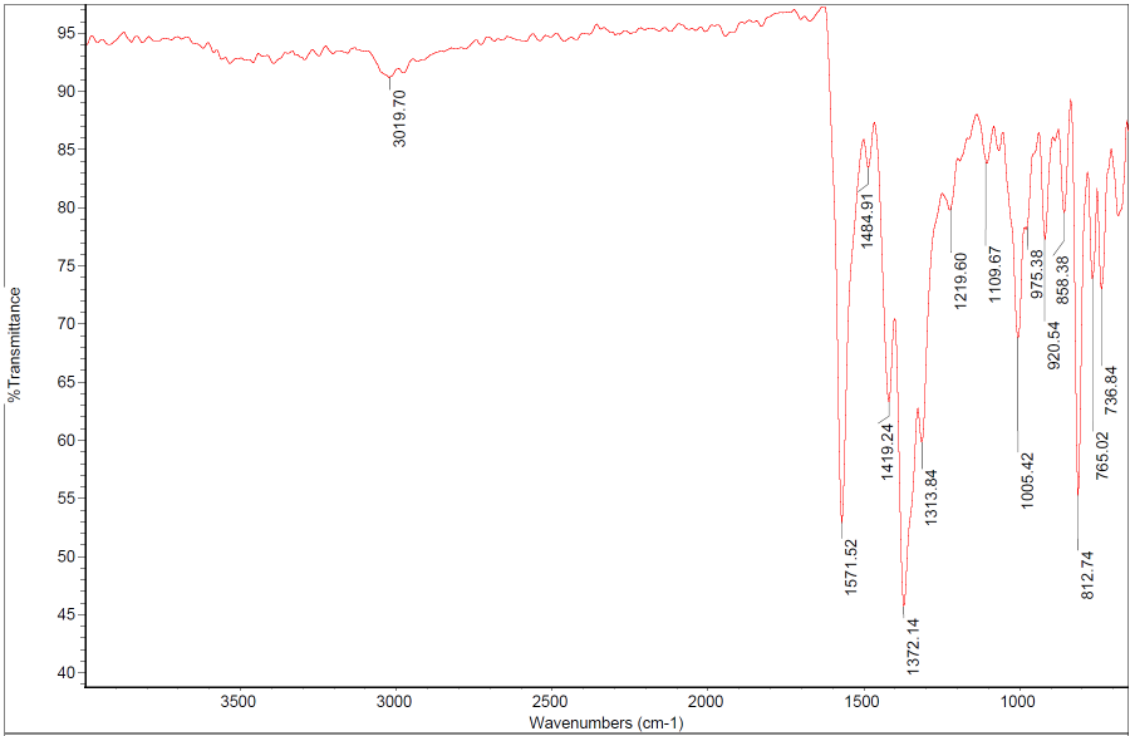

Figure B. 18 FT-IR spectrum of $[Cu(\mathbf{L1})_2(MeOH)_2]_n$.

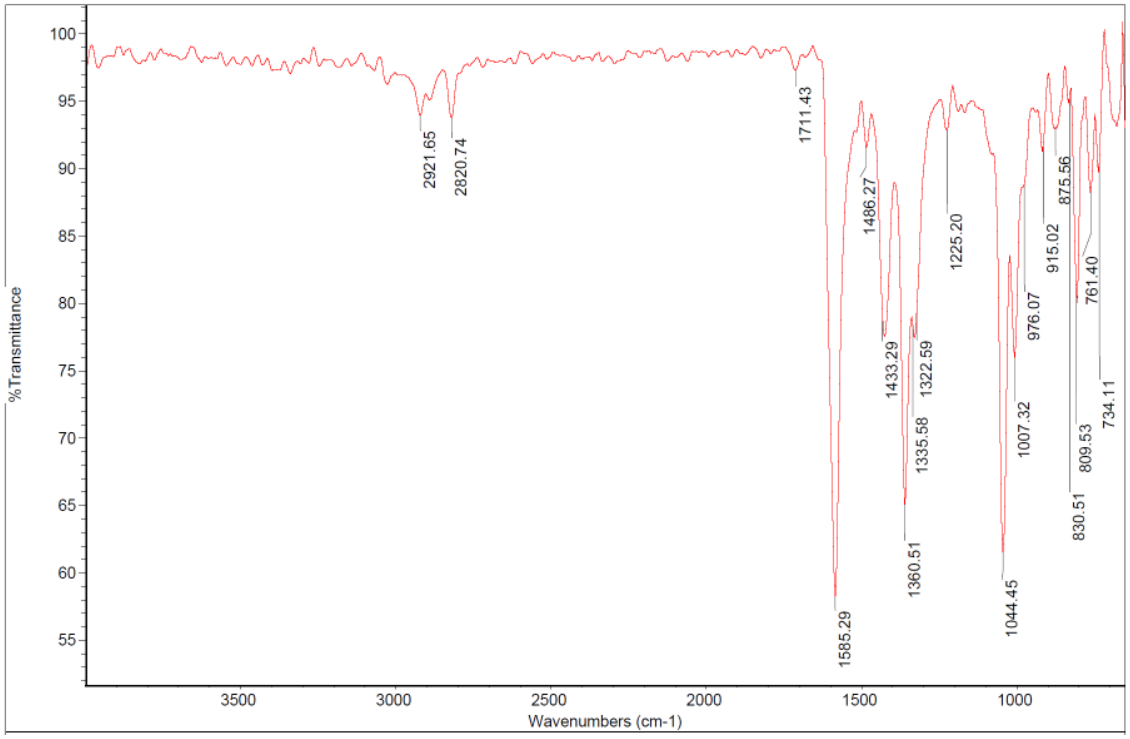

Figure B. 19 FT-IR spectrum of $[Fe(\mathbf{L1})_3]_n$.

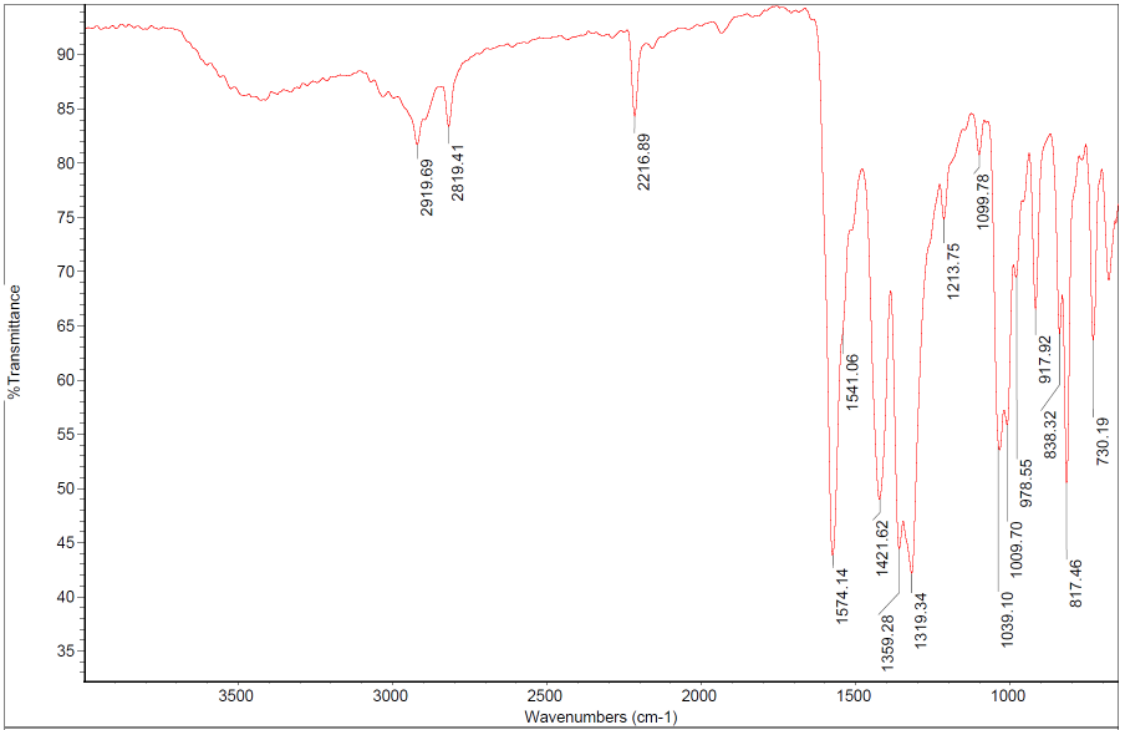

Figure B. 20 FT-IR spectrum of [Fe(**L2**)$_3$].

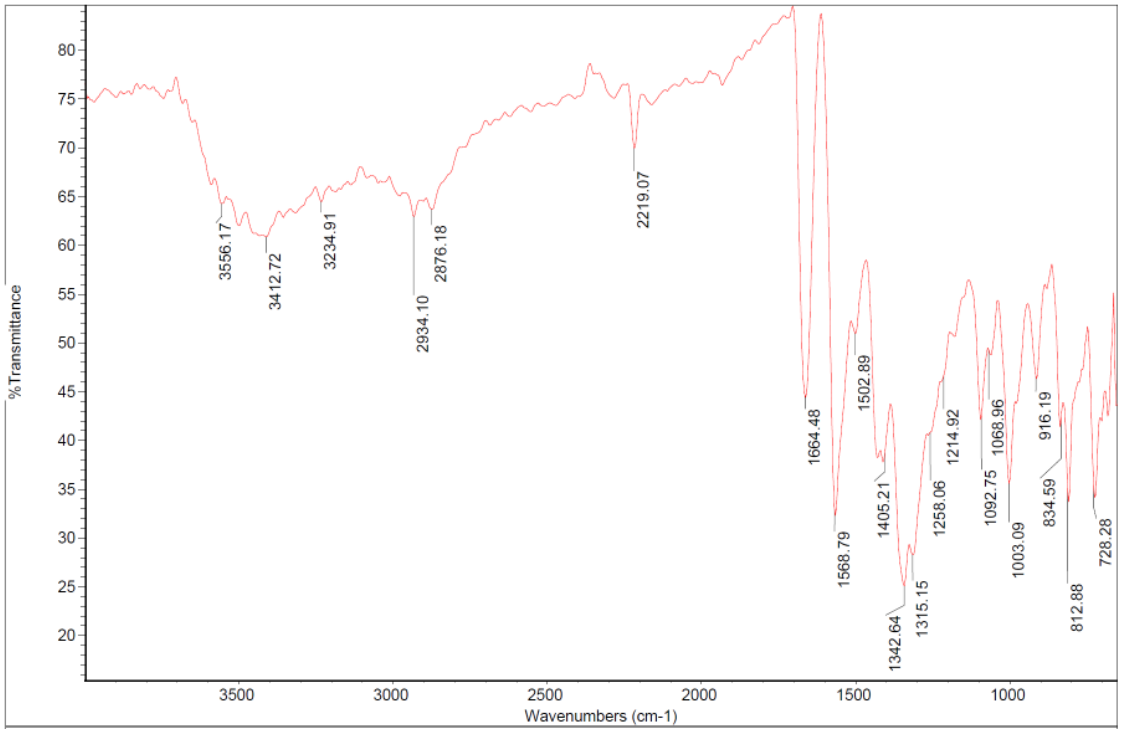

Figure B. 21 FT-IR spectrum of [Cu(**L2**)$_2$(MeOH)$_2$].

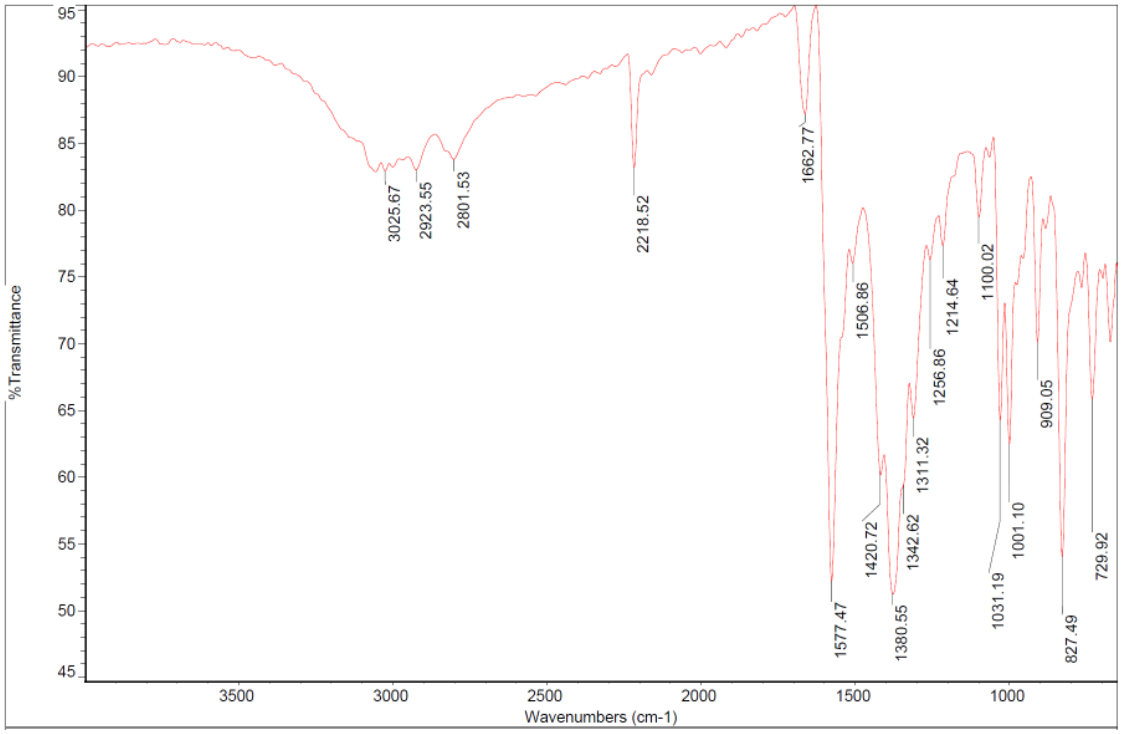

Figure B. 22 FT-IR spectrum of $[Zn(\mathbf{L2})_2(MeOH)_2]$.

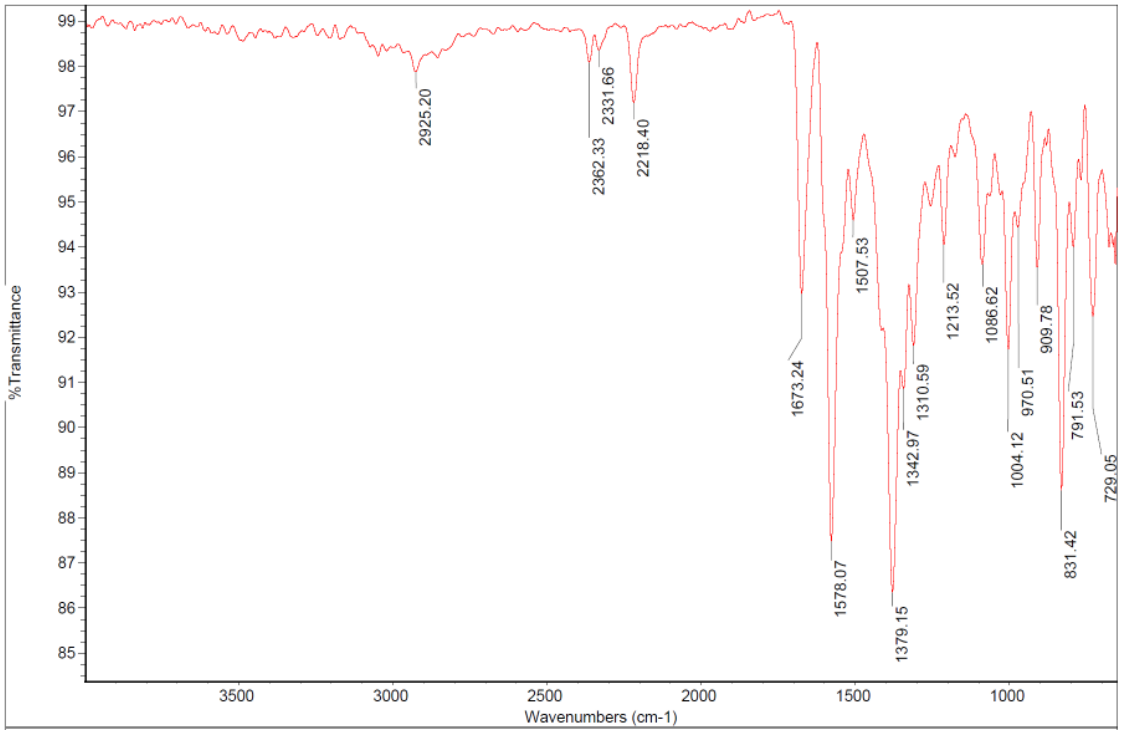

Figure B. 23 FT-IR spectrum of $[Co(\mathbf{L2})_2]_n$.

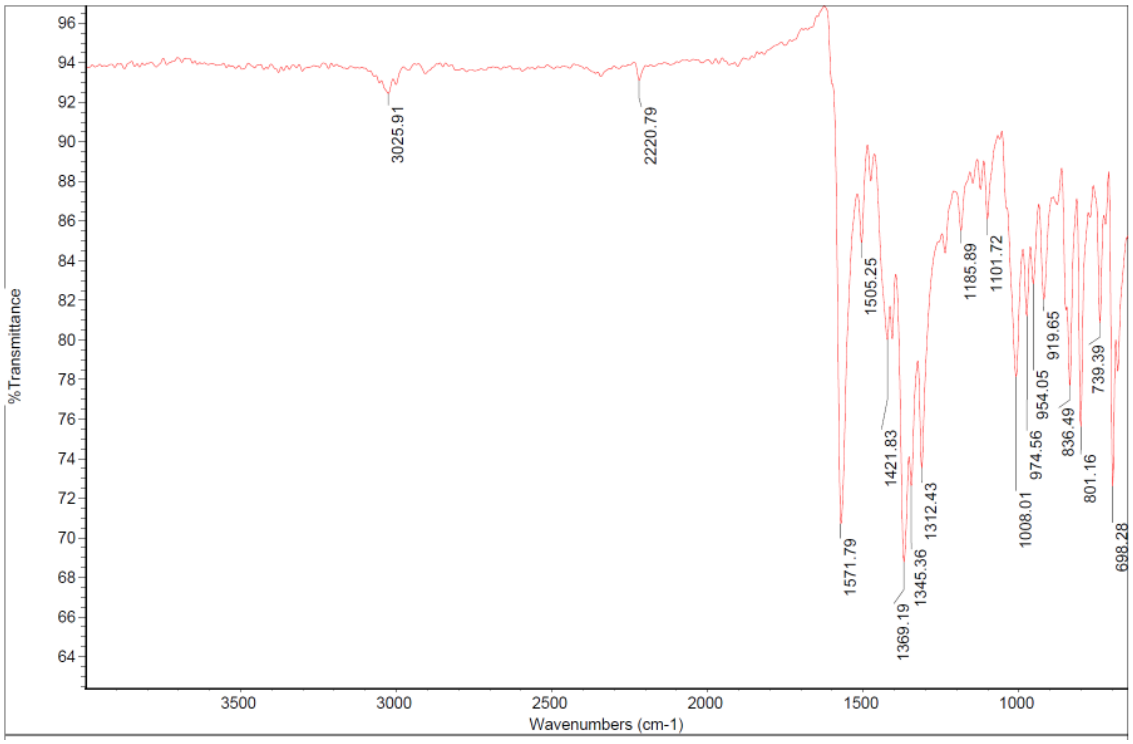

Figure B. 24 FT-IR spectrum of [Cu(**L3**)$_2$].

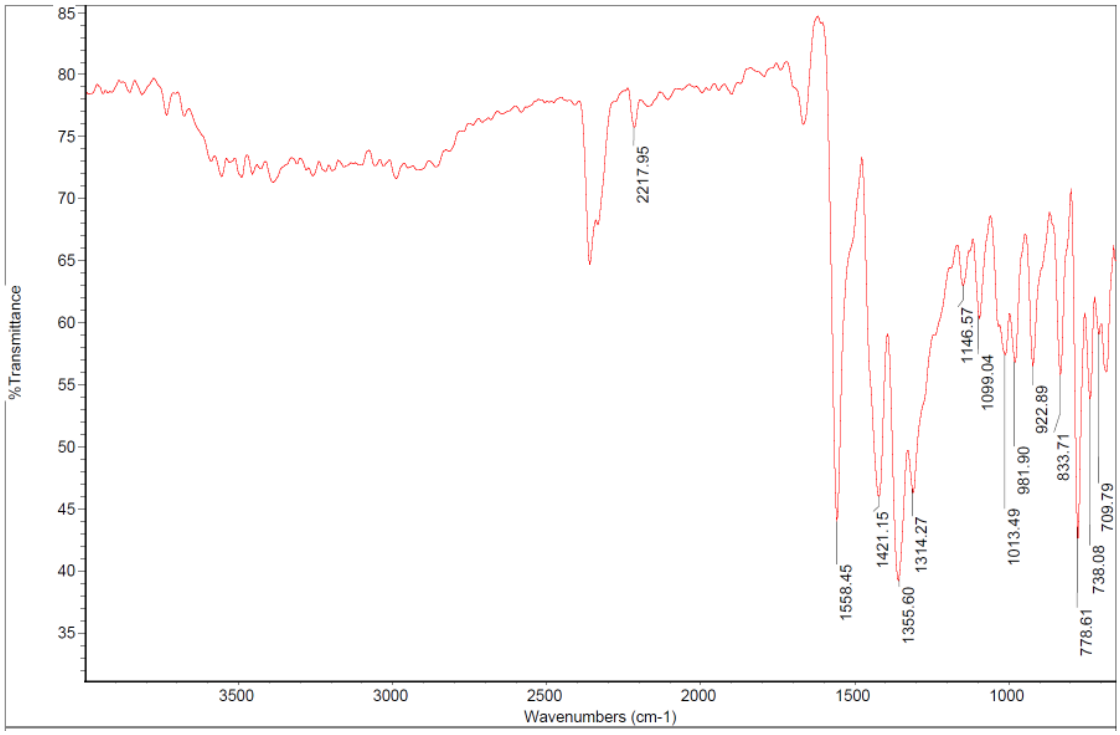

Figure B. 25 FT-IR spectrum of [Cu(**L4**)$_2$].

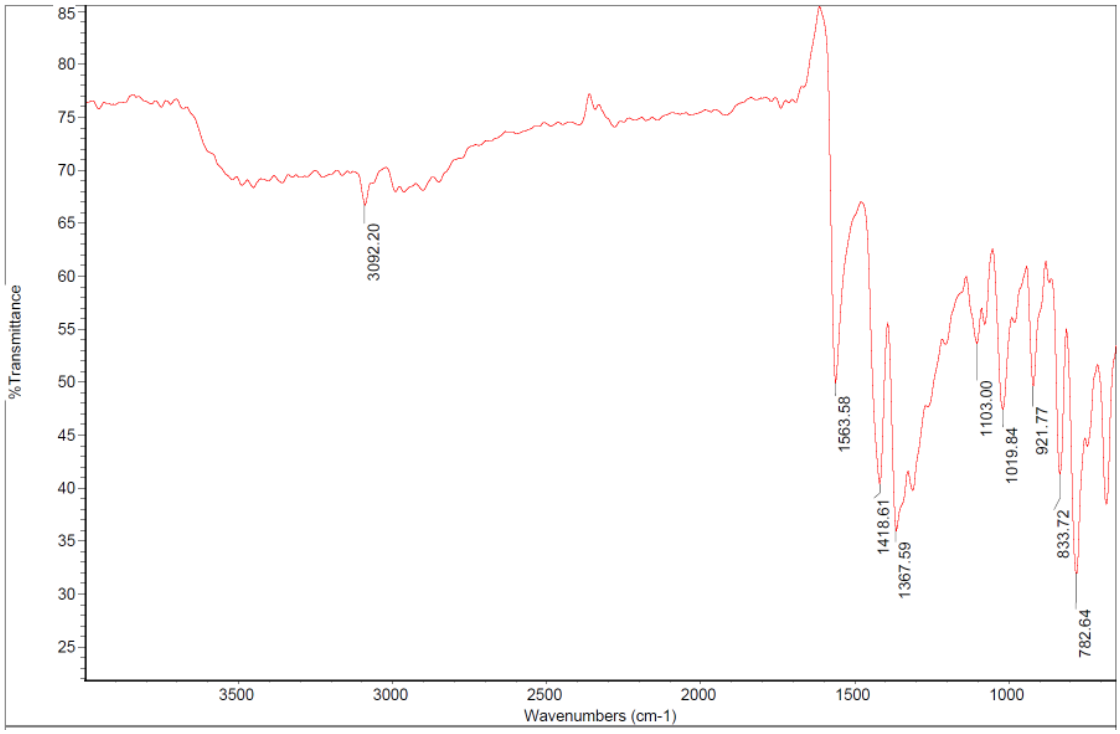

Figure B. 26 FT-IR spectrum of [Cu(**L5**)$_2$].

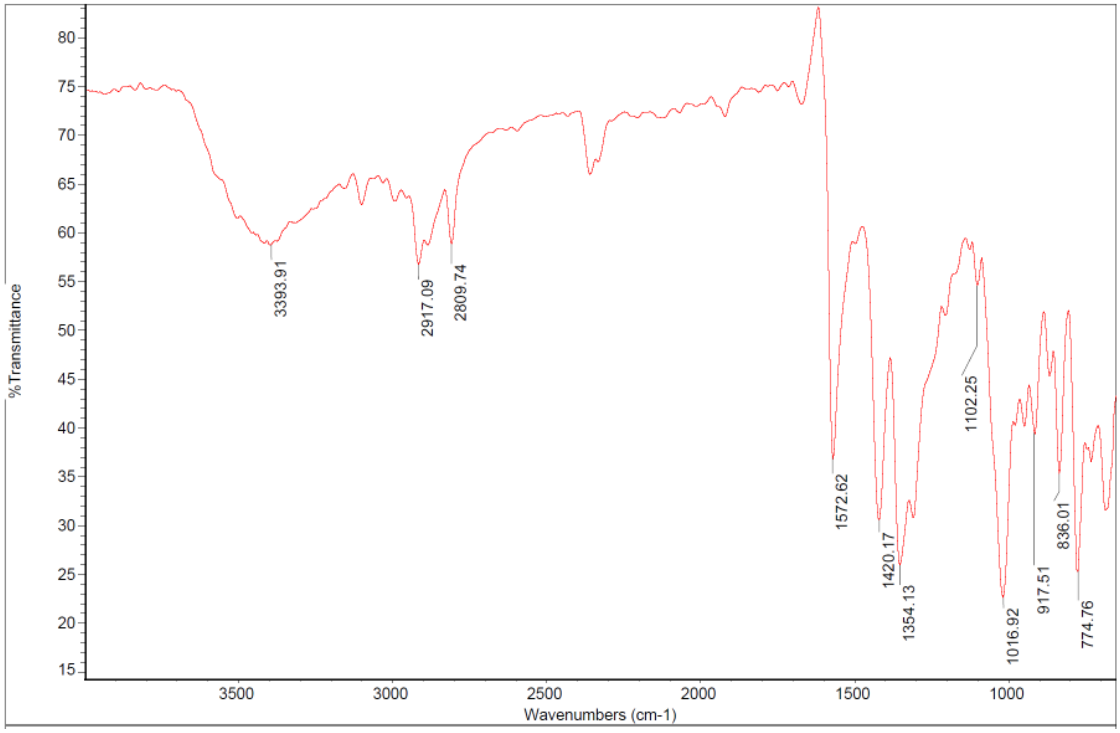

Figure B. 27 FT-IR spectrum of [Cu(**L5**)(OMe)]$_2$.

Appendix C - Additional material for Chapter 4

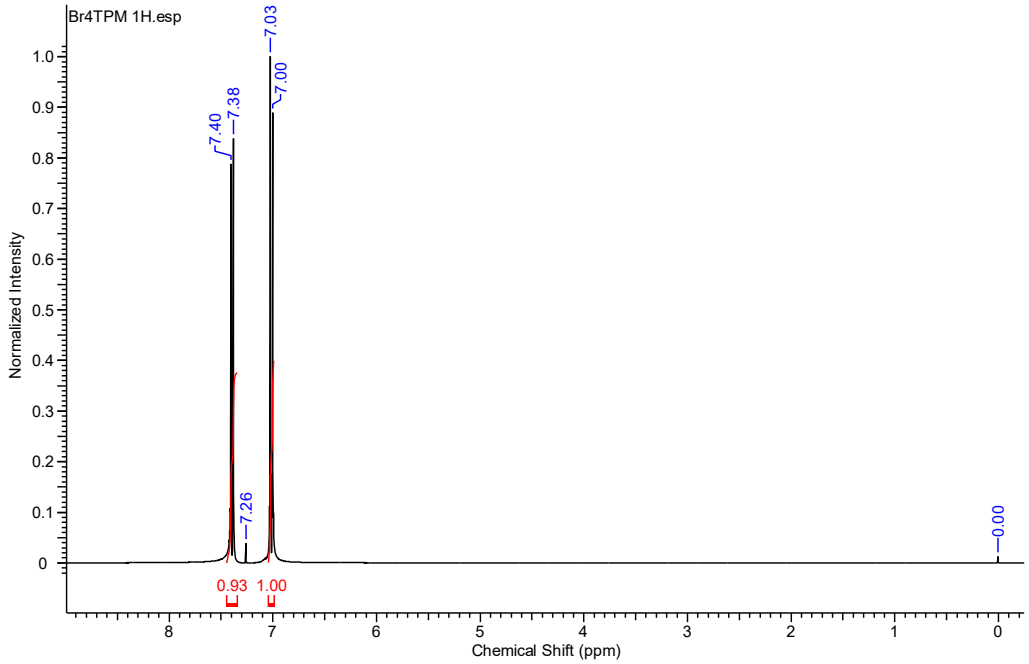

Figure C. 1 ^{1}H-NMR (400 MHz, $CDCl_3$) spectrum of tetrakis(4-bromophenyl)methane.

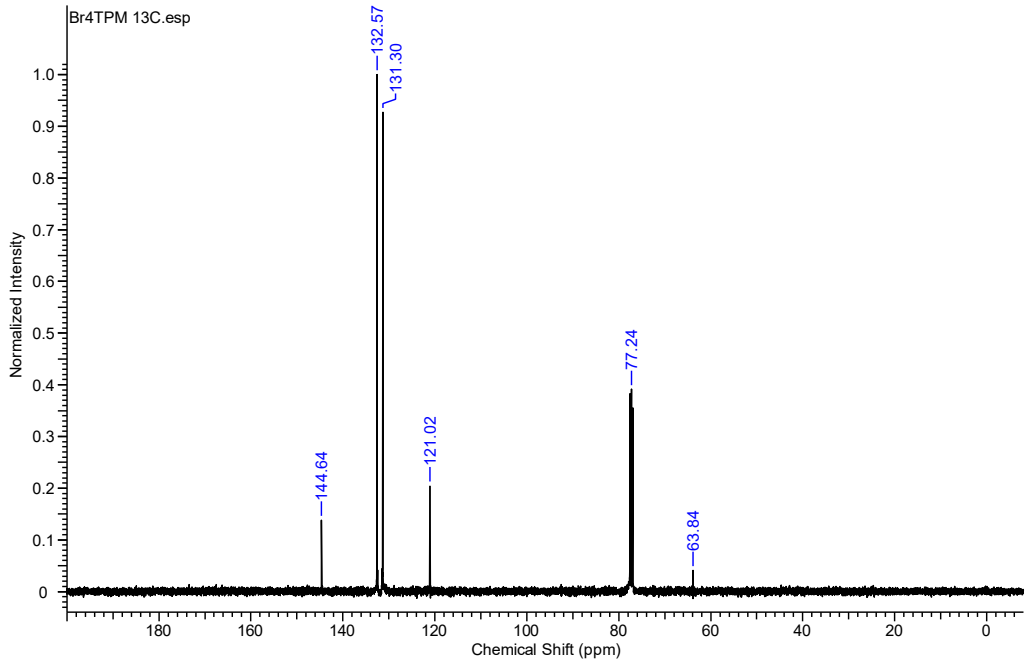

Figure C. 2 ^{13}C-NMR (100 MHz, $CDCl_3$) spectrum of tetrakis(4-bromophenyl)methane.

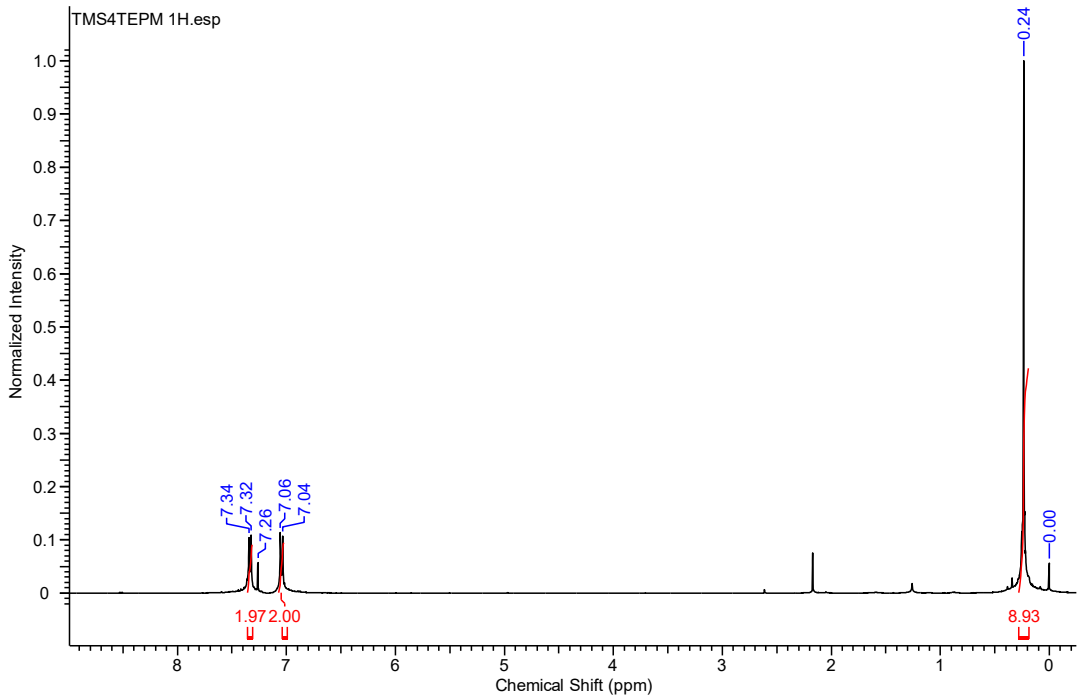

Figure C. 3 ^{1}H-NMR (400 MHz, $CDCl_3$) spectrum of tetrakis(4-((trimethylsilyl)ethynyl)phenyl)methane.

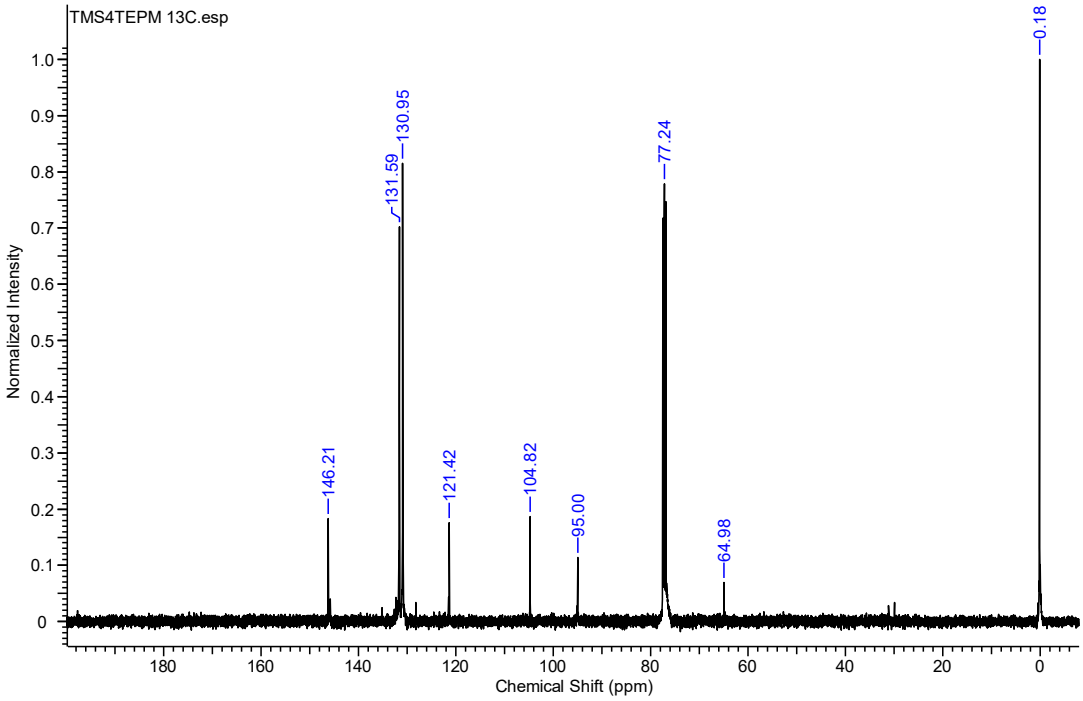

Figure C. 4 ^{13}C-NMR (100 MHz, $CDCl_3$) spectrum of tetrakis(4-((trimethylsilyl)ethynyl)phenyl)methane.

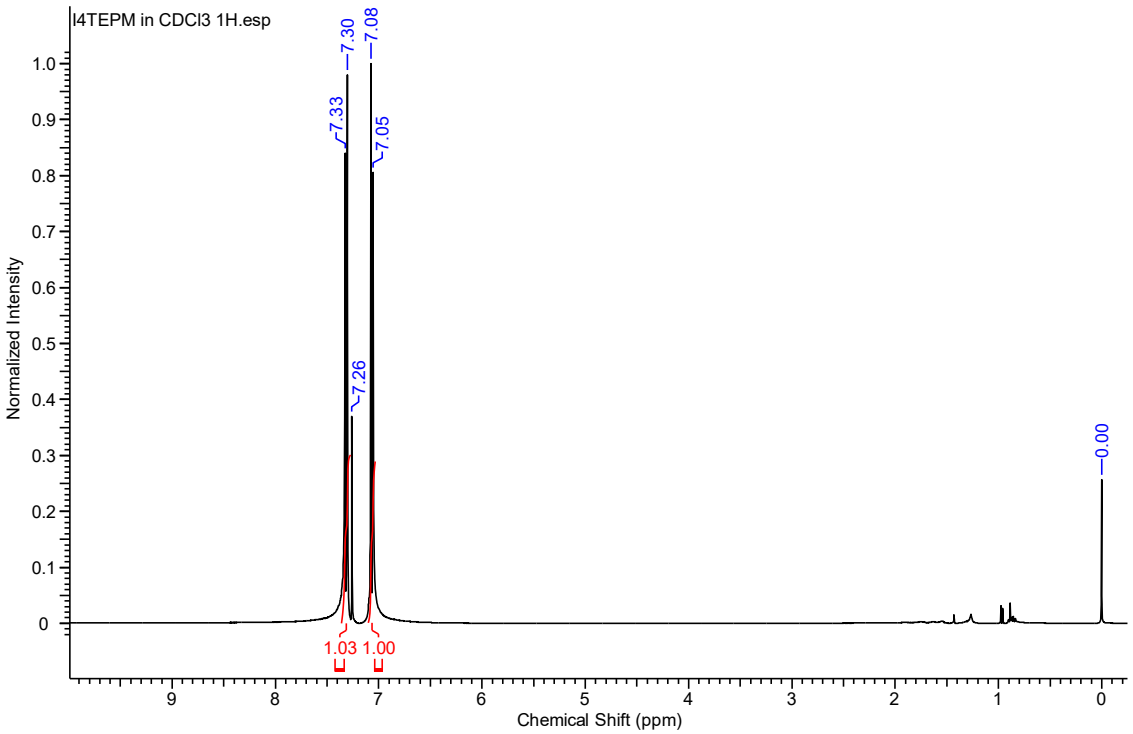

Figure C. 5 ^{1}H-NMR (400 MHz, $CDCl_3$) spectrum of tetrakis(4-(iodoethynyl)phenyl)methane.

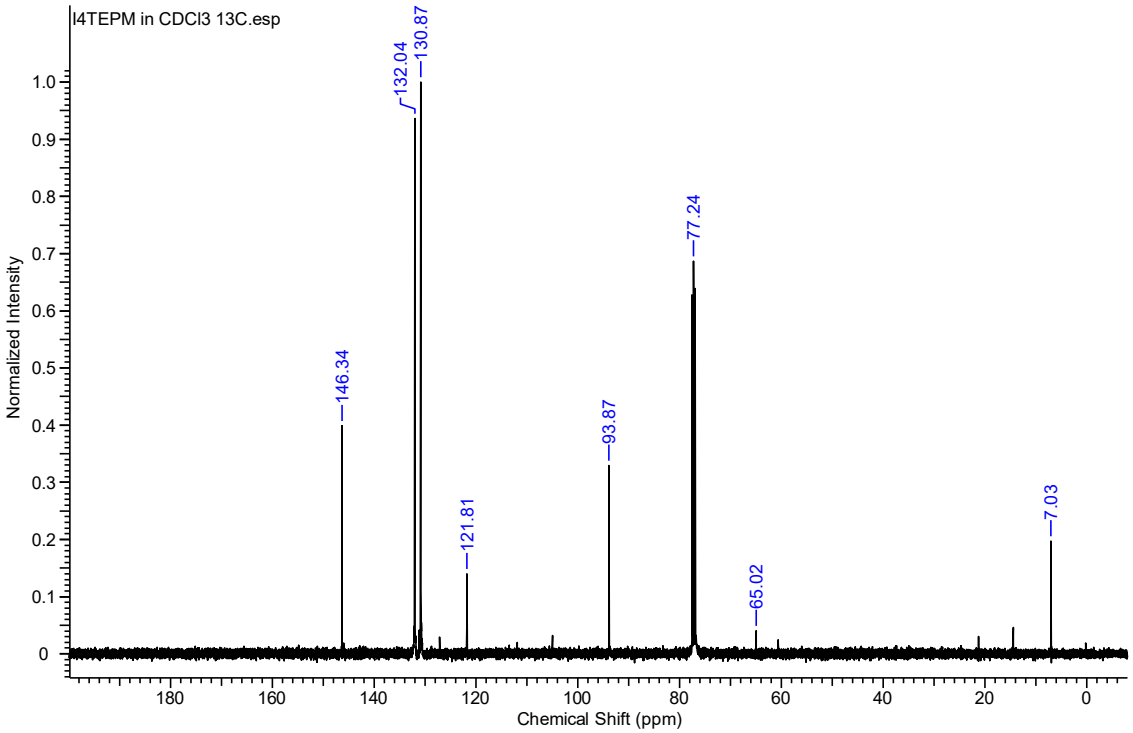

Figure C. 6 ^{13}C-NMR (100 MHz, $CDCl_3$) spectrum of tetrakis(4-(iodoethynyl)phenyl)methane.

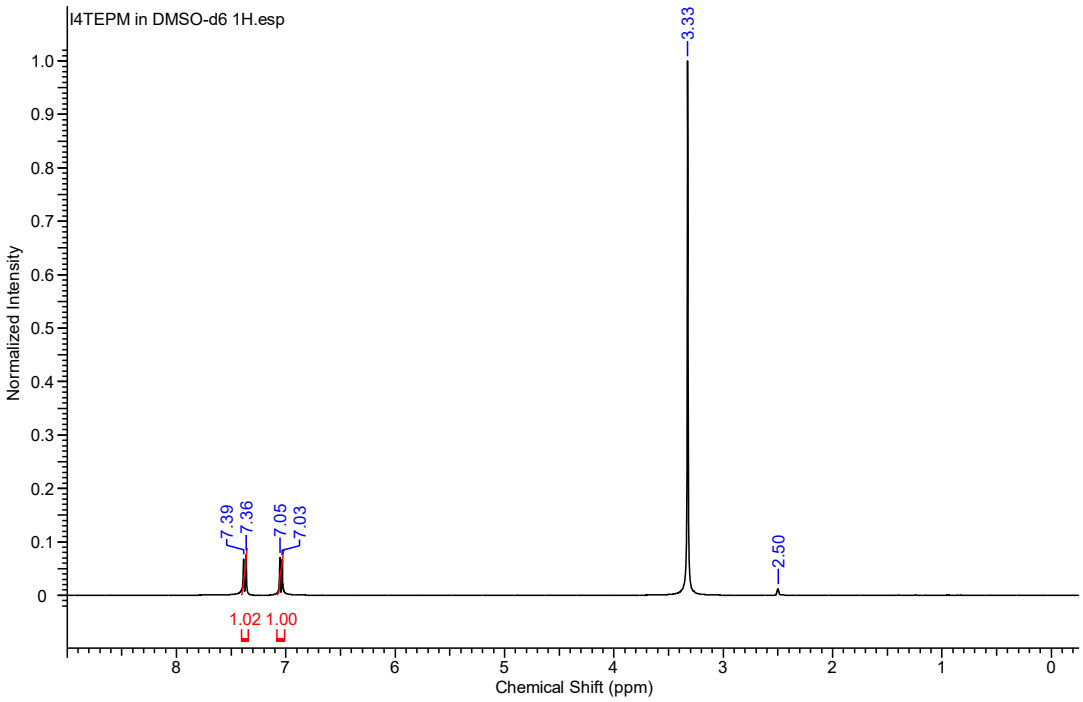

Figure C. 7 ^{1}H-NMR (400 MHz, DMSO-d6) spectrum of tetrakis(4-(iodoethynyl)phenyl)methane.

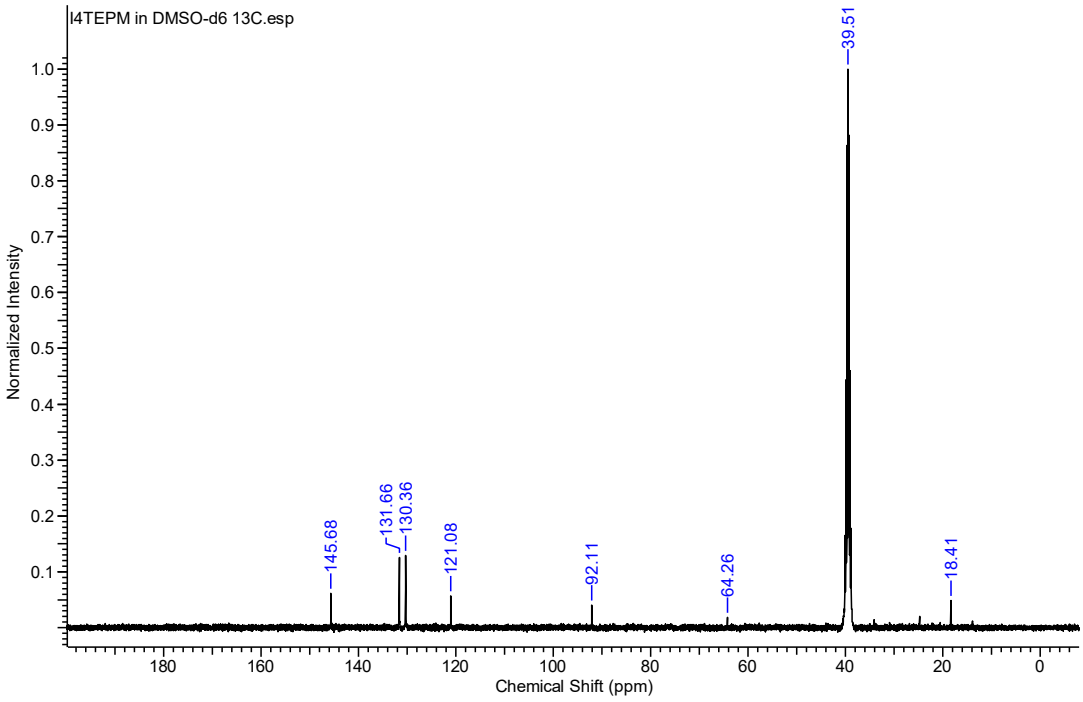

Figure C. 8 ^{13}C-NMR (100 MHz, DMSO-d6) spectrum of tetrakis(4-(iodoethynyl)phenyl)methane.

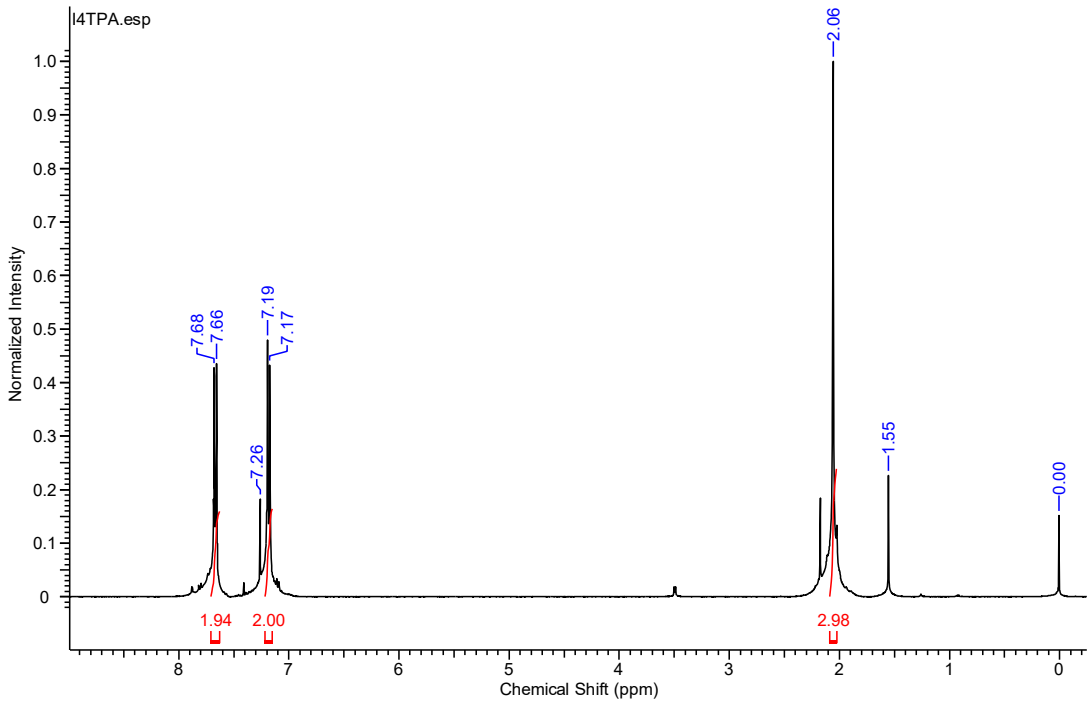

Figure C. 9 ^{1}H-NMR (400 MHz, $CDCl_3$) spectrum of 1,3,5,7-tetrakis(4-iodophenyl)adamantane (**I_4TPA**).

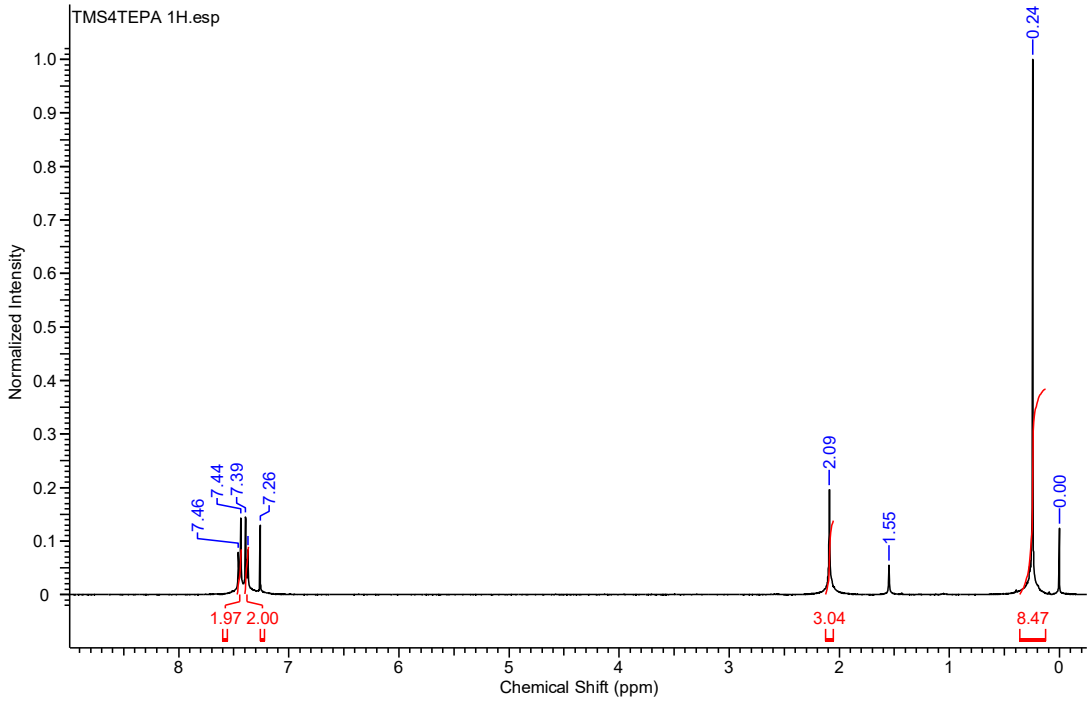

Figure C. 10 ^{1}H-NMR (400 MHz, $CDCl_3$) spectrum of 1,3,5,7-tetrakis(4-((trimethylsilyl)ethynyl)phenyl)adamantane (**TMS_4TEPA**).

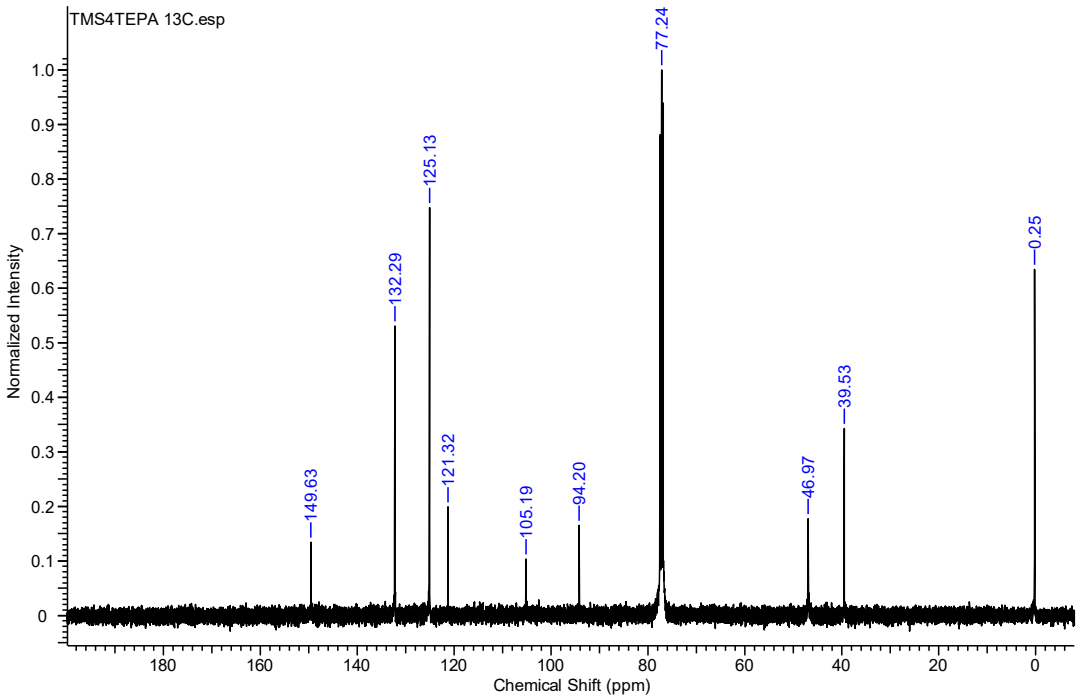

Figure C. 11 ^{13}C-NMR (100 MHz, $CDCl_3$) spectrum of 1,3,5,7-tetrakis(4-((trimethylsilyl)ethynyl)phenyl)adamantane (**TMS$_4$TEPA**).

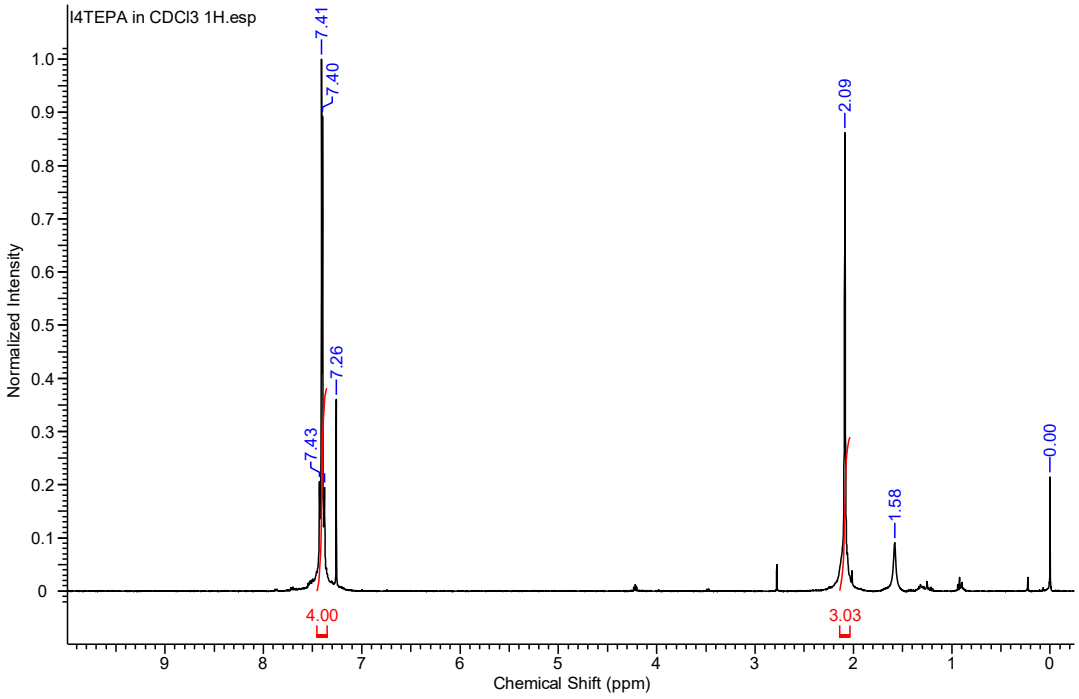

Figure C. 12 ^{1}H-NMR (400 MHz, $CDCl_3$) spectrum of 1,3,5,7-tetrakis(4-(iodoethynyl)phenyl)adamantane (**I$_4$TEPA**).

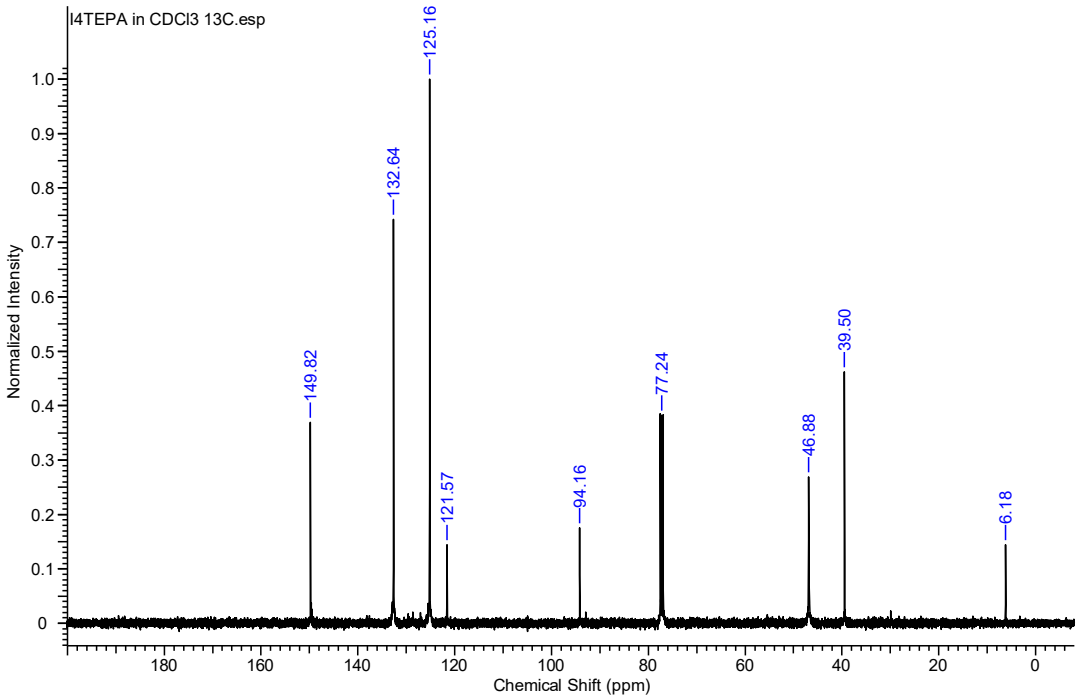

Figure C. 13 ^{13}C-NMR (100 MHz, $CDCl_3$) spectrum of 1,3,5,7-tetrakis(4-(iodoethynyl)phenyl)adamantane (**I$_4$TEPA**).

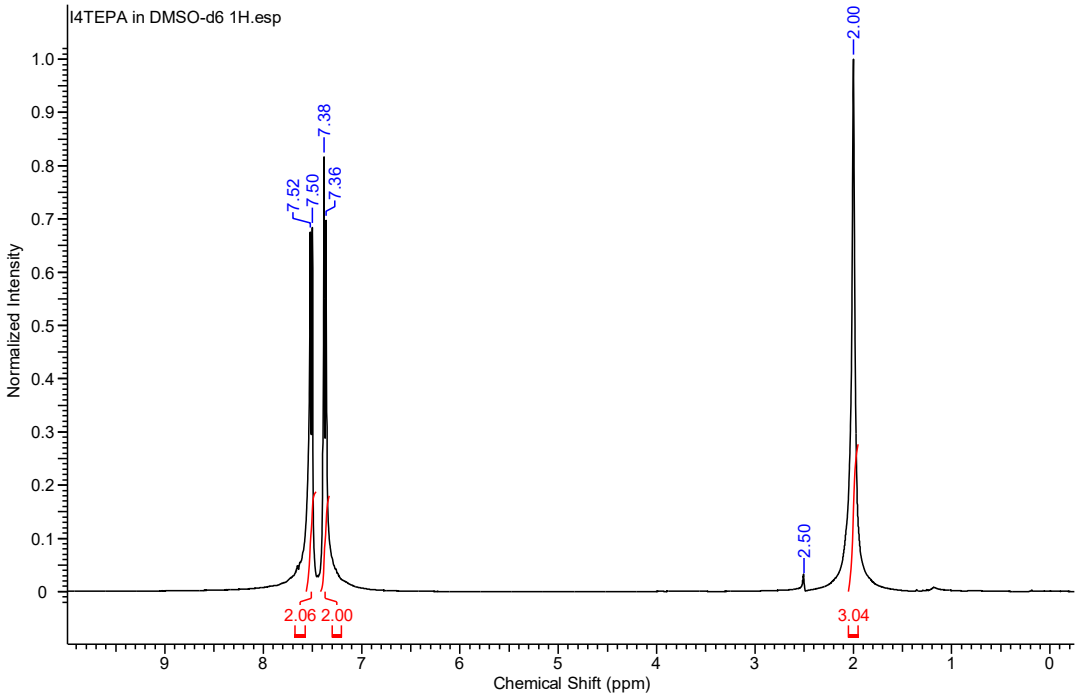

Figure C. 14 ^{1}H-NMR (400 MHz, DMSO-d6) spectrum of 1,3,5,7-tetrakis(4-(iodoethynyl)phenyl)adamantane (**I$_4$TEPA**).

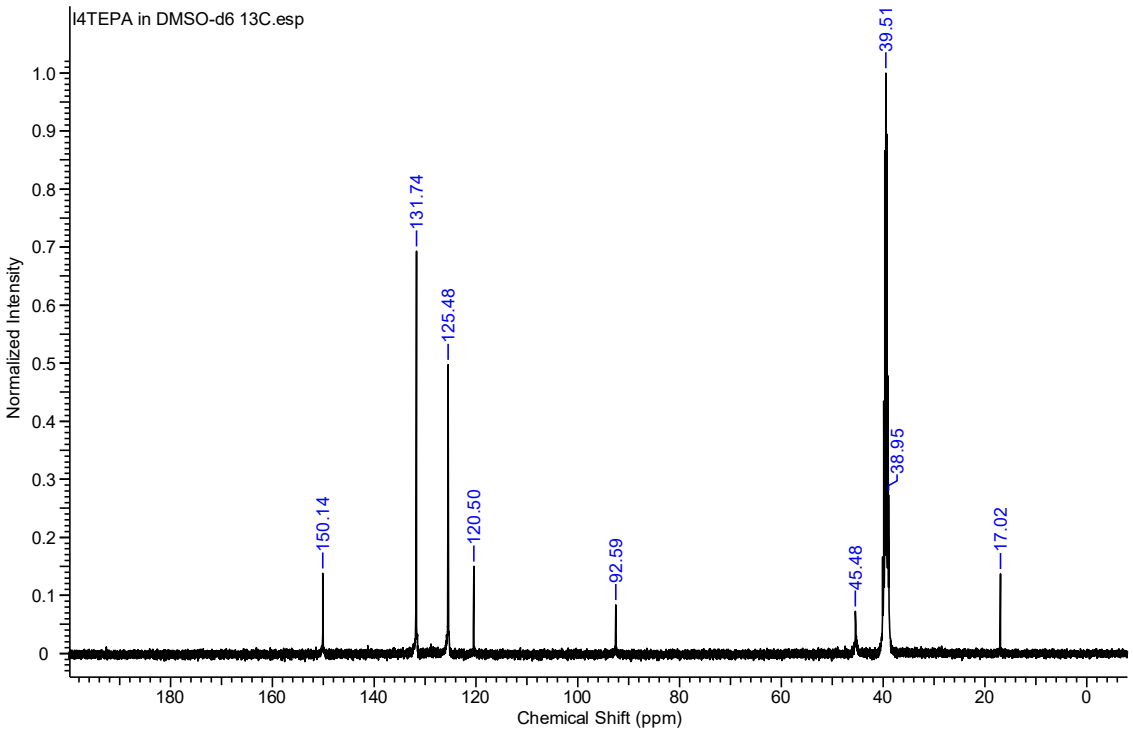

Figure C. 15 ^{13}C-NMR (100 MHz, DMSO-d6) spectrum of 1,3,5,7-tetrakis(4-(iodoethynyl)phenyl)adamantane (**I$_4$TEPA**).

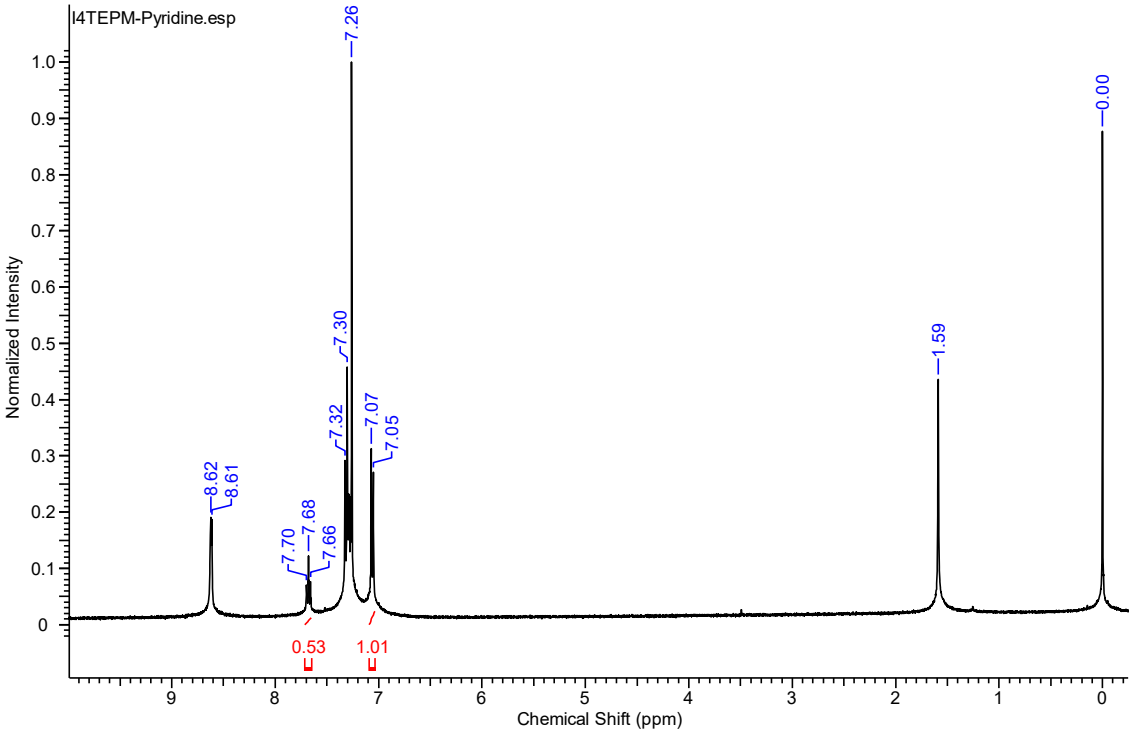

Figure C. 16 ^{1}H-NMR (400 MHz, $CDCl_3$) spectrum of **I$_4$TEPM**·4pyridine crystals.

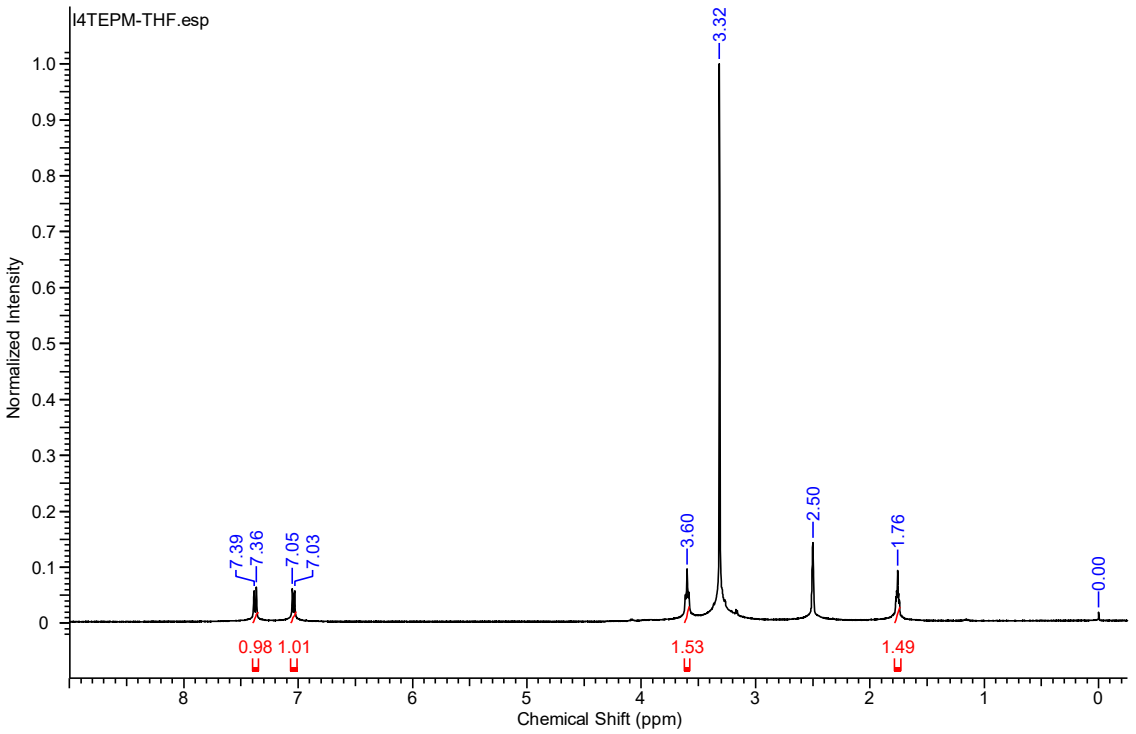

Figure C. 17 ^{1}H-NMR (400 MHz, DMSO-d6) spectrum of **I$_4$TEPM**·2THF crystals.

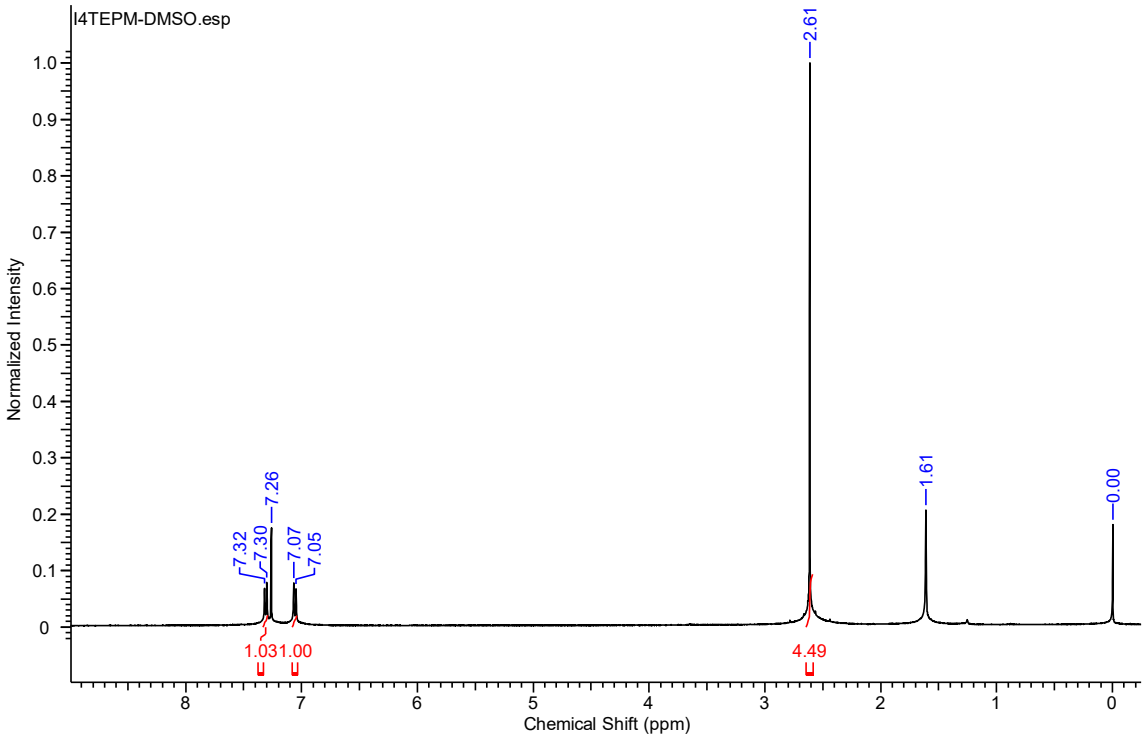

Figure C. 18 ^{1}H-NMR (400 MHz, $CDCl_3$) spectrum of **I$_4$TEPM**·2DMSO crystals.

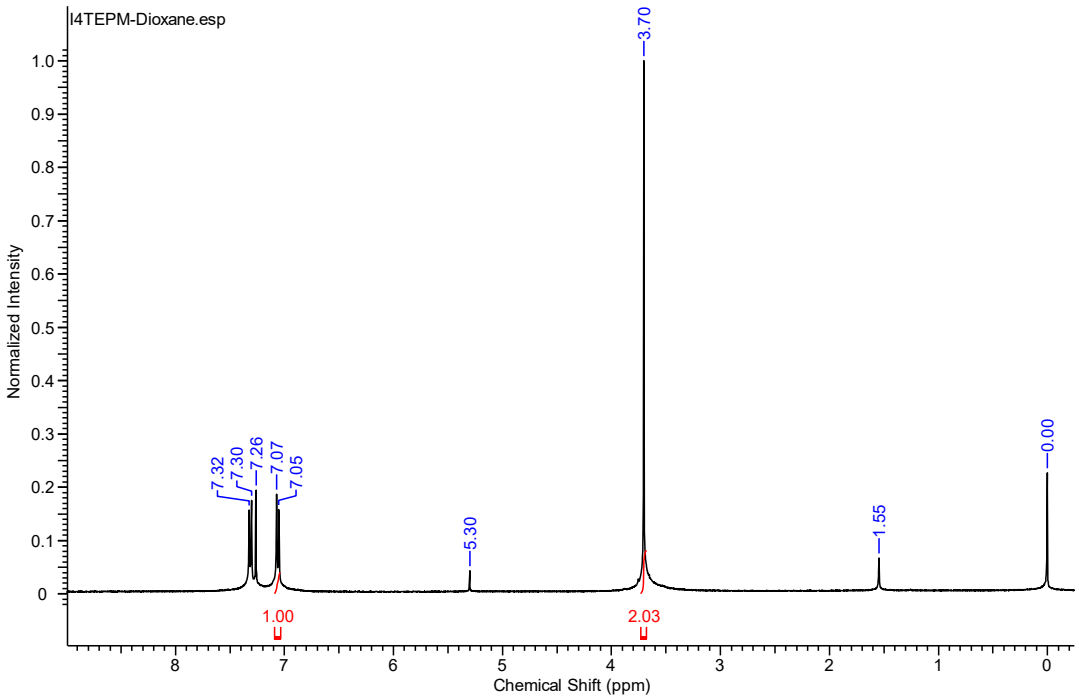

Figure C. 19 ^{1}H-NMR (400 MHz, $CDCl_3$) spectrum of **I_4TEPM**·2dioxane crystals.

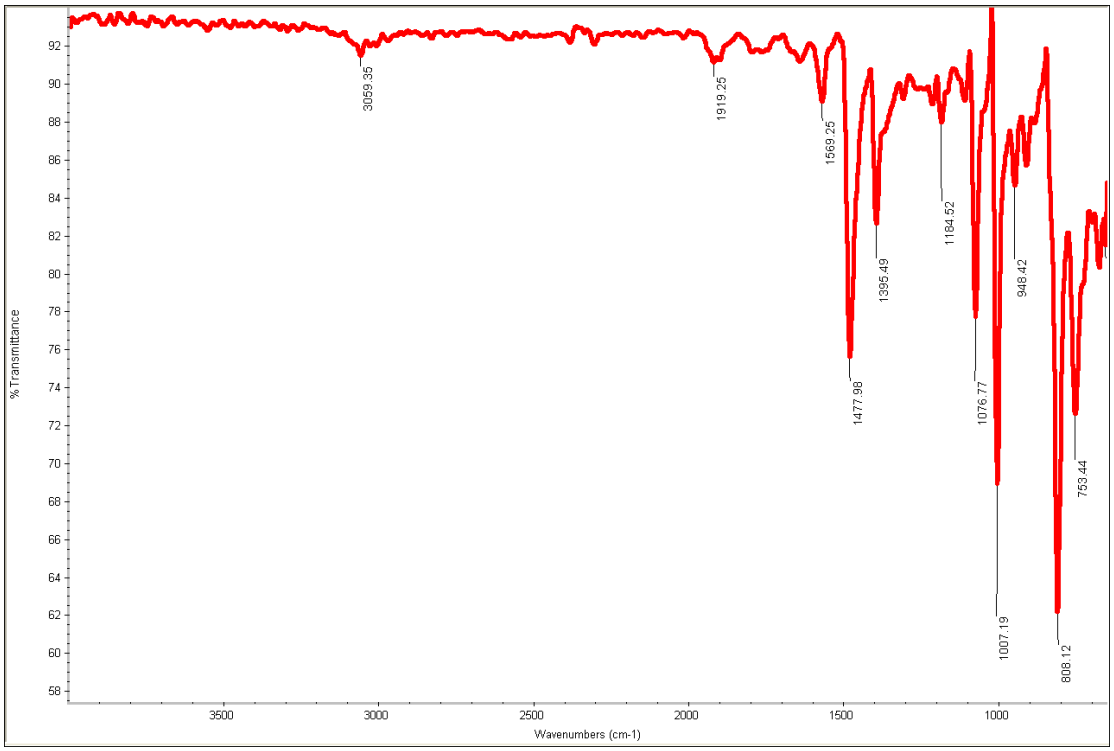

Figure C. 20 FT-IR spectrum of tetrakis(4-bromophenyl)methane.

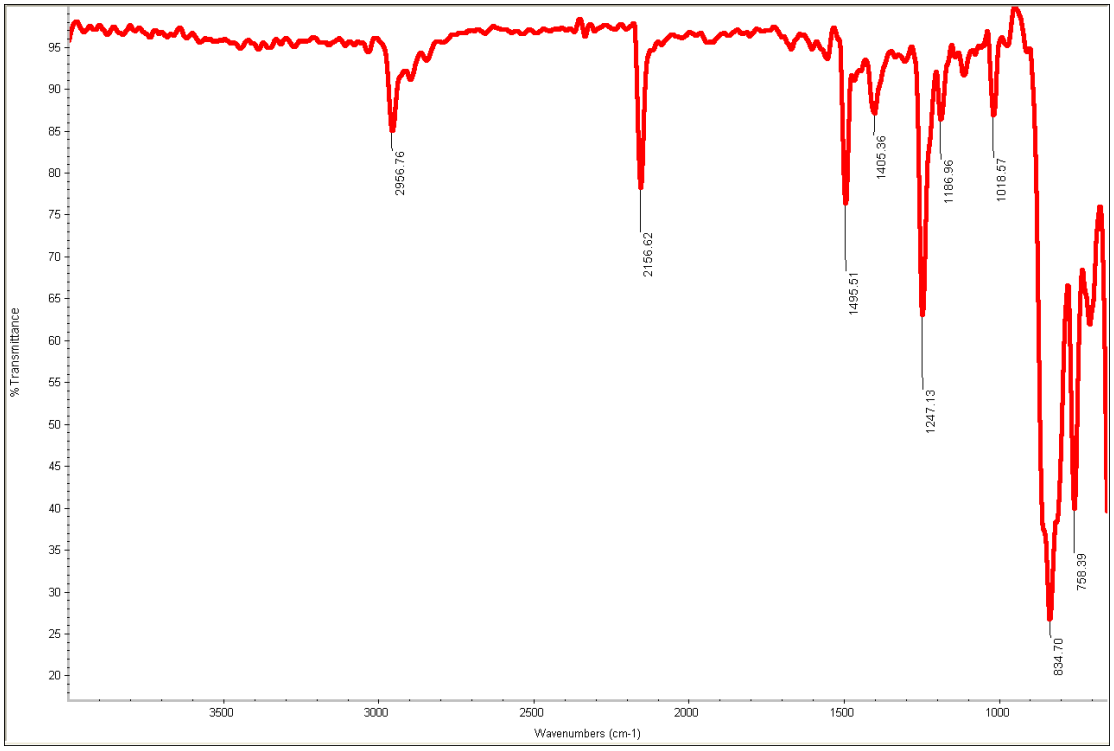

Figure C. 21 FT-IR spectrum of tetrakis(4-((trimethylsilyl)ethynyl)phenyl)methane.

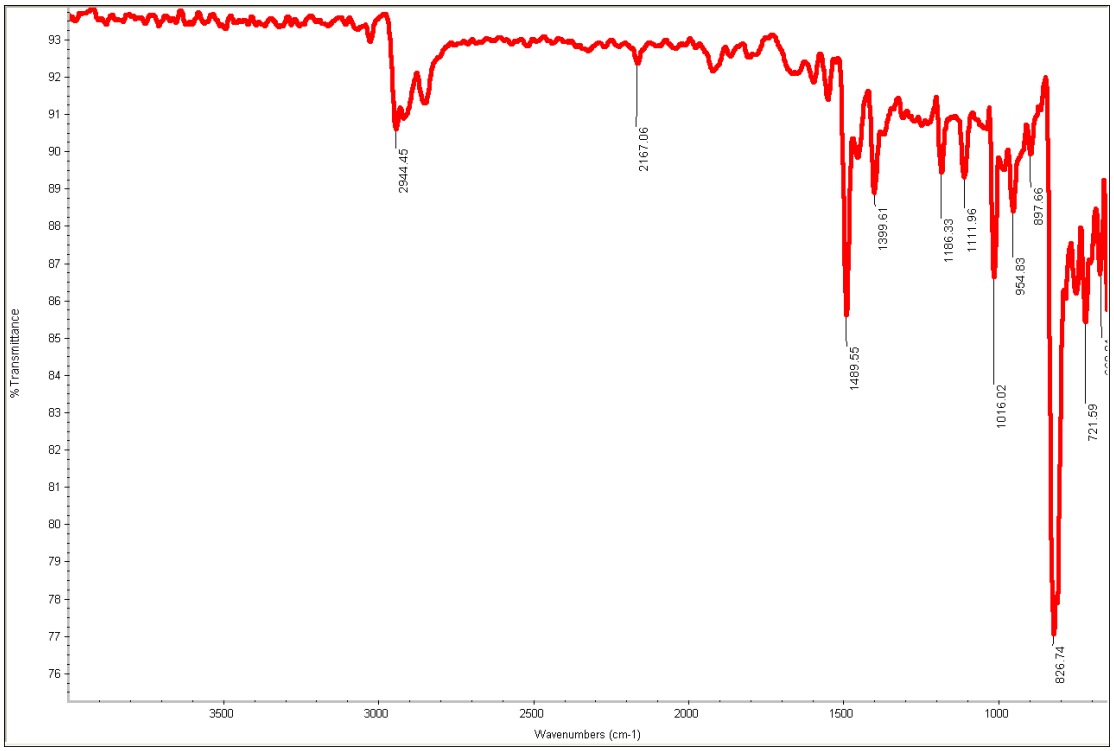

Figure C. 22 FT-IR spectrum of tetrakis(4-(iodoethynyl)phenyl)methane.

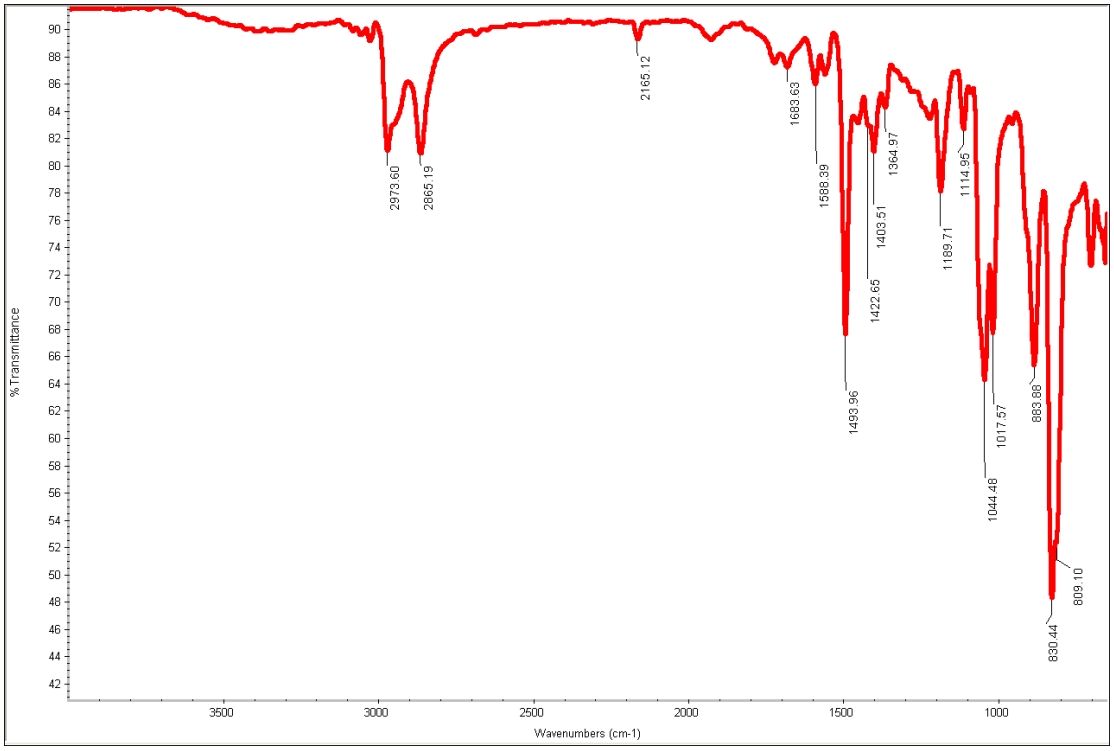

Figure C. 23 FT-IR spectrum of **I_4TEPM**·2THF crystals.

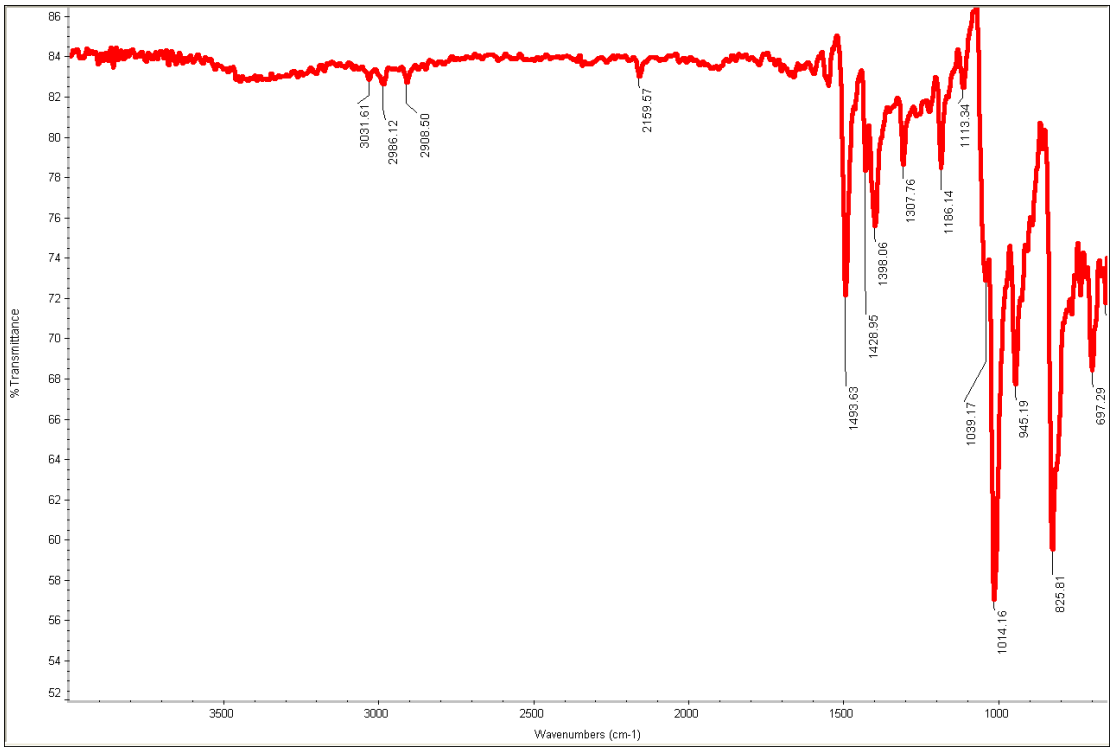

Figure C. 24 FT-IR spectrum of **I$_4$TEPM**·2DMSO crystals.

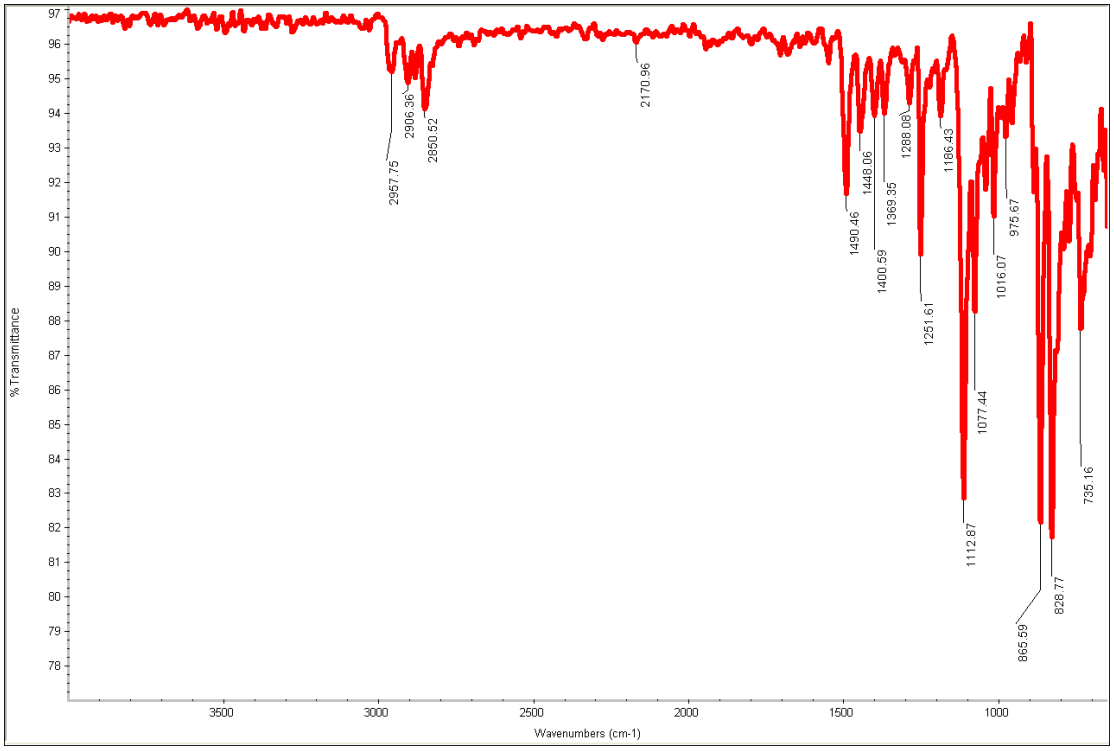

Figure C. 25 FT-IR spectrum of **I$_4$TEPM**·2dioxane crystals.

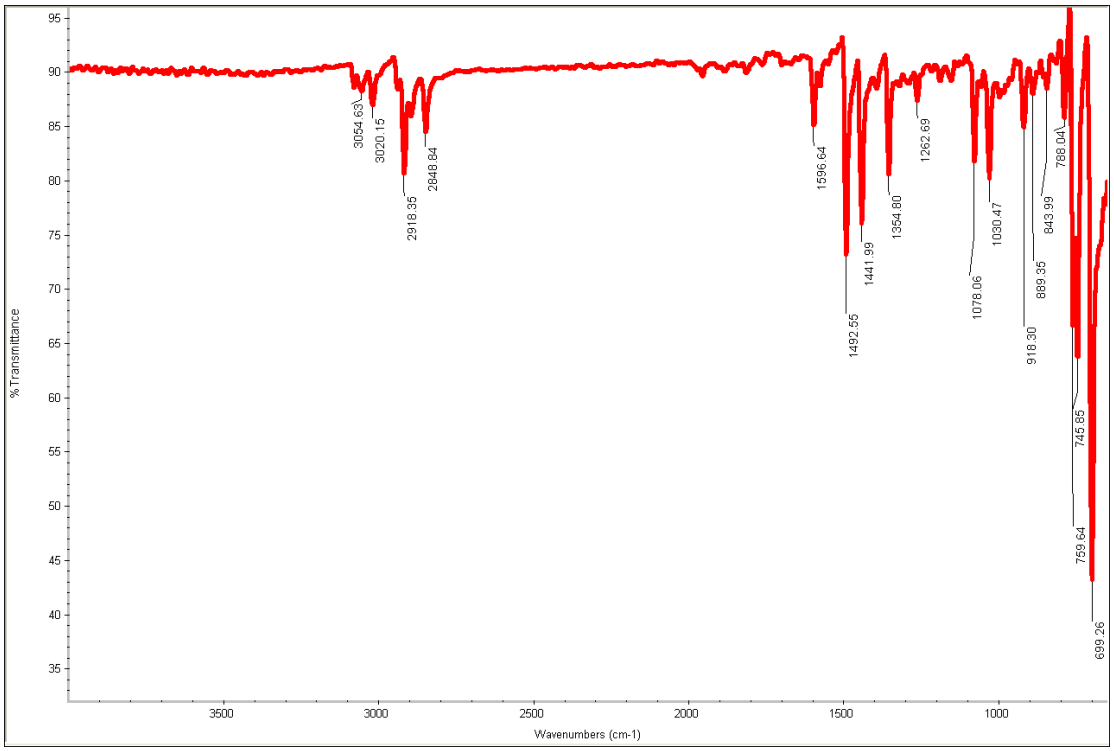

Figure C. 26 FT-IR spectrum of 1,3,5,7-tetraphenyladamantane (**TPA**).

Appendix D - Additional material for Chapter 5

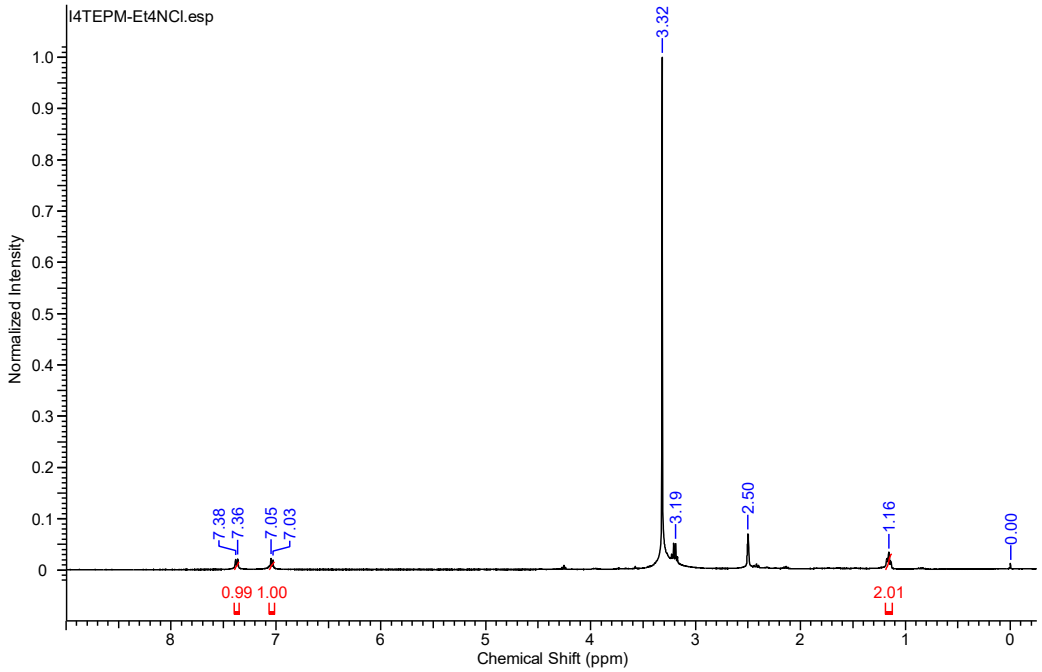

Figure D. 1 ^{1}H-NMR (400 MHz, DMSO-d6) spectrum of 2**I$_4$TEPM**·3Et$_4$N$^+$Cl$^-$ crystals.

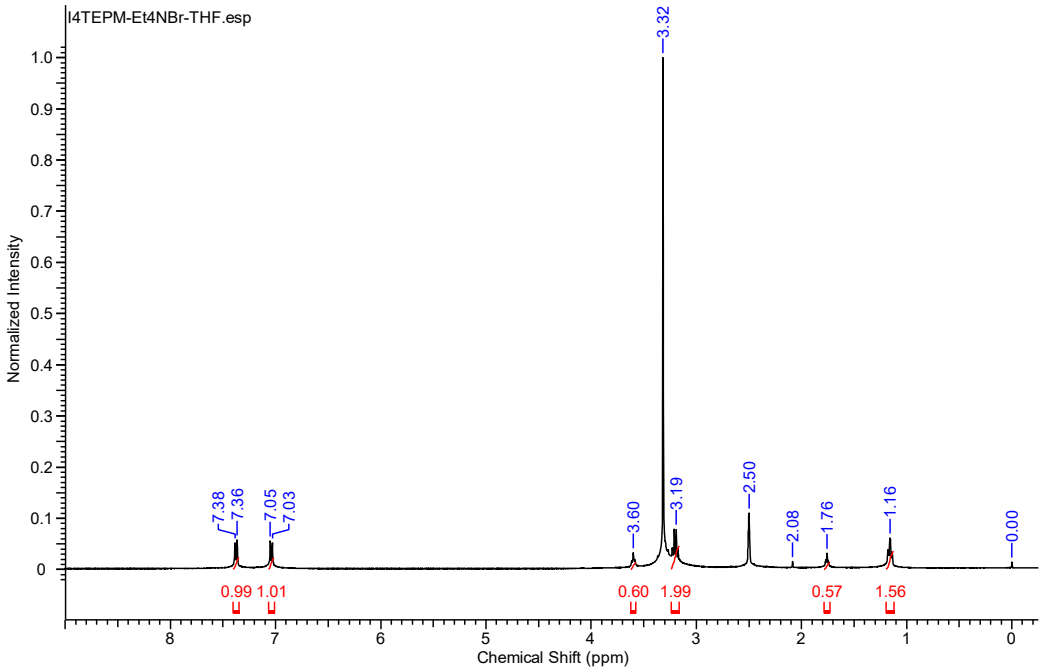

Figure D. 2 ^{1}H-NMR (400 MHz, DMSO-d6) spectrum of **I$_4$TEPM**·Et$_4$N$^+$Br$^-$·THF crystals.

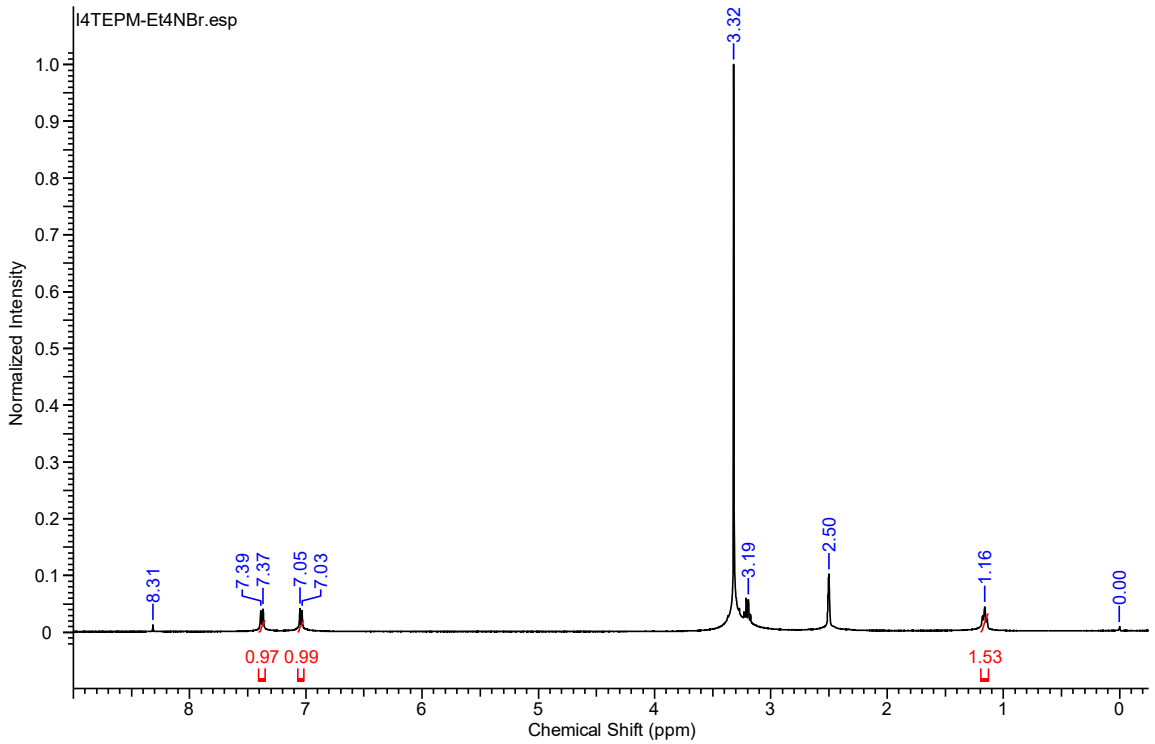

Figure D. 3 ^{1}H-NMR (400 MHz, DMSO-d6) spectrum of **I$_4$TEPM**·Et$_4$N$^+$Br$^-$ crystals.

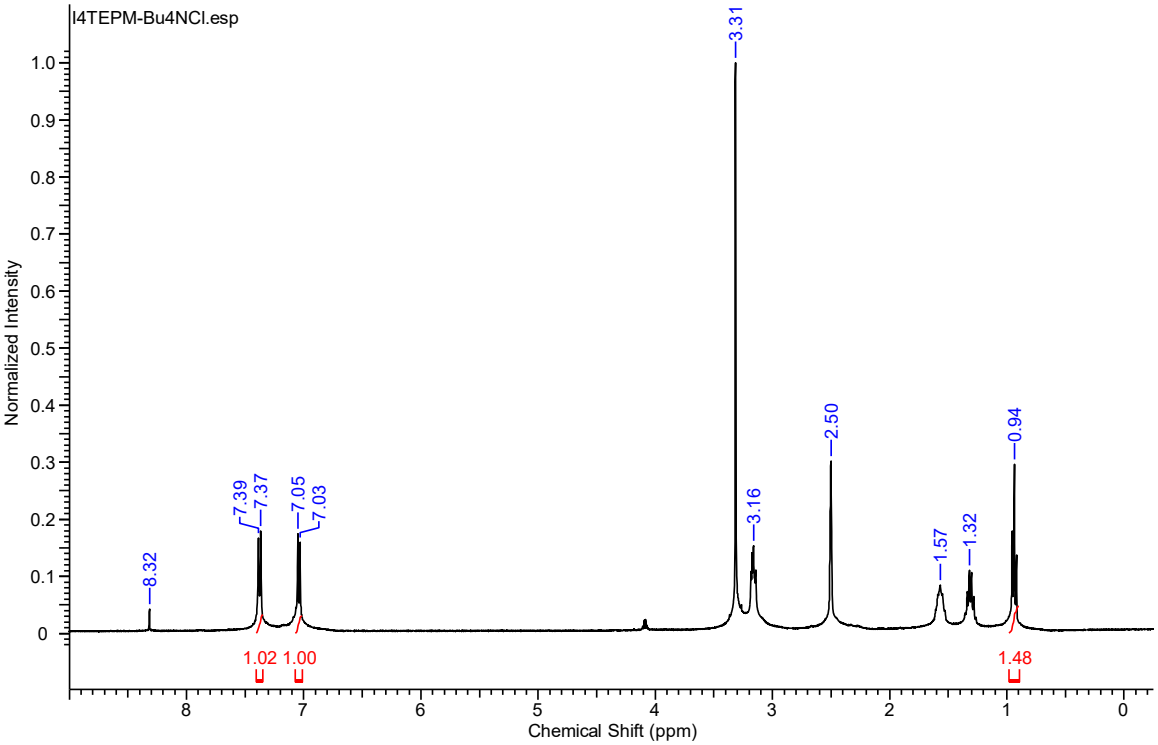

Figure D. 4 ^{1}H-NMR (400 MHz, DMSO-d6) spectrum of **I$_4$TEPM**·Bu$_4$N$^+$Cl$^-$ crystals.

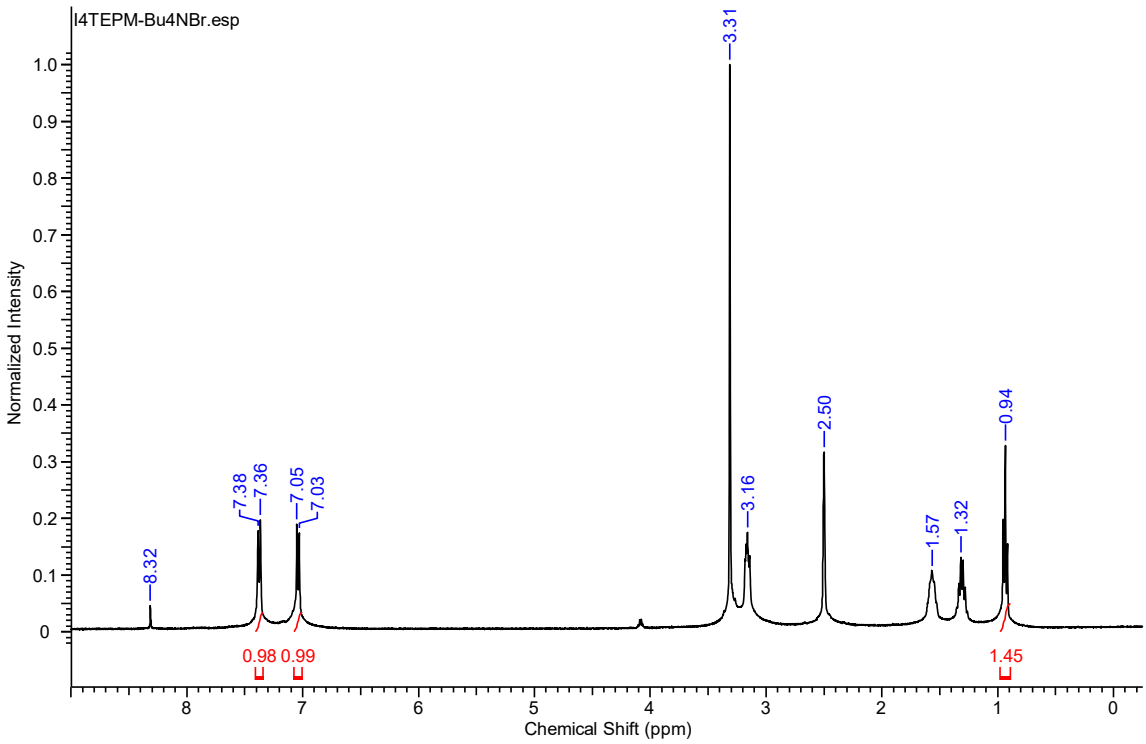

Figure D. 5 ^{1}H-NMR (400 MHz, DMSO-d6) spectrum of **I$_4$TEPM**·Bu$_4$N$^+$Br$^-$ crystals.

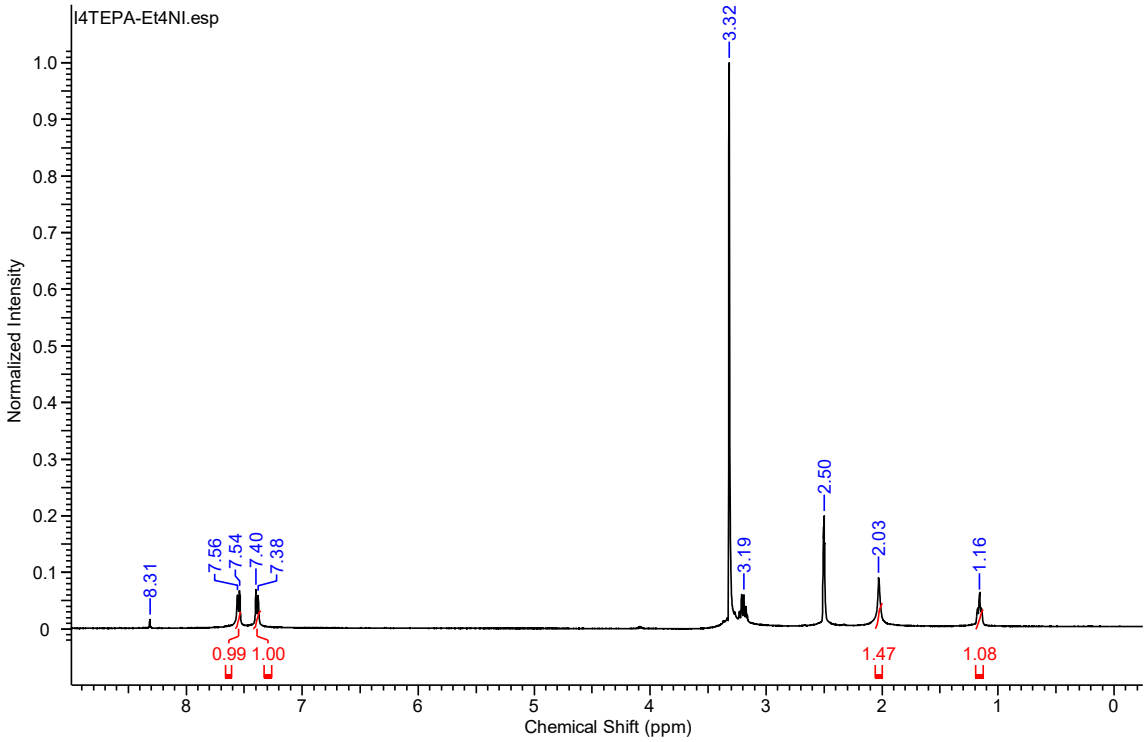

Figure D. 6 ^{1}H-NMR (400 MHz, DMSO-d6) spectrum of 3**I$_4$TEPA**·2Et$_4$N$^+$I$^-$ crystals.

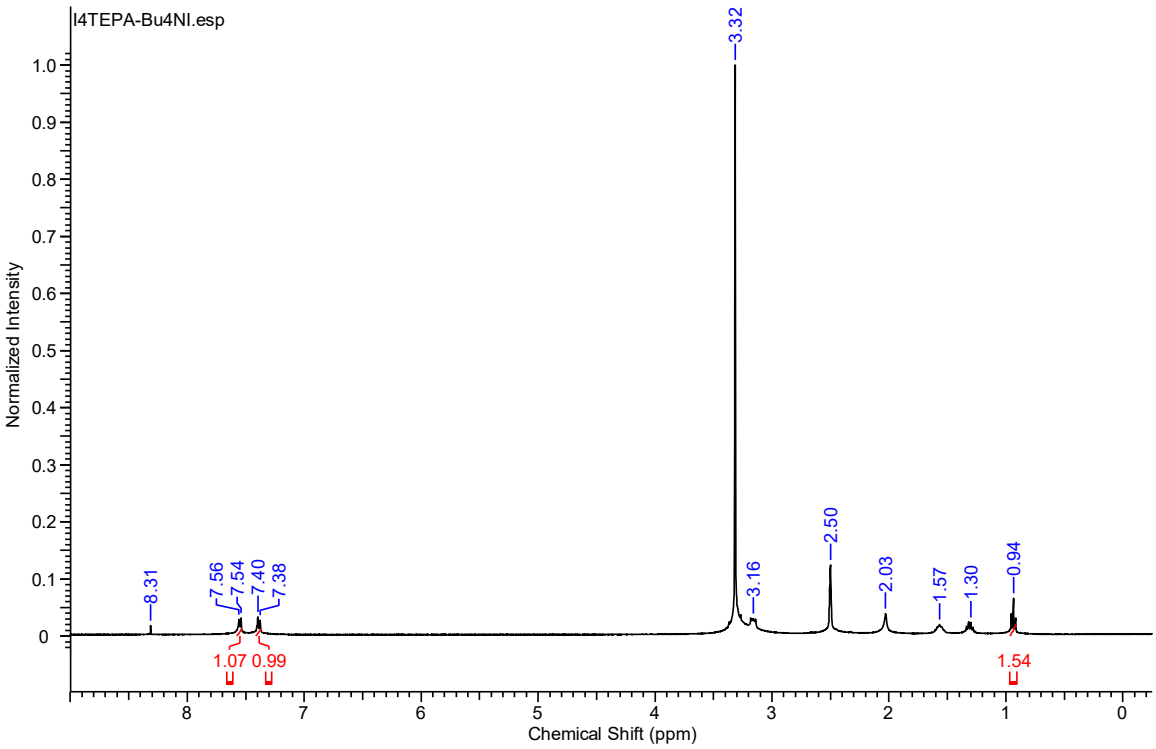

Figure D. 7 ^{1}H-NMR (400 MHz, DMSO-d6) spectrum of **I$_4$TEPA**·Bu$_4$N$^+$I$^-$ crystals.

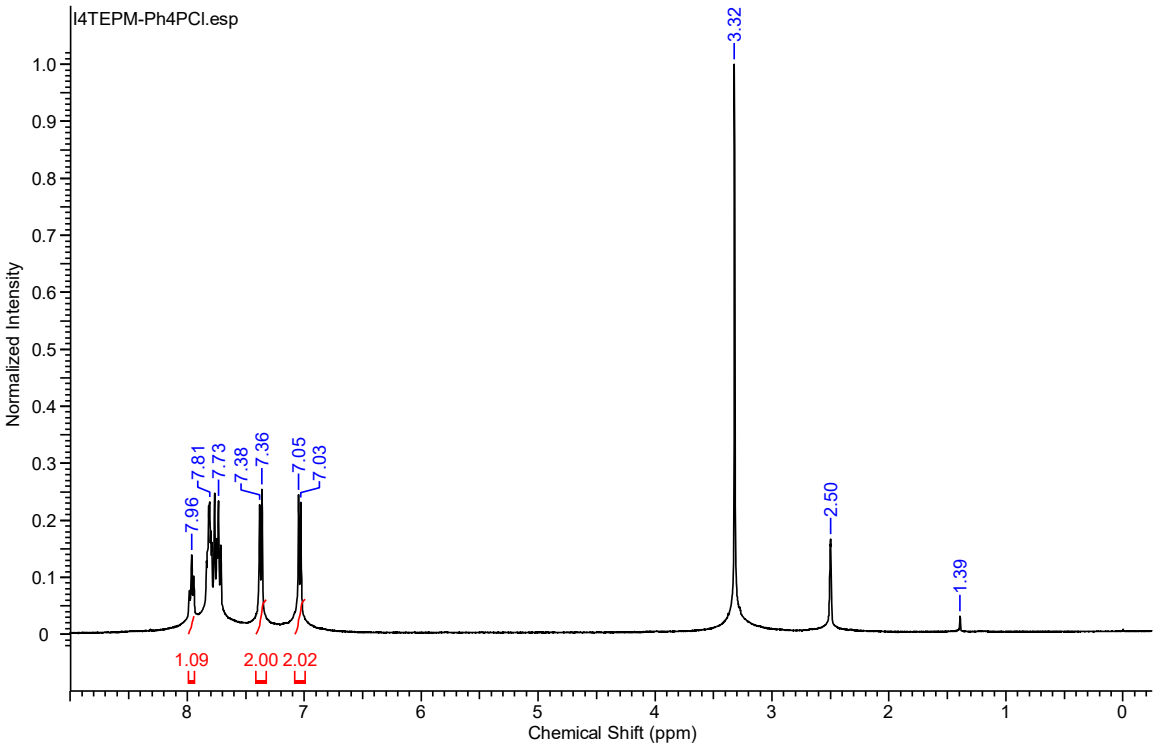

Figure D. 8 ^{1}H-NMR (400 MHz, DMSO-d6) spectrum of **I$_4$TEPM**·Ph$_4$P$^+$Cl$^-$ crystals.

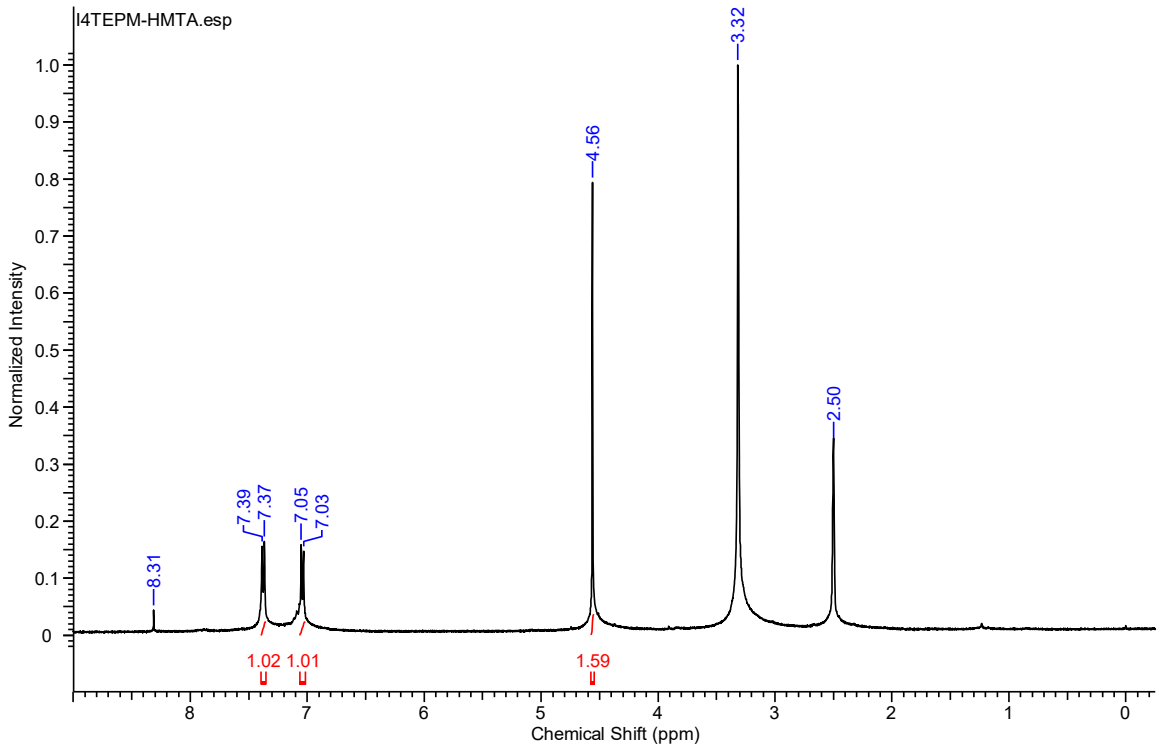

Figure D. 9 ^{1}H-NMR (400 MHz, DMSO-d6) spectrum of **I$_4$TEPM**·HMTA microcrystals.

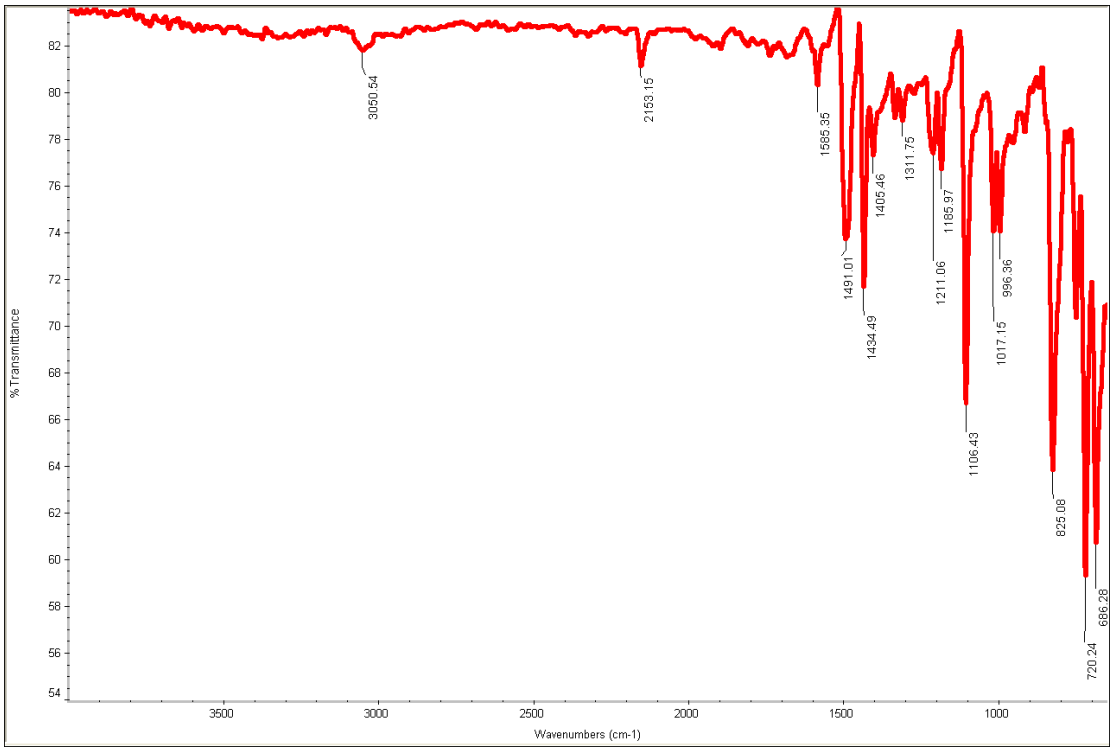

Figure D. 10 FT-IR spectrum of **I$_4$TEPM**·Ph$_4$P$^+$Cl$^-$ crystals.

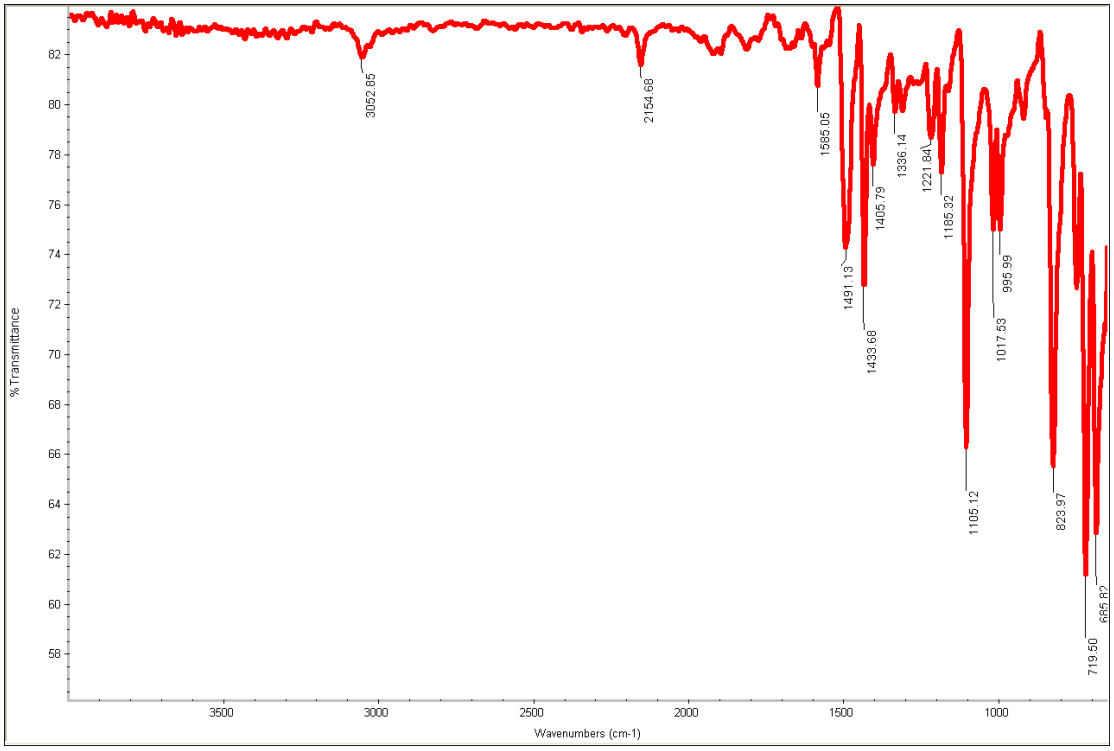

Figure D. 11 FT-IR spectrum of **I$_4$TEPM**·Ph$_4$P$^+$Br$^-$ crystals.

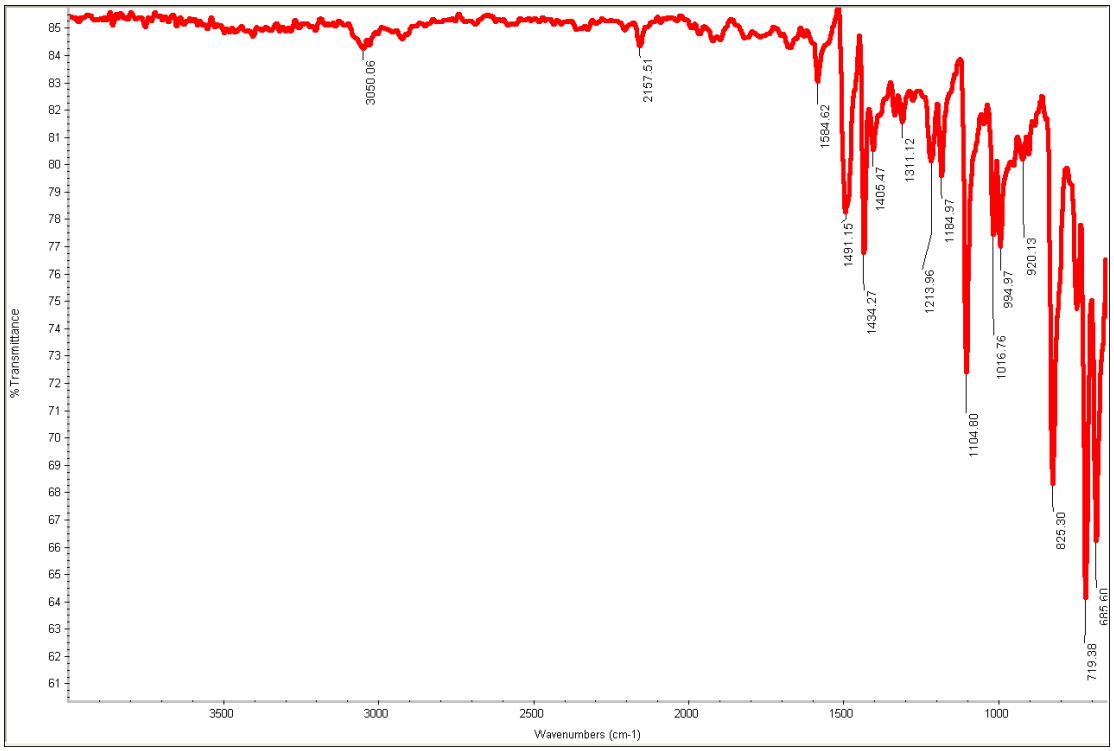

Figure D. 12 FT-IR spectrum of **I$_4$TEPM**·$Ph_4P^+I^-$ crystals.

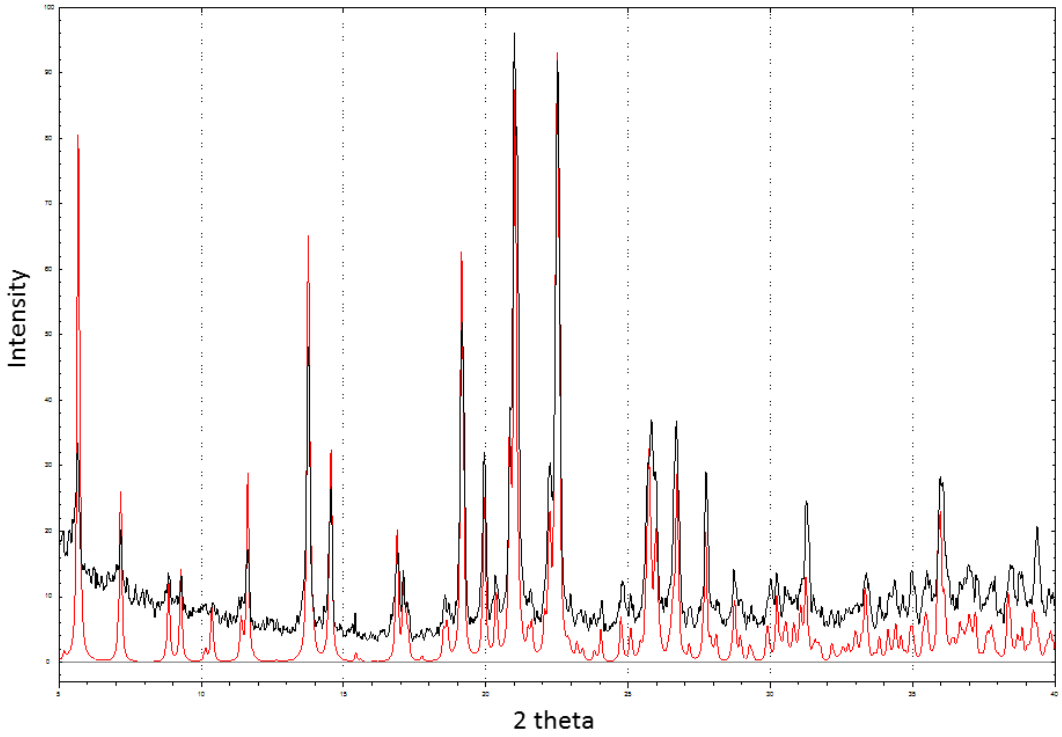

Figure D. 13 PXRD pattern of **I$_4$TEPM**·$Ph_4P^+Br^-$ (top - experimental, bottom - simulated).

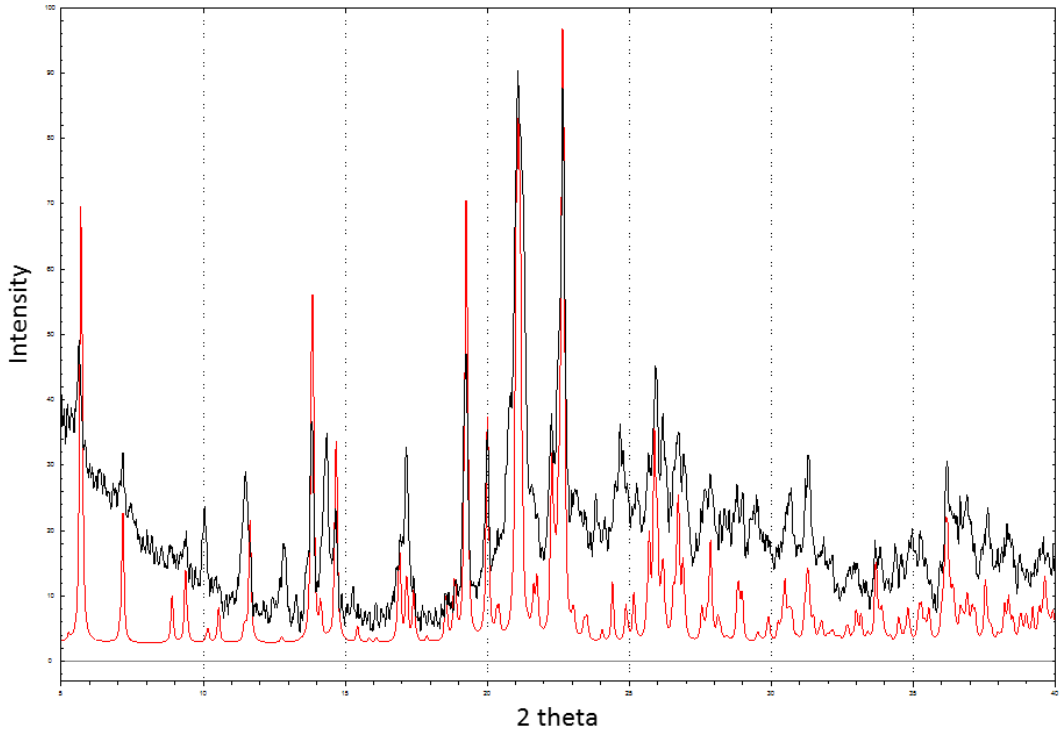

Figure D. 14 PXRD pattern of **I$_4$TEPM**·$Ph_4P^+Cl^-$ (top - experimental, bottom - simulated).

Table D. 1 Crystallographic data for the co-crystals.

Code	**I4TEPM**·$Ph_4P^+Cl^-$	**I4TEPM**·$Ph_4P^+Br^-$	**I4TEPM**·$Ph_4P^+I^-$
Formula moiety	($C_{33}H_{16}I_4$) ($C_{24}H_{20}PCl$)	($C_{33}H_{16}I_4$) ($C_{24}H_{20}PBr$)	($C_{33}H_{16}I_4$) ($C_{24}H_{20}PI$)
Empirical formula	$C_{57}H_{36}ClI_4P$	$C_{57}H_{36}BrI_4P$	$C_{57}H_{36}I_5P$
Molecular weight	1297.88	1339.34	1386.33
Color, Habit	Yellow, block	Yellow, prism	Yellow, plate
Crystal system	Monoclinic	Monoclinic	Monoclinic
Space group, Z	*I*2/*a*, 8	*I*2/*a*, 8	*I*2/*a*, 8
a, Å^3	17.3730(6)	17.4076(9)	17.4190(11)
b, Å^3	17.4497(7)	17.4445(11)	17.3989(8)
c, Å^3	33.5122(11)	34.0495(19)	34.9081(17)
α, °	90.00	90.00	90.00
β, °	90.168(4)	90.184(4)	90.638(6)
γ, °	90.00	90.00	90.00
Volume, Å^3	10159.3(6)	10339.7(10)	10579.0(10)
Density, g/cm^3	1.693	1.721	1.741
Temperature, °K	296(2)	296(2)	296(2)
Crystal size, mm (min × mid × max)	0.34 × 0.38 × 0.56	0.28 × 0.32 × 0.58	0.19 × 0.51 × 0.59
X-ray wavelength, Å	0.71073	0.71073	0.71073
μ, mm^{-1}	2.574	3.250	3.005
Absorption corr	multi-scan	multi-scan	multi-scan
Trans min / max	0.70163 / 1.000	0.607 / 1.000	0.298 / 1.000
θ_{min}, °	4.261	4.256	4.251
θ_{max}, °	27.000	27.000	27.000
Reflections			
collected	22677	23245	26629
independent	11108	11248	10852
observed	7817	7251	6446
Threshold expression	>2σ(I)	>2σ(I)	>2σ(I)
R1 (observed)	0.0571	0.0661	0.0709
wR_2 (all)	0.1620	0.1491	0.1743
Goodness of fit (all)	1.040	1.075	1.046
Δρ max / min	2.018 / -0.695	1.306 / -0.657	0.816 / -1.185
2θ limit	25.24	25.24	25.24
Completeness to 2θ limit	0.996	0.996	0.938

Table D. 2 Halogen bonding features of the co-crystals.

Compound	C–I···X⁻	*d*(I···X⁻)/Å	*nd*	*rr*/%	∠(C–I···X⁻)/°
I₄TEPM·$Ph_4P^+Cl^-$	C9–I1···Cl1	3.1326(14)	0.827	17.35	166.4(2)
	C17–I2···Cl1[a]	3.1734(15)	0.837	16.27	170.2(2)
	C25–I3···Cl1[b]	3.1064(14)	0.820	18.04	177.4(2)
	C33–I4···Cl1[c]	3.1137(14)	0.822	17.84	176.8(2)
I₄TEPM·$Ph_4P^+Br^-$	C9–I1···Br1	3.1984(9)	0.812	18.82	177.5(2)
	C17–I2···Br1[d]	3.2492(9)	0.825	17.53	165.7(2)
	C25–I3···Br1[e]	3.2051(10)	0.813	18.65	176.2(2)
	C33–I4···Br1[f]	3.2705(10)	0.830	16.99	170.7(3)
I₄TEPM·$Ph_4P^+I^-$	C9–I2···I1	3.3758(10)	0.808	19.24	176.6(3)
	C17–I3···I1[g]	3.4470(10)	0.825	17.54	173.1(4)
	C25–I4···I1[h]	3.4126(10)	0.816	18.36	165.8(3)
	C33–I5···I1[i]	3.3807(9)	0.809	19.12	176.3(3)

Normalized distance, $nd = d_{xy}/(r_x + r_y)$, where d_{xy} is the crystallographically determined XB distance, and r_x and r_y are the appropriate (van der Waals or revised Shannon-Prewitt effective ionic) radii for the two involved species, organic iodine atom and the inorganic halide ion (I = 1.98 Å, Cl^- = 1.81 Å, Br^- = 1.96 Å, I^- = 2.20 Å). Radii reduction, *rr* (%) = (1 − *nd*) × 100. Symmetry transformations used to generate equivalent atoms: [a]-1/2+x,1/2+y,1/2+z. [b]-1+x,y,z. [c]-1/2+x,-1/2+y,1/2+z. [d]1+x,y,z. [e]1/2+x,1/2+y,1/2+z. [f]1/2+x,-1/2+y,1/2+z. [g]1/2+x,1/2+y,-1/2+z. [h]1+x,y,z. [i]1/2+x,-1/2+y,-1/2+z.